Fluorescence microscopy: A statistics-optics perspective

Mohamadreza Fazel

Department of Physics, Arizona State University, Tempe, Arizona, USA
and Center for Biological Physics, Arizona State University, Tempe, Arizona, USA

Kristin S. Grussmayer

Department of Bionanoscience, Faculty of Applied Science
and Kavli Institute for Nanoscience, Delft University of Technology, Delft, Netherlands

Boris Ferdman

Russel Berrie Nanotechnology Institute and
Department of Biomedical Engineering, Technion—Israel Institute of Technology, Haifa, Israel

Aleksandra Radenovic

Laboratory of Nanoscale Biology, Institute of Bioengineering,
Ecole Polytechnique Federale de Lausanne (EPFL), Lausanne, Switzerland

Yoav Shechtman

Russel Berrie Nanotechnology Institute and
Department of Biomedical Engineering, Technion—Israel Institute of Technology, Haifa, Israel

Jörg Enderlein

III. Institute of Physics—Biophysics, Georg August University, Göttingen, Germany

Steve Pressé*

Department of Physics, Arizona State University, Tempe, Arizona, USA,
Center for Biological Physics, Arizona State University, Tempe, Arizona, USA,
and School of Molecular Sciences, Arizona State University, Tempe, Arizona, USA

(published 5 June 2024)

Fundamental properties of light unavoidably impose features on images collected using fluorescence microscopes. Accounting for these features is often critical in quantitatively interpreting microscopy images, especially those gathering information at scales on par with or smaller than light's emission wavelength. Here the optics responsible for generating fluorescent images, fluorophore properties, and microscopy modalities leveraging properties of both light and fluorophores, in addition to the necessarily probabilistic modeling tools imposed by the stochastic nature of light and measurement, are reviewed.

DOI: 10.1103/RevModPhys.96.025003

CONTENTS

*Corresponding author: spresse@asu.edu

I. INTRODUCTION

A. A history of optics

The ancient Greeks were divided over whether vision arose from rays entering or leaving the eyes (Darrigol, 2012; Thibodeau, 2016). For instance, atomists believed that perception arose from an atom flux traveling through space to the eyes. Aristotle (384–322 BCE) later proposed the notion of ether serving as a medium for transmission of intrinsic qualities of objects to the eye rather than fluxes of atoms. An alternative formulation advocated by Pythagoras (570–495 BCE) and Euclid (325–270 BCE) proposed the notion of ocular fire whose rays impassively scanned their surroundings. Following this logic, Euclid established a geometric optics explaining the perception of size and angles from the geometry of these ocular rays. Along these same lines, the Chinese philosopher Mo Di (470–391 BCE) established a geometric optics similar to Euclid's explaining the formation of shadows and images in mirrors (Wang and Wang, 2008).

An amalgam of these ideas with fire originating from the eyes coalescing with another fire derived from objects enabling vision was perhaps now demanded on philosophical grounds and promoted by Plato (427–347 BCE). In Ptolemy's optics (100–170 CE), sunlight activated objects whose emitted rays now interacted with visual rays to give rise to perception. In Ptolemy's theory, perception relied on the angular distribution, length, refraction, and reflection of rays from the eye (Smith, 1996; Darrigol, 2012).

Although these early Greek theories appear manifestly naive, emerging notions of geometric optics served as a starting point for Medieval Arabs, who took a decidedly more phenomenological approach. For example, inspired by Euclid's geometric optics Al-Kindi (801–873 CE) demonstrated that visual rays travel in straight lines by simple experiments on shadows (Darrigol, 2012). This early progress was followed by insights from Ibn al-Heytham [latinized as Alhazen (965–1040 CE)], who showed that eyesight is derived from light rays received by the eyes from objects (Nasr and De Santillana, 1968; Darrigol, 2012). Further, Ibn al-Heytham consistently devised experiments to test his theories, including theories on refractive and reflective properties of light rays on boundaries, lenses, spherical mirrors, etc. (Nasr and De Santillana, 1968; Kriss and Kriss, 1998; Tbakhi and Amr, 2007; Darrigol, 2012).

The distribution of Latin translations of Alhazen's *Book of Optics* (Al-Khalili, 2015), among other ancient works, ultimately sparked a renaissance that presages the onset of modern optics in Europe. From the democratization of knowledge driven by the Gutenberg presses followed refractive telescopes attributed to the Dutch spectacle makers Zacharias Janssen (1585–1638 CE) and Hans Lippershey (1570–1619 CE) and reflecting telescopes attributed to Issac Newton (1643–1727 CE) (Bardell, 2004). In contrast to telescopes, there is uncertainty regarding the original inventor of the microscope, though it is often credited to Zacharias Janssen (Kriss and Kriss, 1998; Chung and Liu, 2017).

From the start, the worlds of microscopy and biology were intertwined: the Dutch businessman and scientist Antonie van Leeuwenhoek (1632–1732 CE) exploited his microscope to single-handedly discover bacteria, sperm cells, and red blood cells, among other actors dominating the microscopic realm (Chung and Liu, 2017). Little in this regard has changed throughout history, with sizes, features, and other optical properties of the natural world guiding the design of modern microscopes. Subsequent *compound* microscopes (Gest, 2004), also credited to Janssen and foreshadowing our multilens microscopes, provided improved magnification and were widely used by Robert Hooke (1635–1703 CE) (Gest, 2004), author of the first book on microscopes, *Micrographia*.

Now taken for granted successive properties of light (including diffraction, refraction, reflection, and light's particulate nature) were each individually leveraged in microscope development with diffraction through an aperture first reported by the Italian Jesuit Francesco Maria Grimaldi (1618–1663 CE), followed by a number of discoveries culminating in the electromagnetic theory of Maxwell (1831–1879 CE) and theories on light's quantization (Planck, 1901, Einstein, 1905) attributed to Planck (1858–1947 CE) and Einstein (1879–1955 CE).

Setting aside noteworthy later microscopy advances, including phase imaging (Popescu, 2011; Park, Depeursinge, and Popescu, 2018), we interrupt history to pause at fluorescence microscopy, which has dominated the scene over the last half century, as smaller scales demanded increased contrast between the background and the object of interest (Lichtman and Conchello, 2005). At such scales, the stochastic properties of light intrinsic to quantum mechanics dictate our ability to interpret fluorescence microscopy data and return us to the primary focus of this review: fluorescence microscopy from a statistics-optics perspective.

Modeling light's stochastic properties is not an exercise in mitigating the recurring nuisance of shot noise. It is instead fundamental to how we draw insights on the scales at which

fluorescence microscopy has unraveled. In fact, a fluorescent photon's emission time, absorption time, emission wavelength, and detection location, i.e., where a photon is detected on an image plane, are all random variables. These random variables themselves are drawn from probability distributions. In the classical limit, the probability density for locating photons is proportional to the time-averaged energy flux given by Poynting's theorem (Poynting, 1884), which was introduced by John Henry Poynting (1852–1914 CE). For point-like sources of light such as fluorophores, the normalized spatial distribution, coinciding with a slice orthogonal to the propagation direction, is termed the point spread function (PSF). This inherent randomness in a photon's location, imperfectly detected and reporting only probabilistically on a fluorescent object of interest, introduces multiple levels of stochasticity between the object whose properties we care to characterize and the measurement output. This unavoidably introduces statistical concepts, including notions of latent variables and hierarchical probabilistic models, in the quantitative modeling of imaging systems.

The manipulation of hierarchical dependencies between random variables then requires what is known today as Bayes's theorem. The theorem, attributed to its namesake Thomas Bayes (1702–1761 CE), was popularized by Pierre-Simon de Laplace (1749–1827 CE), who introduced and codified, through seminal texts on probability (Laplace, 1820, 1840), probabilistic modeling to the sciences (Dale, 1982). Before we return to microscopy, we now take a detour to discuss statistical modeling relevant to our future applications.

B. Introduction to statistical modeling

The photon, the electromagnetic force carrying a particle, is intrinsically both wavelike and particulate. While the continuous spatial distributions over a photon's location are dictated by the photon's wave properties, photon detections themselves are necessarily pointillistic and probabilistic. As such, even before other sources of stochasticity like detection are considered, a quantitative picture of microscopy demands at its most fundamental level an exposition of the theory of statistical sampling.

Here we first lay out the main concepts for probabilistic modeling. We then discuss the concept of likelihoods and Bayesian inference that are key to the statistical frameworks introduced throughout this review.

1. Basic concepts and notation

Stochasticity in a system arises from the inherent random nature of the physical system, the measurement noise, or both. Both elements are relevant in quantitative microscopy, and thus we minimally require two layers of stochasticity: at the level of photon shot noise and at the level of detection; see Appendix A. Shortly we also see that additional levels of stochasticity may arise from the behavior of fluorescent labels.

For this reason, we begin by defining the requisite notions of a random variable. A random variable $\mathfrak{R}$ follows the statistics of a probability distribution $\mathbb{P}$. As such, we often write $\mathfrak{R} \sim \mathbb{P}$, which reads, "the random variable $\mathfrak{R}$ is sampled from the probability distribution $\mathbb{P}$." We then denote $\mathfrak{r}$ a particular realization of $\mathfrak{R}$ and $p(\mathfrak{r})$ the probability density associated with the probability distribution $\mathbb{P}$.

Generally the probability distribution itself depends on the parameters ϑ. To make such dependency explicit, we can write $p(\mathfrak{r};\vartheta)$ and $\mathbb{P}(\vartheta)$ (Pressé and Sgouralis, 2023). For example, the location at which the photon is detected is itself a random variable R sampled from a distribution centered at the emitting molecule's location $\mathbf{r}_0$. As such, we write

$$R \sim U(\mathbf{r}_0), \tag{1}$$

$$p(\mathbf{r};\mathbf{r}_0) = U(\mathbf{r};\mathbf{r}_0), \tag{2}$$

where $\vartheta \equiv \mathbf{r}_0$ and $p(\mathbf{r};\vartheta)$ is the probability density, i.e., the PSF, from which $\mathbf{r}$ is drawn.

It is often of interest to compute the probability of obtaining a value from a subset η of the possible values ($\mathfrak{r} \in \eta$) given by

$$\mathcal{P}_\eta = \int_\eta d\mathfrak{r}\, p(\mathfrak{r};\vartheta). \tag{3}$$

By definition if η is the entire set of options, then $\mathcal{P}_\eta = 1$. For instance, the probability of a photon reaching a pixel is given by the integral of the PSF over the pixel area $\mathcal{A}$

$$\mathcal{P}_{\text{pix}} = \int_{\mathcal{A}} U(\mathbf{r};\mathbf{r}_0) d\mathbf{r}. \tag{4}$$

In probabilistic modeling, we often work with many random variables $\mathfrak{R}_1, \mathfrak{R}_2, \ldots, \mathfrak{R}_N$ at once. For this reason, we define the joint density as

$$p(\mathfrak{r}_{1:N};\vartheta) = p(\mathfrak{r}_1, \mathfrak{r}_2, \ldots, \mathfrak{r}_N;\vartheta). \tag{5}$$

The density of any individual $\mathfrak{r}_n$ is then obtained by integrating the joint density with respect to all values of $\mathfrak{r}_{1:n-1}$ and $\mathfrak{r}_{n+1:N}$ as

$$p(\mathfrak{r}_n;\vartheta) = \int d\mathfrak{r}_{1:n-1} d\mathfrak{r}_{n+1:N} p(\mathfrak{r}_{1:N};\vartheta). \tag{6}$$

Equation (6), which is termed a marginalization, results in a marginal density $p(\mathfrak{r}_n;\vartheta)$. Marginalization is often useful in computing, say, the probability over the diffusion coefficient of an emitter (a fluorescently labeled molecule or dye) irrespective (and thus integrating over) its exact location in space. This is later explored in Fig. 69.

If the random variables $\mathfrak{R}_{1:N}$ are independent and identically distributed (i.i.d), then Eq. (5) assumes the simpler form

$$\mathfrak{R}_1, \mathfrak{R}_2, \ldots, \mathfrak{R}_N \overset{\text{i.i.d.}}{\sim} \mathbb{P}(\vartheta), \tag{7}$$

with the understanding that the joint density decomposes into the product of independent densities $p(\mathfrak{r}_1;\vartheta), p(\mathfrak{r}_2;\vartheta), \ldots, p(\mathfrak{r}_N;\vartheta)$. For example, i.i.d. random variables include photon arrival times following pulsed excitation for a static distribution of molecules, as later explored in Fig. 46.

In general, random variables are not independent, such as the position of a molecule in time where the system's state

depends on its state at a previous time point either exactly or by approximation. This dependency, which is explored in the context of fluorophore dynamics in Sec. II.C and Appendix B, is termed the Markov assumption. In this case, we say that values that can be ascribed to $\mathfrak{R}_2$ depend on the realization of a preceding random variable $\mathfrak{r}_1$. This dependency is often expressed as

$$\mathfrak{R}_2|\mathfrak{r}_1,\vartheta \sim \mathbb{P}(\mathfrak{r}_1,\vartheta), \tag{8}$$

which reads, "the random variable $\mathfrak{R}_2$ given the parameters ϑ and realization (or "conditioned on") $\mathfrak{r}_1$ of $\mathfrak{R}_1$ is sampled from the probability distribution $\mathbb{P}(\mathfrak{r}_1,\vartheta)$." The density that we associate with this probability distribution then reads $p(\mathfrak{r}_2|\mathfrak{r}_1,\vartheta)$ and is referred to as a conditional density. In general a random variable $\mathfrak{R}_N$ can depend on many other random variables $\mathfrak{R}_{1:N-1}$ with associated conditional density $p(\mathfrak{r}_N|\mathfrak{r}_{1:N-1},\vartheta)$. Such conditionals will become useful as we build hierarchical models relating random variables across our boxed environments presented as figures.

Bayes's theorem, which is of central importance in expressing hierarchical random variable dependencies, then follows from the observation that conditional densities such as $p(\mathfrak{r}_{1:2}) = p(\mathfrak{r}_2|\mathfrak{r}_1)p(\mathfrak{r}_1)$ satisfy $p(\mathfrak{r}_{1:2}) = p(\mathfrak{r}_{2:1})$ and thus

$$p(\mathfrak{r}_1|\mathfrak{r}_2)p(\mathfrak{r}_2) = p(\mathfrak{r}_2|\mathfrak{r}_1)p(\mathfrak{r}_1). \tag{9}$$

As is customary in physics, we relax notation and denote both random variables and their realizations with lowercase letters. The distinction between the two notions is implied by the context throughout the review.

2. Likelihood

We now introduce the object at the heart of quantitative analysis of microscopy data: the likelihood. The likelihood is a probability distribution over random variables coinciding with K experimental observations $w_{1:K}$ conditioned on ϑ. The likelihood's density is thus written as $p(w_{1:K}|\vartheta)$, where $w_{1:K} = \{w_1, w_2, \ldots, w_K\}$. It is also convenient to denote this set with an overbar: $\bar{w}$.

The term likelihood follows from the notion that $p(w_{1:K}|\vartheta)$ is a likelihood of observing the sequence of observations $w_{1:K}$ under the assumptions of the model (i.e., calibrated values for parameters ϑ of a particular model). Indeed, all box environments in multiple figures in the review contain likelihoods for each statistical framework presented.

As the parameters are themselves unknown, we often ask what values for these parameters maximize the likelihood of the observed sequence $w_{1:N}$. These parameter values are called estimators and are denoted by $\hat{\vartheta}$. For example, we can ask what values of the excited-state lifetime (assuming one fluorophore species) make the photon arrival times observed most probable; see Fig. 46.

For practical reasons, it is common to work with, and maximize, the likelihood's logarithm $\mathcal{L}(w_{1:K}|\vartheta) = \log[p(w_{1:K}|\vartheta)]$, sometimes termed the log-likelihood rather than the likelihood itself; see Sec. V.C. This is because the logarithm both is monotonic with the original function and avoids numerical underflow typical of small probability densities arising as K grows.

Within a maximum likelihood estimation (MLE) framework, ϑ are treated as fixed deterministic parameters and the data $w_{1:K}$ and are understood as realized random variables. While the MLE yields a single value (estimator) for the parameters, the uncertainty around the parameter estimate is captured by computing the likelihood's breadth around its maximum. The breadth is often estimated as

$$\sigma^2_{\vartheta_l} = [\mathcal{Q}(\vartheta)^{-1}]_{ll}, \tag{10}$$

where l counts the elements of the model parameter set ϑ. In Eq. (10) $\mathcal{Q}(\vartheta)$ is the Fisher information matrix defined as (Rao, 1992; Cramér, 1999)

$$\mathcal{Q}_{ll'}(\vartheta) = -\mathbb{E}\left[\frac{\partial^2\mathcal{L}(w_{1:K}|\vartheta)}{\partial\vartheta_l\vartheta_{l'}}\bigg|_{\hat{\vartheta}}\right], \tag{11}$$

where $\mathbb{E}$ denotes the expected value of the expression within the parentheses. As Eq. (10) sets the variance (an uncertainty bound) around the MLE, it is sometimes termed the Cramér-Rao lower bound (CRLB).

As evident, MLE-based approaches present challenges for likelihoods with multiple degenerate maxima or, more importantly, when the model is unknown. What is more, even assuming a model form the MLE provides only a point estimate, not a full distribution over the putative parameter values.

It is for all these reasons that we often turn to a more general Bayesian paradigm. In this setting, we use the likelihood to construct the distribution over the parameters of interest given the observed data $p(\vartheta|w_{1:K})$. The latter object is termed the posterior and is central to Bayesian inference.

3. Posterior

In working with likelihoods, the data are understood as random variables and parameters ϑ as fixed but to be determined. In contrast, in a Bayesian setting both the data and the parameters are random variables. In particular, the data are random variables that are already realized and whose values are used to construct the probability $p(\vartheta|w_{1:K})$ over the unknown random variables ϑ. The Bayesian paradigm allows proper propagation of uncertainty over ϑ from all sources, including detector noise, camera pixelation, motion aliasing, photon shot noise, etc.

The posterior is constructed from the likelihood by invoking Bayes's theorem [Eq. (9)],

$$p(\vartheta|w_{1:K}) = \frac{p(w_{1:K}|\vartheta)p(\vartheta)}{p(w_{1:K})}, \tag{12}$$

where by normalization

$$p(w_{1:K}) = \int d\vartheta p(w_{1:K}|\vartheta)p(\vartheta). \tag{13}$$

In Eqs. (12) and (13) $p(\vartheta)$, termed the prior, provides a means to regulate the parameters. For instance, determining a range

over which nonzero values of the density arise, for example, positive or integer values, prior to considering the data.

Thus, from Bayes's theorem we obtain a clear recipe $w_{1:K}$ by which the prior distribution is updated from the data encoded in the likelihood to determine the posterior $p(\vartheta|w_{1:K})$. To avoid priors biasing posteriors, K must be sufficiently large (McNeish, 2016; Smid *et al.*, 2020; Van de Schoot and Miocević, 2020; Zitzmann *et al.*, 2021). However, even with large datasets the prior may still impact the posterior in cases including degenerate flat likelihoods, a number of unknowns that increases with more data, and priors excluding regions of parameter space warranted by the data (i.e., priors set to zero in those regions) (Gelman *et al.*, 1995; Le Cam and Yang, 2000).

As we see in all applications, likelihoods can generally be constructed from knowledge of the microscopy technique and the physics of the problem, while priors are normally determined by prior belief and computational convenience. The following broad question then arises: Can we determine whether the posterior peaks at some value of ϑ? More concretely, what does our posterior look like?

Note that posteriors rarely attain simple analytic forms on account of the measurement and physics informing the likelihood. As such, values of ϑ are typically numerically sampled from posteriors using Monte Carlo methods. For example, as later discussed in the context of confocal microscopy (see Sec. IV.C), we see that ϑ includes quantities such as diffusion coefficients, emission rates, and emitter locations. As posteriors are thus often multivariate, a common Monte Carlo strategy involves sampling one random variable at a time in a scheme termed Gibbs sampling (Geman and Geman, 1984).

Whether sampling a posterior exactly or numerically, such as with Monte Carlo calculations, it is often computationally convenient to judiciously select prior functional forms. Indeed, some prior forms play a special role in Bayesian modeling by having the unique mathematical property that, when multiplied by the likelihood, results in a posterior of the same form as the original prior (albeit with updated, "renormalized" parameters). As such, we often speak of conjugate prior-likelihood pairs or, for succinctness, conjugate priors when such priors can be identified. While we do not dwell on specialized notions of Bayesian inference in the review, we point out that computational efficiency is what makes it possible to include measurement noise details at marginal added computational cost while improving the spatiotemporal resolution of any fluorescence analysis method. Indeed, whenever possible specialized Monte Carlo schemes [from Gibbs sampling (Geman and Geman, 1984) to the Metropolis-Hastings algorithm (Metropolis *et al.*, 1953; Hastings, 1970) to slice sampling (Murray, Adams, and MacKay, 2010) and beyond (Bishop and Nasrabadi, 2006; Brooks *et al.*, 2011; Pressé and Sgouralis, 2023)] used across all applications discussed here benefit from any available computational advantage.

4. Bayesian nonparametrics

In Eq. (12), we see that constructing a posterior demands a mathematical, i.e., "parametric," form of the likelihood. However, for most practical cases we often do not know which competing models describe a given dataset. We also know, and can demonstrate by way of example, that the more complicated we make a model, the larger its likelihood; i.e., we overfit the data.

Compromising between data underfitting and overfitting is at the heart of the fundamental model selection problem. From the onset, progress in model selection has been critical, for instance, in clustering problems where the number of clusters (i.e., the model) are unknown (Richardson and Green, 1997; Neal, 2000; Gelfand, Kottas, and MacEachern, 2005; Sgouralis and Pressé, 2017). Indeed, the model selection problem manifests itself across microscopy applications, for example, determining the number of molecules within a diffraction-limited spot (i.e., the model) explored in Fig. 66 or determining the number of fluorophore species in lifetime imaging explored in Fig. 46.

While heuristically comparing a fixed set of models to resolve model selection [for example, by relying on information criteria (Quan *et al.*, 2011) and other tools introduced as postprocessing steps] is computationally advantageous, such approaches present theoretical problems. For example, they are often limited to cases where we can exhaustively enumerate models, such as how many emitters in each frame across a stack of frames can we consider in any wide-field tracking application? Even if they are enumerable, how do we assign probabilities to these competing models given the data?

Answers to these questions have led to the formal development of Bayesian nonparametrics (BNPs) (Ferguson, 1973; Pressé and Sgouralis, 2023) alongside Monte Carlo tools to sample from the resulting nonparametric posteriors, including reversible jump Markov Chain Monte Carlo (Green, 1995). In short, BNPs treat model and parameter estimation on the same footing (Orieux *et al.*, 2012; Hines, Bankston, and Aldrich, 2015; Sgouralis and Pressé, 2017; Gabitto *et al.*, 2021) and construct nonparametric posteriors over both models and their associated parameters.

In particular, within a nonparametric treatment we consider *a priori* an infinite number of competing models. We place priors on these models alongside their associated parameters just as we place priors on parameters alone within the regular parametric Bayesian paradigm.

One catch is that BNPs are limited to a particular class of models termed nested models. Note that many models considered across microscopy applications belong to this class. Nested models include all models that can be generated from a more general model by setting parameters to different values (including zero), with the most general model itself being infinite dimensional. For example, a two state model used in analyzing a Förster resonance energy transfer (FRET) time trace, which is explored in Sec. II.A, follows from a three state model where transitions to the third state are all set to zero. Other examples of nested models that we explore in the review include (1) the number of molecules in a diffraction-limited spot (see Figs. 66 and 59), (2) the number of fluorophore species in lifetime imaging (see Fig. 46), and perhaps less intuitively (3) all competing two-dimensional lifetime maps obtained from scanning confocal lifetime imaging; see Fig. 48.

These examples were intentionally numbered. They allow us to introduce three commonly used nonparametric priors

used in constructing nonparametric posteriors. In the order in which these examples are listed, we have the beta-Bernoulli process prior (Hjort, 1990; Paisley and Carin, 2009; Broderick, Jordan, and Pitman, 2012; Shah, Knowles, and Ghahramani, 2015; Al Labadi and Zarepour, 2018; Pressé and Sgouralis, 2023), the Dirichlet process prior (Neal, 2000; Gelfand, Kottas, and MacEachern, 2005; Sgouralis and Pressé, 2017; Sgouralis *et al.*, 2018; Gabitto *et al.*, 2021; Pressé and Sgouralis, 2023), and the Gaussian process (GP) prior (Rasmussen, 2003; Quinonero-Candela and Rasmussen, 2005; Pressé and Sgouralis, 2023).

The beta-Bernoulli process prior is used when we try to estimate the number of discrete elements contributing to the data. These could be the number of clusters or, equivalently, the number of emitters contributing photons generating an image frame or producing a stream of photons within a confocal spot; see Fig. 42. Within a BNP paradigm, we assign a Bernoulli variable (binary random variable) b_m, called a load, to each discrete element (molecule). Considering as many as M loads (and letting M eventually tend to infinity), one finds that the unknowns appearing in ϑ are augmented to include $b_{1:M}$. Thus, ϑ for the single spot confocal would now include the diffusion coefficient, emission rate, molecular locations, and the loads $b_{1:M}$.

When multiplying the likelihood by the appropriate beta-Bernoulli prior process, we can then construct a posterior whose parameters we want to sample, including the loads. The resulting posterior is in turn often sampled using Monte Carlo techniques to determine which loads are sampled mostly as 0s (and thus coincide with molecules not warranted by the data) or coincide with 1s (and thus coincide with molecules warranted by the data). The number of molecules in each draw from the posterior is then determined by summing all loads.

We now turn to the subsequent two nonparametric priors. For instance, the Dirichlet process prior is used when we want to assign probabilities to an infinite number of components, for example, when we want to determine to what degree each unique chemical species contributes photons in a lifetime experiment; see Fig. 46. Ideally, based on Monte Carlo sampling of the nonparametric posterior (obtained from the product of the likelihood and the Dirichlet process prior), we would find which of the infinite species introduced in modeling contribute non-negligibly to the data.

Finally, GP priors are used in estimating smooth functions. Smooth functions of interest in microscopy include the fluorophore density maps explored in Sec. IV.C or even smooth backgrounds for large numbers of emitters. Each of these maps consists of an infinite set of correlated random variables, i.e., values of the map at every point in space. Draws from the nonparametric posterior then assign values to each point on the map. In practice the number of map points whose value we want to deduce is kept finite and limited to a fixed number of points, typically over a uniform mesh grid termed the inducing points (Quinonero-Candela and Rasmussen, 2005; Bryan, Sgouralis, and Pressé, 2020; Fazel, Jazani *et al.*, 2022). The value of the map on a finer spatial grid can then be interpolated from the spatial correlation function already informing the GP prior. Having now introduced key notions from statistics, we turn to microscopy.

C. Basic characteristics of fluorescence microscopy

All optical microscopes use light, one way or another, to interact with the sample under observation. Indeed, bright-field, dark-field, or even phase contrast imaging differ from each other in details pertaining to which part of the excitation or detection arms are altered or blocked to create images at the detector.

However, these microscopes are limited in their ability to discern contrast at molecular and even supramolecular length scales at which life unravels. At such scales, we exploit fluorescence microscopy involving fluorophore-labeled samples, as detailed in Sec. II. When excited, fluorophores emit light that can be selectively filtered from the excitation beam to form an image. In its simplest form, a fluorescence microscope is a two-lens system: an objective lens with small focal length f_1 and a tube lens with long focal length f_2; see Fig. 1.

In modern infinity-corrected research microscopes, the objective converts the diverging spherical wave front emitted by a point emitter in the focal plane in sample space into a planar wave front. The planar wave front is then reconverted by the tube lens into a spherical wave front converging into a point on the image plane.

The two most important characteristics of a microscope are its magnification and its resolution, i.e., how well the sample features are resolved. In Fig. 1, the system's magnification is given by the ratio f_2/f_1 (from the proportionality of vertical to horizontal distances). However, the magnification of an optical microscope today is of secondary importance, as images are recorded with array detectors, such as complementary metal-oxide semiconductor (CMOS) or electron multiplying charge-coupled device (EMCCD) cameras with varying pixel size; see Appendix A. This is in contrast to visual inspections of a sample where our rod and cone cell sizes are fixed. For such wide-field microscopes equipped with a camera, the detector's physical pixel size divided by the microscope's magnification set at an upper bound on the

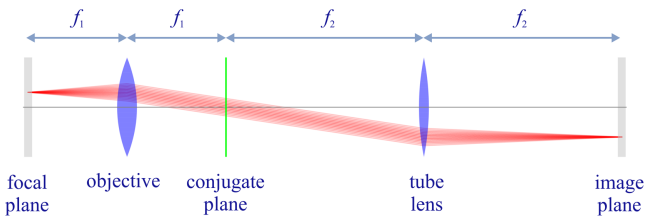

FIG. 1. Schematic of an infinity-corrected wide-field microscope consisting of an ideal objective lens with focal length f_1 and an ideal tube lens with focal length f_2. We show light propagation from a point source in the focal plane (sample space) to the image point in image space. The plane between the lenses, a distance f_1 away from the objective lens and a distance f_2 from the tube lens, is called the conjugate plane (the green vertical line). The conjugate plane is also sometimes termed the back focal plane, Fourier plane, or pupil plane. Here the light from any point source on the focal plane crosses through the same lateral position. By considerations of geometric proportion, the ratio of the lateral displacement of the image point to the lateral displacement of the source point is equal to the ratio of the focal lengths f_2/f_1. This ratio is the microscope's magnification $\mathcal{M}$.

image quality. This effective pixel size should be at least 2 times smaller than the microscope's optical resolution (the Nyquist criterion).

This leads us to the second important microscope characteristic: its resolution. The microscope resolution is limited by a number of factors including the diffraction of light and light collection by objective lenses. These two effects lead to a fundamental resolution limit of approximately half of the wavelength. As such, if the emitted light's wavelength were to be far smaller than typical dimensions of the molecular species of interest, then our review would stop here and textbooks would be filled with real-life images reminiscent of David Goodsell's artistic renderings of life inside the cell (Goodsell, 2009). However, this is not the case.

We discuss resolution of different microscope modalities more thoroughly shortly, though we start with a heuristic visualization of a fundamental microscope's optical resolution limit; see Fig. 2. There we show the far-field electric field distribution of light from two coherent point sources, designated by red dots, before an objective lens. As both point sources are assumed to emit light coherently, the resulting intensity distribution shows characteristic lanes of constructive and destructive interference. When the distance between the two point emitters y is gradually reduced (from left to right in Fig. 2), the two symmetric lanes of destructive interference (directions of zero light intensity) closest to the optical axis migrate toward higher emission angles until they reach the objective lens' edge. At that point, the objective detects only the light of a continuous spherical wave front absent any zero-intensity minima within its light detection cone (with half angle Θ), similar to what the objective would see from a single emitter.

Simple trigonometry dictates that the path difference between (1) the first emitter and the edge of the lens and (2) the second emitter and the same edge of the lens is $y \sin\Theta$. In so doing, we assumed that the separation of the lens and the emitters is much larger than y in the far-field limit. The first destructive interference lane therefore occurs at the angle Θ if the path difference is half the wavelength, i.e., $y_{\min} \sin\Theta = \lambda/2n$, where λ is the vacuum emission wavelength and n is the refractive index of the medium in which the emitters are embedded. As such, the wavelength in this medium is λ/n. Abbe's well-known resolution limit, which was first formulated by Ernst Abbe (1840–1905 CE) in 1873 (Abbe, 1873), follows from this result as

$$y_{\min} = \frac{\lambda}{2n \sin\Theta} = \frac{\lambda}{2\mathrm{NA}}, \tag{14}$$

where NA is the objective's numerical aperture.

A similar simplified consideration can also be applied toward understanding the spatial resolution of a confocal laser-scanning microscope (CLSM). In a CLSM, the sample is scanned with a tightly focused laser beam, and the excited fluorescence light is collected by the microscope optics, focused through a confocal pinhole to suppress out-of-focus light, and finally detected with a point detector (usually a silicon-based photodiode or a photoelectron multiplier tube); see Sec. IV.B.1. The recorded fluorescence light intensity as a function of scan position is then used to reconstruct an image. The fundamental advantage of a CLSM as compared to a wide-field imaging microscope is its optical sectioning capability, i.e., its capability to record true three-dimensional sample images, which is later detailed when the optical transfer functions (OTFs) of both microscope types are considered. If one momentarily neglects a CLSM's confocal detection volume, its lateral resolution is determined by how tightly a laser beam can be focused onto an excitation spot. In a mathematically more precise manner, one asks about the tightest spatial intensity modulation still present in a diffraction-limited focus. The answer is given in Fig. 3, which shows that the tightest modulation is achieved by the interference of the two light rays exiting the objective at the highest possible angle, which is exactly the half angle of light detection Θ of

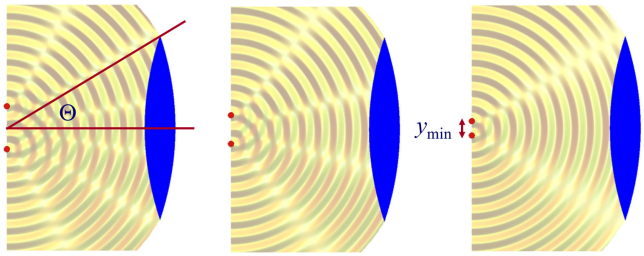

FIG. 2. Visualization of the diffraction limit of resolution. Displayed are the interference patterns of two coherently emitting point emitters, shown by red dots, for three different distances between emitters across panels. The closer the emitters are positioned with respect to each other, the larger the angular positions of the destructive interference lanes (directions of zero light intensity). At a critical distance, shown in the right panel, the first lane of destructive interference is positioned at the half angle Θ of light collection of the objective, and the objective lens receives a continuous wave front absent intensity minima appearing as a single emitter wave front.

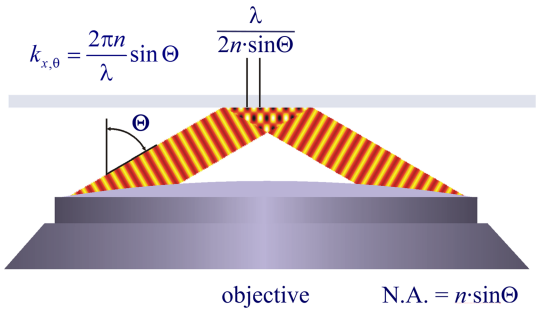

FIG. 3. Lateral resolution limit of a CLSM. The resolution is determined by the highest lateral spatial frequency contained in a focused bright spot. This is generated by the interference of two rays traveling from the edges of the objective to the focal point with the highest possible incidence angle Θ with respect to the optical axis as shown. The associated wave vectors are of equal magnitude $2\pi n/\lambda$, where λ is the vacuum wavelength. The corresponding lateral components $k_{x,\theta}$ of these wave vectors are of equal magnitude given by $k_{x,\theta} = 2\pi n \sin\Theta/\lambda$ and opposite directions resulting in a difference of $4\pi n \sin\Theta/\lambda$. As such, the interference of the two beams leads to a periodic interference pattern in the lateral direction with a periodicity $\lambda/2n \sin\Theta$ that is equal to the lateral resolution limit of a CLSM.

the objective. The spatial periodicity of this intensity modulation is again given by Abbe's formula [Eq. (14)], but with the emission wavelength now replaced by the excitation wavelength (usually shorter than the emission wavelength due to the spectral Stokes shift of fluorescence emission with respect to excitation; see Sec. II).

In a similar vein, we can also obtain the axial resolution limit of a confocal laser-scanning microscope by asking about the tightest spatial intensity modulation achievable when focusing light through the objective. The answer is presented in Fig. 4, where the tightest modulation is now generated by the interference of an axial light ray with a light ray traveling at the highest possible incidence angle Θ. This directly yields the axial resolution limit of an optical microscope, complementary to Abbe's lateral resolution limit, and is given by

$$z_{\min} = \frac{\lambda}{n(1-\cos\Theta)} \approx \frac{2n\lambda}{(\mathrm{NA})^2}, \tag{15}$$

where the approximation on the right-hand side is valid only for small numerical aperture values.

We summarize physical scales associated with lateral and axial resolution of diffraction-limited optical microscopes in Fig. 5. There we show lateral and axial resolutions as functions of the NA for optical wavelengths across the visual spectrum using for concreteness a water immersion objective (i.e., designed for imaging in water with a refractive index of 1.33).

While providing qualitative guidance on the optical system design, the axial and lateral spatial resolution expressions provided in Eqs. (14) and (15) remain theoretical. In particular, such expressions provide an upper bound on a resolution this is otherwise limited by factors including crucial notions of stochastic nature of photons and undesired out-of-focus light.

A final important note is warranted on light (information) collection efficiency and suppression of out-of-focus light from regions outside the focal plane, i.e., limiting light collection to a certain axial range termed optical sectioning.

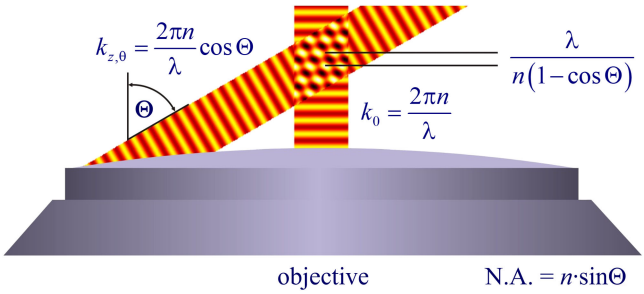

FIG. 4. Axial resolution of a CLSM. Like the lateral resolution, the axial resolution is determined by the tightest spatial modulation of light that can be generated along the optical axis. This is achieved by interfering an axially propagating beam with one traveling at the highest possible incidence angle. The axial component of the wave vector of the former is equal to the full wave-vector length $k_0 = 2\pi n/\lambda$, and the axial component for the latter is $k_{z,\Theta} = 2\pi n\cos\Theta/\lambda$. The resulting interference therefore leads to a spatial intensity modulation along the optical axis with a periodicity $\lambda/n(1-\cos\Theta)$ setting a CLSM's axial resolution limit.

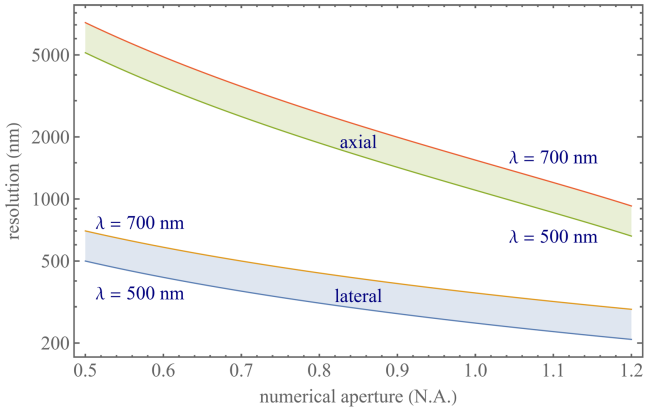

FIG. 5. Lateral and axial resolution in diffraction-limited optical microscopy using a water immersion objective (designed for imaging in water with a refractive index of 1.33) as a function of numerical aperture (NA) and wavelength.

For this purpose, specialized sample illumination and fluorescent light detection techniques have been developed, including total internal reflection fluorescence (TIRF) microscopy (Axelrod, 1981), supercritical angle fluorescence (SAF) microscopy (Enderlein, Ruckstuhl, and Seeger, 1999; Ruckstuhl and Verdes, 2004), metal-induced energy transfer (MIET) microscopy (Chizhik *et al.*, 2014), confocal microscopy (Marvin, 1961), image scanning microscopy (ISM) (Sheppard, 1988; Müller and Enderlein, 2010), two-photon microscopy (Denk, Strickler, and Webb, 1990), 4Pi microscopy (Hell and Stelzer, 1992), structured illumination microscopy (SIM) (Bailey *et al.*, 1993), light-sheet microscopy (Voie, Burns, and Spelman, 1993; Huisken *et al.*, 2004), and multiplane microscopy (Blanchard and Greenaway, 1999; Prabhat *et al.*, 2004).

All of the aforementioned methods accomplish optical sectioning and enhance photon collection efficiency in improving image resolution and contrast. These techniques pushed the optical resolution to its limits, as dictated by Abbe's diffraction barrier. However, it was not until the end of the 20th century that this barrier was overcome to achieve spatial resolutions in far-field light microscopy far beyond the diffraction limit (Hell and Wichmann, 1994). Research on this front is still ongoing and leverages advances in four main components of fluorescence microscopes: fluorescent emitters, optical setups, detectors, and analysis. In what follows, we first discuss fluorescent light sources and then proceed to review the optics of different microscope modalities while presenting statistical analysis frameworks throughout.

II. FLUOROPHORES

Point fluorescent emitters or light sources, often molecules termed fluorophores, are key to the fluorescence imaging of labeled samples. Both conventional fluorescence imaging and microscopy techniques achieving resolution beyond light's diffraction limit rely on tunable properties of fluorophores including emission rates, brightness, absorption and emission spectra, excited-state lifetimes, and other photophysical properties such as blinking and photobleaching (Moerner, Shechtman, and Wang, 2015). Here we discuss quantum

fluorophore properties, alongside their statistical modeling, and relegate classical models to Sec. III.D, where we derive their emission fields.

A. Fluorophore properties

Most molecules do not naturally fluoresce in regimes detectable by modern detectors and cannot easily be excited without inducing photodamage. Thus, one must often resort to specific fluorescence labeling of biological samples (Specht, Braselmann, and Palmer, 2017), for example, to identify and investigate structures against the vast cellular background of proteins, nucleic acids, lipids, and small molecules.

While the addition of fluorescent labels introduces challenges, their intrinsic properties as well as the nonlinear response to light in itself open windows of opportunity, for example, to study molecular interactions (Ciruela, 2008; Luo *et al.*, 2020), determine molecular copy numbers (Gruβmayer, Yserentant, and Herten, 2019; Hummert *et al.*, 2021; Bryan, Sgouralis, and Pressé, 2022), and improve optical resolution (Huang, Bates, and Zhuang, 2009; Schermelleh *et al.*, 2019), as detailed in Sec. V.

The most common labels include fluorescent proteins (Tsien, 1998; Zhang *et al.*, 2002; Dedecker, De Schryver, and Hofkens, 2013); organic dyes (Dempsey *et al.*, 2011; Lavis, 2017), generally small organic molecules containing conjugated π-electron systems; and semiconductor quantum dots, inorganic nanocrystals with especially broad excitation and correspondingly narrow emission spectra (Resch-Genger *et al.*, 2008).

Fluorescent labels include a large variety of fluorophores with excitation and emission wavelength maxima spanning the near-infrared, visible, and UV spectrum (Giepmans *et al.*, 2006; Li and Vaughan, 2018). Less common, "exotic" fluorescent labels providing an even larger color palette and increasingly tunable photophysical properties include carbon nanorods, carbon dots, polymer dots, fluorocubes, and fluorescent defects in diamond or 2D materials (Aharonovich and Neu, 2014; Jin *et al.*, 2018; Saurabh *et al.*, 2022).

Basic fluorophore photophysics is captured by Jablonski diagrams such as Fig. 6 for an organic dye illustrating select transitions between different molecular energy and spin states. More rigorous treatments of transition rules, molecular spectra, and interactions of light and matter were given by Lakowicz (2006) and Valeur and Berberan-Santos (2012).

A molecule in the typically singlet ground state is excited to a singlet excited state by absorbing a photon with a probability depending on the excitation light intensity and the molecule's absorption cross section [linearly related to the molar extinction coefficient (Lakowicz, 2006)]. The molar extinction coefficient ϵ_λ is a measure of how strongly a solution containing 1 mol of a fluorophore absorbs (attenuates) light at wavelength λ. This is expressed using the Lambert-Beer law as (Lakowicz, 2006)

$$\epsilon_\lambda = \frac{A_\lambda}{c_M l} = \frac{\log_{10}(I_{0\lambda}/I_\lambda)}{c_M l}, \tag{16}$$

where A_λ is the measured absorbance, $I_{0\lambda}$ is the initial light intensity of wavelength λ, and I_λ is the light intensity after the light travels the path length l through the solution with molar concentration c_M. From Eq. (16), it is clear that the Système International unit of the molar extinction coefficient is m^2/mol, but the commonly used unit is (l/cm)/mol.

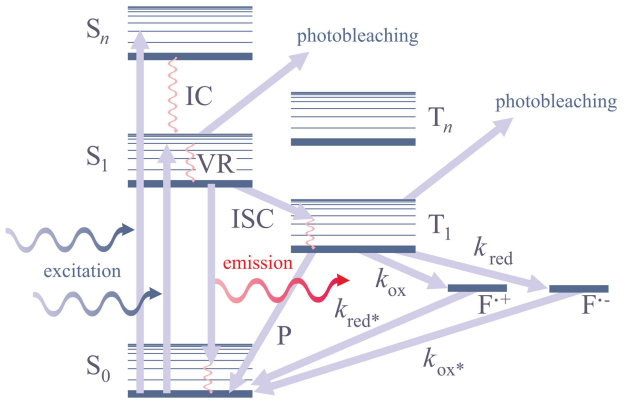

FIG. 6. Simplified Jablonski diagram. The electronic ground state S_0, the singlet excited states S_n, the triplet excited states T_n, and radical cation $F^{\cdot+}$ or anion states $F^{\cdot-}$. The thick lines represent electronic energy levels, the thin lines indicate vibrational energy levels, and rotational energy states are left unmarked. P, phosphorescence; VR, vibrational relaxation; IC, internal conversion; ISC, intersystem crossing. The rates of oxidation and reduction are k_{ox} and k_{red}, respectively. The arrows represent a subsample of all possible transitions between different states.

From ϵ_λ, we immediately arrive at another important fluorophore property, namely, the molecular brightness B_λ. To achieve a high signal-to-noise ratio (SNR), fluorescent labels with a high molecular brightness $B_\lambda = Q_f \epsilon_\lambda$ are desired. Here Q_f is a unitless quantity called fluorescence quantum yield describing how many fluorescence photons are emitted relative to the number absorbed. This is given by the ratio of the sum of radiative transitions to the total transitions, i.e., the sum of transition rates corresponding to all transition paths out of the excited state,

$$Q_f = \frac{\sum k_f}{\sum k_f + \sum k_{\text{non}}}, \tag{17}$$

where k_f and k_{non}, are the rate of fluorescence or radiative decay and the rate of nonradiative decay, respectively.

Another important fluorophore property is the average time τ that a fluorophore remains excited prior to emitting a photon,

$$\tau = \frac{1}{\sum k_f + \sum k_{\text{non}}}. \tag{18}$$

In Eq. (18) τ, termed the fluorescence lifetime, typically lasts on the order of nanoseconds for organic dyes. The fluorescence lifetime is a characteristic property of fluorophores in their unique environment tuned by pH, ion or oxygen concentration, molecular binding, or proximity-dependent intermolecular energy transfers primarily influencing the rate of nonradiative decay (Lakowicz, 2006; Valeur and Berberan-Santos, 2012). As such, differences in fluorophore lifetimes can be employed to distinguish fluorophore species, thereby

broadening the appeal of fluorescence lifetime imaging microscopy (FLIM) (Digman *et al.*, 2008; Datta *et al.*, 2020) in functional and multiplexed imaging of disparate fluorophores with otherwise overlapping spectra (Fereidouni, Bader, and Gerritsen, 2012; Valm *et al.*, 2017; Scipioni *et al.*, 2021); see Sec. IV.B.1.

As described, the quantum yield is tied to the number of possible transitions out of the excited state either nonradiatively or radiatively. Upon fluorophore excitation, one such radiative transition occurs via rapid vibrational relaxation to the lowest energy level of the S_1 excited state followed by radiative decay to a vibrational ground-state level with spontaneous fluorescence emission; see Fig. 6. The fluorescence emission is shifted toward longer wavelengths (Stokes shift) as compared to excitation due to fast internal conversion and vibrational relaxation to the lowest level of the S_1 excited state [Kasha's rule (Kasha, 1950)]. Another radiative transition out of the excited state, of later interest, is stimulated emission. Typically stimulated emission does not play a role at room temperature as long as the excitation intensity is low. However, this nonlinear process is exploited in stimulated emission depletion (STED) superresolution imaging (Hell and Wichmann, 1994), as described in Sec. V.A.1.

In addition to radiative transitions, several alternative nonradiative pathways are available for transition from the first singlet excited state S_1 to the ground state. For instance, the molecule can return to the ground state, thereby dissipating the energy to the environment as heat. Another example is the nonradiative transition to the triplet state T_1 via the intersystem crossing often employed in single-molecule localization microscopy (SMLM); see Sec. V.B.1. Return from T_1 to the ground singlet state (phosphorescence) is typically delayed on account of a forbidden spin flip transition; see Fig. 6. As such, transitions to and from triplet or further reduced or oxidized *off* states (also referred to as bright and dark states, respectively) occur on longer timescales (0.1–100 ms).

To control fluorophore switching between triplet dark and bright states, i.e., to control blinking, oxygen concentration may be adjusted. Upon reaction with dissolved molecular oxygen, fluorophores may transition from the triplet dark state (*off* state) to the singlet ground state (*on* state) by interacting with molecular oxygen's ground triplet state. Molecular oxygen can also accept an electron from a triplet fluorophore, thereby inducing typically undesirable phototoxic effects, i.e., irreversible photobleaching (Zheng *et al.*, 2014) occurring from many states, as shown in Fig. 6.

Though in some applications photobleaching is desirable, in others, such as particle tracking (Shen *et al.*, 2017; Sgouralis *et al.*, 2023; Xu, Sgouralis *et al.*, 2023) and protein-protein interactions via FRET (Förster, 1948; Lerner *et al.*, 2018), photobleaching and blinking are problematic and are suppressed by the removal of dissolved oxygen via oxygen scavenging systems, such as glucose oxidase coupled with catalase (Aitken, Marshall, and Puglisi, 2008), or by the depopulation of dark states, thus leveraging both the reducing and oxidizing agents (Vogelsang *et al.*, 2008).

In many cases, such as in stochastic optical reconstruction microscopy (STORM) (Rust, Bates, and Zhuang, 2006), the blinking of fluorophores is desirable for achieving spatial resolution below the diffraction limit; see Sec. V.B.1. Here many cyanine and rhodamine dyes are used, as they can be reversibly photoswitched from a bright state to a dark state (blink) in a buffer containing enzymatic oxygen scavengers and a primary thiol such as β-mercaptoethylamine or β-mercaptoethanol (Li and Vaughan, 2018; Jradi and Lavis, 2019). Alexa Fluor 647 is the organic dye of choice for state-of-the-art direct stochastic optical reconstruction microscopy (dSTORM) imaging due to its high brightness and efficient switching behavior (Diekmann *et al.*, 2020). For several cyanines, such as Cy5, it has been shown that thiolate anions covalently bind to the fluorophore (Dempsey *et al.*, 2009), thereby disrupting the conjugated system and resulting in a dark state. The dyes can also be chemically reduced by $NaBH_4$ to a nonfluorescent form or synthesized in a caged form that can later be photoactivated, an approach that has been used in different SMLM techniques (Vaughan, Jia, and Zhuang, 2012; Lehmann *et al.*, 2015). Rhodamine dyes can also reversibly switch from a fluorescent to a nonfluorescent form by intramolecular spirocyclization either spontaneously or driven by UV light. This has been exploited to generate sensors and switches and can be used across SMLM applications (Li and Vaughan, 2018; Zheng *et al.*, 2019).

Examples of SMLM include photoactivated localization microscopy (PALM) and fluorescence photoactivated localization microscopy (fPALM) (Betzig *et al.*, 2006; Hess, Girirajan, and Mason, 2006), as well as derivatives such as single particle tracking PALM (Manley *et al.*, 2008). In these applications, fluorescent proteins switch between fluorescent states reversibly (for example, on and off for dronpa by cis-trans isomerization) or through photoactivation (for example, photoactivatable green fluorescent protein by decarboxylation) or photoconversion (for example, green to red wavelength for the photoconvertible green-yellow fluorescent protein mEos by β elimination) (Dedecker, De Schryver, and Hofkens, 2013; Jradi and Lavis, 2019).

More recently studies of protein activity and SMLM have benefited from the discovery of a new class of ligand-activated fluorescent proteins (Kumagai *et al.*, 2013). The prototype UnaG binds the small molecule bilirubin via multiple noncovalent interactions and forms a fluorescent complex. The oxidized (and photobleached) ligand can detach from the protein, allowing a fresh bilirubin molecule to bind and act as a sensor for small molecules, thereby reporting on protein activity (Kwon *et al.*, 2020).

In general fluorescent proteins have the advantage of being genetically encodable, allowing fluorescent labeling of nearly arbitrary target proteins in living cells and organisms through fusion constructs. However, this also means that proteins must undergo appropriate folding followed by chromophore maturation, i.e., formation of a fluorescent molecule typically starting with three amino acids (Dedecker, De Schryver, and Hofkens, 2013). This process can take minutes to hours, may be incomplete, and can impair the temporal accuracy of measurements of rapid processes such as gene expression dynamics (Balleza, Kim, and Cluzel, 2018). While organic dyes circumvent some of these difficulties, both organic dyes and fluorescent proteins often exhibit complex photophysical and photochemical behaviors, therby complicating quantitative analysis. For instance, organic dyes can exhibit spectral blue shifts upon high laser radiation (Cho *et al.*, 2021;

Helmerich *et al.*, 2021) or spectral shifts from substrate (green) to product state (orange), as in the epoxidation of a double bond in conjugation with a BODIPY dye (Rybina *et al.*, 2013). This is useful in mechanistic studies of chemical reactions at the single-molecule level (Cordes and Blum, 2013). Such spectral shifts may affect multicolor applications, such as in superresolution imaging or single particle tracking (SPT), and are problematic to FRET experiments. Moreover, many proteins have additional dark states, for example, mEos cis-trans isomerization (Annibale *et al.*, 2011; De Zitter *et al.*, 2019), and organic dyes may have several conformations with different intensity levels, for example, ATTO647N, with at least three states differing in fluorescent lifetimes (Wang and Moerner, 2013), thereby complicating quantitative single-molecule readout.

B. Förster resonance energy transfer

In Sec. II.A, we discussed fluorophore properties involving radiative or nonradiative transitions. Here we continue by considering nonradiative transitions through intermolecular energy transfer (Valeur and Berberan-Santos, 2012). A few examples of these transitions include photoinduced electron transfer (Escudero, 2016), collisional quenching or FRET, bioluminescence resonance energy transfer (Kobayashi *et al.*, 2019; Syed and Anderson, 2021), protein-induced fluorescence enhancement (Myong *et al.*, 2009; Hwang, Kim, and Myong, 2011), and the recently discovered proximity-assisted photoactivation (Graham *et al.*, 2022). These transitions are distance dependent and thus have been leveraged to probe binding interactions or conformational changes.

In what follows, we focus on FRET, an intermolecular energy transfer process that is widely used to measure molecular interactions and serves as a distance ruler for structural biology (Lakowicz, 2006; Wu *et al.*, 2020; Agam *et al.*, 2023). In FRET, nonradiative energy transfer from a donor to an acceptor fluorophore occurs through dipole-dipole coupling with a rate constant k_{FRET} when the donor's emission spectrum overlaps with the acceptor's absorption spectrum (Förster, 1948). Under the dipolar approximation, the probability for energy transfer to occur, called the FRET efficiency (E_{FRET}), scales with the donor-acceptor distance to the inverse sixth power (Jones and Bradshaw, 2019) and is 50% at the Förster radius R_0,

$$E_{\mathrm{FRET}} = \frac{1}{1+(r/R_0)^6} = \frac{k_{\mathrm{FRET}}}{\sum k_f + \sum k_{\mathrm{non}}} = 1 - \frac{\tau_{DA}}{\tau_D}, \tag{19}$$

where τ_{DA} and τ_D are the donor fluorescence lifetimes in the acceptor's presence and absence, respectively. For typical donor-acceptor pairs, R_0 is a few nanometers (Lakowicz, 2006) and depends on the donor emission-acceptor absorption spectral overlap and the relative orientation of donor-acceptor dipole moments. It is explicitly given by

$$R_0^6 = \frac{9000 \ln 10}{128\pi^5 N_{\mathrm{A}} n^4} \kappa^2 Q_{f,D} \int I_D(\lambda)\epsilon_A(\lambda)\lambda^4 d\lambda, \tag{20}$$

where κ is the so-called orientation factor,

$$\kappa = 3\cos\theta_D \cos\theta_A - \cos\theta_{DA}, \tag{21}$$

$Q_{f,D}$ is the donor's quantum yield in the absence of the acceptor, n is the solution's refractive index, N_{A} is the Avogadro constant, I_D is the donor's normalized fluorescence emission spectrum, ϵ_A is the acceptor's molar extinction coefficient, θ_{DA} is the angle between the donor and acceptor transition moments, and θ_D and θ_A are the angles between these moments and the vector connecting donor to acceptor, respectively. For ϵ_A and λ, respectively, given in (l/cm)/mol and centimeters, R_0 is in centimeters.

Ignoring the angular dependence of the energy transfer for fixed dipoles, as described in Eq. (20), can yield significant biases in FRET distance assessments (Hellenkamp *et al.*, 2018). In practice, the dipoles are often freely and rapidly rotating (rapid compared to the donor deexcitation rate), leading to an average value of $\kappa^2 = 2/3$.

FRET can also occur between spectrally identical molecules (homo-FRET) and is observed by measuring its effect on fluorescence polarization anisotropy (Gradinaru *et al.*, 2010),

$$r = \frac{I_{\parallel} - GI_{\perp}}{I_{\parallel} + 2GI_{\perp}}. \tag{22}$$

In Eq. (22) $I_{\parallel/\perp}$ is the intensity measured when the polarizers in the detection path are aligned parallel or perpendicular to those in the excitation and G is a correction factor for the difference in the instrument's sensitivity to the two orthogonal polarization orientations.

Upon exposure to linearly polarized light, the excitation probability is highest for molecules whose absorption dipole moments are aligned parallel to the polarization vector of the exciting light. In most cases, the absorption and emission dipoles of a molecule are colinear, such that fluorescence emission remains polarized immediately after excitation. Fluorescence remains anisotropic unless the molecule rotates over the fluorescence lifetime or the excitation energy is transferred to a different molecule. Thus, anisotropy or polarization measurements inform us on molecular parameters such as orientation, oligomerization or size, and environmental conditions like viscosity (Gradinaru *et al.*, 2010; Bader *et al.*, 2011). Polarization can also be read out in superresolution imaging, for example, using polarized light in illumination or detection and capturing polarized emission by implementing specifically engineered PSFs sensitive to polarization (Hulleman *et al.*, 2021; Wu, Lu, and Lew, 2022); see Sec. V.C.

Polarization, lifetime, FRET efficiency, and other photophysical markers discussed here are interesting only insofar as their changes report back on the kinetics of the underlying labeled molecules. We now turn to Markov models describing discrete molecular events to extract molecular kinetics from photophysical changes.

C. Markov models for fluorophores

To help encourage the use of Markov models, here we consider them in the analysis of FRET data and the

enumeration of fluorophores within a diffraction-limited region of interest (ROI) is described in Appendix B.

For example, observations from FRET experiments with photons individually recorded [at avalanche photodiodes (APDs)] include a set of photon arrival times along with a set of corresponding colors (wavelengths), designated by $c = 1$ or 2, attributing photons to either a donor or an acceptor channel, respectively.

The set of photon arrival times (data) are measured either with respect to the start of the experiment, for continuous illumination (Saurabh, Safar *et al.*, 2023), or with respect to the pulse immediately preceding a photon detection, as in pulsed illumination (Safar *et al.*, 2022). For illustration, we assume here continuous illumination where data consist of intervals between photon arrivals. We let $K+1$ coincide with the total number of photons and denote the data with $\Delta t_{1:K} = \{\Delta t_1, \ldots, \Delta t_K\}$. The sets of interarrival times are then used to learn transition kinetics between system states comprising molecular and labeled photophysical states. For concreteness, we assume that molecular states coincide with conformational states of a typically large biomolecule.

To collect such typical FRET datasets, the donor is excited using an illumination laser and we assume, only for simplicity here though performed more generally by Saurabh, Fazel *et al.* (2023), that acceptors become excited exclusively via FRET. The rate of donor and acceptor emission then depends on their separation characterizing a conformational state and its corresponding FRET efficiency; see Sec. II.B. As the number of conformational states associated with different FRET efficiencies [E_{FRET} in Eq. (19)] may be unknown, these can be learned nonparametrically (Saurabh, Fazel *et al.*, 2023; Saurabh, Safar *et al.*, 2023). However, for simplicity we again presume here two states termed high and low FRET designated by ξ_m, $m = 1$ and 2. Further, given that both donors and acceptors are rarely simultaneously excited, we consider only three possible photophysical states: $f_1 = (\mathrm{ground}, \mathrm{ground})$, $f_2 = (\mathrm{excited}, \mathrm{ground})$, and $f_3 = (\mathrm{ground}, \mathrm{excited})$, where the first elements represent the donor's state. The entire problem's state space is then spanned by a set of states obtained from the tensor product of photophysical and conformational states termed composite states. To facilitate the notation, we designate composite states by $s_m \in \{(\xi_1, f_1), (\xi_1, f_2), (\xi_1, f_3), (\xi_2, f_1), (\xi_2, f_2), (\xi_2, f_3)\}$, with $m = 1{:}6$.

We can now write a generative model required in constructing the likelihood used in the analysis of FRET experiments. To do so, we start with the rate matrix

$$\mathbb{K} = \begin{bmatrix} 0 & k_{s_1\to s_2} & \cdots & k_{s_1\to s_6} \\ k_{s_2\to s_1} & 0 & \cdots & k_{s_2\to s_6} \\ \vdots & \vdots & \ddots & \vdots \\ k_{s_6\to s_1} & k_{s_6\to s_2} & \cdots & 0 \end{bmatrix}, \tag{23}$$

where self-transitions are by definition disallowed and $k_{s_m\to s_{m'}}$ is the transition rate from state s_m to state $s_{m'}$. Furthermore, elements of the rate matrix coinciding with simultaneous conformational and photophysical transitions are set to zero owing to their rarity. Nonzero matrix elements of the rate matrix thus coincide with (1) transitions between the two FRET conformational states ($k_{\xi_1\to\xi_2}$ and $k_{\xi_2\to\xi_1}$) while the photophysical states remain fixed or (2) transitions between different photophysical states while conformational states remain fixed. To be more precise, photophysical transitions include donor excitation ($k_{s_1\to s_2} = k_{\mathrm{ex}}$), donor radiative relaxation ($k_{s_2\to s_1} = k_d$), acceptor relaxation ($k_{s_3\to s_1} = k_a$), FRET transitions when in ξ_1 ($k_{s_2\to s_3} = k^{(1)}_{\mathrm{FRET}}$), and FRET transitions when in ξ_2 ($k_{s_5\to s_6} = k^{(2)}_{\mathrm{FRET}}$). As such, written explicitly the rate matrix for this simple case reads

$$\mathbb{K} = \begin{bmatrix} 0 & k_{\mathrm{ex}} & 0 & k_{\xi_1\to\xi_2} & 0 & 0 \\ k_d & 0 & k^{(1)}_{\mathrm{FRET}} & 0 & k_{\xi_1\to\xi_2} & 0 \\ k_a & 0 & 0 & 0 & 0 & k_{\xi_1\to\xi_2} \\ k_{\xi_2\to\xi_1} & 0 & 0 & 0 & k_{\mathrm{ex}} & 0 \\ 0 & k_{\xi_2\to\xi_1} & 0 & k_d & 0 & k^{(2)}_{\mathrm{FRET}} \\ 0 & 0 & k_{\xi_2\to\xi_1} & k_a & 0 & 0 \end{bmatrix}. \tag{24}$$

Observations occur only when either the donor or the acceptor emits radiatively. As such, the system may visit intermediate states between photon emissions such as those undergoing conformational transitions. For a perfect detector, ignoring detector dead time (Saurabh, Fazel *et al.*, 2023) and assuming complete detection efficiency (otherwise, k_{ex} is understood as an effective excitation rate), the photon interarrival time coincides with the total time that the system spends avoiding radiative transitions.

To construct the likelihood for a FRET dataset (interphoton arrival times and detection channels), we begin by illustrating how such a dataset can be obtained from a generative model. To do so, we first designate the state of the composite system at time t_n as $s(t_n)$. Next, following the notation introduced in Sec. I.B [see Eq. (8)], a state trajectory is constructed following the Gillespie algorithm (Gillespie, 1976) by first selecting the state to which we transition and then deciding when this transition occurs,

$$s(t_{n+1})|s(t_n) \sim \mathrm{Categorical}\left(\frac{k_{s(t)\to s_1}}{k_{s(t_n)}}, \ldots, \frac{k_{s(t)\to s_6}}{k_{s(t_n)}}\right), \tag{25}$$

$$\delta t_n \sim \mathrm{Exponential}(k_{s(t_n)}). \tag{26}$$

where "Exponential" implies a normalization constant. In Eqs. (25) and (26) $\delta t_n = t_{n+1} - t_n$ is the time that the system spends in state $s(t_n)$ and $k_{s(t_n)}$ is the escape rate out of $s(t_n)$, i.e., the sum of rates pointing out of $s(t_n)$. The Categorical distribution introduced in Eq. (25) is treated as the generalization of the Bernoulli distribution, albeit with more than two outcomes.

Taken together, Eqs. (25) and (26) constitute what is called a generative model, i.e., a model that is helpful not only in generating the data but also in constructing the likelihood. This generative model can indeed be further generalized to include imperfect detectors, dead time, and other artifacts such as direct acceptor excitation and crosstalk (Roy, Hohng, and

Ha, 2008; Bacia, Petrášek, and Schwille, 2012; Sgouralis *et al.*, 2019; Saurabh, Fazel *et al.*, 2023).

We are now presented with a modeling choice. That is, we can learn the trajectory in composite state space (states occupied across time points) and kinetic rates populating the rate matrix (Kilic, Sgouralis, and Pressé, 2021; Safar *et al.*, 2022). Alternatively, we can marginalize [see Eq. (6)] over all trajectories and learn only kinetic rates (Gopich and Szabo, 2005; Saurabh, Fazel *et al.*, 2023).

As it is the most common, we select the latter path and marginalize over all possible nonradiative paths between observations. To achieve this, we use the master equation (Van Kampen, 1992; Gopich and Szabo, 2005; Lee and Pressé, 2012; Pressé and Sgouralis, 2023; Saurabh, Fazel *et al.*, 2023)

$$\frac{d}{dt}\mathbf{P}(t) = \mathbf{P}(t)\mathbf{G} \tag{27}$$

describing the evolution of the probability vector $\mathbf{P}(t)$ collecting the probabilities of occupying different states at the time t. In Eq. (27) the generator matrix $\mathbf{G}$ is related to the rate matrix as follows:

$$\mathbf{G} = \mathbb{K} - \begin{bmatrix} k_{s_1} & 0 & \cdots & 0 \\ 0 & k_{s_2} & \cdots & 0 \\ \vdots & \vdots & \ddots & \vdots \\ 0 & 0 & \ldots & k_{s_6} \end{bmatrix}, \tag{28}$$

where the diagonal matrix has the same size as $\mathbb{K}$ and its nonzero elements coincide with the escape rates. From the generator matrix, we obtain a propagator matrix $\mathbb{Q}$ collecting transition probabilities over an infinitesimal period ε,

$$\mathbb{Q} = \exp[\mathbf{G}\varepsilon]. \tag{29}$$

Therefore, given the probability vector at time $t-\varepsilon$, $\mathbf{P}(t-\varepsilon)$, the probability vector at time t reads $\mathbf{P}(t) = \mathbf{P}(t-\varepsilon)\mathbb{Q}$. As such, given the initial probability vector $\mathbf{P}_{\text{in}}$, we can find the probability at any time by dividing the time interval into N small periods of ε,

$$\mathbf{P} = \mathbf{P}_{\text{in}}\mathbb{Q}_1 \cdots \mathbb{Q}_N, \tag{30}$$

where $\mathbb{Q}_1 = \cdots = \mathbb{Q}_N = \mathbb{Q}$ in the absence of observations. However, in the presence of observations the propagators in Eq. (30) are modified according to the monitored transitions (Saurabh, Fazel *et al.*, 2023). For example, observation of no photon over the nth period ε signifies no radiative transitions, allowing us to set $k_a = k_d = 0$ for this period, which in turn results in a modified propagator designated by $\mathbb{Q}_n^{\text{non}}$. Furthermore, a photon arrival, indicating a radiative transition, forces nonradiative transition rates to be zero, thus leading to a modified propagator $\mathbb{Q}_k^{\text{rad}}$ for the kth photon over an infinitesimal period ε.

The likelihood over a set of observations is now expressed in terms of these modified propagators (Gopich and Szabo, 2006; Saurabh, Fazel *et al.*, 2023),

$$P(\Delta t_{1:K}|\mathbb{K}, \mathbf{P}_{\text{in}}) \propto \mathbf{P}_{\text{in}}\mathbb{Q}_1^{\text{non}} \cdots \mathbb{Q}_k^{\text{rad}} \cdots \mathbb{Q}_N^{\text{non}}\mathbf{P}_{\text{norm}}^T, \tag{31}$$

where $\mathbf{P}_{\text{norm}}$ is a row vector of 1s.

Until now we have assumed a parametric framework with a fixed number of conformational states, often set to two, low and high FRET (McKinney *et al.*, 2003), in the literature. We lift this constraint and treat the number of conformational states as unknown while extending the aforementioned formulation to the nonparametric regime. To do so, we assume an infinite number of conformational states with a load b_m (see Sec. I.B) associated with each mth state resulting in an infinite-dimensional generator matrix; see Saurabh, Fazel *et al.* (2023) and Saurabh, Safar *et al.* (2023). From the nonparametric generator matrix, we compute the corresponding propagator matrices and use them to build a likelihood similar to Eqs. (29)–(31). The nonparametric posterior over the set of unknowns $\vartheta = \{\bar{b}, \mathbb{K}, \mathbf{P}_{\text{in}}\}$ is then constructed by including a beta-Bernoulli process prior (see Sec. I.B) over the loads and appropriate priors over the remaining unknowns [ideally conditionally conjugate priors if available (Pressé and Sgouralis, 2023)]; see Fig. 7. Strictly speaking, in computational applications we often use large albeit finite load numbers M and verify that for large enough M the conclusions drawn are independent of M. Finally, the FRET posterior obtained is sampled using Monte Carlo methods to deduce the set of unknowns (Safar *et al.*, 2022; Saurabh, Fazel *et al.*, 2023; Saurabh, Safar *et al.*, 2023).

An alternative statistical FRET framework makes use of photon counts over equal time windows, i.e., bins, during the experiment, rather than single photons (Gopich and Szabo, 2005; Saurabh, Fazel *et al.*, 2023). In this case, the likelihood is derived using the fact that photon counts over fixed periods are Poisson distributed (ignoring detector noise convoluted with Poisson shot noise required of quantitative analyses)

Statistical Framework : FRET

Data: Photon inter-arrival times

$$\Delta t_{1:K} = \{\Delta t_1, ..., \Delta t_K\}.$$

Parameters: loads, transition rates, initial probability vector

$$\vartheta = \left\{\bar{b}, \mathbb{K}, \mathbf{P}_{\text{in}}\right\}.$$

Likelihood:

$$P(\overline{\Delta t}|\vartheta) \propto \mathbf{P}_{\text{in}}\mathbb{Q}_1^{\text{non}} ... \mathbb{Q}_k^{\text{rad}} ... \mathbb{Q}_N^{\text{non}}\, \mathbf{P}_{\text{norm}}^T.$$

Priors:

$$\begin{aligned} q_m &\sim \text{Beta}(A_q, B_q), m = 1:\infty, \\ b_m &\sim \text{Bernoulli}(q_m), \\ \mathbb{K} &\sim \text{Gamma}(\alpha_{\mathbb{K}}, \beta_{\mathbb{K}}), \\ \mathbf{P}_{\text{in}} &\sim \text{Dirichlet}(\alpha_\Pi). \end{aligned}$$

Posterior:

$$P(\vartheta|\overline{\Delta t}) \propto P(\overline{\Delta t}|\vartheta)P(\vartheta).$$

FIG. 7. Statistical framework: FRET.

(Saurabh, Fazel *et al.*, 2023). The derivation of such likelihoods is more straightforward than in the single-photon case (Patel *et al.*, 2019; Sgouralis *et al.*, 2019), and learning rates (or, more accurately, transition probabilities) are achieved using hidden Markov models (HMMs) (Roy, Hohng, and Ha, 2008). While traditional HMM frameworks require the number of FRET states as input, more recent iterations have leveraged variational tools to determine states, for example, the software package `vbFRET` (Bronson *et al.*, 2009), with recent developments in nonparametric infinite HMMs now allowing posterior probabilities over states warranted by the data to be sampled simultaneously alongside kinetics (Sgouralis and Pressé, 2017; Sgouralis *et al.*, 2019).

However, by virtue of binning photon arrivals, whether by choice or due to the detector used, HMM frameworks naturally compromise our ability to resolve fast kinetics occurring on timescales at or below the bin size. For this reason, other than the potential for computational speedup, there is no reason to bin single-photon data. However, if one uses detectors that unavoidably bin counts across pixels commonly used in wide-field applications (see Appendix A), then fast transitions can be deduced on timescales exceeding data acquisition. This is achieved by leveraging the fact that the signal amounts to an average of the properties over the state visited (Pirchi *et al.*, 2016; Kilic, Sgouralis, and Pressé, 2021; Kilic *et al.*, 2021); see Fig. 67.

Such strategies used to deduce dynamics on timescales at or exceeding data acquisition rely on the Markov jump process (MJP) (Hobolth and Stone, 2009; Kilic, Sgouralis, and Pressé, 2021), which assumes that the system evolves in continuous time. This is in contrast to the HMM paradigm, which approximates dynamics as occurring discretely and only at the measurement time. In other words, the MJP accurately presupposes a continuous time trajectory $\mathcal{S}(t)$ in the discrete state space of the composite system generated using the same procedure as described by Eqs. (25) and (26). The observation for the kth data acquisition period (bin) is therefore (Kilic, Sgouralis, and Pressé, 2021; Kilic *et al.*, 2021)

$$w_k \sim \text{Poisson}\left(\int_{t_k}^{t_k+\delta T} \mu_{\mathcal{S}(t)}\, dt\right), \tag{32}$$

where $\mu_{\mathcal{S}(t)}$ represents the photon emission rate for the instantaneous state $\mu_{\mathcal{S}(t)}$ occupied at a time t.

Having highlighted Markov model applications for the analysis of temporal data from FRET experiments, we relegate further applications (counting fluorophores within a diffraction spot) to Appendix B. In what follows, we turn to spatiotemporal data, andfor this we discuss the optics of different microscope modalities and derive their corresponding PSFs.

III. FLUORESCENCE MICROSCOPY: THE POINT SPREAD FUNCTION

In this section, we develop in a self-contained manner the physical theory of optical imaging using a wide-field fluorescence microscope. We start by deriving the Abbe sine condition subsequently used to describe fundamental properties of electromagnetic wave propagation through optical systems. We then continue to derive the basic principles of how to compute the OTF and PSF of a microscope, discuss the lack of optical sectioning of wide-field microscopes, and illustrate the effect of optical aberrations on PSFs.

A. Fundamental property of microscopic imaging: The Abbe sine condition

To gain a deeper understanding of how a microscope forms an image alongside fundamental principles governing image formation, we start by considering the imaging of a generic point source in sample space into an image point in image space; see Fig. 8. We denote parameters associated with the image and sample spaces with and without a prime, respectively, hereafter. A point source in the focal plane on the optical axis (symmetry axis designated by blue lines) emits concentric electromagnetic waves. The segment of the spherical wave front collected by the objective is then converted by the microscope into a segment of a spherical wave front converging on the corresponding image point. To facilitate subsequent derivations, we assume that the distance between the sample point and the objective lens is large enough that the spherical wave front incident on the objective can be considered as a superposition of planar wave front segments traveling at different propagation angles θ with respect to the optical axis (Fraunhofer diffraction limit). Correspondingly, the transformed spherical wave front in image space is also considered a superposition of planar wave front segments traveling at angles θ' with respect to the optical axis.

We can now obtain a relation between the angle θ and the corresponding angle θ' of a planar wave front segment within the sample and image spaces, respectively; see Fig. 1. We begin by assuming that the point source is shifted laterally away from the optical axis by a distance y; see Fig. 9. Considering a perfect imaging system, the spherical wave fronts from the shifted point source, shown in green, will be converted into spherical wave fronts converging onto a point shifted a distance y' away from the optical axis in the image space where the relation between y' and y is given by $y' = \mathcal{M}y$. Here $\mathcal{M}$ denotes the microscope's magnification.

Now consider two planar wave front segments traveling at an angle θ from a source located at y and on the optical axis. There is a phase difference between these two planar wave front segments that is proportional to $ny \sin\theta$. The microscope transforms these planar wave front patches into two planar wave front patches traveling along an angle θ' in the image

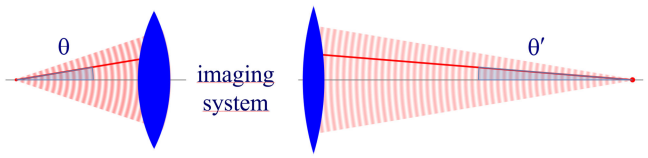

FIG. 8. The optical microscope, i.e., the imaging system, is a wave front transforming system converting (left sketch) the outgoing spherical wave front of a point emitter in sample space into (right sketch) a concentric spherical wave front in image space converging into an image point in the image space.

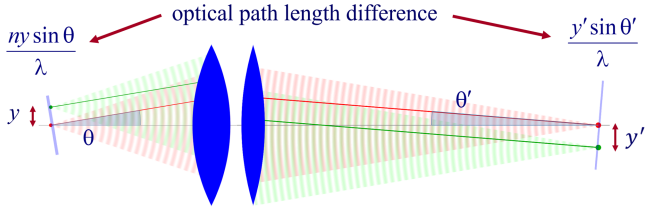

FIG. 9. The phase relation between planar wave front segments propagating along the same angle θ but emanating from two different point sources, where one point source is on the optical axis (red) and the other is laterally shifted by a distance y (green). The image point (the point of convergence of the spherical wave front segment) corresponding to the shifted point source is translated by a distance y' away from the optical axis. The ratio between y' and y is the magnification $\mathcal{M}$. Optical path length differences between wave front segments traveling along angles θ and θ', respectively, are shown as thin blue lines at the emitters' positions and oriented perpendicularly to the propagation directions θ and θ'.

space with a phase difference of $y'\sin\theta'$ between the patches (assuming both here and later that the refractive index of the image space is always that of air, ≈1.0). To attain perfect focus, all planar wave front patches originating from a point source and converging at a corresponding focal point in the image space must have the same phase at the focal point (maximum constructive interference). In other words, the phases of all planar wave components constituting the spherical wave front must be the same at the image point where the spherical wave front converges. We thus find that $ny\sin\theta = y'\sin\theta'$. When considering that the ratio between y' and y is the image magnification, this yields

$$n\sin\theta = \mathcal{M}\sin\theta', \tag{33}$$

which is the so-called Abbe sine condition (Mansuripur, 1998, 2002) for a perfect aplanatic imaging system (i.e., emission from a point at a lateral distance y in the focal plane in sample space is converted into a perfect spherical wave front segment converging on an image point at a position $y' = \mathcal{M}y$ in the image plane).

Invoking similar arguments, we can derive the relation between θ and θ' required for the perfect imaging of point sources along the optical axis into corresponding image points in image space. This situation is illustrated in Fig. 10, where we again compare the phase differences between (1) wave fronts from the point source in the focal plane with the shifted point source and (2) corresponding wave fronts converging on the image points. As such, we now find the following relation between θ and θ':

$$n(\cos\theta - 1) = \mathcal{M}_z(\cos\theta' - 1), \tag{34}$$

where $\mathcal{M}_z$ denotes the axial magnification (Hopkins, 1946; Braat, 1997; Born and Wolf, 2013). It is impossible for both the Abbe sine condition and Eq. (34) to be simultaneously satisfied. This shows that an optical system that perfectly images points from the focal plane onto the conjugate image plane can do so only on these two specific planes and exhibit aberrations, i.e., deviations of wave fronts from spherical shape away from the focal plane. Note that for small values of θ we can expand Eq. (34) into a first order Taylor series, i.e., $n\theta^2/2 \approx \mathcal{M}_z\theta'^2/2$, which can simultaneously be satisfied by the Abbe sine condition if

$$n\sin^2\theta/2 \approx \mathcal{M}_z\sin^2\theta'/2 \tag{35}$$

and $\mathcal{M}_z \approx \mathcal{M}^2/n$. Equation (35) is called Herschel's condition (Steward, 1927; Braat, 1997; Gross, 2005; Botcherby *et al.*, 2008; Born and Wolf, 2013). This shows that a system satisfying the Abbe sine condition (aplanatic imaging system) has an axial magnification of roughly the square of the lateral magnification divided by the sample medium's refractive index.

B. Electromagnetic field of image formation

In this section, we consider a point emitter with incoherent emission in sample space and proceed to derive a relation between the corresponding electromagnetic fields in the sample and image spaces. Specifically, we operate in the Fourier domain to derive electric and magnetic field components in image space in terms of the emissive electric fields in sample space. To begin, we write the emitter's electric field plane wave Fourier representation in sample space as

$$\mathbf{E}(\mathbf{r}) = \int_0^{\Theta} d\theta\,\sin\theta \int_0^{2\pi} d\phi \mathbf{E}_0(\theta,\phi)\exp(i\mathbf{k}\cdot\mathbf{r}), \tag{36}$$

where $\mathbf{r}$ is the position vector in sample space with respect to the objective focal point in sample space; see Fig. 1. Moreover, $\mathbf{E}_0(\theta,\phi)$ is the electric field amplitude for a plane wave traveling along a wave vector $\mathbf{k}$ with a length $|\mathbf{k}| = 2\pi n/\lambda$ and a direction $\hat{\mathbf{k}} = (\cos\phi\sin\theta, \sin\phi\sin\theta, \cos\theta)$ [a hat above a vector always designates a unit vector with components (x, y, z) in Cartesian coordinates]; see Fig. 11. Furthermore, the angular integration extends over the entire cone of light, with the angle Θ detected by the objective (recalling that $n\sin\Theta$ is the objective's numerical aperture; see Fig. 2).

In Fig. 11, considering the plane on which both the optical axis (the z axis in Fig. 11) and $\mathbf{k}$ lie, then it is convenient to split the electric field amplitude $\mathbf{E}_0(\theta,\phi)$ into two orthogonal polarization components, namely, parallel and perpendicular to this plane $\mathbf{E}_0 = E_{0,\parallel}(\theta,\phi)\hat{\mathbf{e}}_\parallel + E_{0,\perp}(\theta,\phi)\hat{\mathbf{e}}_\perp$, where $E_{0,\parallel}$ and $E_{0,\perp}$ are the corresponding electric field amplitudes along the two polarization orientations and the corresponding unit vectors are denoted by $\hat{\mathbf{e}}_\parallel$ and $\hat{\mathbf{e}}_\perp$. These two unit vectors with the unit vector $\hat{\mathbf{k}}$ form an orthonormal set of unit vectors that are given as follows in Cartesian coordinates:

$$\begin{aligned}\hat{\mathbf{k}} &= (\cos\phi\sin\theta, \sin\phi\sin\theta, \cos\theta),\\ \hat{\mathbf{e}}_\parallel &= (-\sin\phi, \cos\phi, 0),\\ \hat{\mathbf{e}}_\perp &= \hat{\mathbf{e}}_\parallel \times \hat{\mathbf{k}} = (\cos\phi\cos\theta, \sin\phi\cos\theta, -\sin\theta).\end{aligned} \tag{37}$$

Equation (37) immediately allows us to write the magnetic field in sample space. We do so by recalling that, for a plane

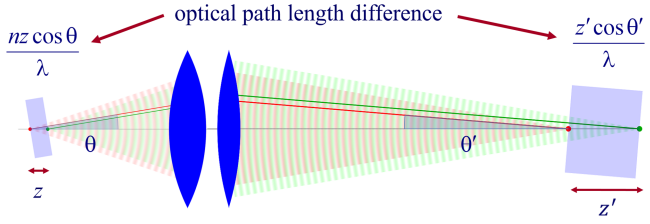

FIG. 10. Phase relation between planar wave front segments propagating along the same angle θ but emanating from two different point sources along the optical axis. As in Fig. 9, optical path differences (phase differences) between wave front segments traveling along angles θ and θ', respectively, are shown as blue rectangles.

wave with a wave vector $\mathbf{k}$ and an electric field amplitude $\mathbf{E}_0$, the magnetic field amplitude is $\mathbf{B}_0 = n\hat{\mathbf{k}} \times \mathbf{E}_0$ (Jackson, 1999). Thus, the magnetic field amplitude in sample space reads $\mathbf{B}_0 = n[-E_{0,\parallel}(\theta,\phi)\hat{\mathbf{e}}_\perp + E_{0,\perp}(\theta,\phi)\hat{\mathbf{e}}_\parallel]$.

The microscope's optics now converts each plane wave component of Eq. (36) into a corresponding plane wave component $\mathbf{E}'_0(\theta',\phi)\exp(i\mathbf{k}'\cdot\mathbf{r}')$ in the image space; see the right image in Fig. 11. Here $\mathbf{r}'$ is centered at the focus of the tube lens (see Fig. 1), the angle ϕ remains the same, and the propagation angles θ and θ' are connected via the Abbe sine condition given by Eq. (33). As before, we split the electric field amplitude into two principal polarization directions $\mathbf{E}'_0 = E'_{0,\parallel}(\theta,\phi)\hat{\mathbf{e}}_\parallel + E'_{0,\perp}(\theta,\phi)\hat{\mathbf{e}}'_\perp$, where the set of unit vectors in the image space is obtained by substituting θ' for θ in Eq. (37). Moreover, we note that $\hat{\mathbf{e}}'_\parallel = \hat{\mathbf{e}}_\parallel$ due to its independence from θ. The corresponding magnetic field amplitude can then be obtained as $\mathbf{B}'_0 = -E'_{0,\parallel}(\theta',\phi)\hat{\mathbf{e}}'_\perp + E'_{0,\perp}(\theta',\phi)\hat{\mathbf{e}}_\parallel$ assuming a refractive index in the image space of unity.

We now relate the electric field amplitudes in sample and image spaces by considering the conservation of energy flux density along the optical axis for every plane wave component absent attenuation (attenuation can be considered a form of the aberration discussed in Sec. III.F). This flux density is given by the z component of the time-averaged Poynting vector $\mathbf{P}$ (Jackson, 1999), which reads

$$P_z = \frac{c}{8\pi}\hat{\mathbf{e}}_z \cdot (\mathbf{E}_0 \times \mathbf{B}_0^*) = \frac{c}{8\pi}\hat{\mathbf{e}}_z \cdot (\mathbf{E}'_0 \times \mathbf{B}_0'^*), \tag{38}$$

where an asterisk denotes complex conjugation. For $\mathbf{B}_0 = n\hat{\mathbf{k}} \times \mathbf{E}_0$ in sample space and $\mathbf{B}'_0 = \hat{\mathbf{k}}' \times \mathbf{E}'_0$ in image space,

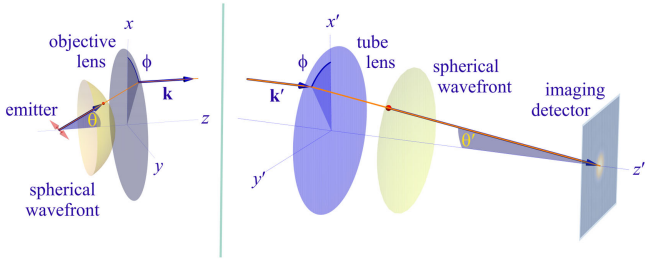

FIG. 11. Geometry of propagation of a narrow section of the wave front from the emitter to the image plane.

we obtain $n|\mathbf{E}_0|^2\cos\theta = |\mathbf{E}'_0|^2\cos\theta'$ from which the electric field amplitudes in image and sample spaces are related

$$|\mathbf{E}'_0| = \sqrt{n\frac{\cos\theta}{\cos\theta'}}|\mathbf{E}_0|. \tag{39}$$

Furthermore, by combining the Abbe sine condition $n\sin\theta = \mathcal{M}\sin\theta'$, Eq. (33), and its differential $n\cos\theta d\theta = \mathcal{M}\cos\theta' d\theta'$, we have

$$\sin\theta d\theta = \left(\frac{\mathcal{M}}{n}\right)^2 \frac{\cos\theta'}{\cos\theta}\sin\theta' d\theta'. \tag{40}$$

Substituting Eq. (40) into the electric field's plane wave representation (36) and leveraging Eq. (39), we arrive at the following expression for a plane wave representation of the image space electric field:

$$\mathbf{E}'(\mathbf{r}') = \frac{\mathcal{M}^2}{n^{3/2}}\int_0^{\Theta'} d\theta' \sin\theta' \sqrt{\frac{\cos\theta'}{\cos\theta}} \int_0^{2\pi} d\phi \times [E_{0,\parallel}\hat{\mathbf{e}}_\parallel + E_{0,\perp}\hat{\mathbf{e}}'_\perp]\exp(i\mathbf{k}'\cdot\mathbf{r}'), \tag{41}$$

where the maximum integration angle derived from the Abbe sine condition for Θ and Θ' is now $\Theta' = \arcsin(n\sin\Theta/\mathcal{M}) = \arcsin(\mathrm{NA}/\mathcal{M})$. Similarly, for the magnetic field we find that

$$\mathbf{B}'(\mathbf{r}') = \frac{\mathcal{M}^2}{\sqrt{n}}\int_0^{\Theta'} d\theta' \sin\theta' \sqrt{\frac{\cos\theta'}{\cos\theta}} \int_0^{2\pi} d\phi \times [-E_{0,\parallel}\hat{\mathbf{e}}'_\perp + E_{0,\perp}\hat{\mathbf{e}}_\parallel]\exp(i\mathbf{k}'\cdot\mathbf{r}'). \tag{42}$$

Recognizing that the previously mentioned equations for both electric and magnetic field components [Eqs. (41) and (42)] are simply Fourier representations [expansions into plane waves $\exp(i\mathbf{k}'\cdot\mathbf{r}')$], we now comment on the frequency support restricted to wave vectors with $k' = |\mathbf{k}'| = (k'^2_x + k'^2_y + k'^2_z)^{1/2} = 2\pi/\lambda$, $0 \le \theta' \le \Theta'$, and $0 < \phi \le 2\pi$. This restriction is illustrated as a spherical cap of radius $k' = 2\pi/\lambda$ in the frequency domain; see the left panels in Figs. 12 and 13. In other words, the Fourier amplitudes of the electric and magnetic fields are only nonzero on this spherical cap in Fourier space. To better see this, we rewrite Eq. (41) as

$$\mathbf{E}'(\mathbf{r}') = \int \frac{d^3\mathbf{k}'}{(2\pi)^3}\tilde{\mathbf{E}}'(\mathbf{k}')\exp(i\mathbf{k}'\cdot\mathbf{r}'), \tag{43}$$

where a variable with a tilde denotes the Fourier representation of the variable hereafter. Now, assuming that the three-dimensional integration extends over the entire $\mathbf{k}$ space (Fourier space), the integration measure in the spherical coordinates is $d^3\mathbf{k}' = k'^2\sin\theta' dk' d\theta' d\phi$, and the electric field Fourier amplitude [the integrand in Eq. (43)] for angles $0 \le \theta' \le \Theta'$ is given by (all constant prefactors omitted)

$$\tilde{\mathbf{E}}'(\mathbf{k}') \propto \delta\left(k' - \frac{2\pi}{\lambda}\right)\sqrt{\frac{\cos\theta'}{\cos\theta}}(E_{0,\parallel}\hat{\mathbf{e}}_\parallel + E_{0,\perp}\hat{\mathbf{e}}'_\perp), \tag{44}$$

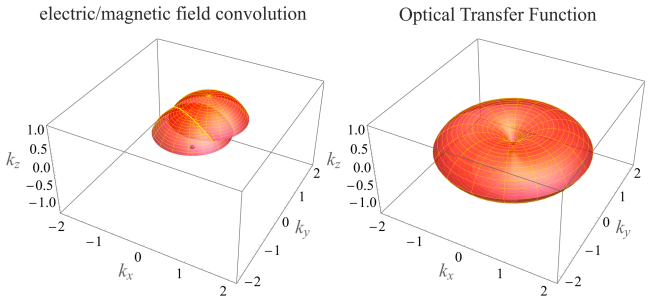

FIG. 12. From electric or magnetic field to intensity. Left panel: two spherical caps show the support of the Fourier representations of electric and magnetic fields given by Eq. (44). Right panel: representation of the extent of frequency support of the imaging OTF obtained by the convolution of the two caps in the left panel; see Eq. (50). The shape of the right panel is termed the butterfly shape, and its missing cone in the middle highlights a wide-field microscope's inability to collect sufficient axial frequencies and thus a lack of optical sectioning.

while it is zero for angles $\theta' > \Theta'$. In Eq. (44) δ denotes Dirac's delta function and guarantees that $k' = 2\pi/\lambda$. The absolute value of the electric field in Eq. (44) is obtained as (see the left panels in Figs. 12 and 13)

$$|\tilde{\mathbf{E}}'| \propto \begin{cases} \sqrt{\frac{\cos\theta'}{\cos\theta}(E_{0,\parallel}^2 + E_{0,\perp}^2)}, & k' = \frac{2\pi}{\lambda}, \quad 0 \le \theta' \le \Theta', \\ 0, & \text{otherwise.} \end{cases} \tag{45}$$

A similar expression holds for the Fourier representation of the magnetic field when $E_{0,\perp}$ is replaced by $-nE_{0,\parallel}$ and $E_{0,\parallel}$ is replaced by $nE_{0,\perp}$.

C. Point spread function

We are now in a position to calculate the PSF denoted by $U(\mathbf{r}')$. The PSF is by its nature a probability density over a photon reaching the point $\mathbf{r}'$ on the image plane, i.e., the detector, where $\mathbf{r}'$ is a random variable. That is, the PSF plays the role of a normalized spatial distribution of light intensity recorded by a detector at the image plane for a pointlike emitter located in the sample space. Most statistical concepts inherent to the modeling of fluorescence microscopy follow from this fundamental probabilistic property of light.

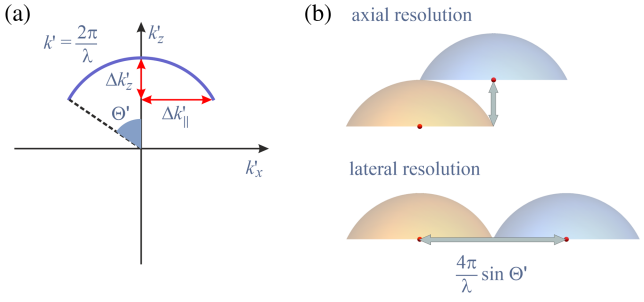

FIG. 13. Visualization of the maximum axial and lateral extents of the Fourier representation of the electric field and the imaging OTF. (a) Cross section of a Fourier representation of the electric field (cap) at $k'_y = 0$. The cross section is an arc with radius $k' = 2\pi/\lambda$ and $0 \le \theta' < \Theta'$; see Eq. (45). The maximum extents of the cap along the lateral and axial directions are given by $\Delta k'_{\parallel} = (2\pi/\lambda)\sin\Theta'$ and $\Delta k'_z = (2\pi/\lambda)(1 - \cos\Theta')$, respectively. (b) Convolution of the caps associated with the electric and magnetic fields along the largest axial and lateral extents beyond which the convolution is zero.

The PSF itself once again follows from the Poynting vector's z component [see Eq. (38)],

$$\begin{aligned} U(\mathbf{r}') &= \frac{c}{8\pi}\hat{\mathbf{e}}_z \cdot [\mathbf{E}'(\mathbf{r}') \times \mathbf{B}'^*(\mathbf{r}')] \\ &= \frac{c}{8\pi}[E'_x(\mathbf{r}')B'^*_y(\mathbf{r}') - E'_y(\mathbf{r}')B'^*_x(\mathbf{r}')]. \end{aligned} \tag{46}$$

As the PSF is known, the image model $\Lambda(\mathbf{r}')$, i.e., the spatial distribution of the expected photon intensity or photon count in image space, for an arbitrary sample follows from the convolution

$$\Lambda(\mathbf{r}') = I \int d^3\mathbf{r}_0 U(\mathbf{r}' - \mathcal{M}\mathbf{r}_0) S(\mathbf{r}_0), \tag{47}$$

where $S(\mathbf{r}_0)$ is the so-called sample function describing the fluorophore distribution. We assume that the PSF U is normalized to unity and that I reflects the total photon emission per fluorophore.

For an aplanatic imaging system, which is shift invariant (see Sec. III.F), Eq. (47) is exact for all emitters on the focal plane, i.e., for $z_0 = 0$. However, it is approximate for emitters outside the focal plane, as follows from the discussion of the Abbe and Herschel conditions in Sec. III.A.

Using the electric field of Eq. (44), one finds that the lateral components of the electric and magnetic fields in the Fourier domain are explicitly given (for $\theta' \le \Theta'$) by

$$\begin{aligned} \begin{pmatrix} \tilde{E}'_x \\ \tilde{E}'_y \end{pmatrix} &\propto \delta\left(k' - \frac{2\pi}{\lambda}\right)\sqrt{\frac{\cos\theta'}{\cos\theta}} \\ &\times \begin{pmatrix} -E_{0,\parallel}\sin\phi + E_{0,\perp}\cos\theta'\cos\phi \\ E_{0,\parallel}\cos\phi + E_{0,\perp}\cos\theta'\sin\phi \end{pmatrix} \end{aligned} \tag{48}$$

and

$$\begin{aligned} \begin{pmatrix} \tilde{B}'_x \\ \tilde{B}'_y \end{pmatrix} &\propto \delta\left(k' - \frac{2\pi}{\lambda}\right)\sqrt{\frac{\cos\theta'}{\cos\theta}} \\ &\times \begin{pmatrix} -E_{0,\parallel}\cos\theta'\cos\phi - E_{0,\perp}\sin\phi \\ -E_{0,\parallel}\cos\theta'\sin\phi + E_{0,\perp}\cos\phi \end{pmatrix}, \end{aligned} \tag{49}$$

where we also use the Cartesian representations of $\hat{\mathbf{e}}_{\parallel}$ and $\hat{\mathbf{e}}'_{\perp}$, as in Eq. (37). Moreover, we remember that the refractive index in image space is assumed to be 1 (air). Thus, no additional prefactor appears in the coinciding magnetic field expression.

With the Fourier representations of the electric and magnetic fields at hand, we now derive the imaging OTF and then the PSF. To start, we note that the PSF is given by the product of the electric and magnetic field components in the spatial domain; see Eq. (46). However, within the Fourier domain, we use the well-known convolution theorem: the Fourier

representation of the product of two functions is proportional to the convolution of their Fourier representations. As such, the imaging OTF is given by

$$\begin{aligned}\tilde{U}(\mathbf{k}') &\propto \tilde{E}'_x(\mathbf{k}') \otimes \tilde{B}'^{*}_y(\mathbf{k}') - \tilde{E}'_y(\mathbf{k}') \otimes \tilde{B}'^{*}_x(\mathbf{k}') \\ &= \int d^3\mathbf{k}''[\tilde{E}'_x(\mathbf{k}'-\mathbf{k}'')\tilde{B}'^{*}_y(\mathbf{k}'') \\ &\quad - \tilde{E}'_y(\mathbf{k}'-\mathbf{k}'')\tilde{B}'^{*}_x(\mathbf{k}'')], \end{aligned} \tag{50}$$

where $\otimes$ denotes convolution. The resulting OTF is then related to the PSF by Fourier transform,

$$U(\mathbf{r}') = \int \frac{d^3\mathbf{k}'}{(2\pi)^3}\tilde{U}(\mathbf{k}')\exp(i\mathbf{k}'\cdot\mathbf{r}'). \tag{51}$$

The convolution of Eq. (50) is depicted in Fig. 12. The two spherical caps (note that it is only the area on the surface) shown in the left panel represent regions where the Fourier amplitudes of the electric and magnetic fields are nonzero; see Eq. (45). The convolution of these caps results in the butterfly-shaped three-dimensional figure shown in the right panel of Fig. 12, where the surface shown represents the maximum extent of frequency support of the OTF. That is, the OTF amplitude vanishes for all frequencies outside this region and takes nonzero values only for frequencies within the three-dimensional shape, which is also termed the microscope's bandpass.

From Fig. 13(a), one finds that the lateral and axial extents of the Fourier representations of the electric and magnetic fields are $\Delta k'_{\|} = 2\pi\sin\Theta'/\lambda$ and $\Delta k'_z = 2\pi(1-\cos\Theta')/\lambda$, respectively. As the OTF is computed from the autoconvolution of the cap associated with the electric and magnetic fields, the lateral and axial sizes of the OTF are then found to be $4\pi\sin\Theta'/\lambda$ and $2\pi(1-\cos\Theta')/\lambda$, respectively; see Fig. 13(b).

In other words, the microscope does not transmit any lateral spatial frequencies beyond $k'_{\|} > 4\pi\sin\Theta'/\lambda$ or any axial spatial frequencies beyond $k'_z > 2\pi(1-\cos\Theta')/\lambda$, where $k'_{\|} = \sqrt{k'^2_x + k'^2_y}$ is the amplitude $\mathbf{k}'$'s projection in the k_x-k_y plane. Thus, the three-dimensional intensity distribution in image space does not transmit lateral spatial modulations smaller than $2\pi/\max k'_{\|} = \lambda/2\sin\Theta'$. This leads to spatial modulations of $\mathcal{M}\lambda/2n\sin\Theta$ in image space using the Abbe sine condition and translates into the smallest discernible spatial variation $\lambda/2n\sin\Theta$ in the sample space when one takes into account that the lateral magnification is $\mathcal{M}$. Therefore, we recover Abbe's resolution limit (14) as 2π over the largest lateral spatial frequency transmitted by the microscope from sample to image space,

$$r^l_{\min} = \frac{2\pi}{k^l_{\max}}, \tag{52}$$

where $r^l_{\min}$ and $k^l_{\max}$ denote the resolution and maximum extent of the OTF along the lth direction, respectively.

While Eq. (52) provides a measure of resolution for lens-based imaging systems with OTF magnitudes consisting of a single lobe monotonically decaying to zero, for example, lateral magnitude of wide-field microscope's OTF, it should be used with care for more complicated OTFs such as axial resolution for wide-field microscopes (see Fig. 12 and Sec. III.E), SIM (see Sec. IV.D), some types of light-sheet microscopes with multiple gaps in their OTF magnitudes (see Sec. IV.E), etc.

As such, regarding the wide-field microscope's axial resolution, the situation is more complicated due to the OTF's shape in the axial direction. Specifically, in the right panel of Fig. 12 one can see that the butterfly-shaped imaging OTF does not support axial frequencies within a cone defined by $k'_z/k'_{\|} > \tan\Theta'$. This is often called the OTF's missing cone. One effect of this missing cone is that a wide-field microscope does not provide *optical sectioning* (z sectioning). That is, for $k'_{\|} \approx 0$ a wide-field microscope collects limited axial spatial frequencies. In other words, the PSF pattern formed by light collected from a fluorophore using a wide-field setup varies slowly with the fluorophore's axial position.

Yet, as seen in Fig. 12, axial frequencies k'_z have nonzero amplitudes for $0 < k'_{\|} < \max k'_{\|} = 4\pi\sin\Theta'/\lambda$. The maximal value $k'_z = 2\pi(1-\cos\Theta')/\lambda$ contained in the OTF shows that the smallest possible spatial modulation of the PSF along the optical axis is approximately $\lambda/(1-\cos\Theta')$. For paraxial optics, i.e., for small values of Θ and Θ' where we have approximately an axial magnification $\mathcal{M}_z = \mathcal{M}^2/n$ (see Sec. III.A) and with the approximation $1-\cos\Theta' \approx \Theta'^2/2 \approx n^2\Theta^2/2\mathcal{M}^2$, this translates into a small axial modulation of $2\lambda/n\Theta^2 \approx 2n\lambda/(\mathrm{NA})^2$ of the sample function transmitted through the microscope. This is in accordance with our previous estimate of the axial resolution limit in Eq. (15). Problems associated with the OTF's missing cone, i.e., the missing z sectioning, is considered in Sec. IV, where we discuss confocal microscopy alongside other modalities.

D. Electromagnetic field emission of an oscillating electric dipole

In Sec. III.C, we derived integral expressions for the OTF and PSF of a wide-field microscope; see Eqs. (46), (50), and (51). Here we evaluate these integrals and obtain a wide-field microscope's exact OTF and PSF using $\mathbf{E}_0(\theta,\phi) = E_{0,\|}\hat{\mathbf{e}}_{\|} + E_{0,\perp}\hat{\mathbf{e}}_{\perp}$ for a fluorescent point emitter; see Eq. (44). We do so by noting that the electromagnetic emission of fluorescence emitters (organic dyes, proteins, quantum dots, etc.) used in fluorescence microscopy are often well approximated as an oscillating electric dipole. Important exceptions on which we can generalize include some emission bands of rare-earth emitters (for example, europium complexes) that exhibit magnetic dipole or electric quadrupole properties (Moskovits and DiLella, 1982; Binnemans, 2015).

To compute the electric dipole's oscillating electromagnetic field, we start with a dipole moment with an amplitude $\mathbf{p}$ and an oscillation frequency ω located at $\mathbf{r}_d = (x_d, y_d, z_d)$ in a sample medium with a refractive index n_d. Moreover, considering that all fields oscillate as $\exp(-i\omega t)$ as the dipole moment oscillations, we focus on the amplitudes of the electric and magnetic fields. In this case, the Maxwell's equations read

$$\nabla \times \mathbf{E} = \frac{i\omega}{c}\mathbf{B},$$
$$\nabla \times \mathbf{B} = -\frac{i\omega\epsilon_d}{c}\mathbf{E} + \frac{4\pi}{c}\mathbf{j}, \tag{53}$$

where $\epsilon_d = n_d^2$ is the dielectric constant of the sample solution in which the dipole is embedded and $\mathbf{j} = -i\omega\mathbf{p}\delta(\mathbf{r}-\mathbf{r}_d)$ is the electric current generated by the oscillating dipole. Thus, we find that $\nabla\times\nabla\times\mathbf{E}_d - k_d^2\mathbf{E}_d = 4\pi k_0^2\mathbf{p}\delta(\mathbf{r}-\mathbf{r}_d)$ for the electric field $\mathbf{E}_d$ of the dipole emitter, where $k_0 = \omega/c$ and $k_d = n_d k_0$. Using $\nabla\times\nabla\times\mathbf{E}_d = \nabla\nabla\cdot\mathbf{E}_d - \nabla^2\mathbf{E}_d$ (Jackson, 1999) and passing to Fourier space yields, for the Fourier amplitude $\tilde{\mathbf{E}}_d$,

$$(k'^2 - k_d^2)\tilde{\mathbf{E}}_d - \mathbf{k}'(\mathbf{k}'\cdot\tilde{\mathbf{E}}_d) = 4\pi k_0^2\mathbf{p}\exp(-i\mathbf{k}'\cdot\mathbf{r}_d), \tag{54}$$

where $\mathbf{k}'$ is the Fourier space coordinate. Multiplying Eq. (54) by $\mathbf{k}'$ yields $\mathbf{k}'\cdot\tilde{\mathbf{E}}_d = -(4\pi/\epsilon_d)(\mathbf{k}'\cdot\mathbf{p})\exp(-i\mathbf{k}'\cdot\mathbf{r}_d)$, which we substitute into Eq. (54) to arrive at

$$\tilde{\mathbf{E}}_d = \frac{4\pi\exp(-i\mathbf{k}'\cdot\mathbf{r}_d)}{\epsilon_d(k'^2 - k_d^2)}[k_d^2\mathbf{p} - \mathbf{k}'(\mathbf{k}'\cdot\mathbf{p})]. \tag{55}$$

In real space, Eq. (55) reads

$$\mathbf{E}_d = \int \frac{d^3\mathbf{k}'}{2\pi^2\epsilon_d}[k_d^2\mathbf{p} - \mathbf{k}'(\mathbf{k}'\cdot\mathbf{p})]\frac{\exp[i\mathbf{k}'\cdot(\mathbf{r}-\mathbf{r}_d)]}{k'^2 - k_d^2}, \tag{56}$$

where $|\mathbf{r}-\mathbf{r}_d|$ is the distance between the electric dipole's location $\mathbf{r}_d$ and the observation point $\mathbf{r}$.

To obtain an expression well suited in modeling the emission of a dipole in a planar system (for example, above a flat cover slide), we perform the integration along the k_z' coordinate in Eq. (56) using Cauchy's residue theorem. To do so, we close the integration path along the real axis and complete a semicircle at infinity over the complex k_z' plane, as shown in Fig. 68. To make sure that the exponent vanishes when the contour is extended into the complex plane, one has to close the contour over the positive imaginary half plane when $z - z_d > 0$ and over the negative imaginary half plane when $z - z_d < 0$. Along the real axis, the integrand has two poles at positions $\pm w_d = \pm\sqrt{k_d^2 - q^2}$, where $q^2 = k_x'^2 + k_y'^2$. However, the integration's result must contain only outgoing plane waves [the Sommerfeld radiation condition (Sommerfeld, 1949)], achieved by deforming the integration contour around the two poles as shown in Fig. 68. Subsequently applying Cauchy's residue theorem yields

$$\mathbf{E}_d = \frac{i}{2\pi\epsilon_d}\int\frac{d^2\mathbf{q}}{w_d}[k_d^2\mathbf{p} - \mathbf{k}_d(\mathbf{k}_d\cdot\mathbf{p})] \times \exp[i\mathbf{q}\cdot(\boldsymbol{\rho}-\boldsymbol{\rho}_d) + iw_d|z - z_d|], \tag{57}$$

where we use the abbreviations $\mathbf{k}_d = (\mathbf{q}, w_d)$, with $w_d = \sqrt{k_d^2 - q^2}$ as the pole location. In Eq. (57) $\boldsymbol{\rho}$ and $\mathbf{q}$ collect lateral coordinates in the real and Fourier spaces, respectively. Further, $(\boldsymbol{\rho}_d, z_d)$ denotes the dipole spatial coordinates. The two-dimensional integration over $\mathbf{q}$ extends over an infinite Fourier plane oriented perpendicularly to the optical axis. Equation (57) is the plane wave representation of the electric field of a free oscillating dipole, also called the Weyl representation (Weyl, 1919; Banõs, 1966; Mertz, 2019a). As we later see, the Weyl representation is particularly suited to modeling the imaging of an emitter through a microscope.

Next we consider the situation where the refractive index n_d of the medium in which the emitting dipole is embedded and the refractive index n of the immersion medium of the microscope's objective differ (for example, imaging with an oil-immersion objective with an emitter in water). This situation is schematically shown in Fig. 14. We use Eq. (57) to model the propagation of the electric field through an interface dividing the sample (dipole) and immersion medium, i.e., the cover slide surface. To do so, we recast the integrand in Eq. (57) as

$$k_d^2\mathbf{p} - \mathbf{k}_d(\mathbf{k}_d\cdot\mathbf{p}) = k_d^2[(\mathbf{p}\cdot\hat{\mathbf{e}}_\parallel)\hat{\mathbf{e}}_\parallel + (\mathbf{p}\cdot\hat{\mathbf{e}}_{d\perp})\hat{\mathbf{e}}_{d\perp}], \tag{58}$$

where we use $\mathbf{p} = (\mathbf{p}\cdot\hat{\mathbf{e}}_\parallel)\hat{\mathbf{e}}_\parallel + (\mathbf{p}\cdot\hat{\mathbf{e}}_{d\perp})\hat{\mathbf{e}}_{d\perp} + (\mathbf{p}\cdot\hat{\mathbf{k}}_d)\hat{\mathbf{k}}_d$ since the unit vectors $\hat{\mathbf{e}}_\parallel$, $\hat{\mathbf{e}}_{d\perp}$, and $\hat{\mathbf{k}}_d$ form an orthonormal set similar to that in Eq. (37). As such, the problem reduces to considering the propagation of s- and p-polarized plane waves through a planar interface.

We now use Eqs. (57) and (58) to write the electric field after it crosses the interface between the two media and travels a distance through the immersion medium (with refractive index n) before arriving in front of the objective lens in terms of the p- and s-polarized components

$$\mathbf{E}_d = \frac{ik_0^2}{2\pi}\int\frac{d^2\mathbf{q}}{w}[t_\parallel(\mathbf{p}\cdot\hat{\mathbf{e}}_\parallel)\hat{\mathbf{e}}_\parallel + t_\perp(\mathbf{p}\cdot\hat{\mathbf{e}}_\perp)\hat{\mathbf{e}}_\perp] \times \exp[i\mathbf{q}\cdot(\boldsymbol{\rho}-\boldsymbol{\rho}_d) - iw_d z_d + iw(z-f)], \tag{59}$$

where $t_{\parallel,\perp}$ are the Fresnel transmission coefficients, $(\boldsymbol{\rho}, z)$ represents the observation point coordinates within the

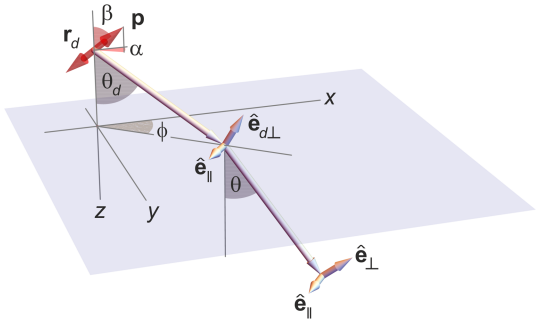

FIG. 14. Angular distribution of the electric field generated by a single dipole emitter. The gray rectangle represents the cover slide (commonly assumed to coincide with the $z = 0$ plane), which is the interface between the electric dipole's embedding medium (above the cover slide) and the immersion medium below the cover slide. The red two-headed arrow depicts the dipole; α and β are the polar and inclination (azimuthal) angles describing the orientation of the dipole, respectively, ϕ is the polar angle of the wave vector, and θ_d and θ are the azimuthal angles of the wave vector above and below the interface.

immersion medium, and the focal distance f is the location of the focal plane with respect to the interface $z = 0$ coinciding with the cover slide surface separating the sample from the immersion medium; see Fig. 14. In Eq. (59) the axial component w of the wave vector $\mathbf{k}$ in the immersion medium is given by $w = \sqrt{k^2 - q^2} = \sqrt{n^2 k_0^2 - q^2}$. Moreover, the unit vector $\hat{\mathbf{e}}_\perp$ is similar to $\hat{\mathbf{e}}_{d\perp}$ but is formed from the wave vector $(\mathbf{q}, \sqrt{n^2 k_0^2 - q^2})$ instead of $(\mathbf{q}, \sqrt{n_d^2 k_0^2 - q^2})$.

Equation (59) can be readily generalized to an arbitrary number of interfaces. For instance, if an emitter is imaged through a stack of several layers characterized by different refractive indices, then the single interface's Fresnel transmission coefficients in Eq. (59) must simply be replaced by those for the stacked structure.

Finally, when considering Fig. 14, we have $w = nk_0 \cos\theta$ and $\mathbf{q} = nk_0(\sin\theta\cos\phi, \sin\theta\sin\phi, 0)$, leading to $d^2\mathbf{q}/w = dq_x dq_y/w = nk_0 \sin\theta d\theta d\phi$ in spherical coordinates. Substituting this result into Eq. (59) and comparing it to Eq. (36) yields the following electric field amplitude $\mathbf{E}_0(\theta, \phi)$ for a dipole emitter (up to some constant factor):

$$\mathbf{E}_0 \propto [t_\parallel(\mathbf{p}\cdot\hat{\mathbf{e}}_\parallel)\hat{\mathbf{e}}_\parallel + t_\perp(\mathbf{p}\cdot\hat{\mathbf{e}}_\perp)\hat{\mathbf{e}}_\perp] \times \exp[-i\mathbf{q}\cdot\boldsymbol{\rho}_d - iw_d z_d - iwf], \tag{60}$$

or more explicitly

$$\begin{pmatrix} E_{0,\parallel} \\ E_{0,\perp} \end{pmatrix} = \begin{pmatrix} \mathbf{E}_0\cdot\mathbf{e}_\parallel \\ \mathbf{E}_0\cdot\mathbf{e}_\perp \end{pmatrix} \propto |\mathbf{p}|\exp(-i\mathbf{q}\cdot\boldsymbol{\rho}_d - iw_d z_d - iwf) \times \begin{pmatrix} -t_\parallel \sin\beta\sin(\phi-\alpha) \\ t_\perp[\sin\beta\cos\theta\cos(\phi-\alpha) - \cos\beta\sin\theta] \end{pmatrix}, \tag{61}$$

where α and β are the dipole orientation angles described in Fig. 14. By inserting these expressions into Eqs. (41), (42), and (46), one can compute the wide-field image PSF of the dipole emitter with arbitrary position and orientation. When doing so, one can present the results in terms of the lateral sample coordinates $\boldsymbol{\rho} = \boldsymbol{\rho}'/\mathcal{M}$ instead of the image space coordinates $\boldsymbol{\rho}'$ and as a function of the axial position z_d (with respect to the cover slide) of the emitter. This notation is applied to all PSF visualizations in this review. Thus, in what follows, when writing the PSF $U(\mathbf{r})$ as a function of $\mathbf{r}$ it is assumed that the lateral coordinates x and y are the coordinates conjugate to x' and y', i.e., $x = x'/\mathcal{M}$ and $y = y'/\mathcal{M}$, and z refers to the axial position z_d of the emitter.

As a first example of a PSF visualization, Fig. 15 shows three-dimensional representations of a dipole emitter's PSF along the optical axis for a dipole oriented along the x axis (left panel) and the z axis (middle panel), and for a rapidly rotating emitter (right panel) where the isotropic PSF $U_{\text{iso}}(\mathbf{r})$ is given by an average of the PSFs calculated for dipole orientations along the x, y, and z axes (Richards and Wolf, 1959),

$$U_{\text{iso}}(\mathbf{r}) = \tfrac{1}{3}[U_x(\mathbf{r}) + U_y(\mathbf{r}) + U_z(\mathbf{r})]. \tag{62}$$

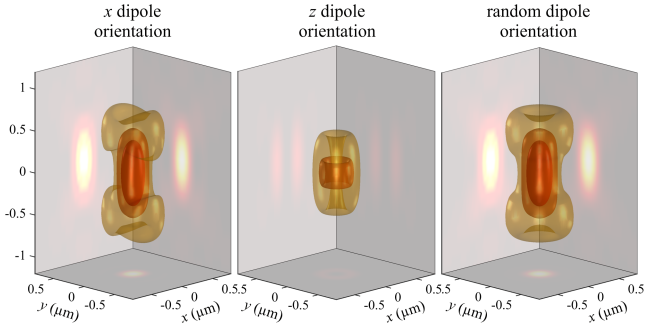

FIG. 15. PSF of a wide-field microscope projected into sample space. Shown are plots of the $1/e$, $1/e^2$, and $1/e^3$ isosurfaces of the maximum PSF value. The lateral coordinates refer to back-projected sample space coordinates $(x, y) = (x', y')/\mathcal{M}$, whereas the axial coordinate refers to an emitter's axial position z_d. We retain this PSF representation throughout the review. The panels are described in the text. Calculations were performed for a NA = 1.2 water immersion objective with $n = 1.33$ and an emission wavelength $\lambda = 550$ nm.

Accounting for the effects of emitter orientation is of key interest in SMLM (Sec. V.B.1), as fixed orientations can lead to systematic mislocalization of emitters in space (Enderlein, Toprak, and Selvin, 2006; Backlund *et al.*, 2014; Deschout *et al.*, 2014; Fazel and Wester, 2022). That being said, fluorescent labels are often coupled to structures with a sufficiently flexible linker that allows us to approximate labels as nearly freely rotating.

As an example, Fig. 16 shows images of single emitters with different axial positions and inclination angles toward the optical axis. For out-of-focus emitters intermediate values of the inclination angle β (see Fig. 14) can lead to considerable shifts in an emitter's image apparent center of mass, which is especially significant for emitters away from the focal plane. The situation worsens when working with oil-immersion objectives with a larger total internal reflection (TIR) critical

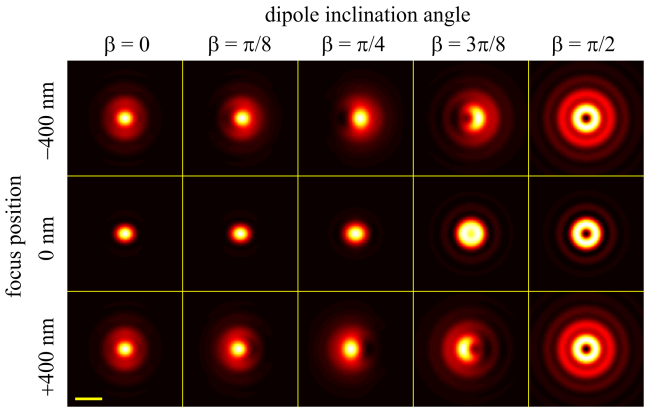

FIG. 16. Effect of orientation on the emitter's image. Top row: images of electric dipole emitters of fixed strength but different orientations in the x-z plane, where β is the inclination angle; see Fig. 14. The emitter is situated 400 nm below the focal plane (NA = 1.2, $n = 1.33$). Middle row: same as the top row, but for an emitter situated in the focal plane. Bottom row: same again but for an emitter situated 400 nm above the focal plane. The scale bar is 0.5 μm.

angle than water immersion objective, which allows fluorescent light with larger incident angles to be collected. In this case, even in-focus positions depend on the emitter's orientation. While this effect hinders the localizations of rigid single molecules under the assumption of a symmetric PSF, it can be exploited to learn three-dimensional orientations of molecules (Backer *et al.*, 2019; Hulleman *et al.*, 2021; Rimoli *et al.*, 2022; Wu, Lu, and Lew, 2022).

Finally, we consider the refractive index mismatch resulting in PSF distortion; see Sec. III.F. As an example, Fig. 17 shows this effect for a slight refractive index mismatch of $\Delta n = 0.05$, again for a water immersion objective with NA = 1.2. We further assume that the objective lens is corrected for the light refraction introduced by the cover slide. This mismatch results primarily in PSF axial stretching and an axial shift between its center position toward larger z values with respect to the actual position of the emitter. However, the lateral PSF cross section at the axial location of its maximum does not change significantly, meaning that the refractive index mismatch does not affect the lateral position of the focused image of an emitter, but does result in its mislocalization along the optical axis.

E. Scalar approximation of the PSF

In Sec. III.D, we derived the exact electric field of an emitter, i.e., the oscillating dipole [see Eq. (61)], and used it to compute the PSF. However, these exact expressions are difficult to computationally manipulate. As such, here we provide a simple approximation to the emitter's electric field and the resulting PSF.

Along these lines, for many practical applications we assume an isotropic emitter, i.e., one with a uniform emission amplitude in all directions. In such a case, we can ignore the vectorial nature of the electric (and magnetic) fields, thus resulting in an approximate scalar model. To derive such scalar approximations, we start with Eq. (41) and replace the amplitude vector $E_{0,\parallel}\hat{\mathbf{e}}_{\parallel} + E_{0,\perp}\hat{\mathbf{e}}'_{\perp}$ with a scalar constant. Therefore, the expression for the now "scalar" electric (magnetic) field in the image plane generated by an isotropic emitter on the optical axis at position $z = z_d$ simplifies (up to a constant factor) to

$$\begin{aligned} E(\mathbf{r}) &\propto \int_0^{\Theta'} d\theta' \, \sin\theta' \sqrt{\frac{\cos\theta'}{\cos\theta}} \int_0^{2\pi} d\phi e^{i\mathbf{q}'\cdot\boldsymbol{\rho}' - ik\cos\theta z} \\ &\propto \int_0^{\Theta'} d\theta' \, \sin\theta' \sqrt{\frac{\cos\theta'}{\cos\theta}} \int_0^{2\pi} d\phi e^{i|\mathbf{q}|\rho\cos\phi - ik\cos\theta z} \\ &\propto \int_0^{\Theta} d(\sin\theta) \sin\theta \frac{J_0(k\sin\theta\rho)}{\sqrt{\cos\theta'\cos\theta}} e^{-ik\cos\theta z}, \end{aligned} \tag{63}$$

where we used $\mathbf{q}'\cdot\boldsymbol{\rho}' = \mathbf{q}\cdot\boldsymbol{\rho} = |\mathbf{q}|\rho\cos\phi$ due to $\rho' = \mathcal{M}\rho$ and the Abbe sine condition $\sin\theta' = (n/\mathcal{M})\sin\theta$ while remembering $|\mathbf{q}'| = k_0\sin\theta'$ and $|\mathbf{q}| = k\sin\theta = nk_0\sin\theta$. In the second step, we performed the integral with respect to ϕ and used the Abbe sine condition and its differential form [see Eq. (40)] and ignored all of the prefactors of n and $\mathcal{M}$. Here J_m is the Bessel function of the first kind of order m (Olver *et al.*, 2010).

Further simplification is possible by replacing the square root factor for unity valid for small values of θ' and θ (far-field limit). Equation (63) therefore simplifies to

$$E(\rho, z) \approx \left(\frac{n}{\mathcal{M}}\right)^2 \int_0^{\sin\Theta} d\eta \, \eta J_0(k\eta\rho) e^{-ik\sqrt{1-\eta^2}z}, \tag{64}$$

where $\eta = \sin\theta$. For the special case of $z = 0$ (emitter in the focal plane), analytic integration then yields

$$E(\rho) \approx \frac{\mathrm{NA}}{\mathcal{M}^2 k_0 \rho} J_1(\mathrm{NA}k_0\rho), \tag{65}$$

where we use $k\sin\Theta = \mathrm{NA}k_0$. In Eq. (65) J_1 is the Bessel function of the first kind of the order of 1 (Olver *et al.*, 2010). The PSF is then given by the absolute square of the scalar electric field. Therefore, for the 2D PSF of an in-focus isotropic emitter in the far-field limit, we find the well-known Airy pattern

$$U(\rho) \propto \left[\frac{J_1(\mathrm{NA}k_0\rho)}{k_0\rho}\right]^2, \tag{66}$$

where we omit a constant factor and where we recall that $k_0 n\sin\Theta = \mathrm{NA}k_0$ is the maximum lateral wave-vector component transmitted by the microscope from the sample to the image plane; see Sec. I.C.

In situations where the scalar approximation is suitable (for example, 3D imaging with molecules more than a wavelength away from the cover slide), this approximate PSF facilitates a computationally lighter model, as calculating Eq. (66) requires a single integration (Fourier transform), while evaluating Eq. (62) requires three integrations. To check the accuracy of this approximation, Fig. 18 shows a comparison of the PSF's line cross section through its center, calculated using the full vectorial model of Secs. III.C and III.D and the scalar approximation of Eq. (66). The scalar approximation shows

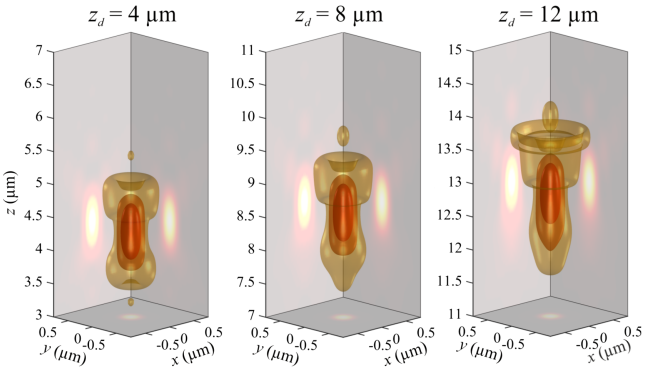

FIG. 17. Effect of a refractive index mismatch on the PSF. The PSF of a rapidly rotating electric dipole emitter (isotropic emitter) is positioned at various distances from a cover slide surface ($z = 0$). The calculations were done for an NA = 1.2 objective corrected for an immersion or medium with $n = 1.33$, while the solution above the cover slide has $n = 1.38$ (i.e., a refractive index mismatch $\Delta n = 0.05$). The bottom of each box shows a density plot of the PSF's cross section through its maximum value.

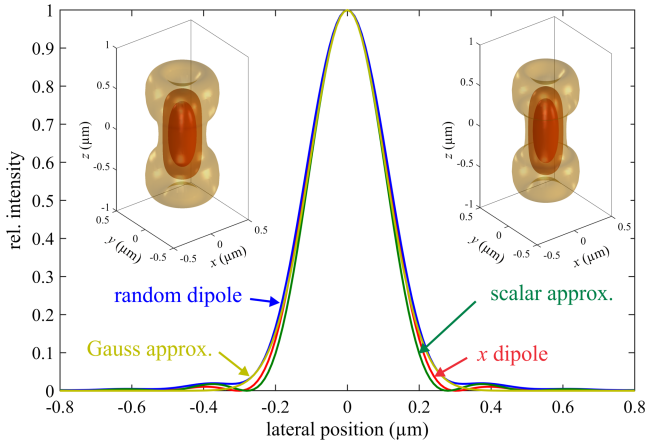

FIG. 18. Comparison between scalar and vector PSF calculations. Shown are cross sections of the PSF across the x axis in the focal plane. The red curve shows the results of the full wave-vector PSF calculation for an electric dipole emitter with a fixed x-axis orientation, the blue curve displays the same calculation for a rapidly rotating isotropic or random emitter, the green curve presents the result of Eq. (66), and the ochre curve shows the Gaussian approximation of Eq. (69). Left inset: three-dimensional isosurface PSF plot using the exact vector field calculation for an isotropic emitter. Right inset: three-dimensional isosurface PSF plot using the exact vector field calculation for the scalar approximation. All calculations were performed for a water immersion objective with NA = 1.2.

negligible deviations from the accurate model for the system considered (water immersion objective with NA = 1.2 and an emission wavelength of 500 nm). In most cases, this approximation is sufficient for quantitative analysis of fluorescence microscopy data, for example, fitting single-molecule images (see Sec. V.B.1) while provided with rapidly rotating molecules.

However, the usefulness of the scalar approximation is further evident when one considers a microscope's OTF. When Eqs. (41) [see also Eq. (45)] and (63) are compared, the *frequency support* of the Fourier transforms for the vector and scalar representations of the electric field are identical and are given by a spherical cap centered at $\mathbf{k}' = \mathbf{0}$ with radius $2\pi/\lambda$ and half opening angle Θ'; see Figs. 12 and 13. As with the PSF visualization, one can show the OTF back-projected to sample space, which is done using the Abbe sine condition as $(k'_x, k'_y) = n/\mathcal{M}(k_x, k_y)$ and the relation $k' = k/n$. Cross sections of the corresponding electric (magnetic) field Fourier representation amplitude is shown in the two leftmost panels of Fig. 19 at $k_y = 0$. In the case of vectorial model, for each of the vector fields $\mathbf{E}$ and $\mathbf{B}$ one has two such cross sections, one for the $E_\parallel$ ($B_\parallel$) component and one for the $E_\perp$ ($B_\perp$) component. Figure 19 represents the scalar approximation with a uniform field amplitude over the entire spherical cap; cf. Eq. (63). In both the exact vector field description and the scalar approximation, the PSF is found by products of the electric and magnetic fields, which translates in Fourier space to a convolution of the corresponding Fourier representations of these fields.

A cross section of the OTF amplitude at $k_y = 0$ is visualized in the right panel of Fig. 19, with the (auto)convolution of the

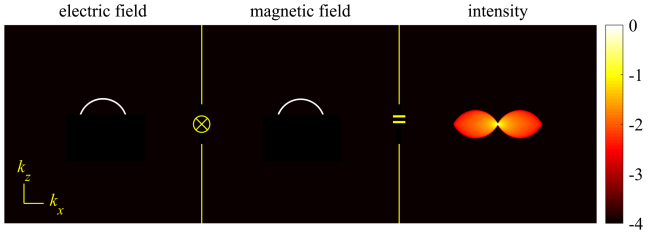

FIG. 19. Scalar approximation of the OTF of a wide-field microscope. Calculations were done for an NA = 1.2 water immersion objective and an emission wavelength of 550 nm. Left panel: $k_x k_z$ cross section of the electric field amplitudes in *sample space* having a frequency support (frequencies with nonzero amplitude) in the shape of a spherical cap with radius $k = 2\pi n/\lambda$ and an opening half angle equal to the objective's maximum half angle Θ. Middle panel: the same distribution for the magnetic field. Right panel: three-dimensional convolution of the left two panels yielding the scalar approximation of the OTF amplitude. All panels show density plots of the *decadic logarithm* of the Fourier amplitude's absolute value (see the color bar on the right-hand side) normalized by the maximum absolute value of the corresponding amplitudes. In all panels, the coordinate origin ($k_x = 0$ and $k_z = 0$) is at the center. Throughout this review, we use the same representation for all OTFs shown.

two Fourier amplitude distributions shown on the left. We note that in general the OTF is a complex quantity and all panels show the OTF amplitudes, which are sometimes called modulation transfer functions but for brevity are simply called OTFs in all subsequent figures. Although the exact amplitude distribution over the butterfly-shaped frequency support of the OTF will be slightly different for the full vector field [see Fig. 12 and Eq. (45)] and the scalar approximation [see Eq. (65)], the frequency support of the OTF remains identical. This is particularly important to emphasize because the limits of this frequency support determines the microscope's optical resolution. Here we again emphasize that the resolution along a given direction is determined by the maximum frequency $k_{\max}$ of this support along the chosen direction by Eq. (52). For the wide-field microscope in Fig. 19, the lateral and axial extents of the OTF's frequency support are $k_{\max,y} = 2nk_0 \sin\Theta$ and $k_{\max,z} = nk_0(1 - \cos\Theta)$, respectively; see also Fig. 13. This leads to the previously derived lateral and axial resolutions [see Secs. I.C and III.C and Eq. (52)]

$$y_{\min} = \frac{2\pi}{k_{\max,y}} = \frac{\lambda}{2n\sin\Theta} = \frac{\lambda}{2\mathrm{NA}} \tag{67}$$

and

$$z_{\min} = \frac{2\pi}{k_{\max,z}} = \frac{\lambda}{n(1-\cos\Theta)} \approx \frac{2n\lambda}{\mathrm{NA}^2}. \tag{68}$$

Equation (67) is Abbe's well-known lateral resolution limit for a wide-field microscope, while the obtained approximate axial resolution in Eq. (68) is valid only for small numerical apertures.

We can further simplify the PSF by approximating Eq. (66) with a 2D Gaussian function

$$U_{\mathrm{Gauss}}(\boldsymbol{\rho}-\boldsymbol{\rho}_0) \propto \exp\left(-\frac{|\boldsymbol{\rho}-\boldsymbol{\rho}_0|^2}{2\sigma_{\mathrm{PSF}}^2}\right), \tag{69}$$

where $\sigma_{\mathrm{PSF}} = \sqrt{2}/\mathrm{NA}k_0 = \lambda/\sqrt{2}\pi n \sin\Theta$, as found when the same curvature values are required at the maximum for both Eqs. (69) and (66); see also Fig. 18. This approximation is useful in creating a simple model, allowing straightforward fitting algorithms for many localization applications (Stallinga and Rieger, 2010; Fazel and Wester, 2022). This model fits the PSF's main lobe and thus is a good approximation when imaging is performed within the depth of focus of an aberration-free microscope. The width σ_{PSF} is usually experimentally fit from a calibration sample or model (Santos and Young, 2000).

F. Optical aberrations

Finally, we discuss the impact of optical aberrations on the PSF. Optical aberrations refer to any deviation from the previously presented idealized imaging models and can be classified into various groups. The first distinction revolves around the wavelength, i.e., monochromatic aberrations occurring for a single wavelength, in contrast to chromatic aberrations originating from the chromatic dispersion of the components in the optical system. The second distinction is characterized by shift invariance, i.e., aberrations similar at every point in the field of view (FOV) versus off-axis aberrations. In the presence of optical aberrations, modeling the PSF as a two-dimensional Fourier transform $\mathcal{F}_{2\mathrm{D}}$ operation is common as the aberrations can then be treated as part of the system's OTF. Here we focus on the scalar model, i.e., Eq. (63). This approach can, however, be generalized to the vectorial case (Backer and Moerner, 2014; Siemons *et al.*, 2018; Ferdman *et al.*, 2020).

As optical aberrations can generally be a function of (ϕ, θ'), we return to Eq. (63) and extend it to include an additional amplitude or phase function that takes aberrations into account. We can then recast it as a $\mathcal{F}_{2\mathrm{D}}$ operation prior to the integration over ϕ,

$$E(\rho, z; \mathbf{r}_0) \propto \mathcal{F}_{2\mathrm{D}}[\mathcal{A}(\theta', \phi) e^{i[\Psi(\theta'; z, f) + \Phi(\theta', \phi)]}], \tag{70}$$

where we ignored the term $\sqrt{\cos\theta'/\cos\theta}$ due to its negligible contribution. In Eq. (70) $\mathcal{A}e^{i(\Psi+\Phi)}$ is the so-called pupil function, whereas $\mathcal{A}(\theta', \phi)$ is the pupil function's amplitude, which, neglecting all constant factors, simplifies to the Fourier plane support, limited by either the NA or n_d as follows:

$$\mathcal{A}(\theta', \phi) = \begin{cases} 1 & \text{if } \sin\theta' \le \min(n_d/n, \mathrm{NA}/n), \\ 0 & \text{otherwise}, \end{cases} \tag{71}$$

where n and n_d are the refractive index of the objective immersion and the dipole (emitter) medium, respectively. In full generality, $\mathcal{A}$ can be a function of θ' and ϕ, for instance, in the presence of aberrations in the form of attenuation of the transmitted electric and magnetic fields. However, these types of aberrations are rare and often induce negligible changes to the PSF compared to the phase terms (Oppenheim and Lim, 1981). Therefore, it is safe to neglect the effect of amplitude and focus on the phase.

The first term in the phase $\Psi(\theta'; z, f)$ is induced by the molecule's shift off axis and out of focus, i.e., the term $-\mathbf{q}\cdot\boldsymbol{\rho}_d - w_d z_d - wfz$ in Eq. (61),

$$\Psi(\theta'; z, f) = k_0 z n_d \sqrt{1 - \sin\theta'^2} - k_0 f n \sqrt{1 - \left(\frac{n_d}{n}\sin\theta'\right)^2}. \tag{72}$$

For instance, the phase $-k\sqrt{1-\eta^2}z$ in Eq. (64), where $\eta = \sin\theta$, is attributable to the out-of-focus location of the emitter. The second phase term $\Phi(\theta', \phi)$ in Eq. (70) describes any additional phases of the pupil function (originating from optical aberrations as described in this section or the PSF modulating elements described in Sec. V.C), which otherwise are null in perfect aplanatic imaging conditions, as in Eq. (64).

We start by considering monochromatic shift-invariant, i.e., (x, y)-independent, aberrations. In this case, aberration terms can be readily added to Eq. (70) as a phase term $\Phi(\theta', \phi)$. This phase function lives on the disklike support $\phi \in \{0, 2\pi\}$ and $\theta' \in \{0, \Theta'\}$ defined by the electric (magnetic) field Fourier amplitude distribution; see Sec. III.B and Fig. 12.

It is often convenient to expand phase aberrations into a system of orthogonal basis functions, namely, Zernike polynomials $Z_l^m(\xi = \sin\theta'/\sin\Theta', \phi)$ [see Noll (1976) and Roddier (1999)],

$$\Phi(\xi, \phi) = \sum_l \sum_{m=-l}^{l} v_{lm} Z_l^m(\xi, \phi), \tag{73}$$

where v_{lm} are coefficients corresponding to Z_l^m. These polynomials are defined by

$$Z_l^m(\xi, \phi) = \begin{cases} R_l^m(\xi)\sin(m\phi) & \text{if } m > 0, \\ R_l^m(\xi)\cos(m\phi) & \text{if } m \le 0, \end{cases} \tag{74}$$

where the radial functions R_l^m are given by

$$R_l^m(\xi) = \sum_{k=0}^{(l-|m|)/2} \frac{(-1)^k (l-k)! \xi^{l-2k}}{k![(l+m)/2-k]![(l-m)/2-k]!} \tag{75}$$

if $l - |m|$ is even, and zero otherwise; see Table I.

Figures 20 and 21 show density plots for the first 12 Zernike polynomials and their impacts on the PSF for an isotropic emitter, respectively. The first three polynomials, namely, horizontal tilt, vertical tilt, and defocus, coincide with phases due to lateral, vertical, and axial shifts in the emitter's position, respectively. All other terms describe PSF distortions due to optical aberrations.

In some cases, aberrations may not be well described by low order Zernike polynomials. For example, when using liquid crystal spatial light modulators (Moser, Ritsch-Marte, and Thalhammer, 2019) or in some PSF engineering methods (Nehme *et al.*, 2021), a sudden phase step in the pupil function may require the aberration to be evaluated in a pixelwise manner (Ferdman *et al.*, 2020).

TABLE I. The first 12 Zernike polynomials.

No.	l	m	Z_n^m	Name
1	1	−1	$\xi\cos\phi$	Horizontal tilt
2	1	1	$\xi\sin\phi$	Vertical tilt
3	2	0	$2\xi^2-1$	Defocus
4	2	−2	$\xi^2\cos 2\phi$	Vertical astigmatism
5	2	2	$\xi^2\sin 2\phi$	Oblique astigmatism
6	3	−1	$(3\xi^2-2)\xi\cos\phi$	Horizontal coma
7	3	1	$(3\xi^2-2)\xi\sin\phi$	Vertical coma
8	4	0	$6\xi^4-6\xi^2+1$	Primary spherical
9	3	−3	$\xi^3\cos 3\phi$	Oblique trefoil
10	3	3	$\xi^3\sin 3\phi$	Vertical trefoil
11	4	−2	$(4\xi^2-3)\xi^2\cos 2\phi$	Vertical secondary astigmatism
12	4	2	$(4\xi^2-3)\xi^2\sin 2\phi$	Oblique secondary astigmatism

The second kind of aberration is chromatic shift invariant. In microscopy, it is common to use achromatic objectives, though dispersion from various other components inducing PSF deviations is unavoidable. These aberrations originate from the broad, nonmonochromatic emission spectrum $S(\lambda)$ of fluorescent molecules describing the probability of emitting at a wavelength λ, often with a width of a few tens of nanometers; see Sec. II.A. In such cases, the image model follows from a superposition integral over the molecule's spectrum,

$$\Lambda(x,y;\mathbf{r}_0)=\int_\lambda S(\lambda)U(x,y;\mathbf{r}_0,\lambda)d\lambda, \tag{76}$$

where $U(x,y;\mathbf{r}_0,\lambda)$ is the λ-dependent PSF (as described in Sec. III.E as a function of $k_0=2\pi/\lambda$). Such aberrations are often detrimental in 3D microscopy. For example, in multifocus microscopy a phase mask (further discussed in Sec. IV.F) with custom chromatic correction gratings are designed to correct the chromatic shifts (Abrahamsson *et al.*, 2013).

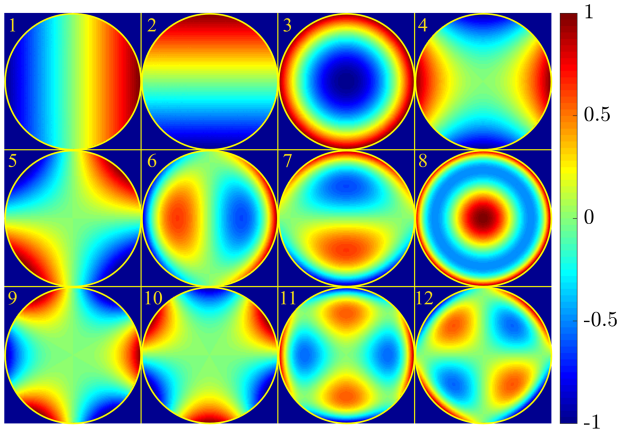

FIG. 20. Density plots for the first 12 Zernike polynomials presented in Table I: (1) horizontal or x tilt, (2) vertical or y tilt, (3) defocus, (4) vertical astigmatism, (5) oblique astigmatism, (6) horizontal coma, (7) vertical coma, (8) primary spherical aberration, (9) oblique trefoil, (10) vertical trefoil, (11) vertical secondary astigmatism, and (12) oblique secondary astigmatism.

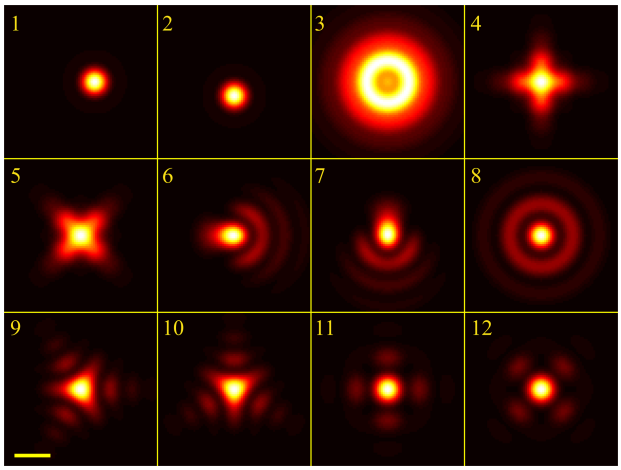

FIG. 21. Model calculations of the image of an isotropic emitter (a rapidly rotating dipole emitter) aberrated by a phase function given by the Zernike polynomials shown in Fig. 20. To better visualize the effects of aberration, all Zernike polynomials were multiplied by a factor of 2.5. Calculations were again done for a water immersion objective with NA = 1.2 and for an emission wavelength of 550 nm. The yellow scale bar is 0.5 μm.

The most challenging aberrations are shift variant, both chromatic and monochromatic, which cannot be simply described by the proposed model of Eq. (70), as the aberration is now a function of the lateral coordinates $\Phi(\theta',\phi,x,y)$. In microscopy, these kinds of aberrations can occur either from the sample itself or from off-axis aberrations in the optical system, namely, systematic aberrations. Sample induced aberrations occur when the sample structure has significant refractive index variations (for example, imaging in deep tissue). This issue can sometimes be addressed with adaptive optics (AO) (Roddier, 1999; Booth *et al.*, 2002; Ji, Milkie, and Betzig, 2010; Tao *et al.*, 2011; Gould *et al.*, 2012; Ji, 2017; Liu *et al.*, 2018; Rodríguez and Ji, 2018; Rodríguez *et al.*, 2021). In AO techniques, the wave front distortion (due to aberrations) of light from fluorescent markers embedded within the sample, called guide stars, is typically measured and then used for a wave front correction. The wave front correction is performed using deformable mirrors to remove the aberrations and achieve a distortion-free wave front. Off-axis aberrations often caused by the optical system, rather than by the sample itself, are typically easier to model as they tend to vary more smoothly. These aberrations can be modeled as 2D polynomial coefficients over the FOV (which multiply Zernike coefficients, for example) (Shajkofci and Liebling, 2020) or addressed by nodal aberration theory (Shack and Thompson, 1980).

IV. FLUORESCENCE MICROSCOPY: MODALITIES

In Sec. III, we described the fundamental optics of the wide-field microscope and derived its OTF and PSF. We also tied the lack of optical sectioning in wide-field microscopes to the OTF's missing cone; see Fig. 12. Here we turn to different fluorescence microscopy modalities achieving optical sectioning and higher resolutions, i.e., near field, point scanning, SIM, light sheet, and multiplane. In deriving their OTFs, we

show that these modalities accomplish optical sectioning by collecting more spatial frequencies along the axial direction through modifications to the illumination and/or detection arms.

A. Near-field methods for enhanced axial resolution

Here we turn to fluorescence imaging methods improving axial resolution using near-field effects. Electromagnetic near fields are nonpropagating (evanescent) fields with intensity gradients exceeding those of propagating waves.

1. Total internal reflection fluorescence microscopy

The first method discussed leverages TIR occurring when a plane wave is incident on an interface separating two media with different refractive indices. We begin with Fresnel's reflection and transmission coefficients $r_\perp$, $r_\parallel$, $t_\perp$, and $t_\parallel$ for s- and p-polarized plane waves reflected at an interface dividing a medium with a refractive index n_1 (incidence medium) from a medium with a refractive index n_2, which are given as follows (Novotny and Hecht, 2012):

$$r_\perp = \frac{n_\star^2 - w_\star}{n_\star^2 + w_\star}, \qquad r_\parallel = \frac{1 - w_\star}{1 + w_\star},$$
$$t_\perp = \frac{2n_\star}{n_\star^2 + w_\star}, \qquad t_\parallel = \frac{2}{1 + w_\star}, \tag{77}$$

where $n_\star = n_2/n_1$ and $w_\star = w_2/w_1 = \sqrt{(n_2^2 - q^2)/(n_1^2 - q^2)}$ defining $w_{1,2}$ as the wave vector's axial components in the first and second media, respectively. Moreover, $q = 2\pi n_1 \sin\theta_{\mathrm{inc}}/\lambda$ is the length of the wave vector's lateral component, with θ_{inc} its incidence angle upon the interface with respect to the normal to the interface within the first medium. Here it is convenient to work in a unit system where the length of the vacuum wave vector is unity. In this unit system, we have $q = n_1 \sin\theta_{\mathrm{inc}}$.

Since electric field and wave vectors are perpendicular, the electric field amplitude of the transmitted wave reads

$$\mathbf{E}_{\perp,\parallel} = E_0 t_{\perp,\parallel} \left(-\frac{w_2 \hat{\mathbf{q}} + q\hat{\mathbf{z}}}{n_2} \right) \exp\left[i w_2 z + i\mathbf{q}\cdot\boldsymbol{\rho} \right], \tag{78}$$

where E_0 is the amplitude of the incident field, with $\hat{\mathbf{q}}$ and $\hat{\mathbf{z}}$ unit vectors along the lateral wave-vector component parallel to the interface and along the axial (z) direction perpendicular to the interface, respectively.

As seen in the definitions of $w_\star$ following Eq. (77), for $q = n_1 \sin\theta_{\mathrm{inc}} > n_2$ the axial component w_2 becomes purely imaginary and the absolute values of the reflection coefficients in Eq. (77) both become unity. Here TIR is possible only if $n_1 > n_2$ and becomes manifest when the critical incidence angle (TIR angle) is $\theta_{\mathrm{TIR}} = \arcsin(n_2/n_1)$. However, as seen in Eq. (78), the electric field in medium 2 does not instantly go to zero but decays exponentially with increasing distance z from the interface. This decaying field in the second medium is termed the evanescent field or wave. The characteristic decay length d_{TIR} of the electric field intensity can be directly derived from Eq. (78) and reads

$$d_{\mathrm{TIR}} = \frac{1}{2|w_2|} = \frac{1}{2\sqrt{n_1^2 \sin^2\theta_{\mathrm{inc}} - n_2^2}}. \tag{79}$$

As such, although evanescent waves do not penetrate far within medium 2, they can still be used to excite fluorophores within a distance of d_{TIR} from the surface, such as in TIRF microscopy (Axelrod, 1981). By the same token, out-of-focus fluorophores deeper than d_{TIR} are less likely to become excited, thereby decreasing undesired out-of-focus light.

To decode emitter axial location, variable angle TIRF (vaTIRF) (Stock *et al.*, 2003) is used where several images are recorded at differing incidence angles of the excitation plane wave above the TIR angle. For increasing incidence angles (see Fig. 22), the excitation intensity's decay becomes steeper. The variation in emitter brightness values across incidence angles is then used to assess its distance from the interface upon deconvolution (Saffarian and Kirchhausen, 2008; El Arawi *et al.*, 2021), with an axial resolution in some cases down to a few nanometers, i.e., by approximately 2 to 3 orders of magnitude better than the diffraction-limited resolution of a confocal microscope, albeit within a limited range ($\approx d_{\mathrm{TIR}}$) from the interface.

2. Supercritical fluorescence microscopy

The second near-field method discussed is SAF microscopy. This method employs the coupling of a fluorophore's near-field emission into propagating modes in the cover slide's glass to improve the axial resolution (Enderlein, Ruckstuhl, and Seeger, 1999; Ruckstuhl and Verdes, 2004; Winterflood *et al.*, 2010; Deschamps, Mund, and Ries, 2014; Oheim, Salomon, and Brunstein, 2020; Dasgupta *et al.*, 2021). To be precise, fields attributed to an oscillating electric dipole have components decaying as $1/r$, $1/r^2$, and $1/r^3$, where only the first term coincides with the propagating term. The other two terms are nonpropagating and represent near-field emissions decaying on short distances ($\approx\lambda$). However, when the electric dipole is located close to a cover slide's interface, nonpropagating near-field dipolar components are converted into

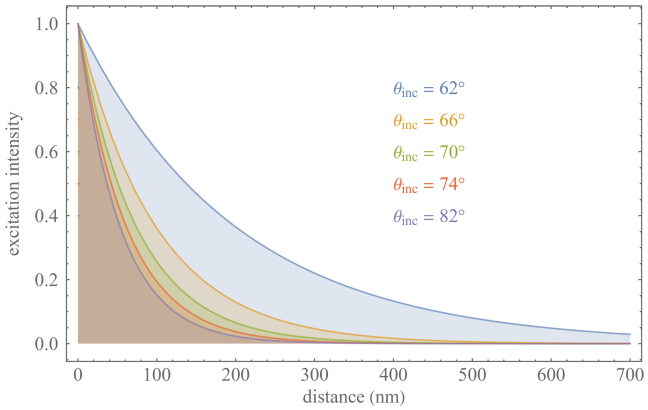

FIG. 22. TIRF microscopy. The excitation intensity above a cover slide interface with the sample medium is displayed as a function of incidence angle. The sample solution and cover slide refractive indices are 1.33 (water) and 1.52, respectively, resulting in a TIR critical angle of ≈61°. The excitation wavelength is taken as 470 nm.

propagating modes upon coupling into the glass, which can then be collected and imaged by the microscope objective. These modes can be decomposed into a superposition of plane waves traveling along directions above the critical TIR angle for the given emission wavelength (supercritical angle fluorescence or SAF emission). The coupling of near-field modes of the fluorophore into propagating modes in the glass decrease with increasing distance from the interface. In contrast, the emission into the angle below the TIR angle [undercritical angle fluorescence (UAF) or UAF emission] is due to the propagation of the emitter's far-field emission into the glass and does not depend on its distance from the surface. Thus, at its core SAF microscopy leverages the variation in SAF to estimate the distance of an emitter from the cover slide's interface by measuring the ratio of its SAF to SAF plus UAF emission intensity.

To calculate the ratio of supercritical to undercritical angle emissions, we use the theoretical framework developed in Sec. III. In particular, for calculating SAF emission intensity, we use Eqs. (41) and (42), but with integration boundaries from $\theta' = \arcsin(n\sin\theta_{\mathrm{TIR}}/\mathcal{M})$, dictated by the critical TIR angle, to $\theta' = \Theta'$, dictated by the numerical aperture. We then compute the energy flux density distribution from Eq. (46). The integral of the resulting energy flux density over the x-y plane is then proportional to the detectable SAF intensity. The UAF intensity is computed analogously but with integration boundaries from $\theta' = 0$ to $\theta' = \arcsin(n\theta_{\mathrm{TIR}}/\mathcal{M})$. As an example, Fig. 23 shows the SAF to SAF plus UAF ratio for a glass-water interface as a function of distance, assuming an isotropic emitter with an emission wavelength of 550 nm. The dynamic range over which one can use this ratio in determining the emitter's distance from the surface is similar to the dynamic range over which vaTIRF is applicable; see Fig. 22.

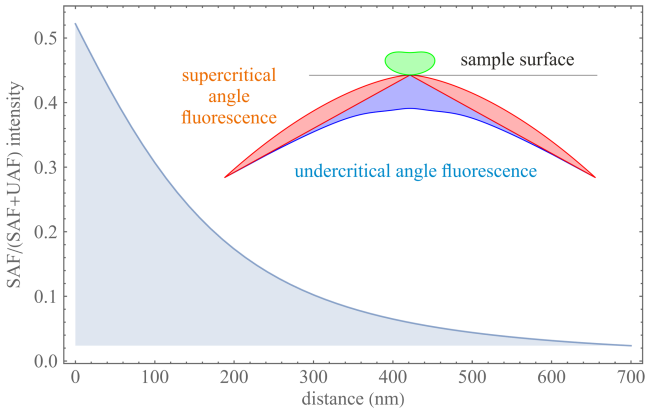

FIG. 23. Supercritical angle fluorescence (SAF) microscopy. Ratio of supercritical to total downward fluorescence emission for a rapidly rotating molecule as a function of distance from the interface of the cover slide and the sample medium. The refractive indices of the sample solution and cover slide are assumed to be 1.33 (water) and 1.52 (glass), respectively, with an emission wavelength of 550 nm. Inset: angular emission intensity distribution of an emitter directly on the interface (with the blue, red, and green curves denoting the UAF and SAF emissions and the emission toward the sample solution, respectively). The SAF emission strongly depends on the emitter's distance to the interface, while the undercritical emission is independent of the emitter axial position. By determining the ratio of SAF to SAF plus UAF emission, we can find the axial position of an emitter.

3. Metal-induced energy transfer imaging

MIET, another near-field method used for axial localization (Chizhik *et al.*, 2014), is based on near-field coupling similar to SAF microscopy. MIET uses the fact that, when a fluorescent emitter (electric dipole emitter) approaches a metal layer, its electric near field excites surface plasmons (coherent metal electron oscillations) in the metal, accelerating deexcitation of the fluorescent emitter's excited state. This is observed as a strong decrease in fluorescence lifetime with decreasing distance from the surface; see Fig. 24 and Eq. (18).

To infer distances from lifetime measurements, we use the theoretical framework developed in Sec. III. The lifetime depends on the emission power requiring the explicit calculation of both the electric and magnetic fields.

We start with the Weyl representation of the electric field of a free dipole emitter obtained in Eq. (57) to derive the electric field distribution above a MIET substrate (denoted by a metal surface in Fig. 25). As shown in Fig. 25, two sources contribute to the electric field above this metal surface: (1) direct emission from the dipole and (2) emission reflected from the surface (i.e., emission from the emitter's image)

$$\begin{aligned}\mathbf{E}_d^{\pm} = \frac{ik_0^2}{2\pi}\int \frac{d^2\mathbf{q}}{w_d}\{&(\mathbf{p}\cdot\hat{\mathbf{e}}_{\parallel})\hat{\mathbf{e}}_{\parallel}(1 + r_{\parallel}e^{iw_d|z+z_d|}) \\ &+ [(\mathbf{p}\cdot\hat{\mathbf{e}}_{\perp}^{\pm})\hat{\mathbf{e}}_{\perp}^{\pm} + (\mathbf{p}\cdot\hat{\mathbf{e}}_{\perp}^{+})\hat{\mathbf{e}}_{\perp}^{-}r_{\perp}e^{iw_d|z+z_d|}]\} \\ &\times \exp[i\mathbf{q}\cdot(\boldsymbol{\rho}-\boldsymbol{\rho}_d) + iw_d|z-z_d|],\end{aligned} \tag{80}$$

where terms with the reflection coefficients $r_{\parallel,\perp}$ describe contributions from the reflected emission. Moreover, the plus sign and minus sign superscripts refer to plane waves moving toward and away from the metal surface. The $r_{\perp,\parallel}$ terms are

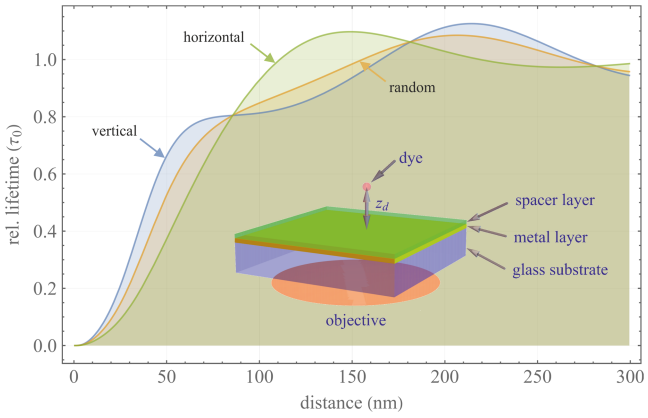

FIG. 24. MIET microscopy: Dependence of the fluorescence lifetime (in terms of the free space lifetime τ_0) on the emitter's distance from the glass substrate (cover slide) coated with a 20 nm gold layer. Calculations were done for an emission wavelength of 550 nm and a unit fluorescence quantum yield. Free curves for the vertical, horizontal, and random emission dipole orientations are shown. Inset: MIET sample geometry.

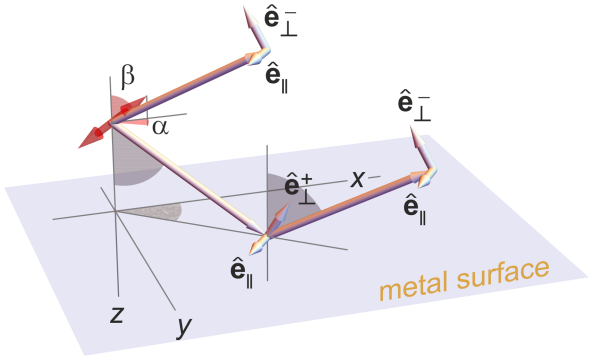

FIG. 25. Geometry for deriving the electric field generated by a single dipole emitter above the MIET substrate (the metal surface). The red double-headed arrow shows a dipole located a distance z_d above the metal surface with an orientation of β and α denoting the polar and inclination azimuthal angles, respectively. The three longer single-headed arrows show plane wave component vectors with the corresponding perpendicular polarization unit vectors $\hat{\mathbf{e}}_{\parallel}$ and $\hat{\mathbf{e}}_{\perp}^{\pm}$. Here $\hat{\mathbf{e}}_{\perp}^{+}$ is the unit vector associated with the wave vector moving toward the metal surface. Similar conventions hold for the other unit vectors.

Fresnel's q-dependent reflection coefficients for p and s waves for the MIET substrate.

For planar structures of arbitrary complexity, these coefficients are readily obtained using the propagation matrix formalism discussed by Heavens (1965), Knittel (1976), Yeh (1988), and Born and Wolf (2013). We now distinguish between two p-wave polarization unit vectors: $\hat{\mathbf{e}}_{\perp}^{+}$ for plane waves traveling toward the substrate and $\hat{\mathbf{e}}_{\perp}^{-}$ for plane waves traveling away from the substrate. The corresponding s-wave polarization unit vector $\hat{\mathbf{e}}_{\parallel}$ is the same for both waves. We note that the result depends on the three-dimensional orientation of the emitter (given by the Euler angles α and β; see Fig. 25) via the scalar products $\mathbf{p}\cdot\hat{\mathbf{e}}_{\perp}^{\pm}$ and $\mathbf{p}\cdot\hat{\mathbf{e}}_{\parallel}$.

Analogously we can find the magnetic field as

$$\begin{aligned}\mathbf{B}_d^{\pm} = \frac{in_d k_0^2}{2\pi}\int \frac{d^2\mathbf{q}}{w_d} & \times\{(\mathbf{p}\cdot\hat{\mathbf{e}}_{\parallel})(\hat{\mathbf{e}}_{\perp}^{\pm} - \hat{\mathbf{e}}_{\perp}^{+} r_{\parallel} e^{iw_d|z+z_d|}) \\ & + [(\mathbf{p}\cdot\hat{\mathbf{e}}_{\perp}^{\pm}) + (\mathbf{p}\cdot\hat{\mathbf{e}}_{\perp}^{+}) r_{\perp} e^{iw_d|z+z_d|}]\hat{\mathbf{e}}_{\parallel}\} \\ & \times \exp[i\mathbf{q}\cdot(\boldsymbol{\rho}-\boldsymbol{\rho}_d) + iw_d|z-z_d|]. \end{aligned} \tag{81}$$

Given both the electric and magnetic fields of Eqs. (80) and (81), the total emission power of the emitter, designated by $S(\beta)$, follows by integrating the outward component of the Poynting vector over two planar interfaces sandwiching the emitter

$$S(\beta) = \frac{n_d c}{8\pi}\int d^2\boldsymbol{\rho}\hat{\mathbf{z}}\cdot\left[(\mathbf{E}^{+}\times\mathbf{B}^{+*})_{z=0} - (\mathbf{E}^{-}\times\mathbf{B}^{-*})_{z<z_d}\right]. \tag{82}$$

The emission power depends only on the dipole's polar orientation angle β, not its azimuthal angle α. The emission power $S(\beta)$ can now be compared to the emission power S_0 of a "free" dipole within a homogeneous medium with a refractive index n_d, given by the well-known formula of Jackson (1999) [and also obtained from Eqs. (81) and (82) by neglecting the contribution from reflected emission including coefficients $r_{\perp,\parallel}$] as $S_0 = cn_d p^2 k_0^4/3$.

The observable enhancement of the radiative deexcitation rate k_f of a fluorescence emitter due to the presence of the metal substrate with respect to the same emitter in a homogeneous environment is then given by the ratio $S(\beta)/S_0$ (Chance, Prock, and Silbey, 2007).

As noted in Sec. II, there is a contribution to the excited-state lifetime from nonradiative decay pathways arising by collision with surrounding molecules and thermal dissipation of the excited-state energy quantified by the fluorescence quantum yield Q_f. Here Q_f is the probability that deexcitation proceeds radiatively with photon emission; see Eq. (17). The observable fluorescence lifetime τ is then the inverse of the total deexcitation rate $k_f + k_{\text{non}}$ [see Eq. (18)], such that its change in the presence of the metal substrate is given by

$$\frac{\tau}{\tau_0} = \frac{S_0}{S(\beta)Q_f + (1-Q_f)S_0}. \tag{83}$$

Equation (83) is the final equation needed for calculating the dependence of the fluorescence lifetime τ on the emitter distance z_d. An example is provided in Fig. 24 for the three cases of a vertically, horizontally, and randomly oriented emitter. In the third case, the orientation-dependent $S(\beta)$ is substituted for its orientational average $\langle S\rangle = (1/2)\int_0^{\pi} d\beta \sin\beta S(\beta)$. As seen in Fig. 24 for a randomly oriented emitter, within a range of up to 200 nm from the surface the lifetime depends monotonically on distance and a unique distance follows from the measured lifetime.

Further recent angstrom spatial resolution along the optical axis has been afforded by the use of materials such as indium tin oxide (Moerland and Hoogenboom, 2016) and single-sheet graphene (graphene-induced energy transfer) (Ghosh *et al.*, 2019), leading to a distance-dependent modulation of the fluorescence lifetime on approximately an 8 times smaller length scale.

B. Point scanning microscopy

Unlike wide-field imaging using multipixel detectors, point scanning microscopes sequentially record images by scanning samples over a set of positions and recording a fluorescence signal for each position scanned. Moreover, in contrast to wide-field imaging, point scanning allows for out-of-focus light reduction, thereby achieving optical sectioning. Here we first consider image formation in the most widely used point scanning microscope: the CLSM (Marvin, 1961; Pawley, 2006). We then discuss the enhanced resolution achieved by ISM, 4Pi, and two-photon microscopy.

1. Confocal laser-scanning microscopy

A schematic of a point scanning microscope is shown in Fig. 26. An excitation laser beam, shown in yellow, is laterally deflected by a beam scanning unit along both directions perpendicularly to the optical axis. Figure 26 shows only one of these scanning directions, where the excitation beam can be directed up and down upon reflection from the scanner by

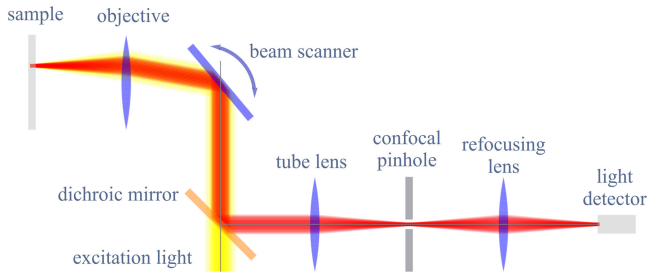

FIG. 26. Schematic of a CLSM. The yellow and red beams show the excitation and emission light, respectively. The emission passes through a confocal pinhole suppressing out-of-focus light; see the text for details.

adjusting the scanner's orientation. Following deflection, the excitation light is focused by the objective into a diffraction-limited focus within the sample. The emitted fluorescence light from the illuminated spot, shown in red, is then collected by the same objective and guided back through the same beam scanner toward the dichroic mirror. This process is known as descanning.

After descanning, fluorescence light is reflected away from the excitation beam by the dichroic mirror, which reflects light only within a range of wavelengths. The fluorescent light is next focused by the tube lens onto the circular aperture of a confocal pinhole obstructing the undesired fluorescent light from out-of-focus fluorophores. After potentially passing additional optical filters for background suppression, the fluorescence light is refocused onto a single-pixel point detector to record the in-focus fluorescence intensity.

In what follows, we derive the confocal PSF for a single scanning spot. To avoid notational confusion, PSFs for the wide field and CLSM are denoted by U_{wf} and U_{cf}, respectively, in the remainder of this section.

To derive the confocal PSF for an isolated emitter sitting in an excitation focal spot in sample space, we first consider major differences with the wide-field setup [described for the most general case and its approximate analytical forms in Secs. III.C and III.D; see Eqs. (66) and (69)]. These differences include (1) the spot illumination procedure and (2) the existence of the confocal pinhole.

We start with the fluorescent light from the emitter proportional to the three-dimensional excitation laser intensity at the focal spot $I_{\mathrm{ex}}(\boldsymbol{\rho}, z)$ (excitation is in the sample space and thus is described by nonprime coordinates). The fluorescent light is in turn collected by the objective and focused onto the confocal pinhole (within image space). This results in a fluorescent intensity $U_{\mathrm{wf}} I_{\mathrm{ex}}$ prior to the pinhole, where U_{wf} is this setup's wide-field PSF in the absence of the pinhole and spot illumination. In the end, the confocal PSF (the imaging PSF of a confocal microscope) is proportional to the fluorescence intensity (ignoring all constant prefactors) following the pinhole,

$$U_{\mathrm{cf}}(\boldsymbol{\rho}, z) \propto [A \otimes U_{\mathrm{wf}}] I_{\mathrm{ex}}(\boldsymbol{\rho}, z) = \int d\boldsymbol{\rho}' A(\boldsymbol{\rho}') U_{\mathrm{wf}}(\boldsymbol{\rho}' - \boldsymbol{\rho}, z) I_{\mathrm{ex}}(\boldsymbol{\rho}, z), \quad (84)$$

where A captures the confocal pinhole, which is set to unity for $\rho' = |\boldsymbol{\rho}'|$ smaller than the aperture radius a, and zero otherwise. In Eq. (84) $U_{\mathrm{wf}}(\boldsymbol{\rho}' - \boldsymbol{\rho}, z)$ represents the wide-field PSF when the fluorescence from an emitter is imaged at position $\mathbf{r} = (\boldsymbol{\rho}, z)$ in sample space onto a lateral position $\boldsymbol{\rho}'$ in the plane of the confocal aperture within the image space (prime coordinates). In other words, the confocal PSF of Eq. (84) is given as a product of $A \otimes U_{\mathrm{wf}}$, describing the detection, sometimes termed detection PSF, and I_{ex}, describing excitation, sometimes termed excitation PSF.

The integral in Eq. (84) is performed over the entire $\boldsymbol{\rho}'$ plane. The excitation PSF (excitation intensity distribution) I_{ex} entering Eq. (84) is itself a function of the absorption dipole orientation $\mathbf{p}_{\mathrm{ex}}$ of a fluorophore via $I_{\mathrm{ex}}(\mathbf{r}) \propto |\mathbf{E}_{\mathrm{ex}}(\mathbf{r}) \cdot \mathbf{p}_{\mathrm{ex}}|^2$, where $\mathbf{E}_{\mathrm{ex}}$ denotes the electric field distribution in the focal spot.

In most cases of practical interest, one deals with rapidly rotating emitters for which the orientationally averaged excitation intensity reads [see also Eq. (62)]

$$I_{\mathrm{ex}}(\mathbf{r}) \propto |E_{\mathrm{ex},x}|^2 + |E_{\mathrm{ex},y}|^2 + |E_{\mathrm{ex},z}|^2. \quad (85)$$

To perform this calculation, we first consider the focusing of a planar wave front through the objective into a diffraction-limited spot; see Fig. 27. As with the Abbe sine condition relating propagation angles of wave front patches in sample and image spaces, there is a similar relation between the distance ρ of a patch on the planar wave front from the optical axis and the propagation angle θ of the corresponding patch after focusing through the objective; see Fig. 27. This relation can be found from the Abbe sine condition when moving the focus in image space to infinity (i.e., the focal length f_{tube} of the tube lens tends toward infinity) and remembering that the magnification $\mathcal{M}$ is given by the focal distance of the tube lens f_{tube} divided by the focal distance f of the objective; see Fig. 1. Thus, we find that $\mathcal{M} \sin\theta' = (f_{\mathrm{tube}}/f) \sin\theta' = n \sin\theta$. When the value f_{tube} is increased to infinity, the angle θ' tends to zero, though the product $\rho = f_{\mathrm{tube}} \sin\theta'$ remains finite and coincides with the distance from the optical axis in the back focal plane. Thus, one

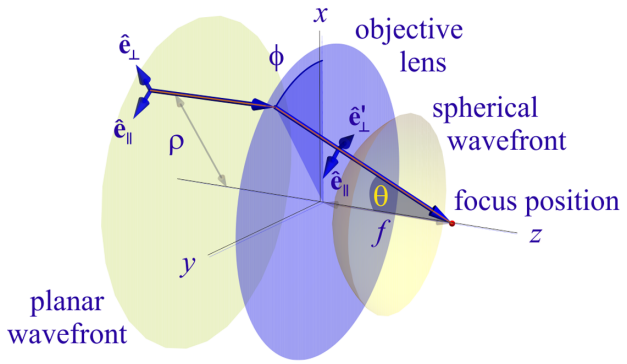

FIG. 27. Schematic of the geometry when a planar laser wave front is focused through the objective into the sample space; see Fig. 26. Wave front patches at distance ρ from the optical axis in the back focal plane are converted into spherical wave front patches traveling at an angle $\theta = \arcsin(\rho/nf)$ with respect to the optical axis z, where f is the focal length of the objective lens; see the text for details.

finds the relation $\rho = nf \sin\theta$ between the distance ρ before the objective and the propagation angle θ in sample space.

Using this relation for ρ, we can expand the electric field in sample space into a plane wave superposition, as what we did in deriving the electric field of a point emitter in image space; see Eq. (41). When reading Eq. (41) in reverse, i.e., replacing all primed variables with nonprimed ones, and vice versa (thus starting with light coming from the back side of the objective focused through the objective into sample space), and when taking into account that the angles θ' for the incoming light are all zero (plane wave front) such that $\cos\theta' \approx 1$, we arrive at

$$\mathbf{E}_{\mathrm{ex}}(\mathbf{r}) \propto \int_0^{\Theta} d\theta\, \sin\theta\sqrt{\cos\theta} \int_0^{2\pi} d\phi [E_{0,\parallel}(\rho,\phi)\hat{\mathbf{e}}_{\parallel} + E_{0,\perp}(\rho,\phi)\hat{\mathbf{e}}'_{\perp}] \exp(i\mathbf{k}_{\mathrm{ex}}\cdot\mathbf{r}), \tag{86}$$

where $\mathbf{k}_{\mathrm{ex}} = (2\pi n/\lambda_{\mathrm{ex}})(\cos\phi\sin\theta, \sin\phi\sin\theta, \cos\theta)$ is now the wave vector of a plane wave with a wavelength λ_{ex} (excitation light wavelength), where the electric field of the incoming laser beam in the back focal plane is expanded into its radially ($E_{0,\perp}$) and azimuthally polarized components ($E_{0,\parallel}$); see Fig. 27. For example, for a linearly polarized laser beam with a polarization direction along x one has $E_{0,\perp} \propto \cos\phi$ and $E_{0,\parallel} \propto -\sin\phi$. This equation can now be used to calculate the three-dimensional excitation PSF in sample space. As an example, the left panel of Fig. 28 shows the CLSM PSF calculated assuming a 470 nm circularly polarized laser focused through a water immersion objective onto a diffraction-limited spot (the planar wave front at the back focal plane).

While we have focused on using Eq. (86) in computing the CLSM PSF, that equation is much more general. For instance, it can be used to calculate the intensity distribution of a doughnut excitation beam appearing in STED microscopy (Hell and Wichmann, 1994). This doughnut intensity distribution, with zero intensity on the crossing of the optical axis with the focal plane (focus center), can be generated in two ways.

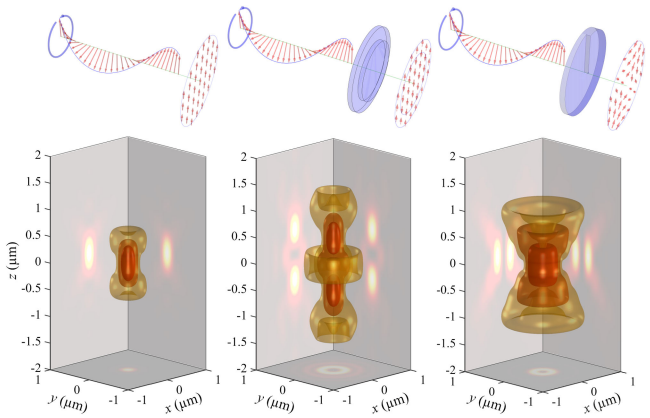

FIG. 28. CLSM and STED intensity distributions at the focus. Shown is a comparison of intensity distribution (left panels) with a conventional CLSM focus, (middle panels) with a z-STED focus, and (right panels) with an xy-STED focus. Calculations were done for a water immersion objective with NA = 1.2 at an excitation wavelength of 470 nm. The excitation polarization and its generating phase plate are shown in the top panels. The bottom panels show 3D contour plots of the $1/e$, $1/e^2$, and $1/e^3$ intensity isosurfaces and projections of x-y, x-z, and y-z cross sections through the center.

The first method generates a doughnut-shaped laser intensity in the focal plane by sending a circularly polarized laser light through a ring-shaped phase plate that is thicker at its center. This results in retardation of the beams of light closer to the optical axis by half a wavelength with respect to the beams passing through the thinner outer part of the plate; see the middle panels in Fig. 28. A snapshot of the resulting polarization structure across the back focal plane is depicted in the top middle panel in Fig. 28. Mathematically this can be described by setting $E_{0,\perp} \propto \cos\phi - i\sin\phi$ and $E_{0,\parallel} \propto -\sin\phi + i\cos\phi$ for $\rho \le \rho_\Phi$, and the same expressions but with opposite signs for $\rho_\Phi < \rho < f\sin\Theta$, where $\rho_\Phi = f\sin\Theta/\sqrt{2}$ is the radius of the thicker central part of the phase plate. This special choice of ρ_Φ ensures that the total excitation intensity in the focus center will indeed be zero.

The second method sends circularly polarized light through a helical wave plate, as shown in the top right panel of Fig. 28. When an appropriate helical pitch is chosen, this leads to an excitation beam with a polarization structure $E_{0,\perp} \propto \sin 2\phi - i\cos 2\phi$ and $E_{0,\parallel} \propto \cos 2\phi + i\sin 2\phi$. Three-dimensional representations of the resulting stimulated emission (STE) intensity distributions and corresponding cross sections are shown in the bottom panels of Fig. 28. Neither the disk phase plate (middle panels) nor the helical phase plate (right panels) lead to an ideal STE intensity distribution, i.e., a perfect doughnut shape with zero intensity in the middle. Whereas the disk phase plate leads to an intensity distribution achieving good axial compression of the STED PSF, it performs poorly in lateral directions. In contrast, helical wave plates lead to excellent compression of the STED PSF laterally, but not along the optical axis. Thus, 3D STED systems use a combination of the two excitation modalities (Sahl and Hell, 2019).

Having an exact description of the excitation PSF (excitation intensity distribution) in place, we can return to the imaging PSF of a CLSM and consider its optical resolution. To do so, we consider its OTF, i.e., the Fourier transform of Eq. (84), in which we replace I_{ex} and U_{wf} of Eq. (84) with their Fourier expansions,

$$U_{\mathrm{wf}}(\boldsymbol{\rho}' - \mathbf{r}) = \int \frac{d\mathbf{k}}{2\pi} \tilde{U}_{\mathrm{wf}}(\mathbf{k}) \exp[i\mathbf{k}\cdot(\boldsymbol{\rho}' - \mathbf{r})],$$
$$I_{\mathrm{ex}}(\mathbf{r}) = \int \frac{d\mathbf{k}}{2\pi} \tilde{I}_{\mathrm{ex}}(\mathbf{k}) \exp(i\mathbf{k}\cdot\mathbf{r}), \tag{87}$$

where we recall that a tilde over a symbol denotes its Fourier amplitude. This immediately leads to

$$U_{\mathrm{cf}}(\mathbf{r}) \propto \int d\boldsymbol{\rho}' \int d\mathbf{k} \int d\mathbf{k}' A(\boldsymbol{\rho}') \tilde{U}_{\mathrm{wf}}(\mathbf{k}') \exp[i\mathbf{k}'\cdot(\boldsymbol{\rho}' - \mathbf{r})] \tilde{I}_{\mathbf{ex}}(\mathbf{k}) \exp(i\mathbf{k}\cdot\mathbf{r}). \tag{88}$$

The integration over $\boldsymbol{\rho}'$ can now be performed analytically, resulting in

$$\int d\boldsymbol{\rho}' A(\boldsymbol{\rho}') \exp\left(i\mathbf{k}'\cdot\boldsymbol{\rho}'\right) = \frac{2\pi a}{q'} J_1(aq'), \tag{89}$$

where a is the radius of the confocal aperture, $q' = \sqrt{k_x'^2 + k_y'^2}$ is the modulus of the radial part of the vector $\mathbf{k}'$, and J_1 is the first order Bessel function of the first kind. Substituting this result into Eq. (88), we write

$$U_{\mathrm{cf}}(\mathbf{r}) \propto \int d\mathbf{k} \int d\mathbf{k}' \frac{2\pi a}{q'} J_1(aq') \tilde{U}_{\mathrm{wf}}(\mathbf{k}') \tilde{I}_{\mathbf{ex}}(\mathbf{k}) \exp\left[i(\mathbf{k}-\mathbf{k}')\cdot\mathbf{r}\right]. \tag{90}$$

Following some algebra, we find for the Fourier transform of $U_{\mathrm{cf}}(\mathbf{r})$, i.e., the CLSM's OTF (up to some constant prefactor),

$$\tilde{U}_{\mathrm{cf}}(\mathbf{k}) \propto \int d\mathbf{k}' \frac{J_1(aq')}{q'} \tilde{U}_{\mathrm{wf}}(\mathbf{k}') \tilde{I}_{\mathrm{ex}}(\mathbf{k}+\mathbf{k}'). \tag{91}$$

Thus, the OTF of the confocal microscope is given by the three-dimensional convolution of a wide-field microscope OTF $\tilde{U}_{\mathrm{wf}}(\mathbf{k})$ modulated by the aperture function $J_1(aq')/q'$ [the Fourier transform of the detection PSF (84), also sometimes termed the detection OTF] and the Fourier transform of the excitation PSF $\tilde{I}_{\mathrm{ex}}(\mathbf{k})$ (also sometimes termed the excitation OTF). This is depicted in Fig. 29, where the left panel shows the amplitude of the excitation OTF $\tilde{I}_{\mathrm{ex}}(\mathbf{k})$, the middle panel is the detection OTF given by the absolute value of the wide-field OTF $\tilde{U}_{\mathrm{wf}}(\mathbf{k})$ multiplied by $J_1(aq')/q'$, and the right panel represents a cross section of the amplitude of confocal OTF obtained by 3D convolution of the previous two panels.

The most noticeable difference between the confocal OTF of Fig. 29 and the wide-field OTF of Fig. 19 is that the confocal OTF has nonzero components along the optical axis (here $k_x = 0$, with the origin at the center), highlighting a confocal microscope's ability for optical sectioning. The corresponding axial resolution is given by 2π divided by the maximum frequency supported along the k_z axis; see Eq. (52).

Figure 30 shows how the confocal OTF changes with the pinhole size. As expected, for a large confocal pinhole radius of 200 μm (top left panel), the confocal OTF approaches that of a wide-field microscope at the same wavelength, as can be seen in a comparison with the right panel of Fig. 19. As the pinhole size shrinks ($a = 1$ μm), optical sectioning and axial resolution are optimized; see the bottom right panel of Fig. 30. In this case, the confocal aperture can be approximated using a delta function so that the integral Eq. (89) results in a constant. As such, the OTF for a small aperture reduces to the convolution of the wide-field OTF $\tilde{U}_{\mathrm{wf}}$ with the excitation OTF $\tilde{I}_{\mathrm{ex}}$. Thus, the maximum frequency passed by the confocal OTF with a small aperture is given by $k_{\max} = k_{\max,\mathrm{ex}} + k_{\max,\mathrm{em}}$, where $k_{\max,\mathrm{ex}}$ and $k_{\max,\mathrm{em}}$ denote the maximum extents of $\tilde{I}_{\mathrm{ex}}$ and $\tilde{U}_{\mathrm{wf}}$, respectively.

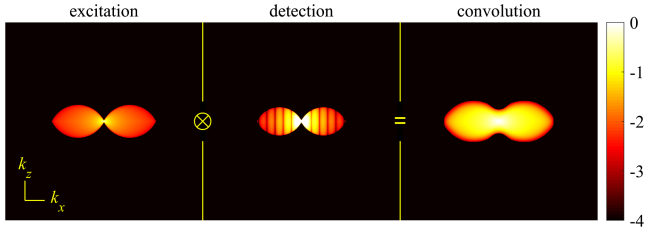

FIG. 29. Anatomy of the OTF (amplitude) of a confocal microscope. Left panel: excitation OTF. Middle panel: detection OTF for a confocal pinhole with a 50 μm radius and 60 times magnification. Right panel: the resulting confocal OTF obtained via a 3D convolution of the two leftmost distributions.

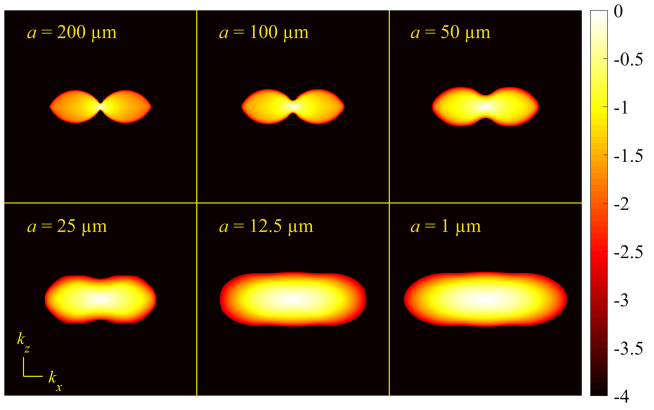

FIG. 30. OTF amplitude of a confocal microscope as a function of confocal aperture size. The confocal aperture radius is given in the top row. We assumed an excitation wavelength of 470 nm, an emission wavelength of 550 nm, and a water immersion objective of NA = 1.2 at 60 times magnification. The top left panel shows the limit of an extremely large confocal pinhole in which the OTF approaches that of a wide-field microscope imaging at the same wavelength as the excitation wavelength of the excitation laser. The bottom right panel shows the limit of a nearly zero-size pinhole ($a = 1$ μm) in which the OTF approaches that of an ISM; see Sec. IV.B.2.

The maximum extents of excitation and detection OTFs in the lateral direction are $k_{\max,\mathrm{ex/\,det}} = 4\pi n \sin\Theta/\lambda_{\mathrm{ex/em}}$, which in turn results in the following lateral resolution [see Eq. (52)]:

$$y_{\min} = \frac{1}{2\mathrm{NA}}\left(\frac{1}{\lambda_{\mathrm{ex}}} + \frac{1}{\lambda_{\mathrm{em}}}\right)^{-1}, \tag{92}$$

and in a similar fashion for the axial resolution,

$$z_{\min} = \frac{1}{2n(1-\cos\Theta)}\left(\frac{1}{\lambda_{\mathrm{ex}}} + \frac{1}{\lambda_{\mathrm{em}}}\right)^{-1}, \tag{93}$$

where λ_{ex} and λ_{em} are the excitation and emission wavelengths, respectively. Thus, ignoring the spectral Stokes shift between excitation and emission, i.e., $\lambda_{\mathrm{em}} \approx \lambda_{\mathrm{ex}}$ (see Sec. II), the confocal microscope with an infinitely small pinhole has a twofold higher lateral resolution than a wide-field microscope, as we see when comparing Eqs. (92) and (67). This improvement in resolution can also be explained in the spatial domain using Eq. (84) by setting $A(\boldsymbol{\rho}') = \delta(\boldsymbol{\rho}' - \boldsymbol{\xi})$ (an infinitely small aperture centered at $\boldsymbol{\xi}$) and adopting Gaussian approximations for both the wide-field PSF as in Eq. (69) and the excitation PSF I_{ex}. In this case, the resulting confocal PSF would be the product of the two Gaussian approximations, which is Gaussian as well (Zhang, Zerubia, and Olivo-Marin, 2007),

$$U_{\mathrm{cf}}(\boldsymbol{\rho}, z) \propto \exp\left(-\frac{(\boldsymbol{\rho}-\xi_\rho)^2}{2\sigma_\rho^2}-\frac{(z-\xi_z)^2}{2\sigma_z^2}\right). \tag{94}$$

In Eq. (94) the widths of the resulting Gaussian PSF σ_ρ and σ_z are smaller than the widths of both the excitation and detection PSFs, thus leading to higher resolutions.

The PSFs corresponding to the OTFs shown in Fig. 30 are presented in Fig. 31, which illustrates how the PSF's lateral width shrinks with decreasing pinhole size and thereby improves the lateral resolutions, albeit at a price. The smaller the confocal pinhole size, the fewer the photons that reach the detector, thereby reducing the SNR (Sheppard *et al.*, 2006). This is quantified in Fig. 32, which shows the relation between the PSF diameter (in the focal plane) and the light detection efficiency for increasing the pinhole radii ($1-200$ μm) while assuming a 470 nm excitation and 550 nm emission wavelength, and for a water immersion microscope with NA $= 1.2$ objective and 60 times magnification. The light detection efficiency decreases as the confocal pinhole radius drops below 20 μm, which encourages the use of ISM (introduced next).

2. Image scanning microscopy

As discussed in Sec. IV.B.1 upon consideration of a confocal PSF, the maximum possible spatial resolution is achieved when an infinitely small confocal pinhole is approached; see Eqs. (92)–(94). However, as this would reduce light detection efficiency to almost zero (see Fig. 32), such an option is often avoided in practice. To simultaneously maximize spatial resolution and light detection efficiency, in the late 1980s Colin Sheppard proposed combining scanning spot illumination of confocal microscopes and wide-field light detection of an array detector, for example, an EMCCD camera, without pinholes mitigating light loss (Sheppard, 1988). This idea, termed ISM, was first experimentally demonstrated more than a decade ago

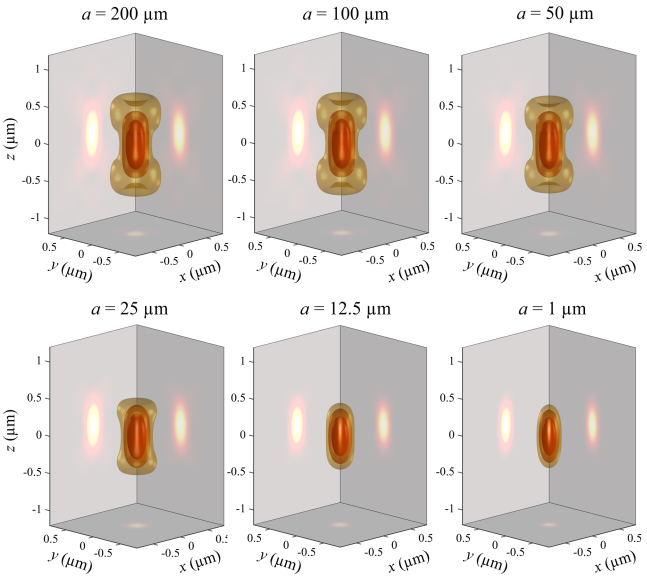

FIG. 31. Confocal microscope PSF for an isotropic emitter as a function of confocal aperture size. The aperture radius is given above each panel. The parameters are similar to those in Fig. 30, with 60 times magnification.

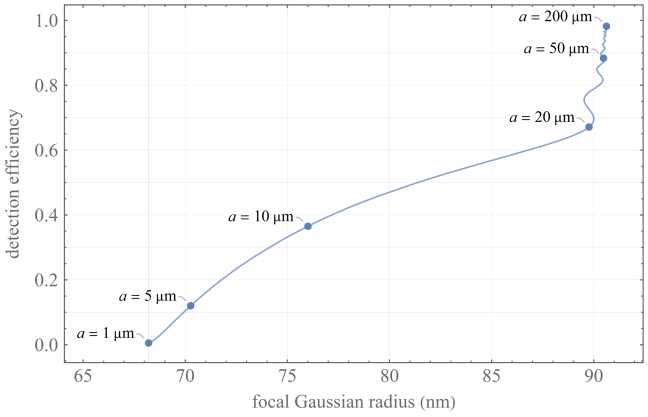

FIG. 32. Relationship between PSF size and detection efficiency in a CLSM. We show the light detection efficiency vs the Gaussian radius σ of the PSF in the focal plane as a function of the confocal aperture's radius (denoted as a). Calculations were made for a water immersion objective with NA $= 1.2$ and an image magnification of 60 times (focal plane to pinhole plane). It was assumed that excitation is achieved with 470 nm circular polarized light focused onto a diffraction-limited spot, and that the fluorescence emission is of 550 nm wavelength. We found the focal radius by fitting a radially symmetric Gaussian approximation $\exp(-\rho^2/2\sigma^2)$ to the PSF in the focal plane. The curve's undulations at the upper right arise from the diffraction effects of light passing through a circular pinhole.

by Müller and Enderlein (2010). The core idea of ISM is to replace the confocal pinhole and the single-pixel detector of a conventional CLSM with an array detector in the image plane (pinhole plane); see Fig. 26. The fluorescence light from an illumination spot at a position $\mathbf{r}$ is then spread across multiple pixels of the detector array. In this setup, a pixel located at $\boldsymbol{\xi}$ records photons from the illuminated spot corresponding to a pinhole located at $\boldsymbol{\xi}$ with the same size as the pixel. The pixel size is often chosen to be small enough that each pixel records an image of the illumination spot with a resolution similar to that of a CLSM with close to a zero pinhole size; see Eqs. (92) and (93). Moreover, as ISM builds on a CLSM, it also provides optical z sectioning.

The ISM setup described here results in N_p recorded images for each illumination spot associated with all N_p pixels of the detector array. As such, upon scanning the sample at N_s locations one acquires $N_p \times N_s$ images. To combine all acquired images into a single high resolution image, we first consider the scan image recorded by one pixel at a given position $\boldsymbol{\xi}$ on the array detector. The PSF of this scan image is easily found when the aperture function $A(\boldsymbol{\rho})$ of Eq. (84) is replaced by the pixel area. However, as an idealization we can consider the pixel area as a delta function $\delta(\boldsymbol{\rho}-\boldsymbol{\xi})$ as compared to the size of the features that we want to determine. As such, the PSF for the scan image recorded by a pixel at a position $\boldsymbol{\xi}$ is

$$U_{\mathrm{pix}}(\mathbf{r}, \boldsymbol{\xi}) \propto U_{\mathrm{wf}}(\boldsymbol{\xi}-\mathbf{r}) I_{\mathrm{ex}}(\mathbf{r}), \tag{95}$$

where U_{wf} is the wide-field imaging PSF (detection PSF) and I_{ex} is the excitation PSF. This is visualized in Fig. 33, where a

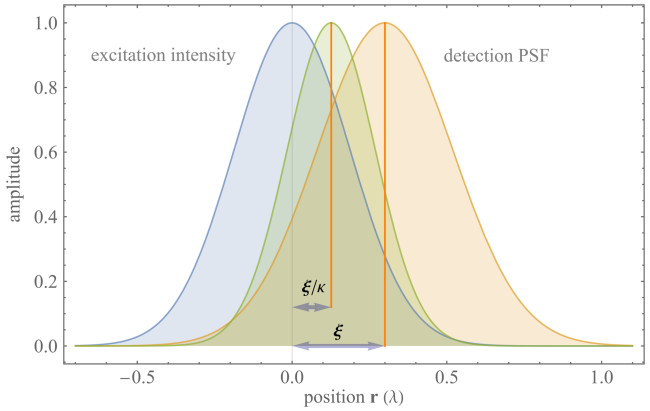

FIG. 33. Image formation in ISM. The blue curve represents the excitation intensity distribution I_{ex} (excitation PSF) with its center at $\boldsymbol{\xi} = 0$ (the optical axis). The yellow curve shows the detection PSF (U_{wf}) for a pixel located at $\boldsymbol{\xi}$ away from the optical axis. The pixel PSF (U_{pix}) describing the image formation is, however, given by the product of the excitation and detection PSFs, which is designated by the green curve and centered at $\boldsymbol{\xi}/\kappa$. Thus, a fluorophore at $\boldsymbol{\xi} = 0$ (the excitation intensity's center) will appear at $\boldsymbol{\xi}/\kappa$.

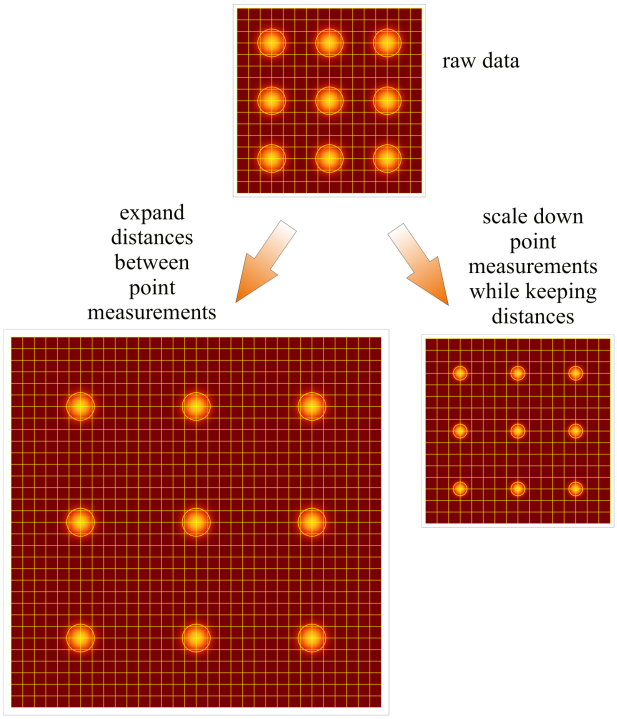

FIG. 34. ISM image reconstruction. Top image: at each scan position, the array detector records a small image of the illuminated region. To reconstruct a final ISM image, we can either downscale each recorded small image by a factor of κ (bottom right image) or leave the recorded images unchanged but place them in the final ISM image by a factor of κ farther way from each other (bottom left image).

cross section of the excitation PSF $I_{\mathrm{ex}}(\mathbf{r})$ is shown together with the detection PSF for a pixel at a position $\boldsymbol{\xi}$ [described by $U_{\mathrm{wf}}(\boldsymbol{\xi} - \mathbf{r})$] and the product of the two; see Eq. (95).

When one estimates the excitation and detection PSFs using Gaussian approximations with variances σ_{ex}^2 and σ_{em}^2, respectively, the product of the two yields

$$I_{\mathrm{ex}}(\mathbf{r}) U_{\mathrm{wf}}(\mathbf{r} - \boldsymbol{\xi}) \propto \exp\left[-\frac{(\mathbf{r} - \boldsymbol{\xi}/\kappa)^2}{2\sigma_{\mathrm{PSF}}^2}\right], \tag{96}$$

with $\sigma_{\mathrm{PSF}}^{-2} = \sigma_{\mathrm{ex}}^{-2} + \sigma_{\mathrm{em}}^{-2}$ and $\kappa = 1 + \sigma_{\mathrm{em}}^2/\sigma_{\mathrm{ex}}^2$. Recalling that σ_{ex} and σ_{em} linearly scale with wavelength [see Eq. (69)], we find that

$$\kappa = 1 + (\lambda_{\mathrm{em}}/\lambda_{\mathrm{ex}})^2, \tag{97}$$

which equals 2 if one neglects the spectral Stokes shift between the excitation and fluorescence emissions. Thus, the maximum of the product of the excitation intensity distribution and the detection PSF is located between the centers of the two at the position $\boldsymbol{\xi}/\kappa$ so that the scan image is shifted by the same amount with respect to an image recorded by a pixel at the position $\boldsymbol{\xi} = 0$; see Fig. 33. This insight yields a recipe for how to superimpose different scan images recorded by different pixels: an image recorded by a pixel at position $\boldsymbol{\xi}$ must be shifted by $\boldsymbol{\xi}/\kappa$ toward the optical axis before being added to the final sum image. Mathematically this is expressed as

$$\begin{aligned} U_{\mathrm{ISM}}(\mathbf{r}) &\propto \int d\boldsymbol{\xi} U_{\mathrm{pix}}\left(\mathbf{r} + \frac{\boldsymbol{\xi}}{\kappa}, \boldsymbol{\xi}\right) \\ &= \int d\boldsymbol{\xi} U_{\mathrm{wf}}\left(\frac{\kappa - 1}{\kappa}\boldsymbol{\xi} - \mathbf{r}\right) I_{\mathrm{ex}}\left(\mathbf{r} + \frac{\boldsymbol{\xi}}{\kappa}\right). \end{aligned} \tag{98}$$

There are two ways to realize this summation in practice. As shown in Fig. 34, one way is to scale down, by a factor of κ, all images recorded by the array detector at each scan position before adding them to the final image at the corresponding scan position (from top to bottom right in Fig. 34). Alternatively, one can leave the recorded array detector images as they are but place them a factor of κ farther away from each other when adding them to the final image (from top to bottom left in Fig. 34).

Both procedures are mathematically equivalent ways to realize the algorithm described by Eq. (98), although the second algorithm is numerically simpler as it does not require any interpolation-based downscaling of the images recorded by the array detector. However, as first demonstrated by York *et al.* (2012) and De Luca *et al.* (2013), both algorithms can be realized in a fully optical way. The first algorithm, which scales down the array detector images, is optically realized by inserting an extra demagnifying lens pair into the detection pathway [as realized by instant SIM (York *et al.*, 2012, 2013), optical photon reassignment (Roth *et al.*, 2013), or confocal spinning disk ISM (Azuma and Kei, 2015)], while the second algorithm, which scales up distances between recorded images, is realized via a double mirror rescan system [rescan microscopy (De Luca *et al.*, 2013)] or by recoupling the emission into the excitation scan system [rapid two-photon-excitation ISM (Gregor *et al.*, 2017)].

By construction both the OTF and the PSF of an ISM are identical to that of a confocal microscope with an infinitely

small confocal pinhole; see the last panels of Fig. 30 (OTF) and Fig. 31 (PSF), respectively. The corresponding achievable optical lateral and axial resolutions then immediately follow from Eqs. (92) and (93). One particularly important property of ISM is that it also "concentrates" the collected fluorescence light into an area of the final image that is 4 times smaller than that of a conventional CLSM ["superconcentration of light" (Roth, Sheppard, and Heintzmann, 2016); see also the top and right panels of Fig. 34], thereby significantly increasing the image contrast. Meanwhile, multiple ISM variants [reviewed by Gregor and Enderlein (2019)] and several commercial systems are available that provide CLSMs with ISM options for improved resolution and high contrast imaging.

3. 4Pi microscopy

One peculiarity of conventional CLSM is the disparity between lateral and axial resolutions [see Eqs. (92) and (93)] due to the PSF's elongated shape along the optical axis, which yields stretched 3D CLSM images; see Fig. 31. To overcome this strongly anisotropic PSF shape, Hell and Stelzer (1992) developed 4Pi microscopy using two opposing objectives to focus (and detect) light. When sending laser excitation light through both objectives in a coherent manner, the resulting interference of the two beams generates a multipeaked interference pattern along the optical axis. The corresponding Fourier representations of the excitation electric fields are shown in the left and middle panels of Fig. 35, and the convolution of the two, i.e., the 4Pi excitation OTF, is shown in the right panel of Fig. 35. In contrast to the CLSM excitation OTF of Fig. 29, its 4Pi counterpart populates high frequencies along the optical axis coinciding with a tight modulation of the excitation intensity along this axis. The corresponding excitation intensity distribution (the excitation PSF) in real space is shown in the left panel of Fig. 36.

Detection in a 4Pi microscope is done as usual in confocal detection mode, whereby two principal options are possible: (1) fluorescence is collected using both objectives and detected by two detectors, resulting in two independent scan images added later to attain a single image [4Pi type A microscope (Lang *et al.*, 2007)], and (2) fluorescence is collected using both objectives and coherently superimposed

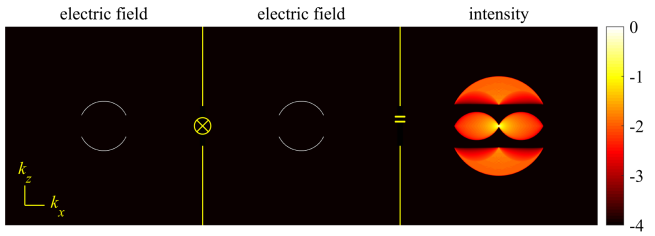

FIG. 35. 4Pi microscope excitation OTF generated by the interference of light focused through two opposing objectives. The left and middle panels show the same Fourier transform of the excitation electric field in sample space. The resulting excitation OTF shown in the right panel is the (auto)convolution of this electric field Fourier transform and represents the Fourier transform of the excitation intensity (the excitation OTF). Excitation is assumed to be done using a water immersion objective with NA = 1.2.

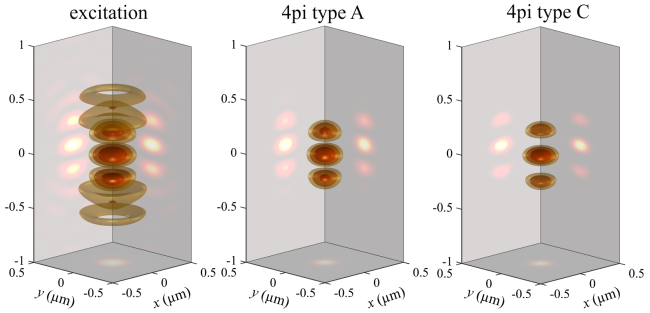

FIG. 36. Excitation PSF and imaging PSF of 4Pi microscopy for a rapidly rotating emitter. Left panel: excitation PSF in the focus of a 4Pi microscope. Middle panel: imaging PSF of a 4Pi type A microscope. Right panel: imagine PSF of a 4Pi type C microscope. Calculations were performed using a water immersion objective with an NA = 1.2, a 470 nm excitation wavelength, and a 550 nm fluorescence emission wavelength, and for a confocal detection in the limit of an infinitely small pinhole.

onto one detector [4Pi type C microscope (Bewersdorf, Schmidt, and Hell, 2006)]. A special case is the 4Pi type B microscope, which performs similarly to the type A microscope, with which excitation is done incoherently (i.e., with no interference pattern generation) but the collected light is superimposed coherently (Hao *et al.*, 2022).

To determine the maximal possible resolution attainable with 4Pi microscopy, we show in Figs. 37 and 38 the OTFs for type A and type C microscopes in the limit of an infinitely small confocal pinhole (realized by combining 4Pi microscopy with ISM). Thus, the OTF of a 4Pi type A microscope, as shown in Fig. 37, is obtained via a convolution of the 4Pi excitation OTF (see Fig. 35) with the OTF of a simple ISM (corresponding to wide-field detection).

As with 4Pi type C microscopes, detection is achieved by coherently superposing fluorescence light from both objectives. The OTF of such a detection looks similar to that of the excitation shown in Fig. 35, except that it is calculated for the fluorescence emission wavelength. The convolution of such a detection OTF with the excitation OTF then yields the OTF of

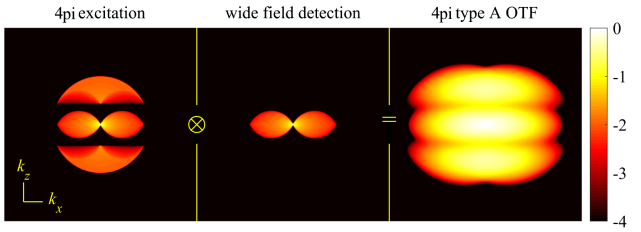

FIG. 37. OTF of a type A 4Pi microscope where excitation is done through two opposing objectives, and detection is performed from one side through a confocal pinhole. For simplicity we consider here only the limiting case of an infinitely small pinhole maximizing the spatial resolution. Left panel: excitation OTF. Middle panel: the OTF of detection with an infinitely small pinhole. Right panel: the resulting 4Pi OTF as a convolution of the two distributions shown on the left. Excitation and detection are achieved using a water immersion objective with an NA = 1.2, and any Stokes shift between excitation and emission light is neglected.

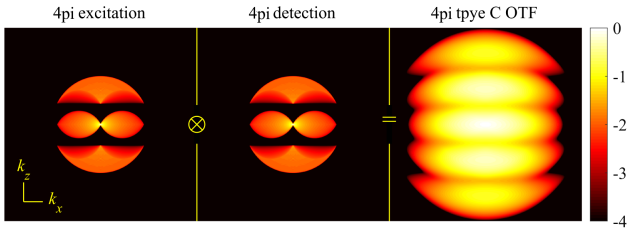

FIG. 38. OTF of a type C 4Pi microscope. Like Fig. 37, but in this configuration both excitation and detection occur through two opposing objectives. Again we consider here only the limiting case of an infinitely small pinhole. Left panel: excitation OTF. Middle panel: the identical Fourier transform for coherent confocal detection from both sides. Right panel: the resulting OTF as a convolution of the two panels shown on the left.

the 4Pi type C microscope; see Fig. 38. The corresponding real space PSFs for both type A and type C 4Pi microscopes are shown in the middle and right panels of Fig. 36.

As seen in Figs. 37 and 38, 4Pi microscopes collect more spatial frequencies than CLSMs (see Fig. 30), thereby improving their axial resolution. As before, we can again obtain quantitative numbers for the lateral and axial resolutions by inspecting the OTF and determining the maximum lateral and axial frequencies supported by the OTF. Concretely the inverse of these maxima multiplied by 2π yields approximate values for the resolution; see Eq. (52). The lateral resolution of a 4Pi microscope (with an infinitely small pinhole) is the same for both type A and type C and equal to that of an ISM; see Eq. (92). However, the axial resolution of a type A 4pi microscope now reads

$$z_{\min} \approx \frac{1}{2}\left[\frac{1}{\lambda_{\mathrm{ex}}} + \frac{1}{\lambda_{\mathrm{em}}}(1-\cos\Theta)\right]^{-1}, \tag{99}$$

and there is a similar approach for the type C 4Pi microscope,

$$z_{\min} \approx \frac{1}{2}\left(\frac{1}{\lambda_{\mathrm{ex}}} + \frac{1}{\lambda_{\mathrm{em}}}\right)^{-1}. \tag{100}$$

As seen in the PSFs of Fig. 36, there are considerable sidelobes neighboring the central maximum along the optical axis, leading to "ghost" images in a recorded 3D scan image of a sample (Bewersdorf, Schmidt, and Hell, 2006). These ghost images are much more pronounced for type A than for type C, though even for type C they must be eliminated, currently by applying deconvolution algorithms (Bewersdorf, Egner, and Hell, 2006; Liu and Huang, 2020). Both the technical complexity of a 4Pi microscope and image deconvolution challenges to eliminate ghost images have prevented their further distribution. However, the ISM lateral resolution of a 4Pi type C (image scanning) microscope together with its axial resolution represent the maximum possible spatial resolutions available along the x and z directions using a diffraction-limited microscope.

4. Two-photon microscopy

An important variant of the point scanning microscope is the two-photon (or multiphoton) excitation scanning microscope (Denk, 2007). Here a fluorophore is excited by a two-photon (or multiphoton) absorption process, typically with an excitation wavelength that is roughly 2 times (or multiple times) as large as that of one-photon absorption fluorescence excitation. Such two-photon excitation microscopes have several important properties (Denk and Svoboda, 1997; Williams, Zipfel, and Webb, 2001). First, owing to the longer excitation wavelength, typically in the infrared, excitation light can penetrate deeper into tissue than visible light. Thus, two-photon excitation microscopes are ideal for deep-tissue imaging in lipid and water-rich samples with high optical absorption in the visible spectrum. Second, there is a critical improvement in the in-focus signal-to-background ratio, i.e., the undesired light from out-of-focus fluorophores, compared to one-photon absorption fluorescence microscopy. This arises from (1) fluorophore excitation taking place at much longer wavelengths than the emission wavelength. In other words, the probability of simultaneous absorption of two or more photons is significant only at a focal spot with high photon density. (2) Excitation light scattering decreases at longer wavelengths. (3) Two-photon (or multiphoton) excitation does not require confocal detection for optical sectioning. This is because the two-photon-excitation PSF is proportional to the square of the excitation light intensity distribution (the probability of two simultaneous photon absorption is given by the square of the one-photon-excitation PSF) (Pawley, 2006), represented by an autoconvolution of the excitation OTF in Fourier space. A similar convolution was already considered in the discussion of the ISM's OTF (as idealized by the last panel of Fig. 30), which covered higher spatial frequencies than are associated with the OTF of a wide-field microscope or the CLSM with a wide pinhole shown in the first panel of Fig. 30. Thus, a two-photon-excitation microscope has an optical sectioning capability that is similar to a confocal (one-photon-excitation) microscope at the same excitation wavelength when it uses an infinitely small detection pinhole (neglecting the spectral Stokes shift between excitation and emission). The required peak power of the excitation pulses, which is orders of magnitude larger than that of single-photon excitation, thereby increasing photodamage and photobleaching (Tauer, 2002), is the primary downside of two-photon-excitation microscopy.

To gain deeper insight into the best possible lateral resolution achievable with a two-photon-excitation microscope, we consider two-photon excitation along with ISM detection, i.e., record at each scan position a small image of the excited region and perform pixel reassignment to obtain the high resolution ISM image; see Sec. IV.B.2. To do so, we approximate the one-photon-excitation PSF and the single-pixel detection PSF once more by Gaussian approximations with variances σ_{ex}^2 and σ_{em}^2; see Sec. IV.B.2. We can visualize the PSF of the scan image recorded by one pixel at position $\boldsymbol{\xi}$ on the array detector, as shown in Fig. 39; see also Eq. (96).

The new reassignment factor κ (see Sec. IV.B.2) is found by looking at the product of the detection PSF with the square of the one-photon-excitation PSF, yielding a Gaussian function with a variance $\sigma^{-2} = 2\sigma_{\mathrm{ex}}^{-2} + \sigma_{\mathrm{em}}^{-2}$ and a midpoint position $\boldsymbol{\xi}/\kappa$, with $\kappa = 1 + 2(\lambda_{\mathrm{em}}/\lambda_{\mathrm{ex}})^2$, which yields for the case $\lambda_{\mathrm{ex}} = 2\lambda_{\mathrm{em}}$ the value $\kappa = 3/2$; see also Eq. (97).

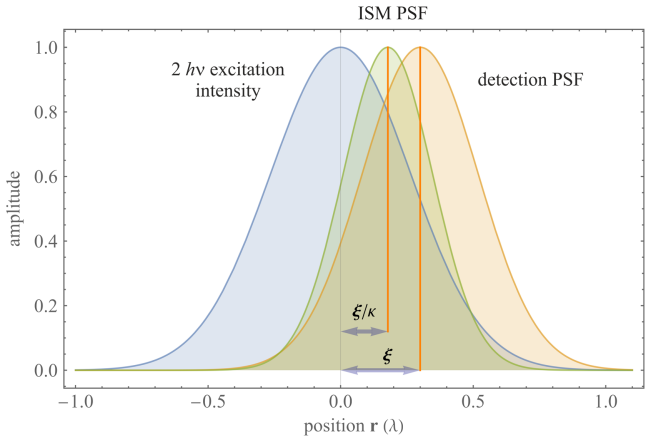

FIG. 39. Pixel reassignment in two-photon-excitation ISM. In contrast to the ISM in Fig. 33, the excitation intensity distribution (one-photon-excitation PSF) in two-photon microscopy has a larger width due to its larger excitation wavelength.

We now compare the performance of such a two-photon-excitation ISM to that of a one-photon-excitation CLSM and ISM at half the wavelength. For simplicity we consider the toy model of a one-dimensional microscope. The Fourier representation of the excitation electric field of such a one-dimensional microscope is a uniform amplitude distribution over the frequency range supported by the microscope (the maximum lateral frequency transmitted is $nk_0 \sin\Theta$). This is shown in Fig. 40 by the tabletop function (electric field). The autoconvolution of this uniform amplitude distribution yields the excitation OTF and is, for the one-dimensional and one-photon case, the triangular function shown in Fig. 40 and denoted by "$1h\nu$ excitation (λ_0)."

The two-photon-excitation PSF for an excitation with a $2\lambda_0$ wavelength is given by the square of the one-photon-excitation PSF. As such, its OTF corresponds to the autoconvolution of the one-photon OTF shown as $1h\nu$ excitation (λ_0) in Fig. 40 but is scaled down along the frequency axis by a factor of 2 (remember that we compare two-photon excitation at $2\lambda_0$ with one-photon excitation at $1\lambda_0$). The corresponding curve is denoted by $2h\nu$ excitation ($2\lambda_0$). The OTFs for the extensions of one-photon-excitation and two-photon-excitation

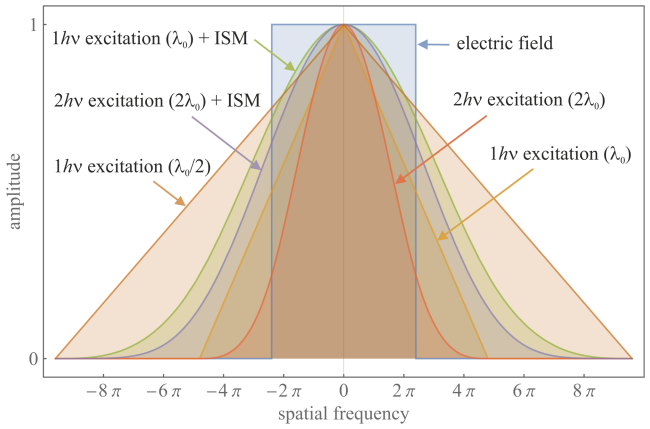

FIG. 40. Comparison of one- and two-photon microscopy. See the text for details.

fluorescence microscopy with ISM are also shown, together with the OTF of the one-photon excitation at $\lambda_0/2$ for comparison.

The frequency support of two-photon excitation at a $2\lambda_0$ wavelength is equal to that of the one-photon excitation at λ_0, but with increased amplitudes at low frequencies and decreased amplitudes at large frequencies. In other words, a two-photon microscope transmits high lateral spatial frequencies less efficiently than a one-photon microscope operating at half the wavelength. This is also true when we compare two-photon ISM with one-photon ISM, as shown by the two curves $1h\nu$ excitation (λ_0) + ISM and $2h\nu$ excitation $(2\lambda_0)$ + ISM in Fig. 40. Both modes have a frequency support equal to that of a one-photon excitation at $\lambda_0/2$, but with considerably damped amplitudes at high spatial frequencies, with one-photon ISM performing slightly better than two-photon ISM. Thus, two-photon (or multiphoton) excitation generally performs worse, in terms of resolution, than one-photon microscopes at half the wavelength, though biological tissue remains more transparent (less scattering) at long wavelengths, giving access to greater penetration depths in two-photon and multiphoton excitation microscopes.

C. Models for single spot confocal analysis

Point scanning microscopes, including confocal and two-photon microscopes, have been used to study both dynamic (Sprague *et al.*, 2004; Digman and Gratton, 2011; Wunderlich *et al.*, 2013; Jazani, Sgouralis, and Pressé, 2019; Jazani *et al.*, 2019) and static phenomena (Berland, So, and Gratton, 1995; Rossow *et al.*, 2010; Kristoffersen *et al.*, 2014; Karpf *et al.*, 2020; Thiele *et al.*, 2020) with both immobile (Berland, So, and Gratton, 1995; Nettels, Hoffmann, and Schuler, 2008; Wunderlich *et al.*, 2013; Jazani, Sgouralis, and Pressé, 2019; Jazani *et al.*, 2019) and scanning spots (Digman *et al.*, 2008; Rossow *et al.*, 2010; Digman and Gratton, 2011; Fazel, Jazani *et al.*, 2022) under continuous or pulsed illumination (Gregor, Patra, and Enderlein, 2005; Jazani, Sgouralis, and Pressé, 2019). Point scanning microscopes, particularly confocal microscopes, provide data for myriad analysis tools, including fluorescence recovery after photobleaching (Sprague *et al.*, 2004; Lorén *et al.*, 2015; Moud, 2022) used in the study of subcellular environments by monitoring diffusion of fluorophores into previously photobleached regions FLIM (Suhling *et al.*, 2015; Datta *et al.*, 2020), where photon arrival time statistics following pulsed excitation are collected and analyzed, and fluorescence correlation spectroscopy (FCS) (Elson and Magde, 1974; Magde, Elson, and Webb, 1974; Digman and Gratton, 2011), where photon arrival times or fluorescence intensities, often collected under constant illumination, are correlated in time to infer dynamical parameters (Jazani, Sgouralis, and Pressé, 2019; Jazani *et al.*, 2019).

Here we begin with a description of FCS where a static confocal spot is used to determine the reaction kinetics and diffusion coefficient of particles freely diffusing through the spot; see Fig. 41(a). In particular, Fig. 41 illustrates a scenario often analyzed using FCS with labeled molecules freely diffusing through a static confocal spot becoming excited in proportion to the local light intensity. In traditional FCS analysis, a fraction of emitted photons are captured and

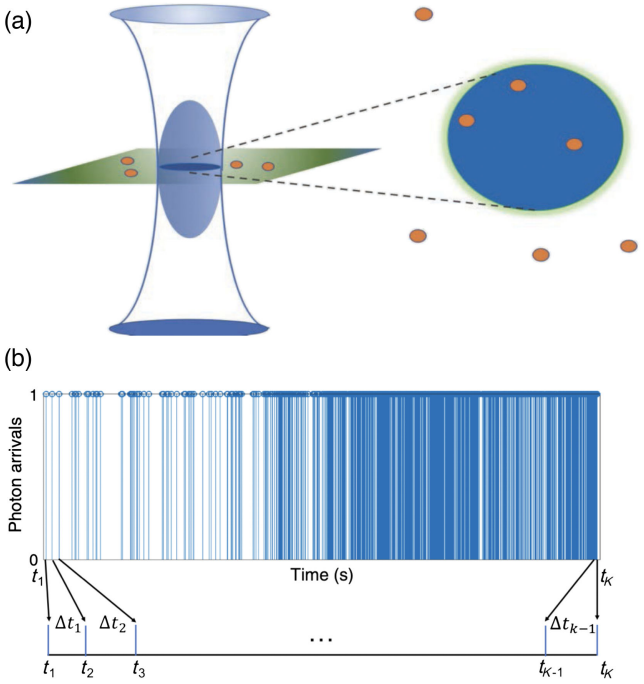

FIG. 41. (a) Schematic of confocal volume (in blue) with labeled molecules emitting photons in proportion to their degree of excitation decaying from the confocal volume center. (b) Synthetic trace with 1500 photons generated assuming four molecules diffusing at 1 $\mu m^2/s$ for 30 ms using background and molecule photon emission rates of 10^3 and 4×10^4 photons/s, respectively. Adapted from Tavakoli, Jazani, Sgouralis, Shafraz *et al.*, 2020.

dynamical properties are obtained by autocorrelating in time the emitted light intensity or photon arrival times (Elson and Magde, 1974; Magde, Elson, and Webb, 1974; Bright *et al.*, 1989; Lakowicz, 2006). While autocorrelating photon arrivals is computationally informative, it is data inefficient and eliminates single-molecule information already encoded in the signal (Jazani *et al.*, 2019, 2022; Tavakoli, Jazani, Sgouralis, Shafraz *et al.*, 2020). What is more, uncertainty is rarely propagated on derived quantities. Thus, a statistical method directly analyzing photon arrivals is warranted to avoid data postprocessing including autocorrelation (Jazani, Sgouralis, and Pressé, 2019; Jazani *et al.*, 2019; Tavakoli, Jazani, Sgouralis, Shafraz *et al.*, 2020). Here we begin by deriving the likelihood for the collection of $K+1$ photons whose interarrival intervals (Tavakoli, Jazani, Sgouralis, Shafraz *et al.*, 2020) are designated by $\Delta t_{1:K} = \{\Delta t_1, \ldots, \Delta t_K\}$ [see Fig. 41(b)] under the assumption of continuous illumination.

We begin by considering the confocal PSF derived earlier in Eq. (94) and for simplicity immediately adopt Cartesian coordinates where $\boldsymbol{r} = (\boldsymbol{\rho}, z)$. For an arbitrary M molecules located at $\boldsymbol{r}_k^m$ at time t_k, we write the following profile:

$$S_k(\boldsymbol{r}) = \sum_{m=1}^{M} \delta(\boldsymbol{r} - \boldsymbol{r}_k^m). \tag{101}$$

As such, the total expected photon emission rate μ_k at time level k follows from

$$\mu_k(r) = \mu_{\mathcal{B}} + \mu_0 \int d\boldsymbol{r} U_{\mathrm{cf}}(r) S_k(\boldsymbol{r}) = \mu_{\mathcal{B}} + \sum_{m=1}^{M} \mu_k^m(\boldsymbol{r}_k^m), \tag{102}$$

where $\mu_k^m(\boldsymbol{r}_k^m) = \mu_0 U_{\mathrm{cf}}(\boldsymbol{r}_k^m)$ is the expected photon emission rate from the mth molecule located at $\boldsymbol{r}_k^m$, μ_0 is the maximum photon emission rate associated with a molecule located at the PSF center, and $\mu_{\mathcal{B}}$ is the background photon emission rate. The photon emission rate μ_k then dictates the photon interval time Δt_k,

$$\Delta t_k \sim \mathrm{Exponential}(\mu_k(r)), \tag{103}$$

where "Exponential" implies a normalization constant and the notation used was introduced in Sec. I.B. This exponential waiting time follows from Poisson distributed photon emission per unit time implying exponentially distributed photon interarrival times.

Finally, under the assumption of a normal diffusion model with open boundary conditions,

$$\boldsymbol{r}_k^m | D \sim \mathrm{Normal}(\boldsymbol{r}_{k-1}^m, 2D\Delta t_k), \tag{104}$$

where D is the diffusion coefficient assumed to be constant across time and space. In Eq. (104) we see that the rate $\mu_k(r)$ inherits its stochasticity from the stochastic positions.

Given the previously described forward model, we now construct the likelihood for K photon interarrival times $\Delta t_{1:K}$ given by Eq. (103). As $\Delta t_{1:K}$ are i.i.d. (see Sec. I.B), the trace's likelihood is simply the product of the likelihood of every individual photon time interval,

$$P(\Delta t_{1:K} | M, D, \bar{\bar{\boldsymbol{r}}}, \mu_0, \mu_{\mathcal{B}}) = \prod_k \mathrm{Exponential}(\Delta t_k; \mu_k(r)), \tag{105}$$

where "Exponential" implies a normalization constant and $\mu_k(r)$ is an implicit function of M, D, μ_0, and $\mu_{\mathcal{B}}$; see Eqs. (102) and (104). Moreover, double overbars represent the set of all possible values for the two associated indices, namely, m and k.

To maximize the likelihood, we need to either determine the number of molecules in advance, i.e., the parametric model, or work within a nonparametric paradigm and infer the number of molecules alongside other parameters. The aforementioned likelihood cannot be naively maximized to obtain parameters due to classic overfitting problems favoring more complex models, i.e., larger numbers of molecules. However, in the former case, assuming an incorrect parametric model with M molecules (Jazani *et al.*, 2019; Tavakoli, Jazani, Sgouralis, Shafraz *et al.*, 2020) can result in incorrect estimates of other parameters, for example, the diffusion coefficient; see Fig. 69.

As such, we abandon the parametric paradigm and start leveraging BNP tools (Ferguson, 1973; Hjort *et al.*, 2010; Gershman and Blei, 2012; Pressé and Sgouralis, 2023). Of particular interest within the BNP paradigm is the beta-Bernoulli process prior (see Sec. I.B) on the number of candidate molecules M formally allowed to tend to infinity ($M \to \infty$) *a priori*. In other words, each molecule is treated as a Bernoulli random variable (a load) b_m determined simultaneously along with other unknowns; see Sec. I.B. The

probability of the load being 1, equivalently, the probability of the molecule being warranted by the data, is the single parameter of the Bernoulli distribution on which we place a beta prior.

Within this framework, Eq. (102) is modified by replacing $\sum_{m=1}^{M}\mu_k^m(\boldsymbol{r}_k^m)$ on the right-hand side with $\sum_{m=1}^{\infty}b_m\mu_k^m(\boldsymbol{r}_k^m)$ and summing over infinite molecules. The likelihood then adopts the form

$$P(\Delta t_{1:K}|\vartheta)=\prod_k \text{Exponential}(\Delta t_k;\mu_k(r)), \quad (106)$$

where "Exponential" implies a normalization constant but ϑ now collects all unknowns, including all loads. Our nonparametric posterior is proportional to the product of this likelihood and all priors, including beta-Bernoulli process priors on each molecule; see Fig. 42.

Now equipped with the posterior, we draw samples using Monte Carlo methods to learn the set of unknowns ϑ. To learn the trajectories $\bar{\bar{r}}$, we use forward filtering backward sampling (Scott, 2002; Bishop and Nasrabadi, 2006; Tavakoli, Jazani, Sgouralis, Shafraz *et al.*, 2020; Pressé and Sgouralis, 2023), while the remaining parameters are sampled either directly or using the brute-force Metropolis-Hastings algorithm; see Sec. I.B. Figure 43 benchmarks the statistical framework of Fig. 42 versus FCS.

While the previous approach returns a trajectory, owing to the symmetry of the confocal PSF [see Eq. (94), the photon emission rate of Eq. (102) and thus the likelihood given by Eq. (106) are invariant under transformations leaving $\sqrt{(\boldsymbol{\rho}/\sigma_\rho)^2+(z/\sigma_z)^2}$ unchanged. As such, equivalent positions lead to the same likelihood, and thus unique positions cannot be determined using a single confocal setup.

In contrast, it is possible to determine absolute molecular locations (trajectories) by breaking the spatial symmetry of the confocal spot by introducing a multifocus confocal setup (Lessard, Goodwin, and Werner, 2007; Wells *et al.*, 2010; Jazani *et al.*, 2022). Such a setup splits the confocal spot by introducing four detectors with axially and laterally offset

Statistical Framework : Confocal under continuous illumination

Data: photon inter-arrival times

$$\Delta t_{1:K}=\{\Delta t_1,...,\Delta t_K\}.$$

Parameters: loads, diffusion coefficient, molecule trajectories, molecule maximum emission rate, background emission rate

$$\vartheta=\left\{\bar{b},D,\bar{\bar{\boldsymbol{r}}},\mu_0,\mu_{\mathcal{B}}\right\}.$$

Likelihood:

$$P\left(\Delta t_{1:K}|\vartheta\right)=\prod_k \text{Exponential}\left(\Delta t_k;\mu_k(r)\right).$$

Priors:

$$\begin{aligned} q_m &\sim \text{Beta}\left(A_q,B_q\right),\ m=1:\infty,\\ b_m &\sim \text{Bernoulli}\left(q_m\right),\\ D &\sim \text{InvGamma}\left(\alpha_D,\beta_D\right),\\ \boldsymbol{r}_k^m &\sim \text{Normal}\left(\boldsymbol{r}_{k-1}^m,2D\Delta t_k\right),\\ \mu_0 &\sim \text{Gamma}\left(\alpha_\mu,\beta_\mu\right),\\ \mu_{\mathcal{B}} &\sim \text{Gamma}\left(\alpha_b,\beta_{\mathcal{B}}\right). \end{aligned}$$

Posterior:

$$P(\vartheta|\Delta t_{1:K})\propto P(\Delta t_{1:K}|\vartheta)P(\vartheta).$$

FIG. 42. Statistical framework: confocal under continuous illumination.

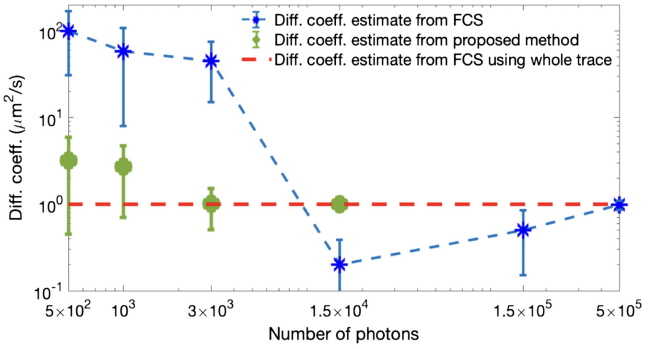

FIG. 43. Comparison of the diffusion coefficients D obtained from the statistical framework vs FCS plotted against photon counts used in the analysis. The photon arrival times were simulated using the parameter values in Fig. 41(b). Adapted from Tavakoli, Jazani, Sgouralis, Shafraz *et al.*, 2020.

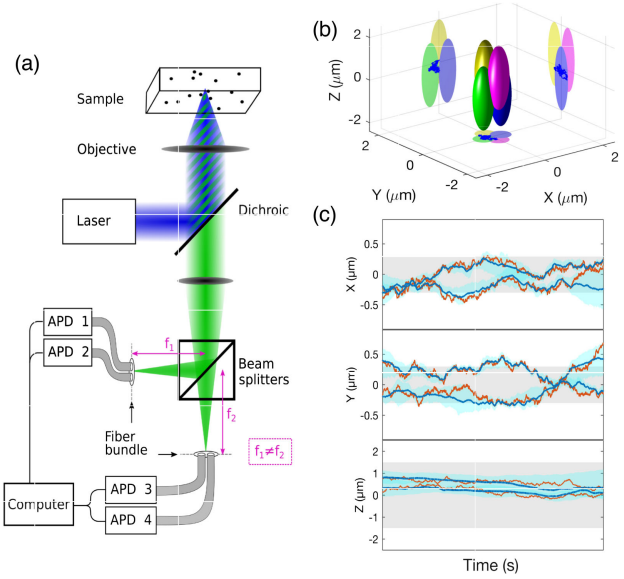

FIG. 44. Multifocal setup uniquely resolving many molecular trajectories simultaneously. (a) A beam splitter is used to divide the fluorescent emission (indicated in green) into two paths later coupled into fibers and detected by four APDs corresponding to different focal spots. (b) PSFs associated with different light paths. (c) Trajectories for two freely diffusing molecules with $D=1$ μm^2/s, $\mu_0=5\times10^4$photons/s, and $\mu_{\mathcal{B}}=10^3$photons/s. The orange and blue curves represent the learned trajectories' ground truth and median, respectively. The blue and gray areas, respectively, denote the 95% confidence intervals and the PSF's width. Adapted from Jazani *et al.*, 2022.

detection volumes; see Figs. 44(a) and 44(b). Photons from molecules in such a setup are detected in the lth detector with the following rate:

$$\mu_k^l(r) = \mu_{\mathcal{B}}^l + \mu_0 \sum_m b_m^l U_{\mathrm{cf}}^l(\mathbf{r}_k^m) \tag{107}$$

at time k; see Eq. (102). The total photon detection rate is in turn the sum of detection rates across all different detectors $\mu_k = \sum_l \mu_k^l$, and the likelihood is similar to the likelihood seen in Eq. (106). From this likelihood follows a posterior analogous to Fig. 42 that, when sampled, yields absolute molecular trajectories; see Fig. 44(c).

It is now conceivable to imagine generalizing the aforementioned treatment to include multiple diffusing species (Bacia and Schwille, 2007), species with donor and acceptor labels (FCS FRET) (Torres and Levitus, 2007; Schuler, 2018), and species undergoing reactions that alter their emission rate and kinetics (Zosel *et al.*, 2018; Xu, Jazani *et al.*, 2023).

This brings us to the merits of statistical approaches compared to FCS. Such approaches are more data efficient, rigorously propagate errors (including effects of finite data via the likelihood), and can deal with any PSF shape and optical aberrations (Enderlein *et al.*, 2004; Sarkar *et al.*, 2019). But also, fundamentally, by avoiding data postprocessing they learn more. For instance, in contrast to FCS the previously described statistical methods can learn properties of individual molecules diffusing through the spot, thereby providing single-molecule resolution, albeit at a computational cost.

Having dealt with continuous illumination, we now turn to pulsed illumination and, for simplicity, assume an immobile sample. Under pulsed illumination, the data acquired are a trace of K photon arrival times $\Delta t_{1:K}$ reported with respect to the immediate preceding pulses. These arrival times, also termed microtimes, encode the excited-state lifetimes τ_m for the mth species of fluorophore species (see Sec. II) present within the confocal spot. They also encode the associated photon ratios (weights) shown by π_m for the mth species related to fluorophore densities, as we later show.

Although there are intuitive methods to determine excited-state lifetimes (Digman *et al.*, 2008), as in Fig. 43 we find that learned lifetimes are sensitive to the parametric assumption on the number of lifetime species considered (Fazel, Vallmitjana *et al.*, 2023). Indeed, existing techniques cannot simultaneously (1) decode the number of fluorophore species present in a trace of photon arrival times; (2) operate on a broad range of lifetimes below the instrument response function (IRF) (see Appendix A) or lifetimes comparable to the laser interpulse times or similar lifetimes; (3) provide uncertainties over parameter estimates; and (4) infer continuous fluorophore densities, i.e., lifetime maps given by $\Omega_m(\boldsymbol{r}) = \mu_m S_m(\boldsymbol{r})$, where S_m and μ_m are the fluorophore densities [see Eq. (101)] and fluorophore excitation probability (for in-focus fluorophores) during a laser pulse for the mth species, respectively.

Here we review statistical frameworks for FLIM analysis addressing the previously highlighted issues with minimal photon budgets. In doing so, we first discuss a framework for a single confocal spot and then generalize to FLIM analysis methods using data from a scanning confocal setup to deduce lifetime maps over large FOVs.

We begin by introducing the likelihood for $\Delta t_{1:K}$ collected from a single spot with M species,

$$P(\Delta t_{1:K}|\lambda_{1:M}, \pi_{1:M}) = \prod_{k=1}^{K} P(\Delta t_k|\lambda_{1:M}, \pi_{1:M}), \tag{108}$$

where λ_m denotes the inverse lifetime $\tau_m = 1/\lambda_m$ and $P(\Delta t_k|\lambda_{1:M}, \pi_{1:M})$ denotes the likelihood of the kth arrival time. To derive $P(\Delta t_k|\lambda_{1:M}, \pi_{1:M})$, we sum over all possibilities that could give rise to this photon, including all M fluorophore species and all N_{pl} previous laser pulses. Assuming a Gaussian IRF, this leads to [see Appendix A and Eq. (A23)] (Fazel, Jazani *et al.*, 2022; Fazel, Vallmitjana *et al.*, 2023)

$$\begin{aligned} P(\Delta t_k|\lambda_{1:M}, \pi_{1:M}) = \Bigg[& \sum_{m=1}^{M} \pi_m \sum_{n=0}^{N_{\mathrm{pl}}} \frac{\lambda_m}{2} \\ & \times \exp\left(\frac{\lambda_m}{2} [2(\tau_{\mathrm{IRF}} - \Delta t_k - nT) + \lambda_m \sigma_{\mathrm{IRF}}^2] \right) \\ & \times \operatorname{erfc}\left(\frac{\tau_{\mathrm{IRF}} - \Delta t_k - nT + \lambda_m \sigma_{\mathrm{IRF}}^2}{\sigma_{\mathrm{IRF}} \sqrt{2}} \right) \Bigg], \end{aligned} \tag{109}$$

where τ_{IRF}, σ_{IRF}^2, and T denote the IRF offset, the variance, and the interpulse time, respectively; see Appendix A. Ignoring excitation by previous pulses considered in Eq. (109), we arrive at the likelihood obtained by Rowley *et al.* (2016).

To summarize, parametrically the number of fluorophore species M is prespecified and often set to 1 or 2 for simplicity; see Rowley *et al.* (2016) and Kaye *et al.* (2017). In contrast, nonparametrically the number of fluorophore species are *a priori* assumed to be infinite (Fazel, Jazani *et al.*, 2022; Fazel, Vallmitjana *et al.*, 2023).

Within the nonparametric paradigm, the single spot FLIM posterior is proportional to the likelihood (109) and priors over all unknown parameters, namely, $\lambda_{1:M}$ and $\pi_{1:M}$. For λ_m, we use a gamma prior to guarantee non-negative values. For π_m, we leverage the nonparametric Dirichlet process prior (Neal, 2000; Gelfand, Kottas, and MacEachern, 2005; Sgouralis and Pressé, 2017) to facilitate inference over the probability in the number of species present warranted by the data, i.e., to address model selection; see Sec. I.B. Within this framework, as before when operating nonparametrically we assume an *a priori* infinite number of species ($M \to \infty$) with associated weights π_m. As we sample these weights, the weights ascribed to species not contributing to the data attain negligible values. Figure 45 shows lifetime histograms for two lifetimes below the IRF and with subnanosecond differences using 500, 1000, and 2000 photons.

We now turn to FLIM over large FOVs, where we estimate how to smooth lifetime maps from confocal scanning data; see Fig. 47. FLIM data over large FOVs are typically collected using a CLSM to scan the sample over uniformly spaced horizontal trajectories where the spacing defines the data pixel size. The collected data are often arranged into a 2D pixel array where each pixel contains a subset of photon arrival times acquired over the pixel.

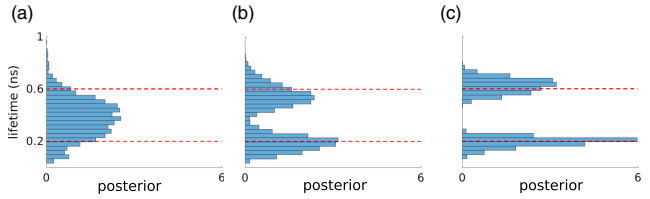

FIG. 45. Lifetime histograms from single-pixel FLIM. Lifetimes are below the IRF and differ by subnanoseconds. (a)–(c) Datasets simulated with 5×10^2, 10^3, and 2×10^3photons, an IRF width of 0.66 ns, and ground truth lifetimes of 0.2 and 0.6 ns denoted by dotted lines. Learning the correct number of fluorophore species here requires >500 photons.

One naive way to process such data is to analyze each pixel independently using the framework of Fig. 46. However, this yields pixelated lifetime maps where information from one pixel does not inform the neighboring pixels. In what follows, we review a framework for multipixel FLIM over large FOVs (Fazel, Jazani *et al.*, 2022, 2023) while reporting lifetime maps below the data pixel size leveraging spatial correlations across pixels by invoking nonparametric GPs; see Sec. I.B and Fig. 47.

The likelihood here is now given by

$$P(\bar{\bar{\mathcal{W}}},\bar{\bar{\Delta t}}|\vartheta)=\prod_i\prod_{k_p}P(\mathcal{W}^i_{k_p}|\vartheta)P(\Delta t^i_{k_p}|\vartheta),\quad(110)$$

where $\mathcal{W}^i_{k_p}$, for the k_pth pulse and ith pixel, is a binary variable designating whether or not a laser pulse leads to a photon detection. As before, ϑ collects all unknowns including the inverse of lifetimes $\lambda_{1:M}$, multipixel lifetime maps $\Omega_{1:M}$, the loads $b_{1:M}$, and hyperparameters $\nu_{1:M}$ over each species. Further, double overbars represent the set of all possible values for the pair of indices associated with the corresponding parameter. In Eq. (110) the likelihood associated with the photon arrival times is similar to Eq. (109) and given by

$$P(\Delta t^i_{k_p}|\vartheta)=\Bigg[\sum_{m=1}^{M}\pi_m\sum_{n=0}^{N_{\rm pl}}\frac{\lambda_m}{2}\times\exp\left(\frac{\lambda_m}{2}[2(\tau_{\rm IRF}-\Delta t^i_{k_p}-nT)+\lambda_m\sigma^2_{\rm IRF}]\right)\times\operatorname{erfc}\left(\frac{\tau_{\rm IRF}-\Delta t^i_{k_p}-nT+\lambda_m\sigma^2_{\rm IRF}}{\sigma_{\rm IRF}\sqrt{2}}\right)\Bigg]^{\mathcal{W}^i_{k_p}},\quad(111)$$

which reduces to 1 for pulses that do not yield any photon detection (empty pulses with $\mathcal{W}^i_{k_p}=0$). In Eq. (111) the weights $\pi_{1:M}$ are directly related to the lifetime maps by $\pi^i_m=(1-P^i_{0m})\prod_{q\neq m}P^i_{0q}$ (Fazel, Jazani *et al.*, 2022), where P^i_{0m} reflects the probability of no photon detection within the ith pixel from the mth species given by

$$P^i_{0m}=\exp\left[-b_m\int\Omega_m(\boldsymbol{r})U_{\rm cf}(\xi^i-\boldsymbol{r})d\boldsymbol{r}\right],\quad(112)$$

where ξ^i is the center of the ith pixel. Moreover, b_m denotes the loads associated with the mth lifetime map (see Sec. I.B), on which we place beta-Bernoulli process priors (as in Fig. 42) to deduce the number of lifetime maps introduced by each fluorophore species present within the data. We note that for species with $b_m=0$ the probability of no photon detection is 1.

After illustrating how to compute $P(\Delta t^i_{k_p}|\vartheta)$, we compute $P(\mathcal{W}^i_{k_p}|\vartheta)$ following the observation that $\mathcal{W}^i_{k_p}$ is Bernoulli distributed with a success probability of $1-\pi^i_0$,

Statistical Framework : Single spot FLIM

Data: photon arrival times

$$\Delta t_{1:K}=\{\Delta t_1,...,\Delta t_K\}.$$

Parameters: inverse lifetimes, weights

$$\vartheta=\{\lambda_{1:M},\pi_{1:M}\}.$$

Likelihood:

$$P(\Delta t_{1:K}|\vartheta)=\prod_k P(\Delta t_k|\vartheta).$$

Priors:

$$\lambda_m\sim\text{Gamma}(\alpha_\lambda,\beta_\lambda),$$
$$\pi_m\sim\text{Dirichlet}_{1:M}\left(\frac{\alpha_\pi}{M},...,\frac{\alpha_\pi}{M}\right),\ M\to\infty$$

Posterior:

$$P(\vartheta|\Delta t_{1:K})\propto P(\Delta t_{1:K}|\vartheta)P(\vartheta).$$

FIG. 46. Statistical framework: single spot FLIM.

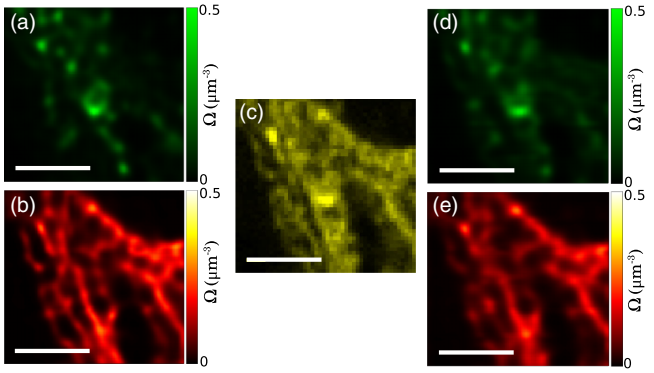

FIG. 47. Experimental FLIM data from mixtures of two cellular structures (lysosome and mitochondria, shown in green and red, respectively) stained with two different fluorophore species. (a), (b) Ground truth lifetime maps. (c) Data acquired from mixtures of two ground truth maps. (d),(e) Resulting subpixel interpolated lifetime maps obtained using the statistical framework of Fig. 48. The average absolute difference between ground the truth and learned maps is ≈4%. Scale bars are 4 μm. Adapted from Fazel, Jazani *et al.*, 2022.

$$\mathcal{W}^i_{k_p} \sim \text{Bernoulli}(1-\pi^i_0). \tag{113}$$

In Eq. (113) π^i_0 is the probability of no photon detection from the ith pixel given by $\pi^i_0 = \prod_{m=1}^{M} P^i_{0m}$.

After introducing the likelihoods, we construct the posterior proportional to the product of the likelihood and priors over all unknown parameters. Our framework is doubly nonparametric, as we use GP priors over continuous lifetime maps and beta-Bernoulli process priors over the loads; see Sec. I.B. The GP priors over lifetime maps comprise an infinite set of correlated random variables, i.e., the value of the map at every point in space

$$\Omega_m \sim \text{GP}(\nu_m, \boldsymbol{K}), \tag{114}$$

where $\mathbf{K}$ and ν_m denote the correlation kernel (also termed a covariance matrix) and the GP prior's mean. The remaining priors are either physically or computationally inspired; see Fig. 48.

With the posterior at hand, we make inferences on ϑ once more by drawing samples from the posterior with Monte Carlo calculations. Of note are elliptical slice samplers (Murray, Adams, and MacKay, 2010) used to sample lifetime maps, as the GP and likelihood do not form a conjugate pair.

Statistical Framework : Multi-pixel FLIM

Data: photon arrival times and pulses being empty or not

$$\overline{\overline{\Delta t}} = \left\{\Delta t^{i=1}_{1:K_p}, ..., \Delta t^{N}_{1:K_p}\right\},$$
$$\overline{\overline{\mathcal{W}}} = \left\{\mathcal{W}^{i=1}_{1:K_p}, ..., \mathcal{W}^{N}_{1:K_p}\right\}.$$

Parameters: loads, inverse lifetimes, lifetime maps, GP prior averages (hyper-parameters)

$$\vartheta = \{b_{1:M}, \lambda_{1:M}, \Omega_{1:M}, \nu_{1:M}\}.$$

Likelihood:

$$P\left(\overline{\overline{\mathcal{W}}}, \overline{\overline{\Delta t}}|\vartheta\right) = \prod_k \prod_n P\left(\mathcal{W}^n_k; \vartheta\right) P\left(\Delta t^n_k; \vartheta\right).$$

Priors:

$$q_m \sim \text{Beta}\left(A_q, B_q\right), \; m = 1:\infty,$$
$$b_m \sim \text{Bernoulli}\left(q_m\right),$$
$$\lambda_m \sim \text{Gamma}\left(\alpha_\lambda, \beta_\lambda\right),$$
$$\Omega_m \sim \text{GP}\left(\nu_m, \boldsymbol{K}\right),$$
$$\nu_m \sim \text{Normal}\left(0, \sigma^2_\chi\right).$$

Posterior:

$$P\left(\vartheta|\overline{\overline{\mathcal{W}}}, \overline{\overline{\Delta t}}\right) \propto P\left(\overline{\overline{\mathcal{W}}}, \overline{\overline{\Delta t}}|\vartheta\right) P(\vartheta).$$

FIG. 48. Statistical framework: multipixel FLIM.

D. Structured illumination microscope

As discussed in Sec. III.C, a major drawback of wide-field fluorescence imaging is the lack of optical sectioning arising from the OTF's missing cone; see Fig. 12. This in turn yields out-of-focus blur that degrades the final images. Previously we discussed near-field and point scanning methods where, for example, conventional confocal microscopes achieved optical sectioning via pinholes; see Sec. IV.B.1. Here we discuss how SIM achieves both optical sectioning and resolution beyond the diffraction limit (Bailey *et al.*, 1993; Heintzmann and Cremer, 1999; Gustafsson, 2000; Ströhl and Kaminski, 2016; Wu and Shroff, 2018; Mertz, 2019a).

Patterned illumination, with a high spatial stripe contrast near the focal plane (Neil, Juškaitis, and Wilson, 1997), was introduced in an effort to attain optical sectioning. The pattern, whose illumination contrast ideally fades away from the focal plane, was then translated twice, yielding three images $\mathcal{I}_l$ with corresponding phase offsets $\phi_l, l = 0{:}2$. One way to attain optical sectioning was to create three images from differences in two images, say, $\Delta\mathcal{I}_{ll'}(\mathbf{r}) = \mathcal{I}_l(\mathbf{r}) - \mathcal{I}_{l'}(\mathbf{r})$, and combine them according to

$$\Lambda_{\text{sec}}(\mathbf{r}) = \sqrt{\Delta\mathcal{I}_{01}(\mathbf{r})^2 + \Delta\mathcal{I}_{12}(\mathbf{r})^2 + \Delta\mathcal{I}_{20}(\mathbf{r})^2},$$
$$\phi_l = \frac{2l\pi}{3}, \qquad l = 0{:}2. \tag{115}$$

The hope was that, by subtracting images, unmodulated (out-of-focus) contributions would cancel as they are approximately homogeneously illuminated.

These early efforts ultimately enabled structured illumination to achieve higher resolution (Heintzmann and Cremer, 1999; Gustafsson, 2000), which we now discuss by considering the SIM image formation model. SIM images are generated from the product of the fluorophores' distribution $S(\mathbf{r})$ (see Sec. IV.C) and the illumination intensity pattern $I_{\text{ex}}(\mathbf{r})$, followed by convolution with the microscope's wide-field detection PSF [see also Eq. (47)],

$$\Lambda(\mathbf{r}) = \mathcal{B} + I[S(\mathbf{r})I_{\text{ex}}(\mathbf{r})] \otimes U_{\text{wf}}(\mathbf{r}), \tag{116}$$

where $\mathcal{B}$ is the background arising from out-of-focus fluorescent features (ignored here for simplicity) and $U_{\text{wf}}(\mathbf{r})$ and I are the wide-field PSF (see Sec. III.E) and fluorophore brightness per frame, respectively.

While various modulated illumination patterns are conceivable for SIM (Heintzmann, 2003; Planchon *et al.*, 2011; Mudry *et al.*, 2012), in practice the sample is typically illuminated using a sinusoidal intensity $I_{\text{ex}}(\mathbf{r})$, with different in-plane phases and angles (see Fig. 49) achieved via interference-based methods (Heintzmann and Huser, 2017; Ma *et al.*, 2021) or using laser scanning (York *et al.*, 2012, 2013; Gregor and Enderlein, 2019).

Under the former method, such intensity patterns are generated by interference with two to three laser beams, followed by rotation and translation of the grating embedded within the setup's illumination arm. For two beam interference, the image formation is described by

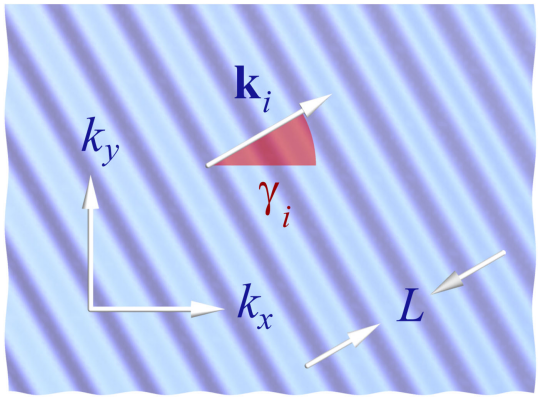

FIG. 49. Sinusoidal illumination pattern for SIM microscopy. $\mathbf{k}_i$ is the wave vector, L is the fringe spacing, and γ_i is the illumination's in-plane angle. The phase is related to the position of the maxima relative to the optical axis.

$$\Lambda^{li}(\mathbf{r}) = I\{S(\mathbf{r})\tfrac{1}{2}[1+\mathfrak{M}\cos(\mathbf{r}\cdot\mathbf{k}_i+\phi_l)]\}\otimes U_{\mathrm{wf}}(\mathbf{r}),$$
$$\gamma_i = \arctan\frac{k_x^i}{k_y^i}, \qquad L = 2\pi/\sqrt{k_x^{i\,2}+k_y^{i\,2}}, \tag{117}$$

where the modulation depth $\mathfrak{M}$ is assumed for simplicity to be 1 in subsequent calculations and $\mathbf{k}_i$ is the wave vector, with the components k_x^i and k_y^i defining the oscillatory pattern's period, i.e., the fringe spacing denoted by L; see Fig. 49. Here

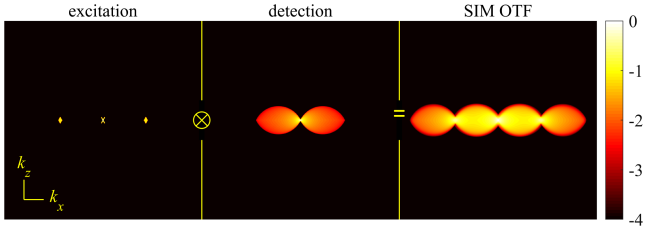

FIG. 50. SIM OTF. Left panel: Fourier transform of the modulated illumination intensity (SIM excitation OTF given by the three delta peaks). Middle panel: Fourier transform of the wide-field detection. Right panel: SIM OTF obtained by convolution of the other two panels; see also Eq. (118).

γ_i and ϕ_l are the lth in-plane illumination angle and the ith phase offset determining the position of the maxima relative to the optical axis, respectively; see Fig. 49 and Eq. (115).

The improved resolution is achieved by exploiting the frequency mixing, i.e., the moiré effect, between the excitation pattern and the sample's spatial frequencies. That is, previously unobservable high frequency information beyond the wide-field OTF's support is shifted down into the microscope's bandpass (i.e., frequency support of the microscope's OTF); see Figs. 19 and 50.

The effect of structured illumination is most intuitively demonstrated in Fourier space. For the sinusoidal pattern given in Eq. (117), its Fourier representation reads

$$\begin{aligned}\tilde{\Lambda}^{li}(\mathbf{k}) &= I[\tilde{S}(\mathbf{k})\otimes\tilde{I}_{\mathrm{ex}}(\mathbf{k})]\mathrm{OTF}_{\mathrm{wf}}(\mathbf{k})\\ &= I\{\tilde{S}(\mathbf{k})\otimes[\delta(0)+\tfrac{1}{2}e^{+i\phi_l}\delta(\mathbf{k}+\mathbf{k}_i)+\tfrac{1}{2}e^{-i\phi_l}\delta(\mathbf{k}-\mathbf{k}_i)]\}\mathrm{OTF}_{\mathrm{wf}}(\mathbf{k})\\ &= I[\tilde{S}(\mathbf{k})+\tfrac{1}{2}e^{+i\phi_l}\tilde{S}(\mathbf{k}+\mathbf{k}_i)+\tfrac{1}{2}e^{-i\phi_l}\tilde{S}(\mathbf{k}-\mathbf{k}_i)]\mathrm{OTF}_{\mathrm{wf}}(\mathbf{k})\\ &= \tilde{\mathcal{I}}_0(\mathbf{k})+\tfrac{1}{2}e^{+i\phi_l}\tilde{\mathcal{I}}_+(\mathbf{k}+\mathbf{k}_i)+\tfrac{1}{2}e^{-i\phi_l}\tilde{\mathcal{I}}_-(\mathbf{k}-\mathbf{k}_i),\end{aligned} \tag{118}$$

where $\mathrm{OTF}_{\mathrm{wf}}(\mathbf{k})$ denotes the wide-field OTF (see Fig. 19 and the middle panel of Fig. 50) and the sinusoidal illumination pattern (for a given angle and phase) is described by three different frequencies in the Fourier domain (see the left panel in Fig. 50) yielding the three SIM harmonics $\tilde{\mathcal{I}}_0$, $\tilde{\mathcal{I}}_+$, and $\tilde{\mathcal{I}}_-$.

In Eq. (118) the first delta function within the parentheses coincides with the Fourier representation of the uniform (wide-field) illumination. However, the two subsequent terms arise from the illumination patterning. These additional terms are two copies of the Fourier representation of the sample $\tilde{S}(\mathbf{k})$ phase shifted by a factor of ϕ_l and frequency shifted by $\mathbf{k}_i$, thereby providing more information than wide-field microscopy.

If one supposes that the OTF cutoff frequency is k_c, the frequency shifted components contain high frequency information that is otherwise absent in the central component (sum frequency $|\mathbf{k}+\mathbf{k}_i|\le k_c$ and difference frequency $|\mathbf{k}-\mathbf{k}_i|\le k_c$ at each sample frequency of k). When imaged, only frequencies inside the support of the wide-field OTF are captured. However, sample information across different (higher) frequency regions now lies within the microscope's bandpass; see Fig. 50.

While the three SIM harmonics $\tilde{\mathcal{I}}_0$, $\tilde{\mathcal{I}}_+$, and $\tilde{\mathcal{I}}_-$ (the wide field and $\pm$ pattern wave vector) already contain frequencies beyond the wide-field bandpass, no subdiffraction resolution can yet be achieved. This is because these components overlap in frequency space. To unmix the overlapping parts, we need to acquire at least three images with different pattern phases ϕ_l designated by $\tilde{\Lambda}^{li}(\mathbf{k})$ in Fourier space. The relation between the three SIM harmonics and these images is best shown in matrix form,

$$\begin{bmatrix}\tilde{\Lambda}^{0i}(\mathbf{k})\\ \tilde{\Lambda}^{1i}(\mathbf{k})\\ \tilde{\Lambda}^{2i}(\mathbf{k})\end{bmatrix} = \begin{pmatrix}1 & 0.5e^{i\phi_0} & 0.5e^{-i\phi_0}\\ 1 & 0.5e^{i\phi_1} & 0.5e^{-i\phi_1}\\ 1 & 0.5e^{i\phi_2} & 0.5e^{-i\phi_2}\end{pmatrix}\begin{bmatrix}\tilde{\mathcal{I}}_0(\mathbf{k})\\ \tilde{\mathcal{I}}_+(\mathbf{k}+\mathbf{k}_i)\\ \tilde{\mathcal{I}}_-(\mathbf{k}-\mathbf{k}_i)\end{bmatrix}.$$

Here we use a mixing matrix (the square matrix) with different phases for the available spectra evenly spaced between 0 and 2π. This allows us to solve for $\tilde{\mathcal{I}}_0$, $\tilde{\mathcal{I}}_+$, and $\tilde{\mathcal{I}}_-$; i.e., we unmix the SIM harmonics. The unmixed components are then recombined by shifting them so that their true zero frequency is aligned with their zero frequency in Fourier space, i.e., the k_0 setting. This yields an effective OTF extended to

frequencies beyond the original OTF's support and thus yields high resolution SIM images, i.e., fluorophore densities $S(\mathbf{r})$ (Lal, Shan, and Xi, 2016; Müller *et al.*, 2016).

Several techniques, mostly operating within the Fourier domain, unmix the SIM harmonics to reconstruct SIM images (Mudry *et al.*, 2012; Lukeš *et al.*, 2014; Lal, Shan, and Xi, 2016; Müller *et al.*, 2016; Perez, Chang, and Stelzer, 2016; Huang *et al.*, 2018; Lai-Tim *et al.*, 2019; Jin *et al.*, 2020; Christensen *et al.*, 2021; Shah *et al.*, 2021; Smith *et al.*, 2021; Cai *et al.*, 2022; Chen *et al.*, 2023; Qiao *et al.*, 2023; Saurabh, Brown *et al.*, 2023). Ideally reconstruction requires knowledge of multiple imaging system properties including the exact OTF, pattern frequency, phases, and modulation depth; see Eq. (117). Inaccurately specified properties can result in imperfect SIM reconstructions that typically exhibit well-known artifacts (Demmerle *et al.*, 2017). For instance, refractive index mismatches (see Fig. 17) may lead to repeated features along the z axis known as ghosting. Similarly, fine hexagonal "honeycomb" pseudostructures can arise when background [$\mathcal{B}$ of Eq. (116)] in 2D SIM images is neglected; a false k_0 setting impacting the OTF leads to so-called hatching, i.e., the appearance of angle-specific stripes in one or more directions.

Working in real space not only allows us to cleanly propagate uncertainty (as all data are collected in real space) but also avoids artifacts tied to Fourier domain, such as the k_0 setting. For this reason, we review SIM reconstruction in real space (Orieux *et al.*, 2012).

The total likelihood is the product of likelihoods corresponding to each phase ϕ_l and wave vector $\mathbf{k}_i$,

$$P(\bar{\bar{w}}_{1:N}|\bar{\bar{\Lambda}}_{1:N}) = \prod_{i=1}^{3}\prod_{l=1}^{3}\prod_{n=1}^{N} P(w_n^{li}|\Lambda_n^{li}), \tag{119}$$

where the double overbars represent all possible values of i and l (an overbar for each index) and $P(w_n^{li}|\Lambda_n^{li})$ is the likelihood over a single pixel. In Eq. (119) w_n^{li} and Λ_n^{li} denote the observed data and the expected photon counts over the pixel n, respectively, using an illumination with phase ϕ_l and wave vector $\mathbf{k}_i$. The expected photon count is given by [see Eqs. (3) and (4)]

$$\Lambda_n^{li} = \iint_{\mathcal{A}_n} dxdy\Lambda^{li}(\mathbf{r}), \tag{120}$$

where $\Lambda^{li}(\mathbf{r})$ is given by Eq. (117) and $\mathcal{A}_n$ is the pixel area. Assuming a high SNR and a charge-coupled device (CCD) camera noise model of Eq. (A12), we arrive at the following single-pixel likelihood:

$$P(w_n^{li}|\Lambda_n^{li}) = \text{Normal}(w_n^{li}; g\Lambda_n^{li} + o, \sigma_w^2), \tag{121}$$

where g, o, and σ_w^2 are the camera gain, offset, and readout variance, respectively; see Appendix A.

Finally, we present a Bayesian framework required in rigorous noise propagation from the SIM data (Orieux *et al.*, 2012). Within this framework, we consider priors over unknowns including the GP priors (see Sec. I.B) over the fluorophore distributions $S(\mathbf{r})$ and priors over the GP's covariance kernel $\boldsymbol{K}(\nu)$. These parameters are collectively regrouped under $\vartheta = \{S(\mathbf{r}), \nu\}$. The complete framework is described in Fig. 51.

Finally, we numerically sample the posterior to learn the unknowns ϑ. The sampling procedure is straightforward for this SIM framework, as the GP prior is conjugate to the Gaussian likelihood resulting in a closed form posterior. At low SNR, this procedure fails, as it does not accurately model photon and detector noise sources resulting in negative values over the fluorophore distribution. While GP priors can be adapted to avoid negative values at computational cost (Fazel, Jazani *et al.*, 2022), these issues have instead been addressed in recent work incorporating photon and detector noise sources applicable to both high and low SNR scenarios by avoiding GP priors altogether (Saurabh, Brown *et al.*, 2023).

The described SIM experiment combined with image reconstruction typically achieves resolutions that are up to approximately 2 times better than the diffraction limit. This is because in practice the illumination pattern is also diffraction limited, thus implying that its corresponding Fourier peaks lie within the support of the system's wide-field OTF, limiting the resolution improvement to a factor of about 2 (not considering the Stokes shift of fluorescence emission; see Sec. II). The resolution of the SIM image is then approximately $2\pi/(k_c + k_i)$ along the direction of $\mathbf{k}_i$; see Eqs. (52), (67), and (68). The process has to be repeated for at least three orientations ($\mathbf{k}_i, i = 1{:}3$) to achieve near isotropic lateral resolution enhancement.

Resolution improvement using structured illumination can also be combined with illumination modalities other than wide-field epifluorescence, thereby providing optical sectioning such as TIRF (Chung, Kim, and So, 2006), grazing incidence illumination (Guo *et al.*, 2018), or light-sheet microscopy (Chen *et al.*, 2014a; Chen *et al.*, 2022; Chang, Meza, and Stelzer, 2017).

While the previous discussion focused on 2D SIM, the principle is extended to three dimensions using three or more

Statistical Framework : SIM

Data: pixel values in ADUs

$$\bar{\bar{w}}_{1:N} = \{\bar{\bar{w}}_1, ..., \bar{\bar{w}}_N\}.$$

Parameters: fluorophore distribution, GP covariance kernel parameter (hyper-parameter)

$$\vartheta = \{S(\mathbf{r}), \nu\}.$$

Likelihood:

$$p(\bar{\bar{w}}_{1:N}|\vartheta) = \prod_{i=1}^{3}\prod_{l=1}^{3}\prod_{n=1}^{N} \text{Normal}(w_n^{li}; g\Lambda_n^{li} + o, \sigma_w^2).$$

Priors:

$$S(\mathbf{r}) \sim \text{GP}(0, \boldsymbol{K}(\nu)),$$
$$\nu \sim \text{Gamma}(\alpha_\nu, \beta_\nu).$$

Posterior:

$$P(\vartheta|\bar{\bar{w}}_{1:N}) \propto P(\bar{\bar{w}}_{1:N}|\vartheta)P(\vartheta).$$

FIG. 51. Statistical framework: SIM.

interfering beams and generating a laterally and axially varying illumination pattern (Frohn, Knapp, and Stemmer, 2001; Gustafsson *et al.*, 2008; Chang *et al.*, 2009; Shao *et al.*, 2011; Fiolka *et al.*, 2012; Heintzmann and Huser, 2017). In three-beam interference, five phase shifts are necessary to unambiguously unmix the frequencies, resulting in five SIM harmonics for all three orientations ($\mathbf{k}_i$) as opposed to three for 2D SIM; see Eq. (118). This leads to 15 SIM harmonics requiring 15 images to unambiguously unmix the harmonics. This process has to be repeated for each z position. Although more complicated than 2D SIM, 3D SIM achieves approximately twofold resolution improvement and optical sectioning as the OTF copies in 3D SIM overlap and fill the wide-field OTF's missing cone; see Fig. 12.

All SIM implementations mentioned thus far use linear fluorescence excitation. This has the advantage of being relatively gentle to living samples as low excitation intensities can be used in this approach compared to other superresolution imaging methods employing nonlinear response of fluorophores to excitation light; see Secs. II and V. While the SIM resolution improvement is restricted to approximately twofold as the illumination pattern itself is limited by diffraction, higher resolution is achievable by combining SIM with nonlinear fluorophore photophysics (Heintzmann, Jovin, and Cremer, 2002; Gustafsson, 2005); see Secs. II and V.A.

For instance, more than twofold resolution improvement was achieved by combining structured illumination with saturation of the excited-state emission, i.e., increasing the excitation intensity above a threshold where fluorophores spend a longer time in the excited state than in the ground state (Gustafsson, 2005), termed saturated SIM (SSIM). In such regimes, fluorophore responses to intensities exceeding the saturation threshold remain unchanged, and thus the effective intensity seen by fluorophores is the saturation intensity. As such, the effective intensity pattern seen by fluorophores beyond the saturation threshold start deviating from the sinusoidal pattern, i.e., the flattop sinusoidal pattern. Such distorted patterns contain more than three harmonics shifting more frequencies within the bandpass of the microscope, in contrast to sinusoidal patterns; see Fig. 49. However, the frequency unmixing now provides more displaced SIM harmonics in Fourier space that require more images to be separated. When this process was repeated at multiple orientations, SSIM achieved an isotropic lateral resolution of approximately 50 nm on fluorescent beads (Gustafsson, 2005).

Alongside higher spatial resolution comes higher computational complexity in unmixing SIM harmonics, and high intensities required for saturation prevent its use for biological imaging. Instead, photoswitchable fluorescent proteins (see Sec. II) cycling between dark and bright states at much lower intensities can be used while remaining live-cell compatible. By leveraging both dye photoswitching with structured illumination patterns, resolutions similar to SSIM are achieved (Rego *et al.*, 2012; Li *et al.*, 2015).

E. Light-sheet microscope

Optical sectioning led to the development of 3D microscopy such as light-sheet fluorescence microscopy (LSFM) (Voie, Burns, and Spelman, 1993). LSFM allows optical sectioning, i.e., increases the OTF's k_z content, by generating a thin light sheet (Power and Huisken, 2017; Olarte *et al.*, 2018; Daetwyler and Fiolka, 2023). In doing so, LSFM simultaneously both minimizes out-of-focus fluorescence otherwise present in naive wide-field microscopy (see Fig. 12) and reduces sample photodamage (Olarte *et al.*, 2018; Stelzer *et al.*, 2021).

In LSFM, illumination and light collection paths are orthogonal, providing volumetric information on the sample when axially scanning the illumination sheet; see Fig. 52 (Chakraborty *et al.*, 2019). This setup facilitates faster volumetric imaging in contrast to previously discussed point-by-point scanning; see Sec. IV.B.1. Moreover, LSFM achieves optical sectioning through illumination, in contrast to other modalities such as CLSM, where sectioning is possible only along the detection path while illuminating large portions of the specimen along the excitation path (Stelzer, 2015). Indeed, while TIRF (see Sec. IV.A) avoids this unnecessary light dose, it is restricted to volumes neighboring the illuminated surface.

In modern LSFM, there are two main approaches to generating a thin light sheet. In the first approach, a digitally scanned laser moves rapidly along a direction perpendicular to the detection axis to achieve a thin light sheet, termed DLSM (Keller and Stelzer, 2008); see Fig. 52(a). In the second approach, termed selective plane illumination microscopy (SPIM) (Huisken *et al.*, 2004), a cylindrical lens is typically used along the excitation path to form an astigmatic Gaussian beam effectively elongating the beam in one dimension to generate a thin, static light sheet; see Fig. 52(b). The SPIM OTF is provided in the right panel of Fig. 53 and obtained by convolving the SPIM light sheet's Fourier representation (the SPIM excitation OTF) in the left panel with the wide-field detection OTF in the middle panel. Compared to the wide-field OTF in Fig. 19, the resulting SPIM OTF has a larger bandpass along the z axis facilitating optical sectioning.

For the previously described Gaussian beam (Huisken *et al.*, 2004; Keller and Stelzer, 2008), LSFM's axial resolution is, as a first approximation, related to the Gaussian beam's thickness at twice the beam waist $z_{\min} = 2w_0$; see Fig. 52(c). Similarly, the FOV is related to the extent of the elongated Gaussian beam given by twice the Raleigh length $2z_r$ (Olarte *et al.*, 2018),

$$z_{\min} \approx 2w_0 = 4\frac{\lambda f}{\pi D} = \frac{2n\lambda}{\pi \mathrm{NA}}, \tag{122}$$

$$\mathrm{FOV} = 2z_r = 2\frac{\pi w_0^2}{\lambda}, \tag{123}$$

where f and D are the focal length and lens diameter, respectively, with $\mathrm{NA} = nD/2f$, which is often smaller than 0.8 for light-sheet microscopes.

The improvement in axial resolution afforded by LSFM can be made clear when the wide-field axial resolution approximately given by Eq. (122) is compared to Eq. (15), as well as differently derived in Eq. (68). According to Eqs. (122) and (123), while thinner light sheets (smaller w_0) improve axial resolution, they lead to smaller FOVs because of worsening illumination uniformity across the FOV. Such

nonuniform illuminations may also result in varying PSFs and OTFs across the FOV (Toader *et al.*, 2022).

To soften the aforementioned trade-off and achieve simultaneous high axial resolutions and large FOVs, a few attempts employing alternatives to Gaussian beams have been made including Bessel beams (Fahrbach, Simon, and Rohrbach, 2010; Planchon *et al.*, 2011), Bessel beam lattices (Chen *et al.*, 2014b; Woringer *et al.*, 2017; Liu *et al.*, 2018, 2023; Tsai *et al.*, 2020; Cao *et al.*, 2021), Airy beams (Vettenburg *et al.*, 2014; Yang *et al.*, 2014), spherically aberrated beams (Fahrbach and Rohrbach, 2010), and double beams (Zhao *et al.*, 2016). While these beams typically achieve a Raleigh length that is larger than the Gaussian beam, it is unclear in practice whether high axial resolutions and contrasts are maintained (Chang, Dean, and Fiolka, 2020; Remacha *et al.*, 2020; Shi, Daugird, and Legant, 2022; Liu *et al.*, 2023). This is because these alternative beams exhibit strong sidelobes, which leads to the contribution of glare worsening axial resolution and contrast. Moreover, owing to these sidelobes the complex form of the resulting OTF does not lend itself to resolution estimates relying on Eq. (52) or (123) (Remacha *et al.*, 2020; Shi, Daugird, and Legant, 2022).

Further efforts at rejecting the light contribution from these sidelobes combined LSFM with CLSM, SIM, and two-photon microscopy (Keller *et al.*, 2010; Palero *et al.*, 2010; Planchon *et al.*, 2011). Moreover, the concepts of reversible saturable optical fluorescence transitions (RESOLFT) (later introduced in Sec. V.A) and STED have been used in conjunction with SPIM to surpass the diffraction limit axially (Friedrich *et al.*, 2011; Hoyer *et al.*, 2016). Light-sheet illumination has also been combined with a nonlinear fluorophore response to light for SMLM (Gebhardt *et al.*, 2013; Galland *et al.*, 2015; Meddens *et al.*, 2016); see Sec. II.

Since the lateral and axial resolutions differ, to avoid anisotropic resolutions advanced LSFM configurations use multiple objectives generating different views of the specimen. These images are then computationally fused, thereby yielding improved isotropic resolution (Huisken and Stainier, 2007; Swoger *et al.*, 2007; Preibisch *et al.*, 2014; Guo *et al.*, 2020). Another approach involves axial swept light-sheet microscopy (Dean *et al.*, 2015, 2022; Chakraborty *et al.*, 2019) generating isotropic images by scanning the sample laterally, i.e., perpendicular to the detection arm, using a tightly focused light sheet synchronized by a moving camera shutter. This allows only fluorescence originating from the well-focused parts of the light sheet to reach the camera.

On the engineering front, orthogonal detection and illumination through separate objectives (see Fig. 52) pose technical challenges when one uses two bulky, high NA objectives, i.e., NA ≈ 0.8. As such, multiple modifications to conventional LSFM have been proposed. For instance, the inverted SPIM design uses two objectives (with NA $= 0.8$–1.1) at a 45° angle with respect to the cover slide (Wu *et al.*, 2011). More recently different approaches have been developed achieving illumination and fluorescent light collection using a single objective allowing use of higher NA objectives (Dunsby, 2008; Galland *et al.*, 2015; Meddens *et al.*, 2016; Sapoznik *et al.*, 2020; Yang *et al.*, 2022).

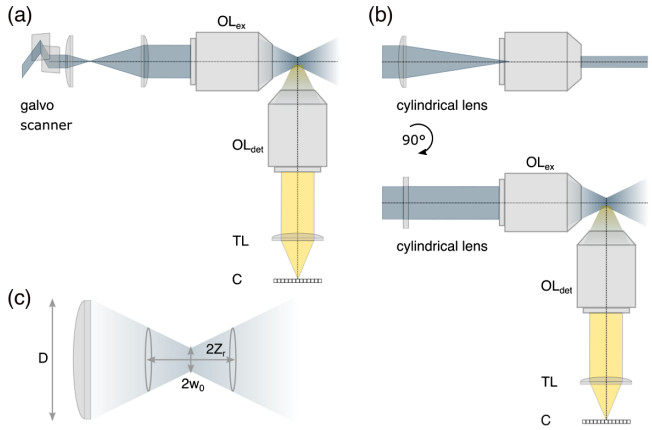

FIG. 52. LSFM setups. (a) In digitally scanned laser light-sheet microscopy (DLSM) a galvanometric (galvo) scanning unit rapidly moves a Gaussian beam perpendicular to the detection axis focused in the sample through the excitation objective lens (OL_{ex}). Signal from the focal plane is collected through the detection objective lens (OL_{det}) and tube lens (TL) onto a camera (C). (b) In SPIM, a static light sheet is formed when a cylindrical lens in the excitation path creates an elongated beam in one direction and the same perpendicular detection optics as in (a). (c) Schematic of the Gaussian beam in (a) and (b) focused through a lens or objective with a diameter D, a beam waist ω_0, and a Raleigh length z_r.

F. Multiplane microscope

To improve upon wide-field microscopy's low axial resolution, we can acquire images from multiple planes across samples. The simplest approach toward achieving this is to move the sample and focus plane with respect to each other; see Fig. 54(a). However, this involves moving a large inertial object (sample, objective, or camera) introducing time lags between planes and mechanical perturbation. Fast adaptive elements or small moving components in a more complex detection path can speed this up but do not eliminate axial scanning. Acquiring data across multiple focal planes simultaneously without moving the sample or the optical components has been achieved by introducing either refractive or diffractive optical elements into the detection arm. These elements split the fluorescent emission into multiple paths leading to simultaneous acquisitions from different focal planes (Blanchard and Greenaway, 1999; Prabhat *et al.*, 2004; Abrahamsson *et al.*, 2013; Descloux *et al.*, 2018; Mertz, 2019b). For a more in-depth review on "snapshot" volumetric microscopy, see Engelhardt and Grußmayer (2022).

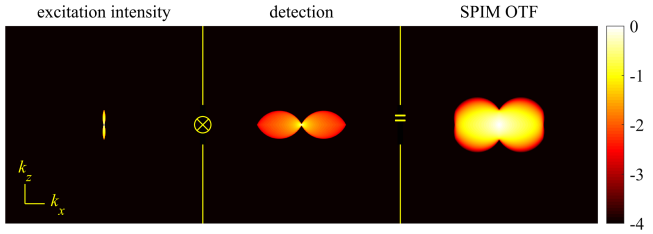

FIG. 53. SPIM OTF. Excitation is achieved by focusing a plane wave through a low-aperture lens (NA $= 0.4$) from the left, resulting in a weakly diverging horizontally elongated excitation region. See the text for further details.

Multiplane microscopy, also termed multifocus microscopy imaging, is versatile and can be combined with wide-field fluorescence or light-sheet excitation (Ma *et al.*, 2016) for a number of applications. These include SPT (Ram *et al.*, 2012; Louis *et al.*, 2020), superresolution microscopy [for statistical modeling of multiplane superresolution SMLM data, see Sec. V.C and Eqs. (135) and (136) (Hajj *et al.*, 2014; Babcock, 2018)], superresolution optical fluctuation imaging (SOFI) (Geissbuehler *et al.*, 2014; Descloux *et al.*, 2018), structured illumination (Abrahamsson *et al.*, 2017; Descloux *et al.*, 2020), and single cell and whole organism imaging (Abrahamsson *et al.*, 2013; Xiao *et al.*, 2020; Hansen *et al.*, 2021). Furthermore, phase imaging (Xiao *et al.*, 2020; Mojiri *et al.*, 2021), polarization (Abrahamsson *et al.*, 2015), and dark-field microscopy (Xiao *et al.*, 2020; Hansen *et al.*, 2021) may also use a multiplane setup.

In their simplest form, multiplane microscopes use beam splitters, i.e., refractive elements, in combination with optical detection paths of different lengths or tube lenses with different foci (Prabhat *et al.*, 2004; Geissbuehler *et al.*, 2014; Itano *et al.*, 2016; Babcock, 2018; Hansen *et al.*, 2021). In such setups, the interplane distance, and thus the axial resolution, can be independently adjusted from the pixel size (which is tied to the lateral resolution; see Sec. I.C).

However, these versatile implementations are susceptible to misalignment of the detection channels due to optomechanical component drift, which is especially relevant in superresolution microscopy; see Sec. V. A better solution involves a cascade of beam splitters fused into a single piece, i.e., a prism (Descloux *et al.*, 2018; Xiao *et al.*, 2020), dividing the fluorescent light into multiple beams traveling optical paths with different lengths; see Fig. 54(b). Here increased mechanical stability arises from having all beam splitting integrated into one optical element, i.e., the prism, minimizing chromatic aberration. This setup can also be extended to simultaneously image several colors across planes using spectral beam splitters (Gregor *et al.*, 2021).

An alternative approach uses a multifocus grating (MFG), i.e., a diffractive element, splitting fluorescence emission into multiple paths corresponding to different diffraction orders. The grating pattern is designed to introduce diffraction-order-dependent defocus phase shifts (see Sec. III.F), leading to different focal planes for each path (Blanchard and Greenaway, 1999); see Fig. 54(c). However, the grating introduces chromatic dispersion, which is improved by introducing a chromatic correction grating (CCG), and a chromatic correction prism (CCP) to reverse the dispersion due to MFG (Abrahamsson *et al.*, 2013) and separate the images laterally on the camera chip; see Fig. 54(c). While aberration-corrected multifocus microscopy grating design can further improve the imaging of thicker samples (Abrahamsson *et al.*, 2013, 2016; Hajj *et al.*, 2017), gratings have a lower transmission, and new gratings are required to alter interplane distances.

V. SUPERRESOLUTION MICROSCOPY

Resolution across fluorescence microscopy, as described in Sec. IV, is fundamentally limited by the frequency bandpass given by the corresponding OTFs. This restricts the maximum

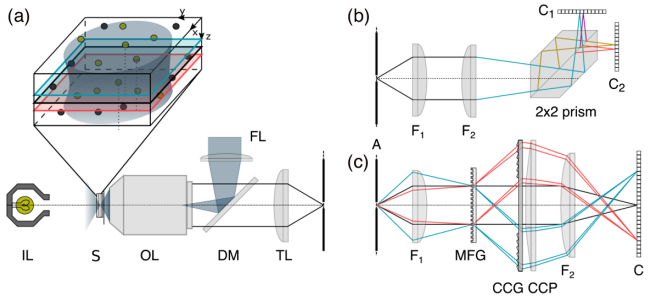

FIG. 54. Multiplane microscopy. (a) A conventional fluorescence microscope with epifluorescence (FL) and white light illumination (IL) acquire images of different focal planes across the sample by moving the objective lens (OL) and the sample with respect to each other. The nominal focal plane is shown in black, while the planes shown in red and blue can be imaged by adjusting the axial positions of the sample. Shown are the sample (S), the objective lens (OL), the dichroic mirror (DM), and the tube lens (YL). (b) A multiplane microscope relays the optical path from the intermediate image formed in the panel via a telescope with lenses of focal lengths F_1 and F_2 and uses a beam-splitting prism, i.e., a refractive element, along the detection path to separate fluorescence emission into multiple channels (here four) with different focal planes projected next to each other on two cameras ($C1$ and $C2$); see Descloux *et al.* (2018). (c) A multifocus microscope uses a multifocus grating (MFG), i.e., a diffractive element, a chromatic correction grating (CCG), and a chromatic correction prism (CCP) to achieve multiple focal planes on one camera; see the text for more details.

achievable resolution to approximately half of the emission wavelength under optimal conditions. This limit can be surpassed by exploiting the nonlinearity in fluorophore response to excitation light; see Sec. II. This in turn has led to the development of two main categories of superresolution, or nanoscopy, methods to which we now turn: (1) targeted switching and (2) stochastic switching techniques.

A. Targeted switching superresolution microscopy

1. Stimulated emission depletion microscopy

Previously introduced fluorescent imaging techniques such as confocal, light-sheet, and multiplane microscopy improve axial resolution using different optical sectioning strategies. Optical sectioning limits the collected fluorescence to an axial subset of fluorescent molecules, thereby preventing interference from fluorophores outside this axial subset. Although these techniques can significantly increase contrast and improve axial resolution, their resolution remains limited by the diffraction of light. Alternatively, superresolution methods such as STED microscopy (Hell and Wichmann, 1994; Klar, Engel, and Hell, 2001) and its generalization RESOLFT (Hofmann *et al.*, 2005; Hell, 2007) are based upon a traditional point scanning microscope with a confocal pinhole in the detection arm that allows for higher resolution imaging while retaining the axial sectioning of confocal microscopy.

STED imaging was first achieved in the mid 1990s by Hell and Wichmann (1994), and its popularity grew thanks to the high spatial resolution, relatively high imaging speed, and

considerable imaging depth. These made the visualization of biomolecular assemblies and live-cell nanoscopy possible (Hell, 2007; Eggeling *et al.*, 2015).

In terms of temporal resolution, imaging times for rapid dynamics in small fields of view as fast as a millisecond were demonstrated by ultrafast STED nanoscopy (Schneider *et al.*, 2015), while spatially the highest reported 3D isotropic resolution (<30 nm in x, y, and z simultaneously) was validated with the ultrastable design of 4Pi-based isotropic STED (Curdt *et al.*, 2015).

In STED, spatial resolution improvement is achieved by adding a second deexcitation (depletion) laser quenching fluorescence around the excitation point confining fluorescence emission to a subdiffraction-limited spot. Stimulated emission is one means by which to depopulate excited states. In this process, which was theoretically discovered by Einstein (1916), the incoming photon triggers the excited system to decay to its ground state, emitting a photon with a phase, frequency, polarization, and momentum identical to the incident photon; see Sec. II.

In STED, stimulated emission must precede spontaneous emission, requiring the excitation light to excite the sample (≈200 ps) prior to laser quenching. The whole imaging protocol is devised in two steps; see Fig. 55. First, fluorophores are excited by a diffraction-limited laser beam with a Gaussian waist (shown in green in Fig. 55). If we wait until molecules spontaneously decay without stimulated emission, no gain in resolution will be achieved. Therefore, it is necessary to introduce the second step, where a fraction of the fluorophores are depleted using a torus-shaped, or doughnut-shaped, diffraction-limited beam (shown in red in Fig. 55) whose central minimum coincides with the Gaussian excitation maximum. As such, the recorded signal originates only from the "doughnut hole" far narrower than the original Gaussian waist shown in orange in Fig. 55. To understand how STED beams are generated, see Sec. IV.B.1 and Fig. 28.

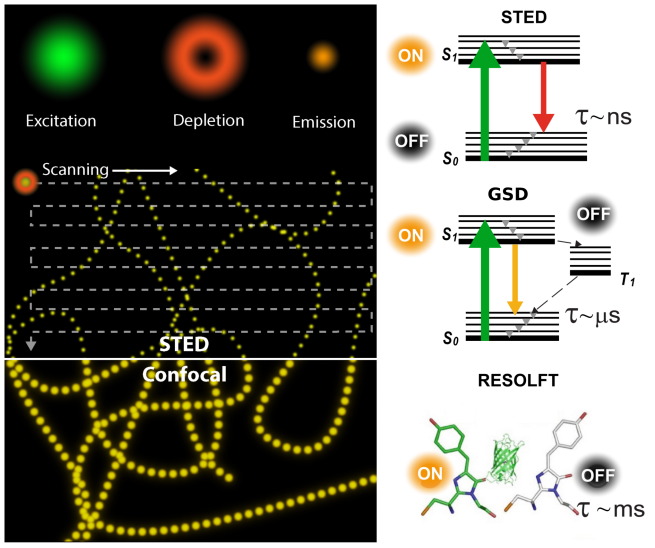

FIG. 55. Schematics for STED imaging. Excitation and depletion beams are used to acquire a subdiffraction-limited image, formed after raster scanning the full sample. The resulting image can be understood as a convolution between the effective PSF formed from the excitation and depletion laser beams and the fluorescent molecule distribution in the sample. Left panel: schematics comparing diffraction-limited confocal images of microtubules with the coinciding STED image. Right panels: electronic transitions of excitation, and stimulated emission in STED (top panel), ground-state depletion GSD (middle panel), and RESOLFT (bottom panels).

The resolution gain y_{STED} in STED set by the inner doughnut radius is given by

$$y_{\mathrm{STED}} = \frac{\lambda}{2\mathrm{NA}\sqrt{1 + I/I_{\mathrm{sat}}}} = \frac{y_{\min}}{\sqrt{1 + I/I_{\mathrm{sat}}}}. \quad (124)$$

In Eq. (124) $y_{\min}$ is the wide-field resolution [see Eq. (14)], I is the depletion laser intensity, and I_{sat} is the depletion intensity required to outperform the fluorescence emission.

Although STED's resolution can theoretically be arbitrarily small provided that there is high enough depletion intensity ($I \to \infty$) (Pawley, 2006), in practice factors limiting resolution include the nature of the fluorophores used (and their absorption cross section of the depletion beam), uncorrected aberrations (residual aberration) of the STED pattern, SNR, and the STED beam's relatively high power and propensity for label photodamage.

Photodamage can be mitigated by working with solid-state fluorescent nanodiamonds hosting negatively charged nitrogen-vacancy point defects. Using such photostable labels, resolutions of ≈10 nm were demonstrated (Wildanger *et al.*, 2009; Arroyo-Camejo *et al.*, 2013). However, the complex functionalization of relatively large size 10–15 nm solid-state probes, including issues related to specificity and cell permeability, limit their applications, especially in live-cell imaging.

While we have focused on two dimensions thus far using interference of two depletion beams (see the implementation of 4Pi microscopy introduced in Sec. IV.B.3), STED superresolution imaging has been extended to three dimensions (Wildanger *et al.*, 2012; Osseforth *et al.*, 2014), though in practice axial resolution gain comes at the cost of lower lateral resolution.

2. Reversible saturable optically linear fluorescence transition microscopy

Numerous efforts in the past two decades have been undertaken to improve upon STED's need for high power depletion beams (Eggeling *et al.*, 2015). RESOLFT, a more general method encompassing STED as a special case, was one such effort proposed in the early 2000s that leveraged fluorophore photophysics (Hell, 2007). This in turn renders RESOLFT more appropriate for live-cell and long-term experiments (Hofmann *et al.*, 2005) including 3D live-cell imaging using a recent implementation of highly parallelized image acquisition with an interference pattern (Bodén *et al.*, 2021).

In contrast to STED, whose high laser power is required to deplete the excited state back to the ground state, RESOLFT uses doughnut-shaped beams to transition fluorophores into any dark state, not just the ground state; see Fig. 55. Thus, RESOLFT requires fluorophores controllably switchable

between dark (*off*), and bright (*on*) states; see Fig. 55. For instance, such fluorophores include reversibly switchable fluorescent proteins and dyes (Grotjohann *et al.*, 2012; Pennacchietti *et al.*, 2018).One such dark state is the triplet state (see Sec. II) at the basis of ground-state depletion (GSD) (Hell and Kroug, 1995), a special case of RESOLFT requiring less intense depletion laser powers; see Fig. 55.

3. Minimal photon fluxes

Owing to the limited photostability of fluorophores, for example, due to photobleaching, first generation nanoscopy methods such as STED and RESOLFT reached practical resolution limits of 20–40 nm. This led to the development of a second generation of fluorescence nanoscopy techniques achieving 1–10 nm resolutions that leveraged patterned illumination (Balzarotti *et al.*, 2017; Gu *et al.*, 2019; Reymond *et al.*, 2019; Cnossen *et al.*, 2020; Jouchet *et al.*, 2021; Masullo, Lopez, and Stefani, 2022; Masullo *et al.*, 2022).

The first implementations of such nanoscopy techniques include minimal photon fluxes (MINFLUX), introduced in 2017 (Balzarotti *et al.*, 2017) which extracts information from a limited photon budget and uses minimal laser intensities (Balzarotti *et al.*, 2017; Eilers *et al.*, 2018; Gwosch *et al.*, 2020). In contrast to STED, MINFLUX uses a doughnut-shaped beam for excitation with the intensity minimum at its center. To illustrate the MINFLUX concept, we assume here a single fluorophore as shown in Fig. 56. The excitation beam is scanned across the sample and the fluorescence signal is collected by a confocal microscope. The number of collected photons depends on the excitation intensity received by the fluorophore and can be used to calculate the fluorophore's distance from the beam's center. For instance, fluorophores precisely at the doughnut-shaped beam center have minimal emission. However, as the exact fluorophore's location is unknown, the beam scans the area at a few locations (see Fig. 56), and the fluorophore's distance from the beam center's locations (designated as blue dots in Fig. 56) are calculated to pinpoint the fluorophore with nanometer precision.

Recently MINFLUX was used to simultaneously perform 3D and multicolor imaging (Gwosch *et al.*, 2020) while achieving high isotropic localization precision (1–3 nm). In addition, MINFLUX was used in SPT (Eilers *et al.*, 2018; Pape *et al.*, 2020) while localizing with a precision below 20 nm within ≈100 μs (Schmidt *et al.*, 2021).

The concept of localizing with respect to patterned illumination has also been implemented using wide-field microscopy for faster imaging substituting doughnut-shaped illumination with other illumination patterns (Gu *et al.*, 2019; Cnossen *et al.*, 2020; Jouchet *et al.*, 2021). For instance, in SIMFLUX fluorophore locations are realized with respect to a sinusoidal pattern (Cnossen *et al.*, 2020).

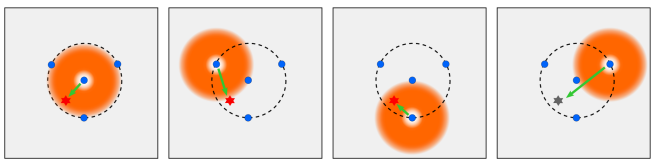

FIG. 56. MINFLUX's working principle. MINFLUX employs a doughnut-shaped excitation beam (orange) with the doughnut translated to four locations (blue circles) at which fluorescence signals are measured and used to determine the fluorophore's position. The red and black stars indicate the excited- and ground-state fluorophores, respectively; see the text for details.

B. Stochastic switching superresolution microscopy

Previously we described superresolution methods based on a targeted switching of fluorophores. Here we discuss single-molecule-based superresolution methods, a family of superresolution techniques achieving subdiffraction resolution by imaging independent and stochastically blinking fluorophores over time (Sigal, Zhou, and Zhuang, 2018; Schermelleh *et al.*, 2019; Lelek *et al.*, 2021). In these methods, the gain in spatial resolution is traded for temporal resolution as the acquisition of many camera frames is required to computationally reconstruct a single superresolved image. In such experiments, a conventional wide-field microscope is typically used to collect fluorescent light from (photo)activatable or switchable probes; see Sec. II.A. Moreover, scanning image acquisitions (York *et al.*, 2011; Vangindertael *et al.*, 2015) and light-sheet microscopy (Galland *et al.*, 2015; Meddens *et al.*, 2016) have also been successfully used to implement superresolution microscopy.

The most common use of stochastic switching is applied to techniques termed SMLM (Lelek *et al.*, 2021). In SMLM, spatially overlapping fluorophores are temporally separated by acquiring image frame sequences. As in each frame only a few fluorophores switch on (< 1%), high precision localization is achieved by avoiding overlapping PSFs; see Fig. 2. The set of nanometer-resolved localizations are then used to reconstruct superresolved structures; see Fig. 57.

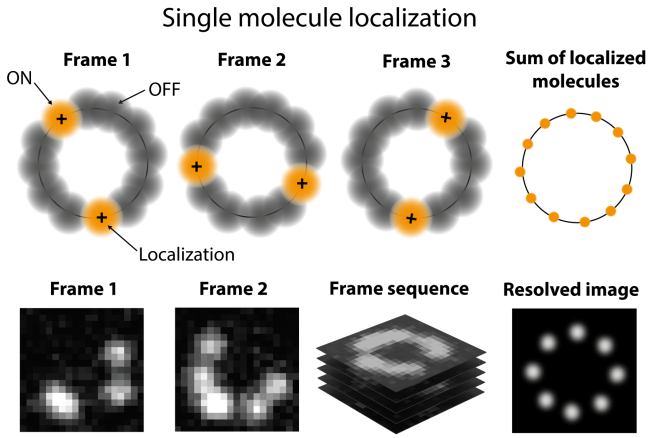

FIG. 57. Single emitters are stochastically activated to become fluorescent. The activated emitters can be precisely localized provided that they are spaced farther apart than the Nyquist limit; see Sec. I.C. The process is repeated for tens of thousands of frames. In each frame, single emitters are identified and fitted to obtain their center of mass, allowing superresolved pointillistic image reconstruction (bottom right panel). Repetitive activation, localization, and deactivation temporally separate spatially unresolved structures in a reconstructed image, with the apparent resolution gain compared to the standard diffraction-limited image (bottom row).

SMLM methods, however, require localizing by chance well-separated molecules, thereby imposing long data acquisition times. Therefore, more recently a range of alternative techniques were developed to improve image resolution while not identifying or localizing single molecules (Opstad *et al.*, 2020; Pawlowska *et al.*, 2022). Rather, such methods analyzed fluctuations in fluorescence emission over time and tolerated a wider range of switching behavior and imaging conditions including SOFI (Dertinger *et al.*, 2009; Dertinger, Heilemann *et al.*, 2010) (see Appendix C), as well as Bayesian analysis of blinking and bleaching (3B analysis) (Cox *et al.*, 2012), superresolution radial fluctuations (Gustafsson *et al.*, 2016), sparsity-based superresolution correlation microscopy (Solomon *et al.*, 2018), mean-shift superresolution (Torres-García *et al.*, 2022), and deblurring by pixel reassignment (Zhao and Mertz, 2023). A common feature of fluctuation-based techniques is that they provide lower resolutions than SMLM methods despite requiring fewer input frames, as well as lower laser powers than SMLM, making them more live-cell compatible.

1. Single-molecule localization microscopy

Almost a decade preceding its experimental realization (Lidke *et al.*, 2005; Betzig *et al.*, 2006), the idea underlying SMLM was theoretically proposed by Betzig (1995), who employed experimental implementations with photoactivatable genetically encoded proteins (Lippincott-Schwartz and Patterson, 2009) and quantum dots (Lidke *et al.*, 2005).

An initial iteration termed fPALM (Betzig *et al.*, 2006; Hess, Girirajan, and Mason, 2006) was followed by STORM (Rust, Bates, and Zhuang, 2006), which exploits photoswitching in organic dyes. While differing only in their means to achieve temporal separation of spatially overlapping fluorophores, PALM leverages photoactivatable or photoconvertible fluorescent proteins (Shroff *et al.*, 2008), allowing for genetic expression of fluorescent proteins. PALM is compatible with live-cell imaging (Shroff *et al.*, 2008), and thus the stoichiometric labeling of target proteins used in the counting (Rollins *et al.*, 2015; Bryan, Sgouralis, and Pressé, 2022). Conversely, organic fluorophore photon emission rates are typically higher than those for photoactivatable or photoconvertible fluorescent proteins, resulting in STORM's slightly better resolution. Further resolution improvements spurred the development of the more general dSTORM, which introduced a pallet of synthetic organic fluorophores as photoswitchable probes (Heilemann *et al.*, 2008), thereby allowing live-cell imaging with site-specific tagging (Wombacher *et al.*, 2010).

A more recent SMLM approach termed DNA point accumulation for imaging in nanoscale topography (PAINT) employs stochastic transient binding of diffusing dyes in solution with a complementary molecules binding to the target structure (Schnitzbauer *et al.*, 2017); see Fig. 58. Upon binding, the dye molecule is temporally immobilized and is detected by the camera, while the freely diffusing dyes, which are strongly aliased and difficult to track, are approximately treated as background. Longer imager strands, increasing binding time, typically lead to higher photon numbers over one binding event and an improved SNR alongside higher spatial resolutions; see Fig. 58(b). DNA

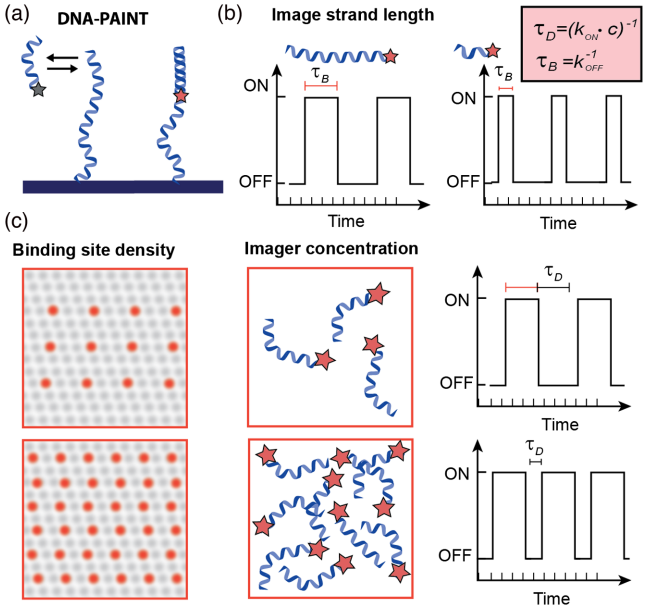

FIG. 58. Imaging with DNA PAINT. (a) Schematics illustrate DNA PAINT where dye-conjugated oligo (imager oligo) transiently hybridizes with a complementary (docking) oligo. (b) The binding time τ_B (or the dissociation rate $1/\tau_B$) depends on the imager strand length. (c) Increasing either imager strand concentration or docking site density decreases the dark times τ_D (interevent lifetime). Adapted from Schnitzbauer *et al.*, 2017.

PAINT exhibits limited photobleaching, as imaging can be continued as long as diffusing dyes are present in the solution, and is furthermore compatible with multiplexing using color and assortment of DNA strands' lengths (Jungmann *et al.*, 2014; Wade *et al.*, 2019; Strauss and Jungmann, 2020).

2. SMLM data analysis

In SMLM, data $w_{1:N}$ typically consist of a set of pixel values (observation) organized as 2D arrays, called image frames. Localizations are then probabilistically determined from pixel values w_n using a likelihood.

To build the likelihood, we begin with the expected photon counts for the pixel n, which are given as

$$\Lambda_n = \mathcal{B} + \sum_{m=1}^{\infty} b_m I_m \mathcal{P}_m^n, \tag{125}$$

where we have immediately generalized our model to the practical case with unknown emitter numbers. That is, we adopt a nonparametric framework with an infinite number of emitters ($m = 1:\infty$) with load b_m associated with each emitter; see Sec. I.B. The loads associated with the emitters not contributing photons are, as usual, recovered as zero. Moreover, I_m and $\mathcal{B}$ represent the intensity of the mth emitter and the uniform background, respectively. Here $\mathcal{P}_m^n$ is the probability of a photon from an emitter m reaching a pixel n given by [see Eqs. (3) and (4)]

$$\mathcal{P}_m^n = \iint_{\mathcal{A}_n} dxdy\, U(x, y; \mathbf{r}_m), \tag{126}$$

where $\mathcal{A}_n$ is the pixel area and $\mathbf{r}_m = (x_m, y_m, z_m)$ is the emitter position. As a simplification, the PSF is sometimes substituted for its value evaluated at the middle of the pixel (Agarwal and Macháň, 2016) or the integral can be evaluated using error functions, say, for Gaussian PSFs. For more complicated cases (engineered PSFs in Sec. V.C), the PSF appearing in the integral of Eq. (126) can also be numerically evaluated over a subpixel grid. Further improvements are also possible using linear or spline PSF interpolations (Liu *et al.*, 2013; Li *et al.*, 2018) between PSF values typically calibrated at select axial positions.

Here we assume a CCD camera (see Appendix A) and arrive at the following likelihood for the pixel n:

$$P(w_n|\vartheta) = \text{Normal}(w_n; g\Lambda_n(\vartheta) + o, \sigma_w^2), \tag{127}$$

where g, o, and σ_w^2 are the detector gain, offset, and variance, respectively. As before, we collect all unknown parameters in $\vartheta = \{\bar{b}, \bar{\mathbf{r}}, \bar{I}, \mathcal{B}\}$, where the overbar denotes quantities over all emitters. Finally, since pixel values are i.i.d (see Sec. I.B), the likelihood of a ROI containing N pixels assumes a product form

$$P(w_{1:N}|\vartheta) = \prod_{n=1}^{N} P(w_n|\vartheta). \tag{128}$$

In parametric frameworks, the likelihood from Eq. (128) is simplified given the known emitter numbers M,

$$\Lambda_n = \mathcal{B} + \sum_{m=1}^{M} I_m \mathcal{P}_m^n. \tag{129}$$

In such frameworks, the number of emitters are typically heuristically set separately using alternate criteria such as Bayesian information criteria (Quan *et al.*, 2011), thresholding (Babcock, Sigal, and Zhuang, 2012), etc. (Huang *et al.*, 2011; Fazel and Wester, 2022). In contrast, in joint (nonparametric) optimization the number of active emitters are treated as random variables (unknowns) on which we place priors (Jazani *et al.*, 2019, 2022). In other words, we obtain the BNP posterior from the product of the likelihood equation (128) and the priors over ϑ; see Sec. I.B. We adopt an empirical prior for fluorophore intensity obtained by fitting isolated emitters from sparse regions of the data (Fazel *et al.*, 2019; van Dijk *et al.*, 2023) and adopt computationally convenient beta-Bernoulli process priors for the loads; see Sec. I.B.

In the review we have discussed the localization of emitters using information from one frame, though leveraging information across frames improves spatial resolution by increasing the photon budget available for analysis. The challenge with using multiple frames is that several low-quality putative localizations, if performed in each frame, must then be linked across frames to improve high resolution localization. This essentially becomes equivalent to the problem of single-molecule tracking dealt with later in this section, where molecule number determination alongside localization and linking are performed simultaneously and self-consistently. However, to avoid computational overhead a method termed the Bayesian grouping of localizations (BaGoL) (Fazel *et al.*, 2022) uses frame-to-frame localization to identify which localizations belong to which emitter. Further, BaGoL efficiently accomplishes subnanometer precision under dense labeling conditions by removing nanometer residual drift within the input data and combining the set of identified localizations from each emitter (Fazel *et al.*, 2022). The idea of combining localizations to improve precision has been also employed in conjunction with orthogonal DNA sequences to achieve angstrom resolutions (Reinhardt *et al.*, 2023).

Having focused on static emitters thus far, we now broaden our discussion to mobile emitters, namely, tracking emitters across frames. In SPT, data consist of N pixel values for each frame $k = 1{:}K$ that are denoted by $w_{1:N}^{1:K} = \{w_1^1, w_2^1, \ldots, w_N^1, w_1^2, \ldots, w_N^K\}$. The parameter set ϑ is now expanded to include particle trajectories across time $\mathbf{r}_m(t)$ for each m particle. By approximation, these can be reduced to locations across frames $\mathbf{r}_m^{1:K}$, though in full generality positions can be interpolated for any interframe time (Kilic, Sgouralis, and Pressé, 2021; Sgouralis *et al.*, 2023; Xu, Sgouralis *et al.*, 2023).

To obtain the SPT likelihood, as in SMLM we start with the expected photon count per pixel. As particles evolve over each exposure, the expected photon count for a pixel n in a frame k $[\Lambda_n^k(\vartheta)]$ follows from Eq. (125) (Sgouralis *et al.*, 2023; Xu, Sgouralis *et al.*, 2023),

$$\Lambda_n^k(\vartheta) = \mathcal{B} + \sum_{m=1}^{\infty} b_m \int_{\text{exposure}_k} dt \mu(t) \mathcal{P}_m^n(t). \tag{130}$$

In Eq. (130) $\mathcal{P}_m^n(t)$ is adapted from Eq. (126) with a time-dependent location and $\mu(t)$ is the time-dependent

Statistical Framework : SMLM

Data: pixel values in ADUs

$$w_{1:N} = \{w_1, ..., w_N\}.$$

Parameters: loads, fluorophore locations, intensities, background

$$\vartheta = \{\bar{b}, \bar{\mathbf{r}}, \bar{I}, \mathcal{B}\}.$$

Likelihood:

$$P(w_{1:N}|\vartheta) = \prod_n \text{Normal}(w_n; g\Lambda_n(\vartheta) + o, \sigma_w^2).$$

Priors:

$$\begin{aligned} q_m &\sim \text{Beta}(A_q, B_q), \ m = 1:\infty, \\ b_m &\sim \text{Bernoulli}(q_m), \\ \mathbf{r}_m &\sim \text{Uniform over FOV}, \\ I_m &\sim \text{Empirical}, \\ \mathcal{B} &\sim \text{Gamma}(\alpha_{\mathcal{B}}, \beta_{\mathcal{B}}). \end{aligned}$$

Posterior:

$$P(\vartheta|w_{1:N}) \propto P(w_{1:N}|\vartheta)P(\vartheta).$$

FIG. 59. Statistical framework: SMLM.

fluorescence emission rate, for example, due to blinking. The time integral of Eq. (130) is stochastic, and numerical integration is often used in its evaluation. Under slow dynamics, for simplicity we can approximate the integrand as a constant resulting in Eq. (126) (Cheezum, Walker, and Guilford, 2001). This approximation fails due to motion blurring artifacts, i.e., aliasing, when particles diffuse rapidly compared to the camera frame rate or exposure time (Wong, Lin, and Ober, 2011; Michalet and Berglund, 2012).

As an alternative, an improved approximation is afforded by the trapezoidal rule

$$\Lambda_n^k(\vartheta) = \mathcal{B} + \sum_{m=1}^{\infty} b_m \sum_{l=1}^{L-1} \frac{\delta t}{2} [\mu_m(t_l^k)\mathcal{P}_m^n(t_l^k) + \mu_m(t_{l+1}^k)\mathcal{P}_m^n(t_{l+1}^k)], \tag{131}$$

with

$$\mathcal{P}_m^n(t_l^k) = \int\int_{\mathcal{A}_n} dxdy U(x, y; \mathbf{r}_m(t_l^k)). \tag{132}$$

In Eqs. (131) and (132) t_1^k represents the beginning of the exposure for frame k, while t_L^k represents its end. The entire exposure period δT is divided into $L-1$ equal panels of a length $\delta t = \delta T/(L-1)$. A motion model, be it free diffusion or any other, can be introduced to connect positions $\mathbf{r}_m(t_{l+1}^k)|\mathbf{r}_m(t_l^k) \sim \text{Normal}(\mathbf{r}_m(t_l^k), 2D\delta t)$, where D is the diffusion coefficient of the emitters, assuming that they all satisfy the same diffusive dynamics.

Though diffusion models are most commonly invoked, alternative models such as anomalous diffusion are also used (Muñoz-Gil *et al.*, 2021). It remains to be seen, however, whether alternative models can be useful in light of the approximations that have often already been made in the analysis, including but not limited to often assuming a number of emitters by hand (Tinevez *et al.*, 2017), a time-independent integrand in Eq. (130), general corrupting noise from the photon count and detectors (Tinevez *et al.*, 2017), and multiple other error sources.

The emission rates μ_m of the emitters can also be described using Markovian models (Rollins *et al.*, 2015; Bryan, Sgouralis, and Pressé, 2022); see Sec. II. However, for simplicity we assume that all emitters maintain the same brightness throughout all frames, thus resulting in the simplification of Eq. (131) to

$$\Lambda_n^k(\vartheta) = \mathcal{B} + \mu \sum_{m=1}^{\infty} b_m \sum_{l=1}^{L-1} \frac{\delta t}{2} [\mathcal{P}_m^n(t_l^k) + \mathcal{P}_m^n(t_{l+1}^k)].$$

Again assuming for simplicity a CCD camera noise model (see Appendix A), the likelihood for pixel n in frame k reads

$$P(w_n|\vartheta) = \text{Normal}(w_n^k; g\Lambda_n^k(\vartheta) + o, \sigma_w^2). \tag{133}$$

As with the SMLM likelihood of Eq. (128), the likelihood of the frame sequence is

$$P(\vartheta|w_{1:N}^{1:K}) = \prod_n \prod_k P(\vartheta|w_n^k). \tag{134}$$

By explicitly specifying all terms in Eq. (134), we see that ϑ now includes $\vartheta = \{\bar{b}, \bar{\mathbf{r}}(t_{1:L}^{1:K}), \mu, \mathcal{B}, D\}$, where an overbar denotes the set of all emitters. Sampling of the resulting posterior is outlined in Fig. 60 (Sgouralis *et al.*, 2023; Xu, Sgouralis *et al.*, 2023).

We do highlight that the unknowns parametrically exclude the loads $\vartheta = \{\bar{\mathbf{r}}(t_{1:L}^{1:K}), \mu, \mathcal{B}, D\}$, and the number of trajectories (emitters) are individually estimated with *ad hoc* metrics (Tinevez *et al.*, 2017). In contrast, nonparametrically trajectories and emitter numbers are jointly estimated alongside other parameters (Jazani *et al.*, 2019, 2022; Sgouralis *et al.*, 2023; Xu, Sgouralis *et al.*, 2023).

We note that this tracking reveals the z position only up to a mirror symmetry above or below the focal plane when using a single illumination plane. Thus, here a note is warranted regarding 3D SMLM. In standard SMLM, localizing the molecule's position along the axial direction is challenging due to the limited depth of field and symmetry of the wide-field PSF with respect to the focal plane, i.e., the lack of optical sectioning; see Sec. III.C. Multiple approaches have been employed to address these issues, including multiplane microscopy (see Sec. IV.F) and PSF engineering (Huang *et al.*, 2008; Pavani *et al.*, 2009; Lew *et al.*, 2011; Shechtman *et al.*, 2014), which is detailed in Sec. V.C.

Statistical Framework : Tracking

Data: pixel values in ADUs

$$w_{1:N}^{1:K} = \{w_1, \ldots, w_N^K\}.$$

Parameters: loads, fluorophore trajectories, emission rate, background, diffusion coefficient

$$\vartheta = \{\bar{b}, \bar{\mathbf{r}}(t_{1:L}^{1:K}), \mu, \mathcal{B}, D\}.$$

Likelihood:

$$P(w_{1:N}^{1:K}|\vartheta) = \prod_{n=1}^{N}\prod_{k=1}^{K} \text{Normal}(w_n^k; g\Lambda_n^k(\vartheta)+o, \sigma_w^2).$$

Priors:

$$\begin{aligned} q_m &\sim \text{Beta}(A_q, B_q), m = 1:\infty \\ b_m &\sim \text{Bernoulli}(q_m), \\ \mathbf{r}_m(t_1^1) &\sim \text{Normal}(\mathbf{r}_0, \sigma_{\mathbf{r}}^2), \\ \mathbf{r}_m(t_{l+1}^k)|\mathbf{r}_m(t_l^k) &\sim \text{Normal}(\mathbf{r}_m(t_l^k), 2D\delta t), \\ \mu &\sim \text{Gamma}(\alpha_\mu, \beta_\mu), \\ \mathcal{B} &\sim \text{Gamma}(\alpha_\mathcal{B}, \beta_\mathcal{B}), \\ D &\sim \text{InvGamma}(\alpha_D, \beta_D). \end{aligned}$$

Posterior:

$$P(\vartheta|w_{1:N}^{1:K}) \propto P(w_{1:N}^{1:K}|\vartheta) P(\vartheta).$$

FIG. 60. Statistical framework: tracking.

C. PSF engineering

To overcome the limited optical sectioning of SMLM imposed by wide-field PSFs (see Sec. III.C), engineered PSFs have been used to intentionally introduce aberrations. This typically involves inserting extra optical components into the setup (Huang *et al.*, 2008) or an adaptive optical element such as a deformable mirror (Izeddin *et al.*, 2012) at the Fourier plane; see Fig. 1 (Pawley, 2006; Backer and Moerner, 2014; Shechtman *et al.*, 2014). The resulting aberrations break the PSF's axial symmetry and thereby encode axial positions of molecules used in 3D localization (Siemons *et al.*, 2020).

Most initial efforts in PSF engineering coincide with PSFs maintaining their shape throughout defocus. One of the earliest PSF engineering applications reduced in-focus spot sizes at the cost of larger sidelobes. This was achieved by implementing a series of amplitude and phase rings in the Fourier plane (Di Francia, 1952). As another example toward achieving extended depth of field (EDOF) a cubic phase mask was used, thereby leading to a PSF minimally changing over a desired axial range (Dowski and Cathey, 1995); see Fig. 61(a). While maintaining EDOF, other improvements were aimed at reducing the required computation and raising the SNR, for example, the log-asphere lens (Chi and George, 2001), Bessel beams (McGloin and Dholakia, 2005), etc. (Ben-Eliezer *et al.*, 2003).

Recently PSFs have been engineered, either heuristically or algorithmically (more details later), to provide improved axial resolutions across different experimental conditions (von Diezmann, Shechtman, and Moerner, 2017) such as emitter density and wavelength. That is, at the other extreme end of design space where PSFs remain similar throughout defocus there are PSFs that are intentionally sensitive to defocus. The purpose of such z-encoding PSFs is to encode axial information (depth) in their shape, thus enabling 3D tracking or imaging (von Diezmann, Shechtman, and Moerner, 2017).

An early instance of z-encoding PSF engineering is induced astigmatism, typically implemented with a cylindrical lens, for evaluations of defocus in compact disc players (Kao and Verkman, 1994), an idea adapted for SMLM (Huang *et al.*, 2008). The astigmatic PSF provides high axial resolution over an axial range of ≈ 1 μm.

Following similar ideas, larger axial ranges were attained using rotating PSFs, based on a linear combination of Laguerre-Gaussian functions (Schechner, Piestun, and Shamir, 1996) that was later adapted to SMLM using the double helix PSF (Pavani *et al.*, 2009). In contrast to wide-field PSFs that spread signal over a large area, resulting in low SNRs away from the focus (see the first row in Fig. 61), multiple 3D engineered PSFs have been designed including the corkscrew (Lew *et al.*, 2011), self-bending beams (Jia, Vaughan, and Zhuang, 2014), tetrapods (Shechtman *et al.*, 2014), etc. (Baddeley, Cannell, and Soeller, 2011; Prasad, 2013). These often attain high resolutions over wider axial ranges and maintain high SNR even at greater defocus.

Several examples of engineered phase masks, i.e., phases intentionally added to the Fourier plane phase (the Fourier plane phase is sometimes also termed the pupil phase), and associated PSFs are shown in Fig. 61. We show both PSFs maintaining their shapes over a wide axial range and those encoding the axial location in their shapes.

We now turn to the question of how we can design phase masks to engineer a desired PSF shape, for example, a PSF maintaining high axial resolution or a high SNR over a wide range. This requires first finding the relation between the measured PSF and the phase mask at the Fourier plane.

To address this, we note the relation between the field at the Fourier plane and the measured PSF intensity, as described in Eqs. (63) and (70). Indeed, the measured PSF intensity contains a Fourier transform of the electric field and an absolute value operation, resulting in the loss of image plane phase information. As such, the problem of recovering the Fourier plane phase, i.e., the pupil phase $\Phi(\theta', \phi)$ [see Eq. (70)], at the heart of PSF engineering is known as phase retrieval (Shechtman *et al.*, 2015). The phase retrieval problem in our context involves estimating the pupil phase $\Phi(\theta', \phi)$ from the measurements $w_{1:N}$ encoding the real space PSF through, for example, detector models such as Eq. (A9). This ill-posed nonconvex optimization presents various challenges, including degenerate solutions and unstable derivatives (Shechtman *et al.*, 2015). As it is impossible to determine the phase using data from one plane, i.e., a single PSF slice, we use data from several planes (a z stack) acquired, for example, by scanning the objective to capture slices of a fluorescent bead's PSF or using a multiplane setup; see Sec. IV.F.

Following the logic presented on an SMLM data analysis, to construct a likelihood we write the expected photon count $\Lambda_n^q(\vartheta, \Phi)$ for a pixel n at a plane q of the z stack, encoding the pupil phase Φ information. For simplicity, we consider a single fluorophore here.

Using this model, a likelihood can be constructed given the data $w_n^q, n = 1{:}N, q = 1{:}Q$, as in Eqs. (127) and (128). Working for convenience with the log-likelihood function, we write the z-stack log-likelihood function as

$$\mathcal{L}(w_{1:N}^{1:Q}; \vartheta, \Phi) = \sum_{n=1}^{N} \sum_{q=1}^{Q} \ell(w_n^q; \vartheta, \Phi), \tag{135}$$

where $\ell(w_n^q; \vartheta, \Phi)$ is the log-likelihood function of a pixel n within a plane q. In the most general case, the detector and shot noise must both be simultaneously considered, as in Eq. (A9). However, ignoring the detector noise for now, we arrive at the single-pixel log-likelihood function used in Eq. (135),

$$\ell(w_n^q; \vartheta, \Phi) = \Lambda_n^q(\vartheta, \Phi) - w_n^q \log [\Lambda_n^q(\vartheta, \Phi)]. \tag{136}$$

To maximize the likelihood in Eqs. (135) and (136), we employ iterative optimization, often relying on knowledge of the likelihood's gradient with respect to the phase (Smith *et al.*, 2016; Ferdman *et al.*, 2020),

$$\frac{\partial \ell}{\partial \Phi} = \frac{\partial \ell}{\partial \Lambda_n^q} \frac{\partial \Lambda_n^q}{\partial \Phi}. \tag{137}$$

The first term on the right-hand side of Eq. (137) can be analytically evaluated as $\partial \ell / \partial \Lambda_n^q = 1 - w_n^q / \Lambda_n^q$. The next term

involves the derivative of the PSF model Λ_n^q with respect to the pupil phase Φ_l, where in practice we discretize the set of spatial frequencies in the Fourier plane $l = 1:L$ and write

$$\frac{\partial \Lambda_n^q}{\partial \Phi_l} = 2\Re\left(\frac{\partial E_n}{\partial \Phi_l} E_n^*\right). \tag{138}$$

In Eq. (138) E_n is the given electric field in the image plane from Eq. (63), $\Re$ indicates the real portion of the expression within the parentheses, and $\partial E_n/\partial \Phi_l$ and $\partial \Lambda_n^q/\partial \Phi_l$ are complex and real matrices of size $N \times L$, respectively.

Finally, we must evaluate $\partial E_n/\partial \Phi_l$. The electric field in the image plane is obtained via a Fourier transform of the electric field in the Fourier plane (designated by $E_{\tilde{l}}'$) that also contains the pupil phase Φ,

$$\frac{\partial E_n}{\partial \Phi_l} = \frac{\partial}{\partial \Phi_l} \mathcal{F}_{\tilde{l}}[E_{\tilde{l}}'] = i \exp\left(\frac{-i2\pi nl}{M}\right) E_{\tilde{l}}' \delta_{l,\tilde{l}}, \tag{139}$$

where $\mathcal{F}_{\tilde{l}}$ is a discrete Fourier transform operation over an index $\tilde{l}$ and $\delta_{l,\tilde{l}}$ is a Kronecker delta. Finally, if $L = N$, the summation over n of Eq. (135) and the exponential of Eq. (139) can be evaluated as a compact Fourier transform providing the desired derivative,

$$\frac{\partial \mathcal{L}}{\partial \Phi_l} = 2\Re\left[E_l' \mathcal{F}_n\left(iE_n^* \frac{\partial \mathcal{L}}{\partial \Lambda_n^q}\right)\right]. \tag{140}$$

The previously described approach can be used either to learn the pupil phase producing a measured PSF or, equivalently, to design a PSF and learn the required pupil phase.

In the realm of a high SNR, it is also common to approximate the likelihood equation (135) via a Gaussian distribution and use least squares minimization to determine the pupil phase. The approximate log-likelihood function can then be minimized using iterative optimization, for example, the Gerchberg-Saxton algorithm or one of its variants (Gerchberg, 1972; Fienup, 1978), possibly estimated over a constrained Zernike polynomial set (Liu *et al.*, 2013; Petrov, Shechtman, and Moerner, 2017).

After describing the approach to derive the pupil phase for a given PSF shape, we turn to the problem of seeking an optimal PSF shape following predefined metrics. The engineered PSFs of Fig. 61 represent the result of various optimization metrics and numerical approaches. For instance, different PSFs exhibit different CRLBs (Badieirostami *et al.*, 2010); CRLB optimization on the phase mask expanded in terms of Zernike polynomials yields the tetrapod PSF (Shechtman *et al.*, 2014), while optimization on the phase mask expanded in terms over Laguerre-Gaussian functions yields the double helix PSF (Pavani and Piestun, 2008; Pavani *et al.*, 2009). Similarly, in the panel on DeepSTORM3D (DS3D) (Nehme *et al.*, 2020) the PSF is optimized to localize emitters within a dense environment using a neural network. Finally, for the EDOF PSF, a cost function is optimized to obtain PSFs

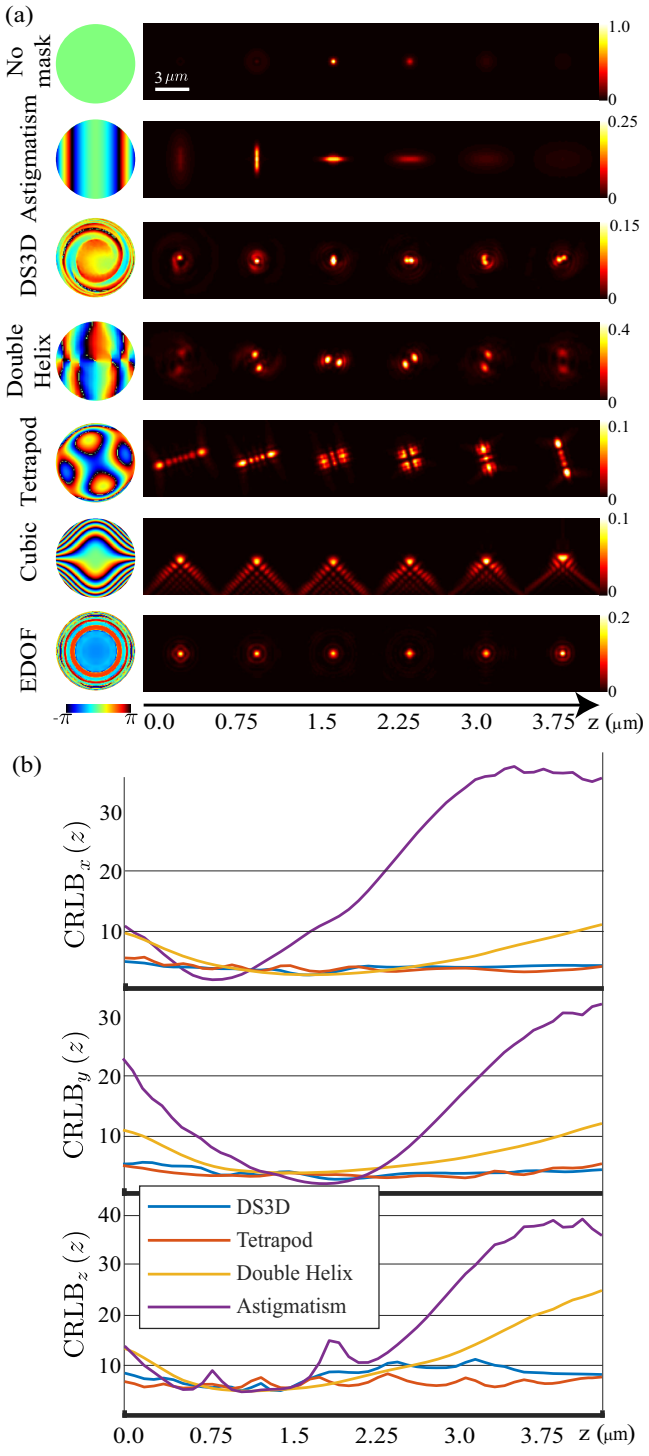

FIG. 61. PSF engineering. (a) Frequently used engineered PSFs, simulated for an objective lens with an NA = 1.49 and a pixel size of 110 nm. The top row is the wide-field PSF. Other rows present commonly used phase masks and their corresponding PSFs over a range of axial positions. (b) CRLB (see Sec. I.B) of the 3D position (each axis individually) plotted as a function of the axial position assuming that the system is laterally shift invariant. The subscripts in the axis labels indicate the coordinate for which the CRLB was calculated.

maintaining their in-focus shape over wider axial ranges (Nehme *et al.*, 2021).

As an example of optimization, to attain a PSF achieving optimal localization precision over a wide axial range we use the Fisher information and CRLB metrics. To derive the relevant CRLB, we start with the Fisher information matrix elements $[\mathcal{Q}(\vartheta;\Phi)]_{i,j}$ of the log-likelihood function given in Eq. (136) (see Sec. I.B),

$$[\mathcal{Q}(\vartheta;\Phi)]_{i,j} = \sum_{n=1}^{N} \frac{\partial}{\partial \vartheta_i}\Lambda_n(\vartheta,\Phi)\frac{\partial}{\partial \vartheta_j}\Lambda_n(n;\vartheta,\Phi) \times \frac{1}{\Lambda_n(n;\vartheta,\Phi)+\mathcal{B}_n}, \tag{141}$$

where ϑ_j is a parameter within the set of unknowns designated by ϑ. After evaluating the Fisher information entries, we can evaluate the CRLB given by Eq. (10).

In a practical implementation of an iterative optimization, the PSFs are scaled to match realistic signal counts encountered in SMLM imaging, i.e., on the scale of a few hundred photons per emitter per frame. Heuristic and CRLB optimized PSFs, optimized for just one emitter, can drastically limit their performance at high labeling density where engineered PSFs, such as the tetrapod (Shechtman *et al.*, 2014), suffer from PSF overlaps due to their large lateral footprint. In such cases, fitting algorithms like MLE designed for sparse cases exhibit a significant drop in performance, with performance slightly improved for the compact DS3D PSF (Nehme *et al.*, 2020). One solution for axial localization in dense environments is to let a neural net learn the optimal pupil phase design (Nehme *et al.*, 2020). In this case, 3D localization and the encoding pupil phase are simultaneously optimized. In a similar vein, for optimizing PSFs for dense localization similar design strategies have been used in multicolor imaging (Shechtman *et al.*, 2016; Smith *et al.*, 2016), where neural networks have been used to optimize phase masks to optimally discriminate between colors (Hershko *et al.*, 2019).

VI. PERSPECTIVES

The world of microscopy and biology have been intertwined from the onset. As early as humankind could peer at the world beyond its visual range, it peered into life (Gest, 2004) and we continue doing so from nuclear pore complexes (Thevathasan *et al.*, 2019), which are key to intracellular communication, individual synaptic spines (Chakraborty *et al.*, 2019), cell adhesion (Fischer *et al.*, 2021) at the basis of tissue formation, actin filaments involved in cell motion and division (Andrews *et al.*, 2008; Riedl *et al.*, 2008; Mazloom-Farsibaf *et al.*, 2021), etc.

Life presents events at all spatiotemporal scales with no clear means of discriminating between object of interest and background. Discrimination from background motivated fluorescence (Renz, 2013), while probing smaller and faster spatiotemporal scales, continues to motivate the experimental and theoretical methodology development. Along these lines, major improvements in fluorescent microscopy have followed four main fronts: fluorescent probes, optical setups, detectors, and data analysis.

Regarding fluorescent probes (see Sec. II), the discovery of green fluorescent proteins was a milestone in fluorescence microscopy (Shimomura, Johnson, and Saiga, 1962; Tsien, 1998). Next came the ability to switch biomarkers from dark and bright states (Hell and Wichmann, 1994; Dickson *et al.*, 1997) resulting in superresolution microscopy and nanometer resolution (Huang, Bates, and Zhuang, 2009; Lelek *et al.*, 2021); see Sec. V.

Concerning optical setups (see Secs. III and IV), the invention of the confocal microscope (Marvin, 1961) marked a milestone accomplishing optical sectioning by inserting a pinhole in the detection arm to filter out-of-focus light. Research in this area is ongoing, leading to the development of different microscopy modalities such as light-sheet microscopy and SIM (as discussed in Sec. IV), yielding unprecedented optical sectioning as well as high lateral resolutions.

On the detector front (see Appendix A), cameras, including CCDs, EMCCDs, and CMOSs, revolutionized fluorescence microscopy and enabled rapid wide-field imaging. Indeed, the need to amplify signal lead to the development of EMCCDs capable of imaging dim fluorescent probes (Madan, Bhaumik, and Vasi, 1983). The recent advent of CMOS cameras then accelerated data acquisition up to hundreds of frames per second over large FOVs with reduced readout noise (Bigas *et al.*, 2006). While we have focused mostly on integrative detectors in the review, increasingly available single-photon avalanche diode arrays (Bruschini *et al.*, 2019; Ulku *et al.*, 2019) may herald an era of unparalleled spatiotemporal resolution.

Finally, data analysis methods grounded in statistics are naturally suited to process fluorescent microscopy data while considering all sources of uncertainty; see Sec. I.B. Moreover, considering the fundamental problem of model selection inherent to fluorescence microscopy, BNP frameworks (see Sec. I.B) show promise across applications. Deep learning methods (Belthangady and Royer, 2019; de Haan *et al.*, 2020; Möckl, Roy, and Moerner, 2020; Volpe *et al.*, 2023) have also recently gained popularity and may likely be critical to the analysis of large volumetric, fluorescence datasets (Wang *et al.*, 2021; Patel *et al.*, 2022), though these tools require continued model training for different applications. A concrete future avenue for data analysis might merge the ideas from both Bayesian and deep learning (Winter *et al.*, 2023).

Despite continued progress in fluorescence microscopy (Pawley, 2006; Sahl, Hell, and Jakobs, 2017; Stockert and Blázquez-Castro, 2017), multiple challenges remain. These include potentially perturbative effects of fluorescent probes on the labeled systems, uncontrolled probe interactions with themselves and their environment, phototoxic effects naturally arising from any form of illumination, labeling and detection challenges in thicker samples and complex environments, rapid volumetric imaging, manipulating large dataset sizes, and many other challenges.

Indeed, as we move to complex environments complementary readouts beyond fluorescence are often desired and, along these lines, a number of other methods continue to be developed. These include refractive index tomography (Lee *et al.*, 2013; Kim *et al.*, 2016), Raman imaging (Camp *et al.*, 2014; Smith and Dent, 2019), phase imaging (Popescu, 2011; Park, Depeursinge, and Popescu, 2018), lens-free imaging

(Bishara *et al.*, 2010), ghost imaging (Gatti *et al.*, 2004; Shapiro, 2008), rotating coherent scattering microscopy (Ruh *et al.*, 2018; Jünger *et al.*, 2022), expansion microscopy (Chen, Tillberg, and Boyden, 2015; Gambarotto *et al.*, 2019), and others that have proven to be useful at the nanoscale. Together these approaches, alongside the development of theoretical and numerical tools, may help us to visualize life events that are otherwise unfolding in environments that remain impenetrable and at scales still beyond our reach.

ACKNOWLEDGMENTS

We thank the Quantitative BioImaging Society (QBI) for providing a venue in which many of us first met and discussed the topics presented here. We also deeply thank Peter T. Brown, Shep Bryan IV, Kunihiko Ishii, Sheng Liu, Tristan Manha, Alex Rojewski, Ayush Saurabh, Douglas Shepherd, Ioannis Sgouralis, and Tahei Tahara, Thorsten Wohland, and Weiqing Xu for carefully reading portions of this review and providing detailed feedback. S. P. acknowledges NIH NIGMS (Grant No. R01GM130745), NIH NIGMS (Grant No. R01GM134426), and NIH MIRA (Grant No. R35GM148237). B. F. and Y. S. acknowledge funding from the European Research Council (ERC) under the European Union's Horizon 2020 research and innovation program (Grant Agreement No. 802567). A. R. acknowledges support from the Swiss National Science Foundation through the National Centre of Competence in Research Bio-Inspired Materials. J. E. thanks the European Research Council (ERC) for financial support via the project "smMIET" (Grant Agreement No. 884488) under the European Union's Horizon 2020 research and innovation program. K. S. thanks the Department of Bionanoscience at TU Delft for its support and the Kavli Institute for Nanosciences Delft for KIND Synergy seed funding.

APPENDIX A: DETECTOR PHYSICS

Every photon carries with it information that can be recorded by detectors and later employed to draw inferences. These detectors comprise one or many pixels arranged as 2D arrays. The former is employed mostly in point scanning microscopy to record single-photon arrival times, for example, in FLIM and FRET. The latter is suitable to wide-field fluorescence.

Ideally, in wide-field detectors pixel values would histogram the photon counts incident on a particular pixel over the course of an exposure. Similarly, single-photon detectors would record precise photon arrival times. However, owing to the stochastic noise inherent to detectors, pixel values and recorded arrival times are related only probabilistically to photon counts and direct photon emission times, respectively (Michalet *et al.*, 2007; Tavakoli, Jazani, Sgouralis, Heo *et al.*, 2020; Fazel, Jazani *et al.*, 2022). This section lays out noise models for values reported by different detectors motivated by the detector physics. Once the model is formulated, its parameters are estimated for specific detectors using data from calibration experiments (Elson and Magde, 1974; Magde, Elson, and Webb, 1974; Weiss, 1999; Huang *et al.*, 2013; Afanasyev *et al.*, 2015; Heintzmann *et al.*, 2016). In what follows, we first describe wide-field detectors (integrative detectors) and next turn to single-photon detectors.

There are three common types of wide-field detectors used in fluorescence microscopy: CCDs (Amelio, Tompsett, and Smith, 1970; Boyle and Smith, 1970; Fossum and Hondongwa, 2014), EMCCDs (Madan, Bhaumik, and Vasi, 1983; Jerram *et al.*, 2001; Basden, Haniff, and Mackay, 2003), and CMOSs (Tian, 2000; Fossum and Hondongwa, 2014). In what follows, we describe the architecture and physics of each detector and, in turn, derive the appropriate noise model.

We begin with a sketch of detector devices. Figure 62 depicts the main components of CCDs and EMCCDs. The green pixel grid represents photoactive capacitors accumulating photoelectrons proportional to the incident photon counts. The blue grid is a set of capacitors that temporarily hold the resulting photoelectrons. The blue grid then transfers its electrons to the red register one row at a time. In CCD cameras there is no electron multiplier (EM) stage, and the transferred electrons follow the arrows to the right in Fig. 62 and go to the charge-to-voltage converter. The voltages are then converted into analog-to-digital units (ADUs) and recorded as pixel values.

By contrast, in EMCCD detectors the transferred electrons follow the arrows to the left in the red register and undergo an amplification stage shown in pink before going to the charge-to-voltage converter; see Fig. 62. In the EM stage, electrons are fed through a chain of avalanche EMs where an electric field is applied to the electrons, giving them sufficient kinetic energy to knock other electrons into the material's conducting band. This creates new electron-hole pairs, thereby amplifying the current. Each stage of the EM process has a small expected gain (≈1%), but the device has many stages dramatically amplifying the current prior to reaching the charge-to-voltage converter.

While CMOS detectors have similar architectures, they use transistors instead of capacitors and every CMOS pixel has its own amplifier; see Fig. 63. This allows for faster data acquisition, a larger FOV, lower power consummation, and larger quantum efficiency. However, such an architecture imposes pixel-dependent noise requiring maps of pixel gain,

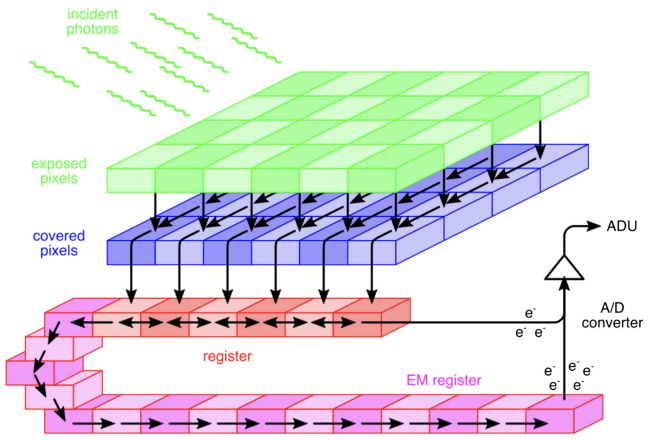

FIG. 62. Sketch of the CCD or EMCCD detector design detailed in the text.

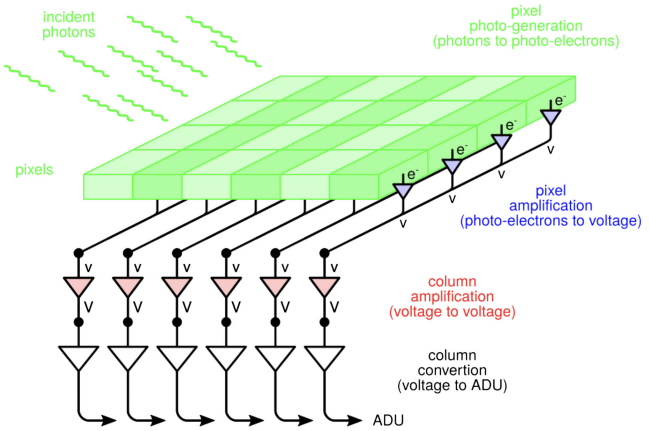

FIG. 63. Sketch of the CMOS detector design detailed in the text.

variance, and offset (Huang *et al.*, 2013; Liu *et al.*, 2017; Mandracchia *et al.*, 2020).

1. Noise models

Every stage involved in detecting and converting incident photons to ADUs in detectors introduces noise to the final reported pixel values. Here we discuss the main noises that are introduced at every stage.

(1) The first source of noise stems from the discrete nature of the photons. Given the expected photon count Λ_n for a pixel n over a fixed exposure time [see Eq. (129)] the measured photon count $N_{\mathrm{ph},n}$ is Poisson distributed, i.e., shot noise limited (Ober, Ram, and Ward, 2004; Zhang and Chen, 2009; Harpsøe, Andersen, and Kjægaard, 2012; Huang *et al.*, 2013),

$$N_{\mathrm{ph},n} \sim \mathrm{Poisson}(\Lambda_n), \tag{A1}$$

where we use notation that was introduced in Sec. I.B.

(2) Only a fraction of the photons incident on the detector generate photoelectrons, with the expected number of photoelectrons per incident photon called the quantum efficiency β (Zhang and Chen, 2009; Quan, Zeng, and Huang, 2010; Hirsch *et al.*, 2013). The number of generated photoelectrons $N_{\mathrm{pe},n}$, therefore follows a Binomial distribution (Hirsch *et al.*, 2013)

$$N_{\mathrm{pe},n} \sim \mathrm{Binomial}(N_{\mathrm{ph},n}, \beta). \tag{A2}$$

The distribution over the number of photoelectrons given the expected number of photons Λ_n can then be obtained by marginalizing over the incident number of photons (see Sec. I.B) as follows:

$$\mathrm{Poisson}(N_{\mathrm{pe},n}; \beta\Lambda_n) = \sum_{N_{\mathrm{ph},n}=N_{\mathrm{pe},n}}^{\infty} \mathrm{Poisson}(N_{\mathrm{ph},n}; \Lambda_i) \times \mathrm{Binomial}(N_{\mathrm{pe},n}; N_{\mathrm{ph},n}, \beta), \tag{A3}$$

where we have distinguished between the Binomial distribution of Eq. (A1) and the Binomial density of Eq. (A3), as detailed in Sec. I.B.

(3) The third source of noise is due to spurious charge consisting of unwanted electrons generated during the transfer process, termed clock-induced charge (CIC) (Daigle *et al.*, 2009; Hirsch *et al.*, 2013). The CIC noise follows a Poisson distribution and gives rise to additional electrons while being transferred to the register

$$N_{\mathrm{te},n} \sim \mathrm{Poisson}(\beta\Lambda_n + C), \tag{A4}$$

where $N_{\mathrm{te},n}$ and C are the number of electrons after the transferring stage and the mean value of the CIC. This noise is small but can be greatly amplified during the electron multiplier step in EMCCD detectors.

(4) The EM process consists of many stages in which new electrons are excited through impact ionization, which can be considered a cascade of stochastic events. These steps are approximately identical; thus, the EM process can be modeled as a cascade of Poisson processes or Bernoulli trials (Tubbs, 2003; Hirsch *et al.*, 2013) or a geometric model of multiplication (Chao, Ward, and Ober, 2012; Chao *et al.*, 2013).

The number of electrons after the EM stage $N_{\mathrm{ae},n}$ is a random variable that approximately follows a Gamma distribution (Basden, Haniff, and Mackay, 2003; Harpsøe, Andersen, and Kjægaard, 2012; Hirsch *et al.*, 2013),

$$N_{\mathrm{ae},n} \sim \mathrm{Gamma}(N_{\mathrm{te},n}, \hat{g}), \tag{A5}$$

where $\hat{g}$ denotes the amplification gain given by the ratio of the output and input electrons to the EM stage. For large values of $N_{\mathrm{te},n}$, this process is further approximated by a Gaussian that is computationally more efficient (Basden, Haniff, and Mackay, 2003; Hirsch *et al.*, 2013),

$$N_{\mathrm{ae},n} \sim \mathrm{Normal}(\hat{g}N_{\mathrm{te},n}, \hat{g}^2 N_{\mathrm{te},n}). \tag{A6}$$

(5) The last stage termed *readout* takes the input electrons following the EM stage $N_{\mathrm{ae},n}$ and converts them (with noise) into discrete pixel values reported as the data w_n in ADUs. This stage introduces another gain γ (ADUs per electron, also sometimes referred to as the sensitivity and typically smaller than 1) and offset μ (the output ADU at zero input electron often added to avoid negative pixel values) modeled by a Gaussian distribution and termed *readout noise*,

$$w_n \sim \mathrm{Normal}(\gamma N_{\mathrm{ae},n} + \mu, \sigma_{\mathrm{ro}}^2), \tag{A7}$$

where σ_{ro}^2 is the readout noise variance.

The combination of the noises introduced via the amplification and readout stages is obtained by marginalizing the intermediate parameter $N_{\mathrm{ae},n}$ (namely, the number of electrons after the EM stage) between Eqs. (A6) and (A7), resulting in

$$w_n \sim \text{Normal}(\tilde{g}N_{\text{te},n} + \mu, \sigma_w^2), \tag{A8}$$

where $\tilde{g} = \gamma\hat{g}$ and $\sigma_w^2 = \gamma^2\hat{g}^2N_{\text{te},n} + \sigma_{\text{ro}}^2$ denote the total gain and variance, respectively. Finally, the entire detector model, which relates the expected photon count (Λ_n) to the reported pixel value (w_n), is obtained by marginalizing the other intermediate parameter $N_{\text{te},n}$ (namely, the number of electrons after the transferring stage) between Eqs. (A4) and (A8),

$$P(w_n|\Lambda_n) = \sum_{N_{\text{te},n}=0}^{\infty} \text{Poisson}(N_{\text{te},n}; \beta\Lambda_n + C) \times \text{Normal}(w_n; \tilde{g}N_{\text{te},n} + \mu, \sigma_w^2). \tag{A9}$$

Since we did not make any assumptions about the gain, offset, or other parameters to derive the aforementioned noise model, it is valid for both CCD and EMCCD detectors. Moreover, if we assume pixel-dependent parameters such as gain and offset, this model would be valid for CMOS detectors as well. As Eq. (A9) remains complex, we make appropriate approximations for computational efficiency to derive simpler noise models specialized to each detector.

We start with CCD detectors lacking an EM amplification stage ($\hat{g} \approx 1$ and $\sigma_w^2 \approx \sigma_{\text{ro}}^2$). These are therefore suitable in detecting large input signals compared to the readout noise variance. This can be quantitatively expressed as

$$\text{SNR} = \frac{\Lambda_n}{\sigma_{\text{ro}}} \gg 1, \tag{A10}$$

thereby implying that the signal is not buried by readout noise. Under the large signal (Λ_n) assumption, the Poisson distribution (A4) is approximated by a Gaussian in which both the mean and the variance are given by the Poisson's mean,

$$P(w_n|\Lambda_n) \approx \sum_{N_{\text{te},n}=0}^{\infty} \text{Normal}(N_{\text{te},n}; \beta\Lambda_n, \beta\Lambda_n) \times \text{Normal}(w_n; \gamma N_{\text{te},n} + \mu, \sigma_w^2), \tag{A11}$$

where we assume that $\tilde{g} = \gamma$ and $\sigma_w^2 = \sigma_{\text{ro}}^2$ and further neglect the spurious charge C in the absence of amplification in CCD cameras. Therefore, Eq. (A11) leads to

$$w_n|\Lambda_n \sim \text{Normal}(g\Lambda_n + o, \sigma_w^2), \tag{A12}$$

where $g = \gamma\beta$, $o = \mu$, and $\sigma_w^2 = \sigma_{\text{ro}}^2$ denote the gain, offset, and variance for CCD detectors, respectively. It is also common to apply the offset and gain to the pixel values (data) and write Eq. (A12) for gain- and offset-corrected pixel values,

$$(w_n - o)/g|\Lambda_n \sim \text{Normal}(\Lambda_n, \sigma_w^2/g^2). \tag{A13}$$

Next we consider EMCCD detectors. These detectors are suitable for a low SNR. The EM stage of these detectors amplifies the signal above the readout noise ($\hat{g} \gg \sigma_w$). In an effort to simplify Eq. (A9) for EMCCDs, we write it in explicit form as

$$P(w_n|\Lambda_n) = \sum_{N_{\text{te},n}=0}^{\infty} \frac{(\beta\Lambda_n)^{N_{\text{te},n}} e^{-\beta\Lambda_n}}{N_{\text{te},n}!} \times \frac{1}{\sqrt{2\pi\sigma_D^2}} \exp\left[-\frac{[N_{\text{te},n} - (w_n - \mu)/\tilde{g}]^2}{2\sigma_w^2/\tilde{g}^2}\right], \tag{A14}$$

where we have factorized $\tilde{g}$ in the exponent. For large amplifications the standard deviation $\sigma_w^2/\tilde{g}^2$ becomes small and results in a narrow Gaussian approximated by a delta function. Therefore, upon marginalization and some algebra we recover (Huang *et al.*, 2013)

$$P((w_n - o)/g|\Lambda_n) = \frac{1}{\Gamma[1 + (w_n - o)/g]} e^{-\beta\Lambda_n} (\beta\Lambda_n)^{(w_n - o)/g}, \tag{A15}$$

where $o = \mu$ and $g = \tilde{g}$ denote the offset and gain, respectively. The aforementioned EMCCD model for the corrected pixel values is similar to a Poisson noise model where the corrected pixel values do not need to be integers (Huang *et al.*, 2013). An alternative EMCCD camera noise model could be obtained by convolution of the Poisson distribution equation (A4) and the gamma noise model for EM amplification (A5), resulting in an approximate gamma noise model for EMCCD detectors (Basden, Haniff, and Mackay, 2003; Hirsch *et al.*, 2013; Bryan, Sgouralis, and Pressé, 2022). The two noise models asymptotically converge to the same model for a large gain g.

After deriving noise models for CCD and EMCCD detectors with a pixel-independent gain g, an offset o, and a variance σ_w^2, we continue by deriving the noise model for CMOSs where the gain, variance, and offset are pixel dependent (Huang *et al.*, 2013; Liu *et al.*, 2017; Mandracchia *et al.*, 2020). Therefore, every pixel follows a different noise model that is similar to Eq. (A9),

$$P(w_n|\Lambda_n) = \sum_{N_{\text{te},n}=0}^{\infty} \text{Poisson}(N_{\text{te},n}; \beta\Lambda_n) \times \text{Normal}(w_n; \tilde{g}_n N_{\text{te},n} + \mu_n, \sigma_{w,n}^2), \tag{A16}$$

where n indexes the pixels. Provided small gain $\tilde{g}_n$ for CMOSs, Eq. (A16) can be approximated via a Poisson distribution assuming an extra source of photon for each n pixel contributing $\sigma_{w,n}^2/g_n^2$ photons (Huang *et al.*, 2013),

$$\hat{w}_n|\Lambda_n \sim \text{Poisson}(\Lambda_n + \sigma_{w,n}^2/g_n^2), \tag{A17}$$

where $\hat{w}_n = (w_n - o_n)/g_n + \sigma_{w,n}^2/g_n^2$, g_n is the gain characterized from calibration experiments, and $o_n = \mu_n$ is the pixel-dependent offset.

After considering wide-field detectors, we proceed to describe noise models for a single-photon detector. We do so by assuming fluorophore excitation using a pulsed laser. This is illustrated in Fig. 64, where the laser pulses are designated as blue spikes with an interpulse window T. In the figure a fluorophore gets excited during a pulse at a time t_{ext}, spends Δt_{ext} time in the excited state and emits a photon, in the most general case, after n pulses at t_{ems}. However, the photon

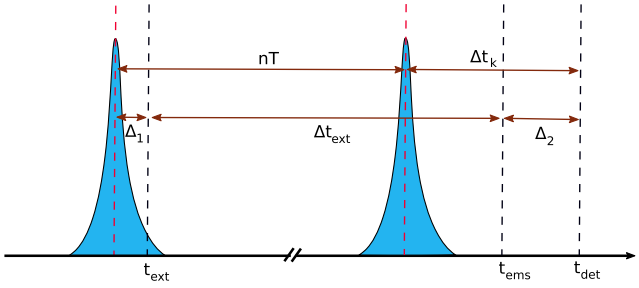

FIG. 64. Single-photon detector. Laser pulses and their centers are shown as blue spikes and dashed red lines with an interpulse window T, respectively. The fluorophore excitation, photon emission, and photon detection events take place at t_{ext}, t_{ems}, and t_{det}, respectively (designated as dashed black lines). The fluorophore spends time Δt_{ext} in the excited state and emits a photon after n pulses. The reported photon arrival time Δt_k is measured with respect to the immediate previous pulse center. Moreover, Δ_1 and Δ_2 denote the difference of the excitation pulse center and the detector delay in reporting the photon arrival time.

arrival time is recorded as t_{det} via a Δ_2 delay in the detector and is reported with respect to the immediate previous pulse given by Δt_k for the kth photon.

Using Fig. 64, we can write the following relation for the reported photon arrival time:

$$\Delta t_k = \Delta t_{\text{ext}} + \Delta t_{\text{IRF}} - nT, \tag{A18}$$

where $\Delta t_{\text{IRF}} = \Delta_1 + \Delta_2$ is the noise introduced by the IRF due to the laser pulses' finite width and the stochastic delay of the detector. Here the reported arrival time is the sum of three random variables. As such, the noise model is given by the convolution of three probability distributions,

$$P(\Delta t_k|\lambda) = P(n|N) \otimes [P(\Delta t_{\text{ext}}|\lambda) \otimes P(\Delta t_{\text{IRF}}|\tau_{\text{IRF}}, \sigma^2_{\text{IRF}})], \tag{A19}$$

where $\lambda, \tau_{\text{IRF}}, \sigma^2_{\text{IRF}}$, and N are the rate of excited state decay [the inverse of the excited state lifetime; see Eq. (18)], the IRF offset, the IRF variance, and the maximum possible number of pulses after which the fluorophore emits, respectively. These distributions are given by

$$\Delta t_{\text{ext}}|\lambda \sim \text{Exponential}(\lambda), \tag{A20}$$

$$\Delta t_{\text{IRF}}|\tau_{\text{IRF}}, \sigma^2_{\text{IRF}} \sim \text{Normal}(\tau_{\text{IRF}}, \sigma^2_{\text{IRF}}), \tag{A21}$$

$$n|A_{1:N} \sim \text{Categorical}(A_0, \ldots, A_N), \tag{A22}$$

where "Exponential" implies a normalization constant and the time spent in the excited state and the IRF time are sampled from Exponential and Gaussian distributions. The pulse at which the fluorophore emits is sampled from a Categorical distribution where A_n is given by the integral of the term inside brackets in Eq. (A19) over pulse n (Fazel, Jazani *et al.*, 2022). Finally, calculating the convolutions in Eq. (A19) we obtain the following noise model for single-photon detectors under pulsed illumination (Fazel, Jazani *et al.*, 2022):

$$P(\Delta t_k|\lambda) = \left[\sum_{n=0}^{N} \frac{\lambda}{2} \text{erfc}\left(\frac{\tau_{\text{IRF}} - \Delta t_k - nT + \lambda\sigma^2_{\text{IRF}}}{\sigma_{\text{IRF}}\sqrt{2}}\right) \times \exp\left(\frac{\lambda}{2}[2(\tau_{\text{IRF}} - \Delta t_k - nT) + \lambda\sigma^2_{\text{IRF}}]\right)\right], \tag{A23}$$

where $\text{erfc}(\cdot)$ denotes the complementary error function (Olver *et al.*, 2010). In many practical cases, the interpulse time is much larger than the fluorophore lifetime (the inverse of the fluorophore radiative decay $T \gg 1/\lambda$) where the fluorophore is emitted before the next pulse. In such cases, the noise model can be simplified by setting $N = 0$ (Tavakoli, Jazani, Sgouralis, Heo *et al.*, 2020).

APPENDIX B: FLUOROPHORE COUNTING

The application of Markov models for FRET data analysis was discussed in Sec. II.C. Here we describe how Markov models are used while enumerating fluorophores (Ulbrich and Isacoff, 2007; Rollins *et al.*, 2015; Tsekouras *et al.*, 2016; Lee *et al.*, 2017; Bryan, Sgouralis, and Pressé, 2022), typically with the intent of determining the stoichiometry of a labeled protein complex within a diffraction-limited spot.

For a single fluorophore we assume for simplicity a state space spanned by three photophysical states, though this treatment is generalized elsewhere (Patel *et al.*, 2019; Bryan, Sgouralis, and Pressé, 2022). These include (1) the bright state f_A, (2) the dark state f_D, and (3) the photobleached state f_B. Transitions between these states include $f_A \to f_A$, $f_A \to f_D$, $f_A \to f_B$, $f_D \to f_D$, $f_D \to f_A$, and $f_B \to f_B$. Here the photobleached state is an absorbing state from which escape is impossible; see Sec. II.A.

Typically in such applications a wide-field detector (see Appendix A) is used to record data from ROIs containing one or multiple putative complexes. The ROIs may contain one or more pixels. The input to the analysis then consists of the sum of the intensity or brightness in each ROI typically obtained by summing the pixel values (ADUs) in each pixel involved. The sum of ADUs for each ROI is then recorded over K successive frames and designated by $\bar{w}_{1:K} = \{w^1_{1:K}, \ldots, w^R_{1:K}\}$, where the overbar represents the set of R ROIs. Typically the last frame is taken after all fluorophores within the ROI have photobleached; see Fig. 65. Assuming only photobleaching and ignoring transitions from bright to dark states, we find that the number of discrete intensity drops in the time trace, if all fluorophores are initially bright, should coincide with the number of photobleaching events and thus the complex stoichiometry. However, not all fluorophores may initially be active, as in the case of PALM (Rollins *et al.*, 2015). What is more, fluorophores blink; see Sec. II.A and Fig. 65.

If our goal is to enumerate the fluorophores, assuming identical complexes across ROIs, then for independent ROIs (i.i.d. variables) the likelihood reads (see Sec. I.B)

$$P(\bar{w}_{1:K}|\bar{\Lambda}_{1:K}, \Xi) = \prod_r \prod_k P(w^r_k|\Lambda^r_k, \Xi), \tag{B1}$$

where Ξ denotes the camera parameters (see Appendix A) and the elements of $\bar{\Lambda}_{1:K}$, namely, Λ^r_k, coincide with the expected photon count, i.e., the brightness obtained from the emission rate multiplied by the camera exposure time, of the rth ROI at a frame k.

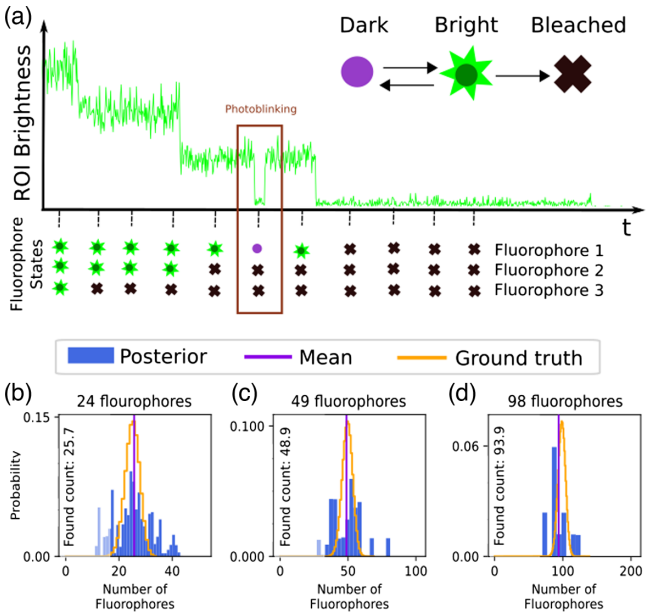

FIG. 65. Fluorophore enumeration. (a) Sketch of the enumeration problem where the ROI intensity varies as fluorophores switch between the dark, bright, and photobleached states. (b)–(d) Histogram of the sampled posterior over the number of fluorophores, i.e., the sum of sampled loads, for experimental data with 24, 49, and 98 fluorophores, respectively, using the statistical framework appearing in Fig. 66. Adapted from Bryan, Sgouralis, and Pressé, 2022.

Decomposed in terms of emission due to background and fluorophores, Λ_k^r reads

$$\Lambda_k^r = \mathcal{B}^r + I_A \sum_{m=1}^{M_r} \delta_{A,s_k^{rm}}, \tag{B2}$$

where m counts M_r fluorophores within the rth ROI. In Eq. (B2) I_A, $\mathcal{B}^r$, and s_k^{rm} denote the fluorophore's brightness, the background brightness of the rth ROI per frame, and the state of the mth fluorophore within the rth ROI at a frame k, respectively. The Kronecker delta $\delta_{A,s_k^{rm}}$ assumes that fluorophores emit only in the bright state. This decomposition assumes, perhaps erroneously in some cases, that the fluorphores do not interact (Saurabh *et al.*, 2022).

Next approximating the fluorophore state as remaining the same over each frame and the state at frame k depending only on its (potentially different) state at frame $k-1$, i.e., the Markov assumption, we can formulate the problem using transition probabilities between different states and avoid transition rates altogether. The transition probabilities associated with a single fluorophore can be collected as elements of a matrix, designated as $\mathbf{\Pi}$, that are analogous to the propagator $\mathbb{Q}$ in Eq. (29) for finite time windows,

$$\mathbf{\Pi} = \exp\left[\mathbf{G}\delta T\right] = \begin{bmatrix} \pi_{A\to A} & \pi_{A\to D} & \pi_{A\to B} \\ \pi_{D\to A} & \pi_{D\to D} & 0 \\ 0 & 0 & 1 \end{bmatrix}. \tag{B3}$$

In Eq. (B3) δT is the fixed period of time between measurements (the frame exposure time) and each line of the transition matrix contains transition probabilities out of a certain state. For instance, we have $\pi_A = [\pi_{A\to A}, \pi_{A\to D}, \pi_{A\to B}]$ for the bright state. The structure of the last row in Eq. (B3) reflects the absorbing nature of the bleached state.

The state of a single fluorophore at frame k given its state at $k-1$ is sampled as follows:

$$s_k^{mr} | s_{k-1}^{mr} \sim \text{Categorical}(\pi_{s_{k-1}^{mr}}), \tag{B4}$$

where $\pi_{s_{k-1}^{mr}}$ collects the set of possible transition probabilities out of s_{k-1}^{mr}. Finally, as fluorophore transitions are assumed to be independent, transitions of the full system are obtained from the product of the individual fluorophore transition probabilities.

While the photophysics of individual fluorophores may be known, the number of fluorophores are themselves unknown. This presents a model selection challenge warranting a nonparametric formulation. Conceptually this is achieved by assuming an infinite number of fluorophores with associated loads; see Sec. I.B. Concretely we modify Eq. (B2) as follows:

$$\Lambda_k^r = \mathcal{B}^r + I_A \sum_{m=1}^{\infty} b_m^r \delta_{A,s_k^{mr}}, \tag{B5}$$

where b_m^r is the load associated with the mth fluorophore in the rth ROI. In this case, the number of fluorophores is replaced by loads for each ROI. We collect the set of unknowns in $\vartheta = \{\bar{\bar{b}}, I_A, \bar{\bar{\mathcal{B}}}, \mathbf{\Pi}, \bar{\bar{\mathcal{S}}}\}$. Here double overbars represent the set of all possible values for the two indices associated with both of the parameters b and $\mathcal{S}$.

Finally, to construct the posterior for the set of parameters in ϑ, we introduce priors. The most notable priors are the beta-Bernoulli process priors on loads and the prior on the transition probabilities, the Dirichlet prior, due to its conjugacy to the Categorical distribution (B4). For the remaining priors in Fig. 66, we opt for computationally efficient priors when possible while leveraging the mathematical structure for the likelihood (Bryan, Sgouralis, and Pressé, 2022); see Sec. I.B. In particular, we invoke multiple Monte Carlo procedures to draw samples of ϑ from the posterior with forward filtering backward sampling specifically used to sample fluorophore trajectories (Scott, 2002; Bishop and Nasrabadi, 2006; Bryan, Sgouralis, and Pressé, 2022).

APPENDIX C: SUPERRESOLUTION OPTICAL FLUCTUATION IMAGING

SOFI (Dertinger *et al.*, 2009; Grußmayer *et al.*, 2020a, 2020b) is a computational postprocessing tool for superresolution single-molecule data. In contrast to SMLM, SOFI is not aimed at resolving isolated molecules and is robust to the presence of overlapping PSFs. Concretely SOFI improves the resolution by exploiting correlations in the stochastic switching of the underlying fluorophores, i.e., by leveraging the fact that a molecule's emission fluctuations spatiotemporally correlate only with themselves and not with neighboring molecules.

The data processed in SOFI consist of photon counts (intensity) w_n^k at pixel n in frame k (time point k) detected on a wide-field camera

Statistical Framework : Counting

Data: Sum of ROIs' pixel values in ADUs

$$\overline{w}_{1:K} = \left\{w^1_{1:K}, ..., w^R_{1:K}\right\}.$$

Parameters: loads, fluorophore intensity, background, transition probabilities, fluorophores' trajectories in the state space

$$\vartheta = \left\{\overline{\overline{b}}, I_A, \overline{\mathcal{B}}, \mathbf{\Pi}, \overline{\overline{\mathcal{S}}}\right\}.$$

Likelihood:

$$P\left(\overline{w}_{1:K}|\vartheta\right) = \prod_{k,r} P(w^r_k|\Lambda^r_k, \Xi).$$

Priors:

$$\begin{aligned} q_m &\sim \text{Beta}(A_q, B_q),\ \ m = 1:\infty, \\ b_m &\sim \text{Bernoulli}(q_m), \\ I_A &\sim \text{Gamma}(\alpha_A, \beta_A), \\ \mathcal{B} &\sim \text{Gamma}\left(\alpha_\mathcal{B}, \beta_\mathcal{B}\right), \\ \mathbf{\Pi} &\sim \text{Dirichlet}(\alpha_\Pi), \\ s^{mr}_k|s^{mr}_{k-1}, \mathbf{\Pi} &\sim \text{Categorical}(\pi_{s^{mr}_{k-1}}). \end{aligned}$$

Posterior:

$$P(\vartheta|\overline{w}_{1:K}) \propto P(\overline{w}_{1:K}|\vartheta)P(\vartheta).$$

FIG. 66. Statistical framework: counting.

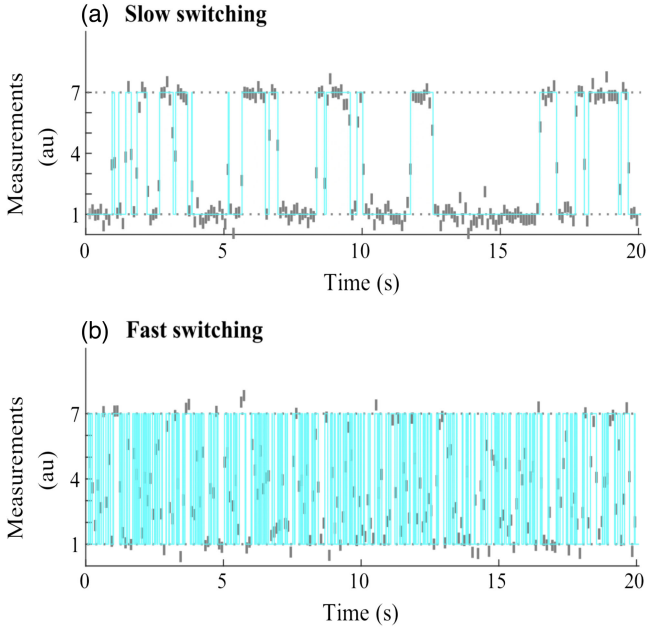

FIG. 67. Data simulated for discrete measurements of two state systems with (a) fast and (b) slow transitions. The system trajectories in the state space, measurements at different times intervals (δT), i.e., bins, and the state signal levels in the absence of noise are denoted as cyan, gray, and dotted lines, respectively. The measurements between the state signal levels coincide with time intervals where the system has switched to a different state at some point during those intervals. In the simulations, data acquisitions take place at every $\delta T = 0.1$ s, where the average time spent in each state is 0.8 and 0.066 s for slow and fast kinetics, respectively. Adapted from Kilic, Sgouralis, and Pressé, 2021.

$$w^k_n = \mathcal{B} + I_0 \sum_{m=1}^{M} U(\mathbf{r}_n - \mathbf{r}_m) s^k_m + \varepsilon^k_n, \tag{C1}$$

with M denoting the fluorophore number, I_0 representing the molecular brightness assumed uniform across molecules, U denoting the optical system's PSF, s^k_m describing the state of fluorophore m as an *off* or *on* state, $\mathcal{B}$ representing an average background, $\mathbf{r}_n$ denoting the location of pixel n, and ε^k_n representing the additive noise. Moreover, the sample is assumed to be stationary over image acquisition, and the PSF's integral over the pixel area is approximated by the integrand's value at the pixel center.

In its simplest implementation, SOFI computes the cumulants $\kappa(w^{1:K}_{1:N})$ of the pixel intensities across frames. For instance, the second order temporal cross cumulant coincides with the covariance in signal intensity across frames in one pixel for different time lags. The lth order cumulant can be approximated as (Deschout *et al.*, 2016)

$$\kappa_l(w^{1:K}_{1:N}) \approx I^l_0 f_l(\rho_{\text{on}}) \sum_{m=1}^{M} U^l(\mathbf{r}_{1:N} - \mathbf{r}_m), \tag{C2}$$

where $f_l(\rho_{\text{on}})$ denotes the lth order cumulant of s^k_m given as an lth order polynomial with respect to the probability of the molecule (ratio of molecules) to be *on* designated by ρ_{on}. Moreover, under assumptions of uncorrelated noise and stationary background, cumulants of the noise and background are zero. In Eq. (C2), which is critical to the SOFI analysis, the PSF is raised to the lth power. Thus, the lth order cumulant, if plotted instead of the original image, yields a PSF $\sqrt{l}$ narrower than the original PSF and offers an up to l-fold enlarged frequency support in Fourier space. As such, the resolution can be increased up to l-fold with postprocessing by either Fourier reweighing (Dertinger, Colyer *et al.*, 2010) or deconvolution (Dertinger *et al.*, 2009; Geissbuehler *et al.*, 2012), as discussed earlier; see Sec. IV.B.1 for a discussion of confocal microscopy and Sec. IV.B.2 for more on ISM microscopy. This can be further generalized to spatiotemporal cross cumulants with various time lags across different pixel combinations to leverage spatial information, albeit at higher computational cost (Dertinger, Colyer *et al.*, 2010; Geissbuehler *et al.*, 2012; Girsault *et al.*, 2016).

One challenge with SOFI postprocessing is the possibility of amplifying signal heterogeneities and potentially masking dimmer structures (Geissbuehler *et al.*, 2012), which is partly addressed by a deconvolution method termed balanced SOFI (Geissbuehler *et al.*, 2012; Deschout *et al.*, 2016). Furthermore, compared to SMLM, SOFI is relatively insensitive to background and tolerates higher labeling densities, higher on-time ratios, lower SNR, and only hundreds to thousands of frames to compute cumulants (allowing less photodamaging), and faster live-cell imaging. Moreover, SOFI achieves optical sectioning and resolution improvement in the z direction using simultaneously acquired multiplane data (Geissbuehler *et al.*, 2014; Descloux *et al.*, 2018).

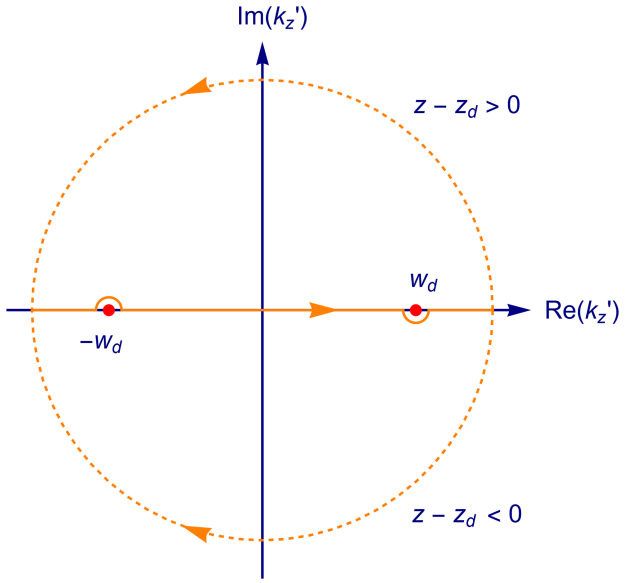

FIG. 68. Contour for the integration over k_z' of Eq. (56) in the complex k_z' plane. For positive values of $z - z_d$, the contour has to be closed at infinity over the positive $\mathrm{Im}(k_z')$ half-space, while for negative values of $z - z_d$ it is closed at infinity over the negative half-space. Along the real axis, the integrand has two poles at $\pm w_d = \pm\sqrt{k_d^2 - q^2}$.

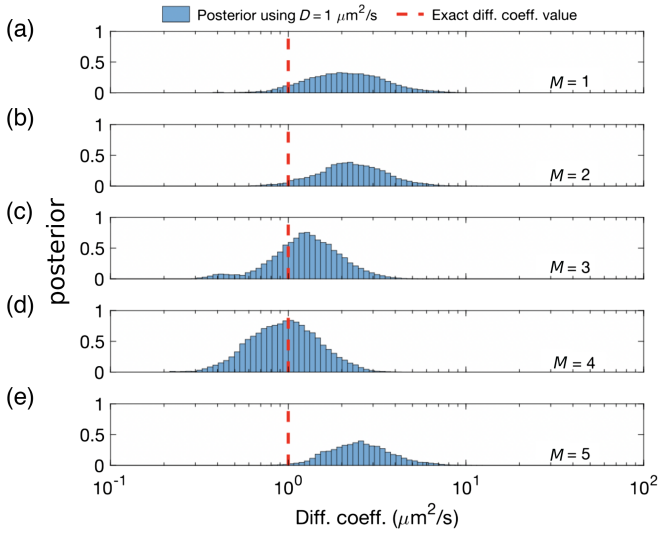

FIG. 69. Posteriors over diffusion coefficients strongly depend on the prespecified M when operating within a parametric Bayesian paradigm. The trace analyzed contains ≈1800 photons generated from four molecules diffusing at $D = 1\ \mu m^2/s$ for 30 ms with a background and maximum molecule photon emission rate of 10^3 and 4×10^4 photons/s, respectively. To deduce D within the parametric paradigm, we assumed a fixed number of molecules: (a) $M = 1$, (b) $M = 2$, (c) $M = 3$, (d) $M = 4$, and (e) $M = 5$. The correct estimate in (d) (and the mismatches in all others) highlights why we must use the available photons to simultaneously learn the number of molecules and D. Adapted from Tavakoli, Jazani, Sgouralis, Shafraz *et al.*, 2020.

APPENDIX D: SUPPLEMENTARY FIGURES

Additional figures are presented in this appendix for the evaluation of the integral of Eq. (56) and the posterior for the single spot confocal analysis discussed in Sec. IV.C.

REFERENCES

Abbe, E., 1873, "Beiträge zur theorie des mikroskops und der mikroskopischen wahrnehmung [Contributions to the theory of microscopy and microscope perception]," Arch. Mikrosc. Anat. **9**, 413–418.

Abrahamsson, S., M. McQuilken, S. B. Mehta, A. Verma, J. Larsch, R. Ilic, R. Heintzmann, C. I. Bargmann, A. S. Gladfelter, and R. Oldenbourg, 2015, "Multifocus polarization microscope (MF-PolScope) for 3D polarization imaging of up to 25 focal planes simultaneously," Opt. Express **23**, 7734–7754.

Abrahamsson, S., *et al.*, 2013, "Fast multicolor 3D imaging using aberration-corrected multifocus microscopy," Nat. Methods **10**, 60–63.

Abrahamsson, S., *et al.*, 2016, "Multifocus microscopy with precise color multi-phase diffractive optics applied in functional neuronal imaging," Biomed. Opt. Express **7**, 855–869.

Abrahamsson, S., *et al.*, 2017, "Multifocus structured illumination microscopy for fast volumetric super-resolution imaging," Biomed. Opt. Express **8**, 4135–4140.

Afanasyev, P., *et al.*, 2015, "*A posteriori* correction of camera characteristics from large image data sets," Sci. Rep. **5**, 10317.

Agam, G., *et al.*, 2023, "Reliability and accuracy of single-molecule FRET studies for characterization of structural dynamics and distances in proteins," Nat. Methods **20**, 523–535.

Agarwal, K., and R. Macháň, 2016, "Multiple signal classification algorithm for super-resolution fluorescence microscopy," Nat. Commun. **7**, 13752.

Aharonovich, I., and E. Neu, 2014, "Diamond nanophotonics," Adv. Opt. Mater. **2**, 911–928.

Aitken, C. E., R. A. Marshall, and J. D. Puglisi, 2008, "An oxygen scavenging system for improvement of dye stability in single-molecule fluorescence experiments," Biophys. J. **94**, 1826–1835.

Al-Khalili, J., 2015, "In retrospect: Book of optics," Nature (London) **518**, 164–165.

Al Labadi, L., and M. Zarepour, 2018, "On approximations of the beta process in latent feature models: Point processes approach," Sankhya Ser. A **80**, 59–79.

Amelio, G. F., M. F. Tompsett, and G. E. Smith, 1970, "Experimental verification of the charge coupled device concept," Bell Syst. Tech. J. **49**, 593–600.

Andrews, N. L., K. A. Lidke, J. R. Pfeiffer, A. R. Burns, B. S. Wilson, J. M. Oliver, and D. S. Lidke, 2008, "Actin restricts FcεRI diffusion and facilitates antigen-induced receptor immobilization," Nat. Cell Biol. **10**, 955–963.

Annibale, P., S. Vanni, M. Scarselli, U. Rothlisberger, and A. Radenovic, 2011, "Quantitative photo activated localization microscopy: Unraveling the effects of photoblinking," PLoS One **6**, e22678.

Arroyo-Camejo, S., M.-P. Adam, M. Besbes, J.-P. Hugonin, V. Jacques, J.-J. Greffet, J.-F. Roch, S. W. Hell, and F. Treussart, 2013, "Stimulated emission depletion microscopy resolves individual nitrogen vacancy centers in diamond nanocrystals," ACS Nano **7**, 10912–10919.

Axelrod, D., 1981, "Cell-substrate contacts illuminated by total internal reflection fluorescence.," J. Cell Biol. **89**, 141–145.

Azuma, T., and T. Kei, 2015, "Super-resolution spinning-disk confocal microscopy using optical photon reassignment," Opt. Express **23**, 15003–15011.

Babcock, H., Y. M. Sigal, and X. Zhuang, 2012, "A high-density 3D localization algorithm for stochastic optical reconstruction microscopy," Opt. Nanosc. **1**, 6.

Babcock, H. P., 2018, "Multiplane and spectrally-resolved single molecule localization microscopy with industrial grade CMOS cameras," Sci. Rep. **8**, 1726.

Bacia, K., Z. Petrášek, and P. Schwille, 2012, "Correcting for spectral cross-talk in dual-color fluorescence cross-correlation spectroscopy," ChemPhysChem **13**, 1221–1231.

Bacia, K., and P. Schwille, 2007, "Practical guidelines for dual-color fluorescence cross-correlation spectroscopy," Nat. Protoc. **2**, 2842–2856.

Backer, A. S., A. S. Biebricher, G. A. King, G. J. Wuite, I. Heller, and E. J. Peterman, 2019, "Single-molecule polarization microscopy of DNA intercalators sheds light on the structure of S-DNA," Sci. Adv. **5**, eaav1083.

Backer, A. S., and W. Moerner, 2014, "Extending single-molecule microscopy using optical Fourier processing," J. Phys. Chem. B **118**, 8313–8329.

Backlund, M. P., M. D. Lew, A. S. Backer, S. J. Sahl, and W. Moerner, 2014, "The role of molecular dipole orientation in single-molecule fluorescence microscopy and implications for super-resolution imaging," ChemPhysChem **15**, 587–599.

Baddeley, D., M. B. Cannell, and C. Soeller, 2011, "Three-dimensional sub-100 nm super-resolution imaging of biological samples using a phase ramp in the objective pupil," Nano Res. **4**, 589–598.

Bader, A. N., S. Hoetzl, E. G. Hofman, J. Voortman, P. M. Van Bergen En Henegouwen, G. Van Meer, and H. C. Gerritsen, 2011, "Homo-FRET imaging as a tool to quantify protein and lipid clustering," ChemPhysChem **12**, 475–483.

Badieirostami, M., M. D. Lew, M. A. Thompson, and W. Moerner, 2010, "Three-dimensional localization precision of the double-helix point spread function versus astigmatism and biplane," Appl. Phys. Lett. **97**, 161103.

Bailey, B., D. L. Farkas, D. L. Taylor, and F. Lanni, 1993, "Enhancement of axial resolution in fluorescence microscopy by standing-wave excitation," Nature (London) **366**, 44–48.

Balleza, E., J. M. Kim, and P. Cluzel, 2018, "Systematic characterization of maturation time of fluorescent proteins in living cells," Nat. Methods **15**, 47–51.

Balzarotti, F., Y. Eilers, K. C. Gwosch, A. H. Gynnå, V. Westphal, F. D. Stefani, J. Elf, and S. W. Hell, 2017, "Nanometer resolution imaging and tracking of fluorescent molecules with minimal photon fluxes," Science **355**, 606–612.

Banõs, Jr., A., 1966, *Dipole Radiation in the Presence of a Conducting Half-Space* (Pergamon Press, Oxford).

Bardell, D., 2004, "The invention of the microscope," Bios **75**, 78–84.

Basden, A., C. Haniff, and C. Mackay, 2003, "Photon counting strategies with low-light-level CCDs," Mon. Not. R. Astron. Soc. **345**, 985–991.

Belthangady, C., and L. A. Royer, 2019, "Applications, promises, and pitfalls of deep learning for fluorescence image reconstruction," Nat. Methods **16**, 1215–1225.

Ben-Eliezer, E., Z. Zalevsky, E. Marom, and N. Konforti, 2003, "All-optical extended depth of field imaging system," J. Opt. A **5**, S164.

Berland, K. M., P. So, and E. Gratton, 1995, "Two-photon fluorescence correlation spectroscopy: Method and application to the intracellular environment," Biophys. J. **68**, 694–701.

Betzig, E., 1995, "Proposed method for molecular optical imaging," Opt. Lett. **20**, 237–239.

Betzig, E., G. H. Patterson, R. Sougrat, O. W. Lindwasser, S. Olenych, J. S. Bonifacino, M. W. Davidson, J. Lippincott-Schwartz, and H. F. Hess, 2006, "Imaging intracellular fluorescent proteins at nanometer resolution," Science **313**, 1642–1645.

Bewersdorf, J., A. Egner, and S. W. Hell, 2006, "4Pi microscopy," in *Handbook of Biological Confocal Microscopy*, edited by J. B. Pawley (Springer, New York), pp. 561–570.

Bewersdorf, J., R. Schmidt, and S. Hell, 2006, "Comparison of I5M and 4Pi-microscopy," J. Microsc. **222**, 105–117.

Bigas, M., E. Cabruja, J. Forest, and J. Salvi, 2006, "Review of CMOS image sensors," Microelectron. J. **37**, 433–451.

Binnemans, K., 2015, "Interpretation of europium(III) spectra," Coord. Chem. Rev. **295**, 1–45.

Bishara, W., T.-W. Su, A. F. Coskun, and A. Ozcan, 2010, "Lensfree on-chip microscopy over a wide field-of-view using pixel super-resolution," Opt. Express **18**, 11181–11191.

Bishop, C. M., and N. M. Nasrabadi, 2006, *Pattern Recognition and Machine Learning*, Vol. 4 (Springer, New York).

Blanchard, P. M., and A. H. Greenaway, 1999, "Simultaneous multiplane imaging with a distorted diffraction grating," Appl. Opt. **38**, 6692–6699.

Bodén, A., F. Pennacchietti, G. Coceano, M. Damenti, M. Ratz, and I. Testa, 2021, "Volumetric live cell imaging with three-dimensional parallelized RESOLFT microscopy," Nat. Biotechnol. **39**, 609–618.

Booth, M. J., M. A. Neil, R. Juškaitis, and T. Wilson, 2002, "Adaptive aberration correction in a confocal microscope," Proc. Natl. Acad. Sci. U.S.A. **99**, 5788–5792.

Born, M., and E. Wolf, 2013, *Principles of Optics: Electromagnetic Theory of Propagation, Interference and Diffraction of Light* (Elsevier, New York).

Botcherby, E. J., R. Juškaitis, M. J. Booth, and T. Wilson, 2008, "An optical technique for remote focusing in microscopy," Opt. Commun. **281**, 880–887.

Boyle, W. S., and G. E. Smith, 1970, "Charge coupled semiconductor devices," Bell Syst. Tech. J. **49**, 587–593.

Braat, J. J., 1997, "Abbe sine condition and related imaging conditions in geometrical optics," in *Fifth International Topical Meeting on Education and Training in Optics*, edited by C. H. F. Velzel, SPIE Proceedings Vol. 3190 (SPIE—International Society for Optical Engineering, Bellingham, WA), pp. 59–64.

Bright, G. R., G. W. Fisher, J. Rogowska, and D. L. Taylor, 1989, "Fluorescence ratio imaging microscopy," in *Fluorescence Microscopy of Living Cells in Culture Part B: Quantitative Fluorescence Microscopy—Imaging and Spectroscopy*, Methods in Cell Biology Vol. 30, edited by D. L. Taylor and Y.-L. Wang (Elsevier, New York), pp. 157–192.

Broderick, T., M. I. Jordan, and J. Pitman, 2012, "Beta processes, stick-breaking and power laws," Bayesian Anal. **7**, 439–476, https://projecteuclid.org/journals/bayesian-analysis/volume-7/issue-2/Beta-Processes-Stick-Breaking-and-Power-Laws/10.1214/12-BA715.pdf.

Bronson, J. E., J. Fei, J. M. Hofman, R. L. Gonzalez, and C. H. Wiggins, 2009, "Learning rates and states from biophysical time series: A Bayesian approach to model selection and single-molecule FRET data," Biophys. J. **97**, 3196–3205.

Brooks, S., A. Gelman, G. Jones, and X.-L. Meng, 2011, *Handbook of Markov Chain Monte Carlo* (CRC Press, Boca Raton).

Bruschini, C., H. Homulle, I. M. Antolovic, S. Burri, and E. Charbon, 2019, "Single-photon avalanche diode imagers in biophotonics: Review and outlook," Light Sci. Appl. **8**, 87.

Bryan, J. S., I. Sgouralis, and S. Pressé, 2020, "Inferring effective forces for Langevin dynamics using Gaussian processes," J. Chem. Phys. **152**, 124106.

Bryan IV, J. S., I. Sgouralis, and S. Pressé, 2022, "Diffraction-limited molecular cluster quantification with Bayesian nonparametrics," Nat. Comput. Sci. **2**, 102–111.

Cai, M., H. Zhu, Y. Sun, L. Yin, F. Xu, H. Wu, X. Hao, R. Zhou, C. Kuang, and X. Liu, 2022, "Total variation and spatial iteration-based 3D structured illumination microscopy," Opt. Express **30**, 7938–7953.

Camp, Jr., C. H., Y. J. Lee, J. M. Heddleston, C. M. Hartshorn, A. R. H. Walker, J. N. Rich, J. D. Lathia, and M. T. Cicerone, 2014, "High-speed coherent Raman fingerprint imaging of biological tissues," Nat. Photonics **8**, 627–634.

Cao, B., S. Coelho, J. Li, G. Wang, and A. Pertsinidis, 2021, "Volumetric interferometric lattice light-sheet imaging," Nat. Biotechnol. **39**, 1385–1393.

Chakraborty, T., *et al.*, 2019, "Light-sheet microscopy of cleared tissues with isotropic, subcellular resolution," Nat. Methods **16**, 1109–1113.

Chance, R. R., A. Prock, and R. Silbey, 2007, "Molecular fluorescence and energy transfer near interfaces", in *Advances in Chemical Physics*, edited by I. Prigogine and S. A. Rice (Wiley-Blackwell, Hoboken, NJ), pp. 1–65.

Chang, B. J., V. D. P. Meza, and E. H. Stelzer, 2017, "csiLSFM combines light-sheet fluorescence microscopy and coherent Structured illumination for a lateral resolution below 100 nm," Proc. Natl. Acad. Sci. U.S.A. **114**, 4869–4874.

Chang, B.-J., L.-J. Chou, Y.-C. Chang, and S.-Y. Chiang, 2009, "Isotropic image in structured illumination microscopy patterned with a spatial light modulator," Opt. Express **17**, 14710–14721.

Chang, B.-J., K. M. Dean, and R. Fiolka, 2020, "Systematic and quantitative comparison of lattice and Gaussian light-sheets," Opt. Express **28**, 27052–27077.

Chao, J., S. Ram, E. S. Ward, and R. J. Ober, 2013, "Two approximations for the geometric model of signal amplification in an electron-multiplying charge-coupled device detector," in *Three-Dimensional and Multidimensional Microscopy: Image Acquisition and Processing XX*, edited by C. J. Cogswell, T. G. Brown, J.-A. Conchello, and T. Wilson, SPIE Proceedings Vol. 8589 (SPIE—International Society for Optical Engineering, Bellingham, WA), p. 858905.

Chao, J., E. S. Ward, and R. J. Ober, 2012, "Fisher information matrix for branching processes with application to electron-multiplying charge-coupled devices," Multidimens. Syst. Signal Process. **23**, 349–379.

Cheezum, M. K., W. F. Walker, and W. H. Guilford, 2001, "Quantitative comparison of algorithms for tracking single fluorescent particles," Biophys. J. **81**, 2378–2388.

Chen, B., *et al.*, 2022, "Resolution doubling in light-sheet microscopy via oblique plane structured illumination," Nat. Methods **19**, 1419–1426.

Chen, B. C., *et al.*, 2014a, "Lattice light-sheet microscopy: Imaging molecules to embryos at high spatiotemporal resolution," Science **346**, 1257998.

Chen, B.-C., *et al.*, 2014b, "Lattice light-sheet microscopy: Imaging molecules to embryos at high spatiotemporal resolution," Science **346**, 1257998.

Chen, F., P. W. Tillberg, and E. S. Boyden, 2015, "Expansion microscopy," Science **347**, 543–548.

Chen, X., S. Zhong, Y. Hou, R. Cao, W. Wang, D. Li, Q. Dai, D. Kim, and P. Xi, 2023, "Superresolution structured illumination microscopy reconstruction algorithms: A review," Light Sci. Appl. **12**, 172.

Chi, W., and N. George, 2001, "Electronic imaging using a logarithmic asphere," Opt. Lett. **26**, 875–877.

Chizhik, A. I., J. Rother, I. Gregor, A. Janshoff, and J. Enderlein, 2014, "Metal-induced energy transfer for live cell nanoscopy," Nat. Photonics **8**, 124–127.

Cho, Y., H. J. An, T. Kim, C. Lee, and N. K. Lee, 2021, "Mechanism of cyanine5 to cyanine3 photoconversion and its application for high-density single-particle tracking in a living cell," J. Am. Chem. Soc. **143**, 14125–14135.

Christensen, C. N., E. N. Ward, M. Lu, P. Lio, and C. F. Kaminski, 2021, "ML-SIM: Universal reconstruction of structured illumination microscopy images using transfer learning," Biomed. Opt. Express **12**, 2720–2733.

Chung, E., D. Kim, and P. T. So, 2006, "Extended resolution wide-field optical imaging: Objective-launched standing-wave total internal reflection fluorescence microscopy," Opt. Lett. **31**, 945–947.

Chung, K.-T., and J.-K. Liu, 2017, *Pioneers in Microbiology: The Human Side of Science* (World Scientific, Singapore).

Ciruela, F., 2008, "Fluorescence-based methods in the study of protein-protein interactions in living cells," Curr. Opin. Biotechnol. **19**, 338–343.

Cnossen, J., T. Hinsdale, R. Ø. Thorsen, M. Siemons, F. Schueder, R. Jungmann, C. S. Smith, B. Rieger, and S. Stallinga, 2020, "Localization microscopy at doubled precision with patterned illumination," Nat. Methods **17**, 59–63.

Cordes, T., and S. A. Blum, 2013, "Opportunities and challenges in single-molecule and single-particle fluorescence microscopy for mechanistic studies of chemical reactions," Nat. Chem. **5**, 993–999.

Cox, S., E. Rosten, J. Monypenny, T. Jovanovic-Talisman, D. T. Burnette, J. Lippincott-Schwartz, G. E. Jones, and R. Heintzmann, 2012, "Bayesian localization microscopy reveals nanoscale podosome dynamics," Nat. Methods **9**, 195–200.

Cramér, H., 1999, *Mathematical Methods of Statistics*, Princeton Landmarks in Mathematics Vol. 43 (Princeton University Press, Princeton, NJ).

Curdt, F., S. J. Herr, T. Lutz, R. Schmidt, J. Engelhardt, S. J. Sahl, and S. W. Hell, 2015, "isoSTED nanoscopy with intrinsic beam alignment," Opt. Express **23**, 30891–30903.

Daetwyler, S., and R. P. Fiolka, 2023, "Light-sheets and smart microscopy, an exciting future is dawning," Commun. Biol. **6**, 502.

Daigle, O., C. Carignan, J.-L. Gach, C. Guillaume, S. Lessard, C.-A. Fortin, and S. Blais-Ouellette, 2009, "Extreme faint flux imaging with an EMCCD," Publ. Astron. Soc. Pac. **121**, 866.

Dale, A. I., 1982, "Bayes or Laplace? An examination of the origin and early applications of Bayes' theorem," Arch. Hist. Exact Sci. **27**, 23–47.

Darrigol, O., 2012, *A History of Optics from Greek Antiquity to the Nineteenth Century* (Oxford University Press, New York).

Dasgupta, A., J. Deschamps, U. Matti, U. Hübner, J. Becker, S. Strauss, R. Jungmann, R. Heintzmann, and J. Ries, 2021, "Direct supercritical angle localization microscopy for nanometer 3D superresolution," Nat. Commun. **12**, 1180.

Datta, R., T. M. Heaster, J. T. Sharick, A. A. Gillette, and M. C. Skala, 2020, "Fluorescence lifetime imaging microscopy: Fundamentals and advances in instrumentation, analysis, and applications," J. Biomed. Opt. **25**, 071203.

Dean, K. M., P. Roudot, E. S. Welf, G. Danuser, and R. Fiolka, 2015, "Deconvolution-free subcellular imaging with axially swept light sheet microscopy," Biophys. J. **108**, 2807–2815.

Dean, K. M., *et al.*, 2022, "Isotropic imaging across spatial scales with axially swept light-sheet microscopy," Nat. Protoc. **17**, 2025–2053.

Dedecker, P., F. C. De Schryver, and J. Hofkens, 2013, "Fluorescent proteins: Shine on, you crazy diamond," J. Am. Chem. Soc. **135**, 2387–2402.

de Haan, K., Y. Rivenson, Y. Wu, and A. Ozcan, 2020, "Deep-learning-based image reconstruction and enhancement in optical microscopy," Proc. IEEE **108**, 30–50.

De Luca, G. M., R. M. Breedijk, R. A. Brandt, C. H. Zeelenberg, B. E. de Jong, W. Timmermans, L. N. Azar, R. A. Hoebe, S. Stallinga, and E. M. Manders, 2013, "Re-scan confocal microscopy: Scanning twice for better resolution," Biomed. Opt. Express **4**, 2644–2656.

Demmerle, J., C. Innocent, A. J. North, G. Ball, M. Müller, E. Miron, A. Matsuda, I. M. Dobbie, Y. Markaki, and L. Schermelleh, 2017, "Strategic and practical guidelines for successful structured illumination microscopy," Nat. Protoc. **12**, 988–1010.

Dempsey, G. T., M. Bates, W. E. Kowtoniuk, D. R. Liu, R. Y. Tsien, and X. Zhuang, 2009, "Photoswitching mechanism of cyanine dyes," J. Am. Chem. Soc. **131**, 18192–18193.

Dempsey, G. T., J. C. Vaughan, K. H. Chen, M. Bates, and X. Zhuang, 2011, "Evaluation of fluorophores for optimal performance in localization-based super-resolution imaging," Nat. Methods **8**, 1027–1036.

Denk, W., 2007, "Principles of multiphoton-excitation fluorescence microscopy," Cold Spring Harbor Protoc. pdb.

Denk, W., J. H. Strickler, and W. W. Webb, 1990, "Two-photon laser scanning fluorescence microscopy," Science **248**, 73–76.

Denk, W., and K. Svoboda, 1997, "Photon upmanship: Why multiphoton imaging is more than a gimmick," Neuron **18**, 351–357.

Dertinger, T., R. Colyer, G. Iyer, S. Weiss, and J. Enderlein, 2009, "Fast, background-free, 3D super-resolution optical fluctuation imaging (SOFI)," Proc. Natl. Acad. Sci. U.S.A. **106**, 22287–22292.

Dertinger, T., R. Colyer, R. Vogel, J. Enderlein, and S. Weiss, 2010, "Achieving increased resolution and more pixels with superresolution optical fluctuation imaging (SOFI)," Opt. Express **18**, 18875–18885.

Dertinger, T., M. Heilemann, R. Vogel, M. Sauer, and S. Weiss, 2010a, "Superresolution optical fluctuation imaging with organic dyes," Angew. Chem., Int. Ed. **49**, 9441–9443.

Deschamps, J., M. Mund, and J. Ries, 2014, "3D superresolution microscopy by supercritical angle detection," Opt. Express **22**, 29081–29091.

Deschout, H., F. C. Zanacchi, M. Mlodzianoski, A. Diaspro, J. Bewersdorf, S. T. Hess, and K. Braeckmans, 2014, "Precisely and accurately localizing single emitters in fluorescence microscopy," Nat. Methods **11**, 253–266.

Deschout, H., *et al.*, 2016, "Complementarity of PALM and SOFI for super-resolution live-cell imaging of focal adhesions," Nat. Commun. **7**, 13693.

Descloux, A., *et al.*, 2018, "Combined multi-plane phase retrieval and super-resolution optical fluctuation imaging for 4D cell microscopy," Nat. Photonics **12**, 165–172.

Descloux, A., *et al.*, 2020, "High-speed multiplane structured illumination microscopy of living cells using an image-splitting prism," Nanophotonics **9**, 143–148.

De Zitter, E., D. Thédié, V. Mönkemöller, S. Hugelier, J. Beaudouin, V. Adam, M. Byrdin, L. Van Meervelt, P. Dedecker, and D. Bourgeois, 2019, "Mechanistic investigation of mEos4b reveals a strategy to reduce track interruptions in sptPALM," Nat. Methods **16**, 707–710.

Dickson, R. M., A. B. Cubitt, R. Y. Tsien, and W. E. Moerner, 1997, "On/off blinking and switching behaviour of single molecules of green fluorescent protein," Nature (London) **388**, 355–358.

Diekmann, R., M. Kahnwald, A. Schoenit, J. Deschamps, U. Matti, and J. Ries, 2020, "Optimizing imaging speed and excitation intensity for single-molecule localization microscopy," Nat. Methods **17**, 909–912.

Di Francia, G. T., 1952, "Super-gain antennas and optical resolving power," Nuovo Cimento **9**, 426–438.

Digman, M. A., V. R. Caiolfa, M. Zamai, and E. Gratton, 2008, "The phasor approach to fluorescence lifetime imaging analysis," Biophys. J. **94**, L14–L16.

Digman, M. A., and E. Gratton, 2011, "Lessons in fluctuation correlation spectroscopy," Annu. Rev. Phys. Chem. **62**, 645–668.

Dowski, E. R., and W. T. Cathey, 1995, "Extended depth of field through wave-front coding," Appl. Opt. **34**, 1859–1866.

Dunsby, C., 2008, "Optically sectioned imaging by oblique plane microscopy," Opt. Express **16**, 20306–20316.

Eggeling, C., K. I. Willig, S. J. Sahl, and S. W. Hell, 2015, "Lens-based fluorescence nanoscopy," Q. Rev. Biophys. **48**, 178–243.

Eilers, Y., H. Ta, K. C. Gwosch, F. Balzarotti, and S. W. Hell, 2018, "MINFLUX monitors rapid molecular jumps with superior spatiotemporal resolution," Proc. Natl. Acad. Sci. U.S.A. **115**, 6117–6122.

Einstein, A., 1905, "Über die von der molekularkinetischen theorie der Wärme geforderte Bewegung von in ruhenden Flüssigkeiten suspendierten Teilchen," Ann. Phys. (Berlin) **322**, 549–560.

Einstein, A., 1916, "Strahlungs-Emission und Absorption nach der Quantentheorie [On the quantum theory of radiation]," Dtsch. Phys. Ges. **18**, 318, https://www.informationphilosopher.com/solutions/scientists/einstein/1917_Radiation.pdf.

El Arawi, D., C. Vézy, R. Déturche, M. Lehmann, H. Kessler, M. Dontenwill, and R. Jaffiol, 2021, "Advanced quantification for single-cell adhesion by variable-angle TIRF nanoscopy," Biophys. Rep. **1**, 100021.

Elson, E. L., and D. Magde, 1974, "Fluorescence correlation spectroscopy. I. Conceptual basis and theory," Biopolymers **13**, 1–27.

Enderlein, J., I. Gregor, D. Patra, and J. Fitter, 2004, "Art and artefacts of fluorescence correlation spectroscopy," Curr. Pharm. Biotechnol. **5**, 155–161.

Enderlein, J., T. Ruckstuhl, and S. Seeger, 1999, "Highly efficient optical detection of surface-generated fluorescence," Appl. Opt. **38**, 724–732.

Enderlein, J., E. Toprak, and P. R. Selvin, 2006, "Polarization effect on position accuracy of fluorophore localization," Opt. Express **14**, 8111–8120.

Engelhardt, M., and K. Grußmayer, 2022, "Mapping volumes to planes: Camera-based strategies for snapshot volumetric microscopy," Front. Phys. **10**, 1010053.

Escudero, D., 2016, "Revising intramolecular photoinduced electron transfer (PET) from first-principles," Acc. Chem. Res. **49**, 1816–1824.

Fahrbach, F. O., and A. Rohrbach, 2010, "A line scanned light-sheet microscope with phase shaped self-reconstructing beams," Opt. Express **18**, 24229–24244.

Fahrbach, F. O., P. Simon, and A. Rohrbach, 2010, "Microscopy with self-reconstructing beams," Nat. Photonics **4**, 780–785.

Fazel, M., S. Jazani, L. Scipioni, A. Vallmitjana, E. Gratton, M. A. Digman, and S. Pressé, 2022, "High resolution fluorescence lifetime maps from minimal photon counts," ACS Photonics **9**, 1015–1025.

Fazel, M., S. Jazani, L. Scipioni, A. Vallmitjana, S. Zhu, E. Gratton, M. Digman, and S. Presse, 2023, "Building fluorescence lifetime

maps photon-by-photon by leveraging spatial correlations," ACS Photonics **10**, 3558–3569.
Fazel, M., A. Vallmitjana, L. Scipioni, E. Gratton, M. A. Digman, and S. Presse, 2023, "Fluorescence lifetime: Beating the IRF and interpulse window," Biophys. J. **122**, 672–683.
Fazel, M., and M. J. Wester, 2022, "Analysis of super-resolution single molecule localization microscopy data: A tutorial," AIP Adv. **12**, 010701.
Fazel, M., M. J. Wester, H. Mazloom-Farsibaf, M. Meddens, A. S. Eklund, T. Schlichthaerle, F. Schueder, R. Jungmann, and K. A. Lidke, 2019, "Bayesian multiple emitter fitting using reversible jump Markov chain Monte Carlo," Sci. Rep. **9**, 13791.
Fazel, M., *et al.*, 2022, "High-precision estimation of emitter positions using Bayesian grouping of localizations," Nat. Commun. **13**, 7152.
Ferdman, B., E. Nehme, L. E. Weiss, R. Orange, O. Alalouf, and Y. Shechtman, 2020, "VIPR: Vectorial implementation of phase retrieval for fast and accurate microscopic pixel-wise pupil estimation," Opt. Express **28**, 10179–10198.
Fereidouni, F., A. N. Bader, and H. C. Gerritsen, 2012, "Spectral phasor analysis allows rapid and reliable unmixing of fluorescence microscopy spectral images," Opt. Express **20**, 12729–12741.
Ferguson, T. S., 1973, "A Bayesian analysis of some nonparametric problems," Ann. Stat. **1**, 209–230.
Fienup, J. R., 1978, "Reconstruction of an object from the modulus of its Fourier transform," Opt. Lett. **3**, 27–29.
Fiolka, R., L. Shao, E. H. Rego, M. W. Davidson, and M. G. Gustafsson, 2012, "Time-lapse two-color 3D imaging of live cells with doubled resolution using structured illumination," Proc. Natl. Acad. Sci. U.S.A. **109**, 5311–5315.
Fischer, L. S., C. Klingner, T. Schlichthaerle, M. T. Strauss, R. Böttcher, R. Fässler, R. Jungmann, and C. Grashoff, 2021, "Quantitative single-protein imaging reveals molecular complex formation of integrin, talin, and kindlin during cell adhesion," Nat. Commun. **12**, 919.
Förster, T., 1948, "Zwischenmolekulare energiewanderung und fluoreszenz [Intermolecular energy migration and fluorescence]," Ann. Phys. (Berlin) **437**, 55–75.
Fossum, E. R., and D. B. Hondongwa, 2014, "A review of the pinned photodiode for CCD and CMOS image sensors," IEEE J. Electron Devices Soc. **2**, 33–43.
Friedrich, M., Q. Gan, V. Ermolayev, and G. S. Harms, 2011, "STED-SPIM: Stimulated emission depletion improves sheet illumination microscopy resolution," Biophys. J. **100**, L43–L45.
Frohn, J., H. Knapp, and A. Stemmer, 2001, "Three-dimensional resolution enhancement in fluorescence microscopy by harmonic excitation," Opt. Lett. **26**, 828–830.
Gabitto, M. I., H. Marie-Nelly, A. Pakman, A. Pataki, X. Darzacq, and M. I. Jordan, 2021, "A Bayesian nonparametric approach to super-resolution single-molecule localization," Ann. Appl. Stat. **15**, 1742–1766.
Galland, R., G. Grenci, A. Aravind, V. Viasnoff, V. Studer, and J.-B. Sibarita, 2015, "3D high-and super-resolution imaging using single-objective SPIM," Nat. Methods **12**, 641–644.
Gambarotto, D., *et al.*, 2019, "Imaging cellular ultrastructures using expansion microscopy (U-ExM)," Nat. Methods **16**, 71–74.
Gatti, A., E. Brambilla, M. Bache, and L. A. Lugiato, 2004, "Ghost Imaging with Thermal Light: Comparing Entanglement and Classical Correlation," Phys. Rev. Lett. **93**, 093602.
Gebhardt, J. C. M., D. M. Suter, R. Roy, Z. W. Zhao, A. R. Chapman, S. Basu, T. Maniatis, and X. S. Xie, 2013, "Single-molecule imaging of transcription factor binding to DNA in live mammalian cells," Nat. Methods **10**, 421–426.
Geissbuehler, S., N. L. Bocchio, C. Dellagiacoma, C. Berclaz, M. Leutenegger, and T. Lasser, 2012, "Mapping molecular statistics with balanced super-resolution optical fluctuation imaging (bSOFI)," Opt. Nanosc. **1**, 4.
Geissbuehler, S., *et al.*, 2014, "Live-cell multiplane three-dimensional super-resolution optical fluctuation imaging," Nat. Commun. **5**, 5830.
Gelfand, A. E., A. Kottas, and S. N. MacEachern, 2005, "Bayesian nonparametric spatial modeling with Dirichlet process mixing," J. Am. Stat. Assoc. **100**, 1021–1035.
Gelman, A., J. B. Carlin, H. S. Stern, and D. B. Rubin, 1995, *Bayesian Data Analysis* (Chapman and Hall, London).
Geman, S., and D. Geman, 1984, "Stochastic relaxation, Gibbs distributions, and the Bayesian restoration of images," IEEE Trans. Pattern Anal. Mach. Intell. **PAMI-6**, 721–741.
Gerchberg, R. W., 1972, "A practical algorithm for the determination of phase from image and diffraction plane pictures," Optik **35**, 237–246, https://www.semanticscholar.org/paper/A-practical-algorithm-for-the-determination-of-from-Gerchberg/5a114d3050a0a33f8cc6d28d55fa048a5a7ab6f2.
Gershman, S. J., and D. M. Blei, 2012, "A tutorial on Bayesian nonparametric models," J. Math. Psych. **56**, 1–12.
Gest, H., 2004, "The discovery of microorganisms by Robert Hooke and Antoni Van Leeuwenhoek, fellows of the Royal Society," Notes Rec. R. Soc. **58**, 187–201.
Ghosh, A., A. Sharma, A. I. Chizhik, S. Isbaner, D. Ruhlandt, R. Tsukanov, I. Gregor, N. Karedla, and J. Enderlein, 2019, "Graphene-based metal-induced energy transfer for sub-nanometre optical localization," Nat. Photonics **13**, 860–865.
Giepmans, B. N., S. R. Adams, M. H. Ellisman, and R. Y. Tsien, 2006, "The fluorescent toolbox for assessing protein location and function," Science **312**, 217–224.
Gillespie, D. T., 1976, "A general method for numerically simulating the stochastic time evolution of coupled chemical reactions," J. Comput. Phys. **22**, 403–434.
Girsault, A., T. Lukes, A. Sharipov, S. Geissbuehler, M. Leutenegger, W. Vandenberg, P. Dedecker, J. Hofkens, and T. Lasser, 2016, "SOFI simulation tool: A software package for simulating and testing super-resolution optical fluctuation imaging," PLoS One **11**, e0161602.
Goodsell, D. S., 2009, *The Machinery of Life* (Springer Science +Business Media, New York).
Gopich, I., and A. Szabo, 2005, "Theory of photon statistics in single-molecule Förster resonance energy transfer," J. Chem. Phys. **122**, 014707.
Gopich, I. V., and A. Szabo, 2006, "Theory of the statistics of kinetic transitions with application to single-molecule enzyme catalysis," J. Chem. Phys. **124**, 154712.
Gould, T. J., D. Burke, J. Bewersdorf, and M. J. Booth, 2012, "Adaptive optics enables 3D STED microscopy in aberrating specimens," Opt. Express **20**, 20998–21009.
Gradinaru, C. C., D. O. Marushchak, M. Samim, and U. J. Krull, 2010, "Fluorescence anisotropy: From single molecules to live cells," Analyst **135**, 452–459.
Graham, T. G. W., J. J. Ferrie, G. M. Dailey, R. Tjian, and X. Darzacq, 2022, "Detecting molecular interactions in live-cell single-molecule imaging with proximity-assisted photoactivation (PAPA)," eLife **11**, e76870.
Green, P. J., 1995, "Reversible jump Markov chain Monte Carlo computation and Bayesian model determination," Biometrika **82**, 711–732.
Gregor, I., E. Butkevich, J. Enderlein, and S. Mojiri, 2021, "Instant three-color multiplane fluorescence microscopy," Biophys. Rep. **1**, 100001.

Gregor, I., and J. Enderlein, 2019, "Image scanning microscopy," Curr. Opin. Chem. Biol. **51**, 74–83.

Gregor, I., D. Patra, and J. Enderlein 2005, "Optical saturation in fluorescence correlation spectroscopy under continuous-wave and pulsed excitation," ChemPhysChem **6**, 164–170.

Gregor, I., M. Spiecker, R. Petrovsky, J. Großhans, R. Ros, and J. Enderlein, 2017, "Rapid nonlinear image scanning microscopy," Nat. Methods **14**, 1087–1089.

Gross, H., 2005, *Handbook of Optical Systems* (Wiley Online Library, New York).

Grotjohann, T., I. Testa, M. Reuss, T. Brakemann, C. Eggeling, S. W. Hell, and S. Jakobs, 2012, "rsEGFP2 enables fast RESOLFT nanoscopy of living cells," eLife **1**, e00248.

Grußmayer, K., T. Lukes, T. Lasser, and A. Radenovic, 2020a, "Self-blinking dyes unlock high-order and multi-plane super-resolution optical fluctuation imaging," arXiv:2002.10224.

Grußmayer, K., T. Lukes, T. Lasser, and A. Radenovic, 2020b, "Self-blinking dyes unlock high-order and multiplane super-resolution optical fluctuation imaging," ACS Nano **14**, 9156–9165.

Gruβmayer, K. S., K. Yserentant, and D. P. Herten, 2019, "Photons in–numbers out: Perspectives in quantitative fluorescence microscopy for *in situ* protein counting," Methods Appl. Fluoresc. **7**, 012003.

Gu, L., Y. Li, S. Zhang, Y. Xue, W. Li, D. Li, T. Xu, and W. Ji, 2019, "Molecular resolution imaging by repetitive optical selective exposure," Nat. Methods **16**, 1114–1118.

Guo, M., *et al.*, 2020, "Rapid image deconvolution and multiview fusion for optical microscopy," Nat. Biotechnol. **38**, 1337–1346.

Guo, Y., *et al.*, 2018, "Visualizing intracellular organelle and cytoskeletal interactions at nanoscale resolution on millisecond timescales," Cell **175**, 1430–1442.

Gustafsson, M. G., 2000, "Surpassing the lateral resolution limit by a factor of two using structured illumination microscopy," J. Microsc. **198**, 82–87.

Gustafsson, M. G., 2005, "Nonlinear structured-illumination microscopy: Wide-field fluorescence imaging with theoretically unlimited resolution," Proc. Natl. Acad. Sci. U.S.A. **102**, 13081–13086.

Gustafsson, M. G., L. Shao, P. M. Carlton, C. J. Wang, I. N. Golubovskaya, W. Z. Cande, D. A. Agard, and J. W. Sedat, 2008, "Three-dimensional resolution doubling in wide-field fluorescence microscopy by structured illumination," Biophys. J. **94**, 4957–4970.

Gustafsson, N., S. Culley, G. Ashdown, D. M. Owen, P. M. Pereira, and R. Henriques, 2016, "Fast live-cell conventional fluorophore nanoscopy with `ImageJ` through super-resolution radial fluctuations," Nat. Commun. **7**, 12471.

Gwosch, K. C., J. K. Pape, F. Balzarotti, P. Hoess, J. Ellenberg, J. Ries, and S. W. Hell, 2020, "MINFLUX nanoscopy delivers 3D multicolor nanometer resolution in cells," Nat. Methods **17**, 217–224.

Hajj, B., L. Oudjedi, J. B. Fiche, M. Dahan, and M. Nollmann, 2017, "Highly efficient multicolor multifocus microscopy by optimal design of diffraction binary gratings," Sci. Rep. **7**, 5284.

Hajj, B., J. Wisniewski, M. E. Beheiry, J. Chen, A. Revyakin, C. Wu, and M. Dahan, 2014, "Whole-cell, multicolor superresolution imaging using volumetric multifocus microscopy," Proc. Natl. Acad. Sci. U.S.A. **111**, 17480–17485.

Hansen, J. N., A. Gong, D. Wachten, R. Pascal, A. Turpin, J. F. Jikeli, U. B. Kaupp, and L. Alvarez, 2021, "Multifocal imaging for precise, label-free tracking of fast biological processes in 3D," Nat. Commun. **12**, 4574.

Hao, X., Y. Li, S. Fu, Y. Li, Y. Xu, C. Kuang, and X. Liu, 2022, "Review of 4Pi fluorescence nanoscopy," Engineering **11**, 146–153.

Harpsøe, K. B., M. I. Andersen, and P. Kjægaard, 2012, "Bayesian photon counting with electron-multiplying charge coupled devices (EMCCDs)," Astron. Astrophys. **537**, A50.

Hastings, W. K., 1970, "Monte Carlo sampling methods using Markov chains and their applications," Biometrika **57**, 97–109.

Heavens, O. S., 1965, *Optical Properties of Thin Solid Films* (Dover, New York), p. 69.

Heilemann, M., S. Van De Linde, M. Schüttpelz, R. Kasper, B. Seefeldt, A. Mukherjee, P. Tinnefeld, and M. Sauer, 2008, "Subdiffraction-resolution fluorescence imaging with conventional fluorescent probes," Angew. Chem., Int. Ed. **47**, 6172–6176.

Heintzmann, R., 2003, "Saturated patterned excitation microscopy with two-dimensional excitation patterns," Micron **34**, 283–291.

Heintzmann, R., and C. G. Cremer, 1999, "Laterally modulated excitation microscopy: Improvement of resolution by using a diffraction grating," in *Optical Biopsies and Microscopic Techniques III*, edited by I. J. Bigio, H. Schneckenburger, J. Slavik, K. Svanberg, and P. M. Viallet, SPIE Proceedings Vol. 3568 (SPIE—International Society for Optical Engineering, Bellingham, WA).

Heintzmann, R., and T. Huser, 2017, "Super-resolution structured illumination microscopy," Chem. Rev. **117**, 13890–13908.

Heintzmann, R., T. M. Jovin, and C. Cremer, 2002, "Saturated patterned excitation microscopy—A concept for optical resolution improvement," J. Opt. Soc. Am. A **19**, 1599–1609.

Heintzmann, R., P. K. Relich, R. P. Nieuwenhuizen, K. A. Lidke, and B. Rieger, 2016, "Calibrating photon counts from a single image," arXiv:1611.05654.

Hell, S., and E. H. Stelzer, 1992, "Fundamental improvement of resolution with a 4Pi-confocal fluorescence microscope using two-photon excitation," Opt. Commun. **93**, 277–282.

Hell, S. W., 2007, "Far-field optical nanoscopy," Science **316**, 1153–1158.

Hell, S. W., and M. Kroug, 1995, "Ground-state-depletion fluorescence microscopy: A concept for breaking the diffraction resolution limit," Appl. Phys. B **60**, 495–497.

Hell, S. W., and J. Wichmann, 1994, "Breaking the diffraction resolution limit by stimulated emission: Stimulated-emission-depletion fluorescence microscopy," Opt. Lett. **19**, 780–782.

Hellenkamp, B., *et al.*, 2018, "Precision and accuracy of single-molecule FRET measurements—A multi-laboratory benchmark study," Nat. Methods **15**, 669–676.

Helmerich, D. A., G. Beliu, S. S. Matikonda, M. J. Schnermann, and M. Sauer, 2021, "Photoblueing of organic dyes can cause artifacts in super-resolution microscopy," Nat. Methods **18**, 253–257.

Hershko, E., L. E. Weiss, T. Michaeli, and Y. Shechtman, 2019, "Multicolor localization microscopy and point-spread-function engineering by deep learning," Opt. Express **27**, 6158–6183.

Hess, S. T., T. P. Girirajan, and M. D. Mason, 2006, "Ultra-high resolution imaging by fluorescence photoactivation localization microscopy," Biophys. J. **91**, 4258–4272.

Hines, K. E., J. R. Bankston, and R. W. Aldrich, 2015, "Analyzing single-molecule time series via nonparametric Bayesian inference," Biophys. J. **108**, 540–556.

Hirsch, M., R. J. Wareham, M. L. Martin-Fernandez, M. P. Hobson, and D. J. Rolfe, 2013, "A stochastic model for electron multiplication charge-coupled devices—From theory to practice," PLoS One **8**, e53671.

Hjort, N. L., 1990, "Nonparametric Bayes estimators based on beta processes in models for life history data," Ann. Stat. **18**, 1259–1294.

Hjort, N. L., C. Holmes, P. Müller, and S. G. Walker, 2010, Eds., *Bayesian Nonparametrics*, Cambridge Series in Statistical and Probabilistic Mathematics Vol. 28 (Cambridge University Press, Cambridge, England).

Hobolth, A., and E. A. Stone, 2009, "Simulation from endpoint-conditioned, continuous-time Markov chains on a finite state space, with applications to molecular evolution," Ann. Appl. Stat. **3**, 1204–1231.

Hofmann, M., C. Eggeling, S. Jakobs, and S. W. Hell, 2005, "Breaking the diffraction barrier in fluorescence microscopy at low light intensities by using reversibly photoswitchable proteins," Proc. Natl. Acad. Sci. U.S.A. **102**, 17565–17569.

Hopkins, H., 1946, "Herschel's condition," Proc. Phys. Soc. London **58**, 100.

Hoyer, P., *et al.*, 2016, "Breaking the diffraction limit of light-sheet fluorescence microscopy by RESOLFT," Proc. Natl. Acad. Sci. U.S.A. **113**, 3442–3446.

Huang, B., M. Bates, and X. Zhuang, 2009, "Super-resolution fluorescence microscopy," Annu. Rev. Biochem. **78**, 993–1016.

Huang, B., W. Wang, M. Bates, and X. Zhuang, 2008, "Three-dimensional super-resolution imaging by stochastic optical reconstruction microscopy," Science **319**, 810–813.

Huang, F., S. L. Schwartz, J. M. Byars, and K. A. Lidke, 2011, "Simultaneous multiple-emitter fitting for single molecule super-resolution imaging," Biomed. Opt. Express **2**, 1377–1393.

Huang, F., *et al.*, 2013, "Video-rate nanoscopy using sCMOS camera–specific single-molecule localization algorithms," Nat. Methods **10**, 653–658.

Huang, X., *et al.*, 2018, "Fast, long-term, super-resolution imaging with Hessian structured illumination microscopy," Nat. Biotechnol. **36**, 451–459.

Huisken, J., and D. Y. Stainier, 2007, "Even fluorescence excitation by multidirectional selective plane illumination microscopy (mSPIM)," Opt. Lett. **32**, 2608–2610.

Huisken, J., J. Swoger, F. Del Bene, J. Wittbrodt, and E. H. Stelzer, 2004, "Optical sectioning deep inside live embryos by selective plane illumination microscopy," Science **305**, 1007–1009.

Hulleman, C. N., R. Ø. Thorsen, E. Kim, C. Dekker, S. Stallinga, and B. Rieger, 2021, "Simultaneous orientation and 3D localization microscopy with a vortex point spread function," Nat. Commun. **12**, 5934.

Hummert, J., K. Yserentant, T. Fink, J. Euchner, Y. X. Ho, S. A. Tashev, and D.-P. Herten, 2021, "Photobleaching step analysis for robust determination of protein complex stoichiometries," Mol. Biol. Cell **32**, ar35.

Hwang, H., H. Kim, and S. Myong, 2011, "Protein induced fluorescence enhancement as a single molecule assay with short distance sensitivity," Proc. Natl. Acad. Sci. U.S.A. **108**, 7414–7418.

Itano, M. S., M. Bleck, D. S. Johnson, and S. M. Simon, 2016, "Readily accessible multiplane microscopy: 3D tracking the HIV-1 genome in living cells," Traffic **17**, 179–186.

Izeddin, I., M. El Beheiry, J. Andilla, D. Ciepielewski, X. Darzacq, and M. Dahan, 2012, "PSF shaping using adaptive optics for three-dimensional single-molecule super-resolution imaging and tracking," Opt. Express **20**, 4957–4967.

Jackson, J. D., 1999, *Classical Electrodynamics* (John Wiley & Sons, New York).

Jazani, S., I. Sgouralis, and S. Pressé, 2019, "A method for single molecule tracking using a conventional single-focus confocal setup," J. Chem. Phys. **150**, 114108.

Jazani, S., I. Sgouralis, O. M. Shafraz, M. Levitus, S. Sivasankar, and S. Pressé, 2019, "An alternative framework for fluorescence correlation spectroscopy," Nat. Commun. **10**, 3662.

Jazani, S., L. W. Q. Xu, I. Sgouralis, D. P. Shepherd, and S. Presse, 2022, "Computational proposal for tracking multiple molecules in a multifocus confocal setup," ACS Photonics **9**, 2489–2498.

Jerram, P., P. J. Pool, R. Bell, D. J. Burt, S. Bowring, S. Spencer, M. Hazelwood, I. Moody, N. Catlett, and P. S. Heyes, 2001, "The LLCCD: Low-light imaging without the need for an intensifier," in *Sensors and Camera Systems for Scientific, Industrial, and Digital Photography Applications II*, edited by N. Sampat, J. Canosa, M. M. Blouke, J. Canosa, and N. Sampat, SPIE Proceedings Vol. 4306 (SPIE—International Society for Optical Engineering, Bellingham, WA), pp. 178–186.

Ji, N., 2017, "Adaptive optical fluorescence microscopy," Nat. Methods **14**, 374–380.

Ji, N., D. E. Milkie, and E. Betzig, 2010, "Adaptive optics via pupil segmentation for high-resolution imaging in biological tissues," Nat. Methods **7**, 141–147.

Jia, S., J. C. Vaughan, and X. Zhuang, 2014, "Isotropic three-dimensional super-resolution imaging with a self-bending point spread function," Nat. Photonics **8**, 302–306.

Jin, D., P. Xi, B. Wang, L. Zhang, J. Enderlein, and A. M. Van Oijen, 2018, "Nanoparticles for super-resolution microscopy and single-molecule tracking," Nat. Methods **15**, 415–423.

Jin, L., B. Liu, F. Zhao, S. Hahn, B. Dong, R. Song, T. C. Elston, Y. Xu, and K. M. Hahn, 2020, "Deep learning enables structured illumination microscopy with low light levels and enhanced speed," Nat. Commun. **11**, 1934.

Jones, G. A., and D. S. Bradshaw, 2019, "Resonance energy transfer: From fundamental theory to recent applications," Front. Phys. **7**, 100.

Jouchet, P., C. Cabriel, N. Bourg, M. Bardou, C. Poüs, E. Fort, and S. Lévêque-Fort, 2021, "Nanometric axial localization of single fluorescent molecules with modulated excitation," Nat. Photonics **15**, 297–304.

Jradi, F. M., and L. D. Lavis, 2019, "Chemistry of photosensitive fluorophores for single-molecule localization microscopy," ACS Chem. Biol. **14**, 1077–1090.

Jünger, F., *et al.*, 2022, "100 Hz ROCS microscopy correlated with fluorescence reveals cellular dynamics on different spatiotemporal scales," Nat. Commun. **13**, 1758.

Jungmann, R., M. S. Avendaño, J. B. Woehrstein, M. Dai, W. M. Shih, and P. Yin, 2014, "Multiplexed 3D cellular super-resolution imaging with DNA-PAINT and Exchange-PAINT," Nat. Methods **11**, 313–318.

Kao, H. P., and A. Verkman, 1994, "Tracking of single fluorescent particles in three dimensions: Use of cylindrical optics to encode particle position," Biophys. J. **67**, 1291–1300.

Karpf, S., C. T. Riche, D. Di Carlo, A. Goel, W. A. Zeiger, A. Suresh, C. Portera-Cailliau, and B. Jalali, 2020, "Spectro-temporal encoded multiphoton microscopy and fluorescence lifetime imaging at kilohertz frame-rates," Nat. Commun. **11**, 2062.

Kasha, M., 1950, "Characterization of electronic transitions in complex molecules," Discuss. Faraday Soc. **9**, 14–19.

Kaye, B., P. J. Foster, T. Y. Yoo, and D. J. Needleman, 2017, "Developing and testing a Bayesian analysis of fluorescence lifetime measurements," PLoS One **12**, e0169337.

Keller, P. J., A. D. Schmidt, A. Santella, K. Khairy, Z. Bao, J. Wittbrodt, and E. H. Stelzer, 2010, "Fast, high-contrast imaging of animal development with scanned light sheet–based structured-illumination microscopy," Nat. Methods **7**, 637–642.

Keller, P. J., and E. H. Stelzer, 2008, "Quantitative *in vivo* imaging of entire embryos with digital scanned laser light sheet fluorescence microscopy," Curr. Opin. Neurobiol. **18**, 624–632.

Kilic, Z., I. Sgouralis, W. Heo, K. Ishii, T. Tahara, and S. Pressé, 2021, "Extraction of rapid kinetics from smFRET measurements using integrative detectors," Cell Rep. Phys. Sci. **2**, 100409.

Kilic, Z., I. Sgouralis, and S. Pressé, 2021, "Generalizing HMMs to continuous time for fast kinetics: Hidden Markov jump processes," Biophys. J. **120**, 409–423.

Kim, K., J. Yoon, S. Shin, S. Lee, S.-A. Yang, and Y. Park, 2016, "Optical diffraction tomography techniques for the study of cell pathophysiology," J. Biomed. Photonics Eng. **2**, 020201.

Klar, T. A., E. Engel, and S. W. Hell, 2001, "Breaking Abbe's diffraction resolution limit in fluorescence microscopy with stimulated emission depletion beams of various shapes," Phys. Rev. E **64**, 066613.

Knittel, Z., 1976, *Optics of Thin Films* (Wiley, London), p. 41.

Kobayashi, H., L.-P. Picard, A.-M. Schönegge, and M. Bouvier, 2019, "Bioluminescence resonance energy transfer–based imaging of protein-protein interactions in living cells," Nat. Protoc. **14**, 1084–1107.

Kriss, T. C., and V. M. Kriss, 1998, "History of the operating microscope: From magnifying glass to microneurosurgery", Neurosurgery **42**, 899–907.

Kristoffersen, A. S., S. R. Erga, B. Hamre, and Ø. Frette, 2014, "Testing fluorescence lifetime standards using two-photon excitation and time-domain instrumentation: Rhodamine B, coumarin 6 and lucifer yellow," J. Fluoresc. **24**, 1015–1024.

Kumagai, A., R. Ando, H. Miyatake, P. Greimel, T. Kobayashi, Y. Hirabayashi, T. Shimogori, and A. Miyawaki, 2013, "A bilirubin-inducible fluorescent protein from eel muscle," Cell **153**, 1602–1611.

Kwon, J., J. S. Park, M. Kang, S. Choi, J. Park, G. T. Kim, C. Lee, S. Cha, H. W. Rhee, and S. H. Shim, 2020, "Bright ligand-activatable fluorescent protein for high-quality multicolor live-cell super-resolution microscopy," Nat. Commun. **11**, 273.

Lai-Tim, Y., L. M. Mugnier, F. Orieux, R. Baena-Gallé, M. Paques, and S. Meimon, 2019, "Jointly super-resolved and optically sectioned Bayesian reconstruction method for structured illumination microscopy," Opt. Express **27**, 33251–33267.

Lakowicz, J. R., 2006, *Principles of Fluorescence Spectroscopy*, 3rd ed. (Springer, New York), pp. 1–954.

Lal, A., C. Shan, and P. Xi, 2016, "Structured illumination microscopy image reconstruction algorithm," IEEE J. Sel. Top. Quantum Electron. **22**, 50–63.

Lang, M., T. Müller, J. Engelhardt, and S. W. Hell, 2007, "4Pi microscopy of type A with 1-photon excitation in biological fluorescence imaging," Opt. Express **15**, 2459–2467.

Laplace, P.-S., 1820, *Théorie Analytique des Probabilités*, Vol. 7 (Courcier, Paris).

Laplace, P.-S., 1840, *Essai Philosophique sur les Probabilités* (Bachelier, Paris).

Lavis, L. D., 2017, "Chemistry is dead. Long live chemistry!," Biochemistry **56**, 5165–5170.

Le Cam, L. M., and G. L. Yang, 2000, *Asymptotics in Statistics: Some Basic Concepts* (Springer Science+Business Media, New York).

Lee, A., K. Tsekouras, C. Calderon, C. Bustamante, and S. Pressé, 2017, "Unraveling the thousand word picture: An introduction to super-resolution data analysis," Chem. Rev. **117**, 7276–7330.

Lee, J., and S. Pressé, 2012, "A derivation of the master equation from path entropy maximization," J. Chem. Phys. **137**, 074103.

Lee, K., K. Kim, J. Jung, J. Heo, S. Cho, S. Lee, G. Chang, Y. Jo, H. Park, and Y. Park, 2013, "Quantitative phase imaging techniques for the study of cell pathophysiology: From principles to applications," Sensors **13**, 4170–4191.

Lehmann, M., B. Gottschalk, D. Puchkov, P. Schmieder, S. Schwagerus, C. P. Hackenberger, V. Haucke, and J. Schmoranzer, 2015, "Multicolor caged dSTORM resolves the ultrastructure of synaptic vesicles in the brain," Angew. Chem., Int. Ed. **54**, 13230–13235.

Lelek, M., M. T. Gyparaki, G. Beliu, F. Schueder, J. Griffié, S. Manley, R. Jungmann, M. Sauer, M. Lakadamyali, and C. Zimmer, 2021, "Single-molecule localization microscopy," Nat. Rev. Methods Primers **1**, 39.

Lerner, E., T. Cordes, A. Ingargiola, Y. Alhadid, S. Chung, X. Michalet, and S. Weiss, "Toward dynamic structural biology: Two decades of single-molecule Förster resonance energy transfer," Science **359**, eaan1133, 2018.

Lessard, G. A., P. M. Goodwin, and J. H. Werner, 2007, "Three-dimensional tracking of individual quantum dots," Appl. Phys. Lett. **91**, 224106.

Lew, M. D., S. F. Lee, M. Badieirostami, and W. Moerner, 2011, "Corkscrew point spread function for far-field three-dimensional nanoscale localization of pointlike objects," Opt. Lett. **36**, 202–204.

Li, D., *et al.*, 2015, "Extended-resolution structured illumination imaging of endocytic and cytoskeletal dynamics," Science **349**, aab3500.

Li, H., and J. C. Vaughan, 2018, "Switchable fluorophores for single-molecule localization microscopy," Chem. Rev. **118**, 9412–9454.

Li, Y., M. Mund, P. Hoess, J. Deschamps, U. Matti, B. Nijmeijer, V. J. Sabinina, J. Ellenberg, I. Schoen, and J. Ries, 2018, "Real-time 3D single-molecule localization using experimental point spread functions," Nat. Methods **15**, 367–369.

Lichtman, J. W., and J.-A. Conchello, 2005, "Fluorescence microscopy," Nat. Methods **2**, 910–919.

Lidke, K. A., B. Rieger, T. M. Jovin, and R. Heintzmann, 2005, "Superresolution by localization of quantum dots using blinking statistics," Opt. Express **13**, 7052–7062.

Lippincott-Schwartz, J., and G. H. Patterson, 2009, "Photoactivatable fluorescent proteins for diffraction-limited and super-resolution imaging," Trends Cell Biol. **19**, 555–565.

Liu, G., X. Ruan, D. E. Milkie, F. Görlitz, M. Mueller, W. Hercule, A. Killilea, E. Betzig, and S. Upadhyayula, 2023, "Characterization, comparison, and optimization of lattice light sheets," Sci. Adv. **9**, eade6623.

Liu, S., and F. Huang, 2020, "Enhanced 4Pi single-molecule localization microscopy with coherent pupil based localization," Commun. Biol. **3**, 220.

Liu, S., E. B. Kromann, W. D. Krueger, J. Bewersdorf, and K. A. Lidke, 2013, "Three dimensional single molecule localization using a phase retrieved pupil function," Opt. Express **21**, 29462–29487.

Liu, S., M. J. Mlodzianoski, Z. Hu, Y. Ren, K. McElmurry, D. M. Suter, and F. Huang, 2017, "sCMOS noise-correction algorithm for microscopy images," Nat. Methods **14**, 760–761.

Liu, T.-L., *et al.*, 2018, "Observing the cell in its native state: Imaging subcellular dynamics in multicellular organisms," Science **360**, eaaq1392.

Lorén, N., *et al.*, 2015, "Fluorescence recovery after photobleaching in material and life sciences: Putting theory into practice," Q. Rev. Biophys. **48**, 323–387.

Louis, B., R. Camacho, R. Bresolí-Obach, S. Abakumov, J. Vandaele, T. Kudo, H. Masuhara, I. G. Scheblykin, J. Hofkens, and S. Rocha,

2020, "Fast-tracking of single emitters in large volumes with nanometer precision," Opt. Express **28**, 28656–28671.
Lukeš, T., P. Křížek, Z. Švindrych, J. Benda, M. Ovesný, K. Fliegel, M. Klíma, and G. M. Hagen, 2014, "Three-dimensional super-resolution structured illumination microscopy with maximum *a posteriori* probability image estimation," Opt. Express **22**, 29805–29817.
Luo, F., G. Qin, T. Xia, and X. Fang, 2020, "Single-molecule imaging of protein interactions and dynamics," Annu. Rev. Anal. Chem. **13**, 337–361.
Ma, Q., B. Khademhosseinieh, E. Huang, H. Qian, M. A. Bakowski, E. R. Troemel, and Z. Liu, 2016, "Three-dimensional fluorescent microscopy via simultaneous illumination and detection at multiple planes," Sci. Rep. **6**, 31445.
Ma, Y., K. Wen, M. Liu, J. Zheng, K. Chu, Z. J. Smith, L. Liu, and P. Gao, 2021, "Recent advances in structured illumination microscopy," J. Phys. Photonics **3**, 024009.
Madan, S. K., B. Bhaumik, and J. Vasi, 1983, "Experimental observation of avalanche multiplication in charge-coupled devices," IEEE Trans. Electron Devices **30**, 694–699.
Magde, D., E. L. Elson, and W. W. Webb, 1974, "Fluorescence correlation spectroscopy. II. An experimental realization," Biopolymers **13**, 29–61.
Mandracchia, B., X. Hua, C. Guo, J. Son, T. Urner, and S. Jia, 2020, "Fast and accurate sCMOS noise correction for fluorescence microscopy," Nat. Commun. **11**, 94.
Manley, S., J. M. Gillette, G. H. Patterson, H. Shroff, H. F. Hess, E. Betzig, and J. Lippincott-Schwartz, 2008, "High-density mapping of single-molecule trajectories with photoactivated localization microscopy," Nat. Methods **5**, 155–157.
Mansuripur, M., 1998, "Abbe's sine condition," Opt. Photonics News **9**, 56–60.
Mansuripur, M., 2002, *Classical Optics and Its Applications* (Cambridge University Press, Cambridge, England).
Marvin, M., 1961, "Microscopy apparatus," U.S. Patent No. 3,013,467.
Masullo, L. A., L. F. Lopez, and F. D. Stefani 2022, "A common framework for single-molecule localization using sequential structured illumination," Biophys. Rep. **2**, 100036.
Masullo, L. A., A. M. Szalai, L. F. Lopez, M. Pilo-Pais, G. P. Acuna, and F. D. Stefani, 2022, "An alternative to MINFLUX that enables nanometer resolution in a confocal microscope," Light Sci. Appl. **11**, 199.
Mazloom-Farsibaf, H., F. Farzam, M. Fazel, M. J. Wester, M. B. Meddens, and K. A. Lidke, 2021, "Comparing lifeact and phalloidin for super-resolution imaging of actin in fixed cells," PLoS One **16**, e0246138.
McGloin, D., and K. Dholakia, 2005, "Bessel beams: Diffraction in a new light," Contemp. Phys. **46**, 15–28.
McKinney, S. A., A.-C. Déclais, D. M. Lilley, and T. Ha, 2003, "Structural dynamics of individual Holliday junctions," Nat. Struct. Biol. **10**, 93–97.
McNeish, D., 2016, "On using Bayesian methods to address small sample problems," Struct. Equation Model. **23**, 750–773.
Meddens, M. B., S. Liu, P. S. Finnegan, T. L. Edwards, C. D. James, and K. A. Lidke, 2016, "Single objective light-sheet microscopy for high-speed whole-cell 3D super-resolution," Biomed. Opt. Express **7**, 2219–2236.
Mertz, J., 2019a, *Introduction to Optical Microscopy* (Cambridge University Press, Cambridge, England).
Mertz, J., 2019b, "Strategies for volumetric imaging with a fluorescence microscope," Optica **6**, 1261–1268.
Metropolis, N., A. W. Rosenbluth, M. N. Rosenbluth, A. H. Teller, and E. Teller, 1953, "Equation of state calculations by fast computing machines," J. Chem. Phys. **21**, 1087–1092.
Michalet, X., and A. J. Berglund, 2012, "Optimal diffusion coefficient estimation in single-particle tracking," Phys. Rev. E **85**, 061916.
Michalet, X., O. Siegmund, J. Vallerga, P. Jelinsky, J. Millaud, and S. Weiss, 2007, "Detectors for single-molecule fluorescence imaging and spectroscopy," J. Mod. Opt. **54**, 239.
Möckl, L., A. R. Roy, and W. Moerner, 2020, "Deep learning in single-molecule microscopy: Fundamentals, caveats, and recent developments," Biomed. Opt. Express **11**, 1633–1661.
Moerland, R. J., and J. P. Hoogenboom, 2016, "Subnanometer-accuracy optical distance ruler based on fluorescence quenching by transparent conductors," Optica **3**, 112–117.
Moerner, W., Y. Shechtman, and Q. Wang, 2015, "Single-molecule spectroscopy and imaging over the decades," Faraday Discuss. **184**, 9–36.
Mojiri, S., S. Isbaner, S. Mühle, H. Jang, A. J. Bae, I. Gregor, A. Gholami, and J. Enderlein, 2021, "Rapid multi-plane phase-contrast microscopy reveals torsional dynamics in flagellar motion," Biomed. Opt. Express **12**, 3169–3180.
Moser, S., M. Ritsch-Marte, and G. Thalhammer, 2019, "Model-based compensation of pixel crosstalk in liquid crystal spatial light modulators," Opt. Express **27**, 25046–25063.
Moskovits, M., and D. DiLella, 1982, "Intense quadrupole transitions in the spectra of molecules near metal surfaces," J. Chem. Phys. **77**, 1655–1660.
Moud, A. A., 2022, "Fluorescence recovery after photobleaching in colloidal science: Introduction and application," ACS Biomater. Sci. Eng. **8**, 1028–1048.
Mudry, E., K. Belkebir, J. Girard, J. Savatier, E. Le Moal, C. Nicoletti, M. Allain, and A. Sentenac, 2012, "Structured illumination microscopy using unknown speckle patterns," Nat. Photonics **6**, 312–315.
Müller, C. B., and J. Enderlein, 2010, "Image Scanning Microscopy," Phys. Rev. Lett. **104**, 198101.
Müller, M., V. Mönkemöller, S. Hennig, W. Hübner, and T. Huser, 2016, "Open-source image reconstruction of super-resolution structured illumination microscopy data in `ImageJ`," Nat. Commun. **7**, 10980.
Muñoz-Gil, G., *et al.*, 2021, "Objective comparison of methods to decode anomalous diffusion," Nat. Commun. **12**, 6253.
Murray, I., R. Adams, and D. MacKay, 2010, "Elliptical slice sampling," in *Proceedings of the Thirteenth International Conference on Artificial Intelligence and Statistics, Sardinia, Italy, 2010*, edited by Y. W. Teh and M. Titterington, pp. 541–548, https://proceedings.mlr.press/v9/murray10a.html.
Myong, S., S. Cui, P. V. Cornish, A. Kirchhofer, M. U. Gack, J. U. Jung, K.-P. Hopfner, and T. Ha, 2009, "Cytosolic viral sensor RIG-I is a 5'-triphosphate–dependent translocase on double-stranded RNA," Science **323**, 1070.
Nasr, S. H., and G. De Santillana, 1968, *Science and Civilization in Islam*, Vol. 16 (Harvard University Press, Cambridge, MA).
Neal, R. M., 2000, "Markov chain sampling methods for Dirichlet process mixture models," J. Comput. Graph. Stat. **9**, 249–265.
Nehme, E., B. Ferdman, L. E. Weiss, T. Naor, D. Freedman, T. Michaeli, and Y. Shechtman, 2021, "Learning optimal wavefront shaping for multi-channel imaging," IEEE Trans. Pattern Anal. Mach. Intell. **43**, 2179–2192.
Nehme, E., D. Freedman, R. Gordon, B. Ferdman, L. E. Weiss, O. Alalouf, T. Naor, R. Orange, T. Michaeli, and Y. Shechtman, 2020,

"DeepSTORM3D: Dense 3D localization microscopy and PSF design by deep learning," Nat. Methods **17**, 734–740.

Neil, M. A. A., R. Juškaitis, and T. Wilson, 1997, "Method of obtaining optical sectioning by using structured light in a conventional microscope," Opt. Lett. **22**, 1905–1907.

Nettels, D., A. Hoffmann, and B. Schuler, 2008, "Unfolded protein and peptide dynamics investigated with single-molecule FRET and correlation spectroscopy from picoseconds to seconds," J. Phys. Chem. B **112**, 6137–6146.

Noll, R. J., 1976, "Zernike polynomials and atmospheric turbulence," J. Opt. Soc. Am. **66**, 207.

Novotny, L., and B. Hecht, 2012, *Principles of Nano-optics* (Cambridge University Press, Cambridge, England).

Ober, R. J., S. Ram, and E. S. Ward, 2004, "Localization accuracy in single-molecule microscopy," Biophys. J. **86**, 1185–1200.

Oheim, M., A. Salomon, and M. Brunstein, 2020, "Supercritical angle fluorescence microscopy and spectroscopy," Biophys. J. **118**, 2339–2348.

Olarte, O. E., J. Andilla, E. J. Gualda, and P. Loza-Alvarez, 2018, "Light-sheet microscopy: A tutorial," Adv. Opt. Photonics **10**, 111–179.

Olver, F. W., D. W. Lozier, R. F. Boisvert, and C. W. Clark, 2010, *NIST Handbook of Mathematical Functions* (Cambridge University Press, Cambridge, England).

Oppenheim, A. V., and J. S. Lim, 1981, "The importance of phase in signals," Proc. IEEE **69**, 529–541.

Opstad, I. S., S. Acuña, L. E. V. Hernandez, J. Cauzzo, N. Škalko-Basnet, B. S. Ahluwalia, and K. Agarwal, 2020, "Fluorescence fluctuations-based super-resolution microscopy techniques: An experimental comparative study," arXiv:2008.09195.

Orieux, F., E. Sepulveda, V. Loriette, B. Dubertret, and J.-C. Olivo-Marin, 2012, "Bayesian estimation for optimized structured illumination microscopy," IEEE Trans. Image Process. **21**, 601–614.

Osseforth, C., J. R. Moffitt, L. Schermelleh, and J. Michaelis, 2014, "Simultaneous dual-color 3D STED microscopy," Opt. Express **22**, 7028–7039.

Paisley, J., and L. Carin, 2009, "Nonparametric factor analysis with beta process priors," in *Proceedings of the 26th Annual International Conference on Machine Learning, Montreal, 2009*, edited by A. Danyluk, L. Bottou, and M. Littman (Association for Computing Machinery, New York), pp. 777–784.

Palero, J., S. I. Santos, D. Artigas, and P. Loza-Alvarez, 2010, "A simple scanless two-photon fluorescence microscope using selective plane illumination," Opt. Express **18**, 8491–8498.

Pape, J. K., T. Stephan, F. Balzarotti, R. Büchner, F. Lange, D. Riedel, S. Jakobs, and S. W. Hell, 2020, "Multicolor 3D MINFLUX nanoscopy of mitochondrial MICOS proteins," Proc. Natl. Acad. Sci. U.S.A. **117**, 20607–20614.

Park, Y., C. Depeursinge, and G. Popescu, 2018, "Quantitative phase imaging in biomedicine," Nat. Photonics **12**, 578–589.

Patel, K. B., *et al.*, 2022, "High-speed light-sheet microscopy for the *in-situ* acquisition of volumetric histological images of living tissue," Nat. Biomed. Eng. **6**, 569–583.

Patel, L., N. Gustafsson, Y. Lin, R. Ober, R. Henriques, and E. Cohen, 2019, "A hidden Markov model approach to characterizing the photo-switching behavior of fluorophores," Ann. Appl. Stat. **13**, 1397–1429.

Pavani, S. R. P., and R. Piestun, 2008, "High-efficiency rotating point spread functions," Opt. Express **16**, 3484–3489.

Pavani, S. R. P., M. A. Thompson, J. S. Biteen, S. J. Lord, N. Liu, R. J. Twieg, R. Piestun, and W. E. Moerner, 2009, "Three-dimensional, single-molecule fluorescence imaging beyond the diffraction limit by using a double-helix point spread function," Proc. Natl. Acad. Sci. U.S.A. **106**, 2995–2999.

Pawley, J. B., 2006, Ed., *Handbook of Biological Confocal Microscopy* (Springer Science+Business Media, New York).

Pawlowska, M., R. Tenne, B. Ghosh, A. Makowski, and R. Lapkiewicz, 2022, "Embracing the uncertainty: The evolution of SOFI into a diverse family of fluctuation-based super-resolution microscopy methods," J. Phys. Photonics **4**, 012002.

Pennacchietti, F., E. O. Serebrovskaya, A. R. Faro, I. I. Shemyakina, N. G. Bozhanova, A. A. Kotlobay, N. G. Gurskaya, A. Bodén, J. Dreier, and D. M. Chudakov, 2018, "Fast reversibly photoswitching red fluorescent proteins for live-cell RESOLFT nanoscopy," Nat. Methods **15**, 601–604.

Perez, V., B.-J. Chang, and E. H. K. Stelzer, 2016, "Optimal 2D-SIM reconstruction by two filtering steps with Richardson-Lucy deconvolution," Sci. Rep. **6**, 37149.

Petrov, P. N., Y. Shechtman, and W. Moerner, 2017, "Measurement-based estimation of global pupil functions in 3D localization microscopy," Opt. Express **25**, 7945–7959.

Pirchi, M., R. Tsukanov, R. Khamis, T. E. Tomov, Y. Berger, D. C. Khara, H. Volkov, G. Haran, and E. Nir, 2016, "Photon-by-photon hidden Markov model analysis for microsecond single-molecule FRET kinetics," J. Phys. Chem. B **120**, 13065–13075.

Planchon, T. A., L. Gao, D. E. Milkie, M. W. Davidson, J. A. Galbraith, C. G. Galbraith, and E. Betzig, 2011, "Rapid three-dimensional isotropic imaging of living cells using Bessel beam plane illumination," Nat. Methods **8**, 417–423.

Planck, M., 1901, "On the law of distribution of energy in the normal spectrum," Ann. Phys. (Berlin) **4**, 553–562, http://strangepaths.com/files/planck1901.pdf.

Popescu, G., 2011, *Quantitative Phase Imaging of Cells and Tissues* (McGraw-Hill Education, New York).

Power, R. M., and J. Huisken, 2017, "A guide to light-sheet fluorescence microscopy for multiscale imaging," Nat. Methods **14**, 360–373.

Poynting, J. H., 1884, "XV. On the transfer of energy in the electromagnetic field," Phil. Trans. R. Soc. London **175**, 343–361.

Prabhat, P., S. Ram, E. Sally Ward, and R. J. Ober, 2004, "Simultaneous imaging of different focal planes in fluorescence microscopy for the study of cellular dynamics in three dimensions," IEEE Trans. NanoBiosci. **3**, 237–242.

Prasad, S., 2013, "Rotating point spread function via pupil-phase engineering," Opt. Lett. **38**, 585–587.

Preibisch, S., F. Amat, E. Stamataki, M. Sarov, R. H. Singer, E. Myers, and P. Tomancak, 2014, "Efficient Bayesian-based multiview deconvolution," Nat. Methods **11**, 645–648.

Pressé, S., and I. Sgouralis, 2023, *Data Modeling for the Sciences: Applications, Basics, Computations* (Cambridge University Press, Cambridge, England).

Qiao, C., *et al.*, 2023, "Rationalized deep learning super-resolution microscopy for sustained live imaging of rapid subcellular processes," Nat. Biotechnol. **41**, 367–377.

Quan, T., S. Zeng, and Z. Huang, 2010, "Localization capability and limitation of electron-multiplying charge-coupled, scientific complementary metal-oxide semiconductor, and charge-coupled devices for superresolution imaging," J. Biomed. Opt. **15**, 066005.

Quan, T., H. Zhu, X. Liu, Y. Liu, J. Ding, S. Zeng, and Z.-L. Huang, 2011, "High-density localization of active molecules using structured sparse model and Bayesian information criterion," Opt. Express **19**, 16963–16974.

Quinonero-Candela, J., and C. E. Rasmussen, 2005, "A unifying view of sparse approximate Gaussian process regression," J. Mach.

Learn. Res. **6**, 1939–1959, https://www.jmlr.org/papers/volume6/quinonero-candela05a/quinonero-candela05a.pdf.

Ram, S., D. Kim, R. J. Ober, and E. S. Ward, 2012, "3D single molecule tracking with multifocal plane microscopy reveals rapid intercellular transferrin transport at epithelial cell barriers," Biophys. J. **103**, 1594–1603.

Rao, C. R., 1992, "Information and the accuracy attainable in the estimation of statistical parameters," in *Breakthroughs in Statistics*, Springer Series in Statistics, edited by S. Kotz and N. L. Johnson (Springer, New York), pp. 235–247.

Rasmussen, C. E., 2003, "Gaussian processes in machine learning," in *Advanced Lectures on Machine Learning*, Lecture Notes in Computer Science Vol. 3176, edited by O. Bousquet, U. von Luxburg, and G. Rätsch (Springer, Berlin), pp. 63–71.

Rego, E. H., L. Shao, J. J. Macklin, L. Winoto, G. A. Johansson, N. Kamps-Hughes, M. W. Davidson, and M. G. Gustafsson, 2011, "Nonlinear structured-illumination microscopy with a photoswitchable protein reveals cellular structures at 50-nm resolution," Proc. Natl. Acad. Sci. U.S.A. **109**, E135–E143.

Reinhardt, S. C., *et al.*, 2023, "Ångström-resolution fluorescence microscopy," Nature (London) **617**, 711–716.

Remacha, E., L. Friedrich, J. Vermot, and F. O. Fahrbach, 2020, "How to define and optimize axial resolution in light-sheet microscopy: A simulation-based approach," Biomed. Opt. Express **11**, 8–26.

Renz, M., 2013, "Fluorescence microscopy—A historical and technical perspective," Cytometry Part A **83**, 767–779.

Resch-Genger, U., M. Grabolle, S. Cavaliere-Jaricot, R. Nitschke, and T. Nann, 2008, "Quantum dots versus organic dyes as fluorescent labels," Nat. Methods **5**, 763–775.

Reymond, L., J. Ziegler, C. Knapp, F.-C. Wang, T. Huser, V. Ruprecht, and S. Wieser, 2019, "SIMPLE: Structured illumination based point localization estimator with enhanced precision," Opt. Express **27**, 24578–24590.

Richards, B., and E. Wolf, 1959, "Electromagnetic diffraction in optical systems. II. Structure of the image field in an aplanatic system," Proc. R. Soc. A **253**, 358.

Richardson, S., and P. J. Green, 1997, "On Bayesian analysis of mixtures with an unknown number of components (with discussion)," J. R. Stat. Soc. B **59**, 731–792.

Riedl, J., *et al.*, 2008, "Lifeact: A versatile marker to visualize F-actin," Nat. Methods **5**, 605–607.

Rimoli, C. V., C. A. Valades-Cruz, V. Curcio, M. Mavrakis, and S. Brasselet, 2022, "4polar-STORM polarized super-resolution imaging of actin filament organization in cells," Nat. Commun. **13**, 301.

Roddier, F., 1999, *Adaptive Optics in Astronomy* (Cambridge University Press, Cambridge, England).

Rodríguez, C., and N. Ji, 2018, "Adaptive optical microscopy for neurobiology," Curr. Opin. Neurobiol. **50**, 83–91.

Rodríguez, C., *et al.*, 2021, "An adaptive optics module for deep tissue multiphoton imaging *in vivo*," Nat. Methods **18**, 1259–1264.

Rollins, G. C., J. Y. Shin, C. Bustamante, and S. Pressé, 2015, "Stochastic approach to the molecular counting problem in superresolution microscopy," Proc. Natl. Acad. Sci. U.S.A. **112**, E110–E118.

Rossow, M. J., J. M. Sasaki, M. A. Digman, and E. Gratton, 2010, "Raster image correlation spectroscopy in live cells," Nat. Protoc. **5**, 1761–1774.

Roth, S., C. J. Sheppard, and R. Heintzmann, 2016, "Superconcentration of light: Circumventing the classical limit to achievable irradiance," Opt. Lett. **41**, 2109–2112.

Roth, S., C. J. Sheppard, K. Wicker, and R. Heintzmann, 2013, "Optical photon reassignment microscopy (OPRA)," Opt. Nanosc. **2**, 5.

Rowley, M. I., A. C. Coolen, B. Vojnovic, and P. R. Barber, 2016, "Robust Bayesian fluorescence lifetime estimation, decay model selection and instrument response determination for low-intensity FLIM imaging," PLoS One **11**, e0158404.

Roy, R., S. Hohng, and T. Ha, 2008, "A practical guide to single-molecule FRET," Nat. Methods **5**, 507–516.

Ruckstuhl, T., and D. Verdes, 2004, "Supercritical angle fluorescence (SAF) microscopy," Opt. Express **12**, 4246–4254.

Ruh, D., J. Mutschler, M. Michelbach, and A. Rohrbach, 2018, "Superior contrast and resolution by image formation in rotating coherent scattering (ROCS) microscopy," Optica **5**, 1371–1381.

Rust, M. J., M. Bates, and X. Zhuang, 2006, "Sub-diffraction-limit imaging by stochastic optical reconstruction microscopy (STORM)," Nat. Methods **3**, 793–796.

Rybina, A., C. Lang, M. Wirtz, K. Grußmayer, A. Kurz, F. Maier, A. Schmitt, O. Trapp, G. Jung, and D. P. Herten, 2013, "Distinguishing alternative reaction pathways by single-molecule fluorescence spectroscopy," Angew. Chem., Int. Ed. **52**, 6322–6325.

Safar, M., A. Saurabh, M. Fazel, I. Sgouralis, and S. Pressé, 2022, "Single photon smFRET. III. Application to pulsed illumination," Biophys. Rep. **2**, 100088.

Saffarian, S., and T. Kirchhausen, 2008, "Differential evanescence nanometry: Live-cell fluorescence measurements with 10-nm axial resolution on the plasma membrane," Biophys. J. **94**, 2333–2342.

Sahl, S. J., and S. W. Hell, 2019, "High-resolution 3D light microscopy with STED and RESOLFT," in *High Resolution Imaging in Microscopy and Ophthalmology*, edited by J. Bille (Springer, Cham, Switzerland), pp. 3–32.

Sahl, S. J., S. W. Hell, and S. Jakobs, 2017, "Fluorescence nanoscopy in cell biology," Nat. Rev. Mol. Cell Biol. **18**, 685–701.

Santos, A., and I. T. Young, 2000, "Model-based resolution: Applying the theory in quantitative microscopy," Appl. Opt. **39**, 2948–2958.

Sapoznik, E., *et al.*, 2020, "A versatile oblique plane microscope for large-scale and high-resolution imaging of subcellular dynamics," eLife **9**, e57681.

Sarkar, A., J. Gallagher, I. Wang, G. Cappello, J. Enderlein, A. Delon, and J. Derouard, 2019, "Confocal fluorescence correlation spectroscopy through a sparse layer of scattering objects," Opt. Express **27**, 19382–19397.

Saurabh, A., P. T. Brown, J. S. Bryan IV, Z. R. Fox, R. Kruithoff, D. P. Shepherd, and S. P. Presse, 2023, "A structured illumination microscopy framework with spatial-domain noise propagation," 10.1101/2023.12.07.570701.

Saurabh, A., M. Fazel, M. Safar, I. Sgouralis, and S. Pressé, 2023, "Single photon smFRET. I. Theory and conceptual basis," Biophys. Rep. **3**, 100089.

Saurabh, A., S. Niekamp, I. Sgouralis, and S. Pressé, 2022, "Modeling non-additive effects in neighboring chemically identical fluorophores," J. Phys. Chem. B **126**, 4216–4225.

Saurabh, A., M. Safar, M. Fazel, I. Sgouralis, and S. Pressé, 2023, "Single photon smFRET. II. Application to continuous illumination," Biophys. Rep. **3**, 100087.

Schechner, Y. Y., R. Piestun, and J. Shamir, 1996, "Wave propagation with rotating intensity distributions," Phys. Rev. E **54**, R50(R).

Schermelleh, L., A. Ferrand, T. Huser, C. Eggeling, M. Sauer, O. Biehlmaier, and G. P. Drummen, 2019, "Super-resolution microscopy demystified," Nat. Cell Biol. **21**, 72–84.

Schmidt, R., T. Weihs, C. A. Wurm, I. Jansen, J. Rehman, S. J. Sahl, and S. W. Hell, 2021, "MINFLUX nanometer-scale 3D imaging

and microsecond-range tracking on a common fluorescence microscope," Nat. Commun. **12**, 1478.
Schneider, J., J. Zahn, M. Maglione, S. J. Sigrist, J. Marquard, J. Chojnacki, H.-G. Kräusslich, S. J. Sahl, J. Engelhardt, and S. W. Hell, 2015, "Ultrafast, temporally stochastic STED nanoscopy of millisecond dynamics," Nat. Methods **12**, 827–830.
Schnitzbauer, J., M. T. Strauss, T. Schlichthaerle, F. Schueder, and R. Jungmann, 2017, "Super-resolution microscopy with DNA-PAINT," Nat. Protoc. **12**, 1198–1228.
Schuler, B., 2018, "Perspective: Chain dynamics of unfolded and intrinsically disordered proteins from nanosecond fluorescence correlation spectroscopy combined with single-molecule FRET," J. Chem. Phys. **149**, 010901.
Scipioni, L., A. Rossetta, G. Tedeschi, and E. Gratton, 2021, "Phasor S-FLIM: A new paradigm for fast and robust spectral fluorescence lifetime imaging," Nat. Methods **18**, 542–550.
Scott, S. L., 2002, "Bayesian methods for hidden Markov models: Recursive computing in the 21st century," J. Am. Stat. Assoc. **97**, 337–351.
Sgouralis, I., A. P. Jalihal, L. W. Xu, N. G. Walter, and S. Presse, 2023, "Dynamic superresolution by Bayesian nonparametric image processing," 10.1101/2023.04.03.535459.
Sgouralis, I., S. Madaan, F. Djutanta, R. Kha, R. F. Hariadi, and S. Pressé, 2019, "A Bayesian nonparametric approach to single molecule Förster resonance energy transfer," J. Phys. Chem. B **123**, 675–688.
Sgouralis, I., and S. Pressé, 2017, "An introduction to infinite HMMs for single-molecule data analysis," Biophys. J. **112**, 2021–2029.
Sgouralis, I., M. Whitmore, L. Lapidus, M. J. Comstock, and S. Pressé, 2018, "Single molecule force spectroscopy at high data acquisition: A Bayesian nonparametric analysis," J. Chem. Phys. **148**, 123320.
Shack, R. V., and K. Thompson, 1980, "Influence of alignment errors of a telescope system on its aberration field," in *Optical Alignment I*," edited by R. N. Shagam and W. C. Sweatt, SPIE Proceedings Vol. 251 (SPIE—International Society for Optical Engineering, Bellingham, WA), pp. 146–153.
Shah, A., D. Knowles, and Z. Ghahramani, 2015, "An empirical study of stochastic variational inference algorithms for the beta Bernoulli process," in *International Conference on Machine Learning, Lille, France, 2015*, pp. 1594–1603, https://proceedings.mlr.press/v37/shahb15.pdf.
Shah, Z. H., M. Müller, T.-C. Wang, P. M. Scheidig, A. Schneider, M. Schüttpelz, T. Huser, and W. Schenck, 2021, "Deep-learning based denoising and reconstruction of super-resolution structured illumination microscopy images," Photonics Res. **9**, B168–B181.
Shajkofci, A., and M. Liebling, 2020, "Spatially-variant CNN-based point spread function estimation for blind deconvolution and depth estimation in optical microscopy," IEEE Trans. Image Process. **29**, 5848–5861.
Shao, L., P. Kner, E. H. Rego, and M. G. Gustafsson, 2011, "Super-resolution 3D microscopy of live whole cells using structured illumination," Nat. Methods **8**, 1044–1046.
Shapiro, J. H., 2008, "Computational ghost imaging," Phys. Rev. A **78**, 061802.
Shechtman, Y., Y. C. Eldar, O. Cohen, H. N. Chapman, J. Miao, and M. Segev, 2015, "Phase retrieval with application to optical imaging: A contemporary overview," IEEE Signal Process. Mag. **32**, 87–109.
Shechtman, Y., S. J. Sahl, A. S. Backer, and W. E. Moerner, 2014, "Optimal Point Spread Function Design for 3D Imaging," Phys. Rev. Lett. **113**, 133902.
Shechtman, Y., L. E. Weiss, A. S. Backer, M. Y. Lee, and W. Moerner, 2016, "Multicolour localization microscopy by point-spread-function engineering," Nat. Photonics **10**, 590–594.
Shen, H., L. J. Tauzin, R. Baiyasi, W. Wang, N. Moringo, B. Shuang, and C. F. Landes, 2017, "Single particle tracking: From theory to biophysical applications," Chem. Rev. **117**, 7331–7336.
Sheppard, C. J., 1988, "Super-resolution in confocal imaging," Optik (Jena, Ger.) **80**, 53, https://www.researchgate.net/publication/235994020_Super-resolution_in_confocal_imaging.
Sheppard, C. J., X. Gan, M. Gu, and M. Roy, 2006, "Signal-to-noise ratio in confocal microscopes," in *Handbook of Biological Confocal Microscopy*, edited by J. B. Pawley (Springer, New York), pp. 442–452.
Shi, Y., T. A. Daugird, and W. R. Legant, 2022, "A quantitative analysis of various patterns applied in lattice light sheet microscopy," Nat. Commun. **13**, 4607.
Shimomura, O., F. H. Johnson, and Y. Saiga, 1962, "Extraction, purification and properties of aequorin, a bioluminescent protein from the luminous hydromedusan, Aequorea," J. Cell. Comp. Physiol. **59**, 223–239.
Shroff, H., C. G. Galbraith, J. A. Galbraith, and E. Betzig, 2008, "Live-cell photoactivated localization microscopy of nanoscale adhesion dynamics," Nat. Methods **5**, 417–423.
Siemons, M., B. M. Cloin, D. M. Salas, W. Nijenhuis, E. A. Katrukha, and L. C. Kapitein, 2020, "Comparing strategies for deep astigmatism-based single-molecule localization microscopy," Biomed. Opt. Express **11**, 735–751.
Siemons, M., C. Hulleman, R. Thorsen, C. Smith, and S. Stallinga, 2018, "High precision wavefront control in point spread function engineering for single emitter localization," Opt. Express **26**, 8397–8416.
Sigal, Y. M., R. Zhou, and X. Zhuang, 2018, "Visualizing and discovering cellular structures with super-resolution microscopy," Science **361**, 880–887.
Smid, S. C., D. McNeish, M. Miočević, and R. van de Schoot, 2020, "Bayesian versus frequentist estimation for structural equation models in small sample contexts: A systematic review," Struct. Equation Model. **27**, 131–161.
Smith, A. M., 1996, *Ptolemy's Theory of Visual Perception: An English Translation of the Optics*, Vol. 82 (American Philosophical Society, Philadelphia).
Smith, C., M. Huisman, M. Siemons, D. Grünwald, and S. Stallinga, 2016, "Simultaneous measurement of emission color and 3D position of single molecules," Opt. Express **24**, 4996–5013.
Smith, C. S., *et al.*, 2021, "Structured illumination microscopy with noise-controlled image reconstructions," Nat. Methods **18**, 821–828.
Smith, E., and G. Dent, 2019, *Modern Raman Spectroscopy: A Practical Approach* (John Wiley & Sons, New York).
Solomon, O., M. Mutzafi, M. Segev, and Y. C. Eldar, 2018, "Sparsity-based super-resolution microscopy from correlation information," Opt. Express **26**, 18238–18269.
Sommerfeld, A., 1949, *Partial Differential Equations in Physics* (Academic Press, New York).
Specht, E. A., E. Braselmann, and A. E. Palmer, 2017, "A critical and comparative review of fluorescent tools for live-cell imaging," Annu. Rev. Physiol. **79**, 93–117.
Sprague, B. L., R. L. Pego, D. A. Stavreva, and J. G. McNally, 2004, "Analysis of binding reactions by fluorescence recovery after photobleaching," Biophys. J. **86**, 3473–3495.
Stallinga, S., and B. Rieger, 2010, "Accuracy of the Gaussian point spread function model in 2D localization microscopy," Opt. Express **18**, 24461–24476.

Stelzer, E. H., 2015, "Light-sheet fluorescence microscopy for quantitative biology," Nat. Methods **12**, 23–26.

Stelzer, E. H., F. Strobl, B.-J. Chang, F. Preusser, S. Preibisch, K. McDole, and R. Fiolka, 2021, "Light sheet fluorescence microscopy," Nat. Rev. Methods Primers **1**, 73.

Steward, G. C., 1927, "On Herschel's condition and the optical cosine law," Proc. Cambridge Philos. Soc. **23**, 703–712.

Stock, K., R. Sailer, W. S. Strauss, M. Lyttek, R. Steiner, and H. Schneckenburger, 2003, "Variable-angle total internal reflection fluorescence microscopy (VA-TIRFM): Realization and application of a compact illumination device," J. Microsc. **211**, 19–29.

Stockert, J. C., and A. Blázquez-Castro, 2017, *Fluorescence Microscopy in Life Sciences* (Bentham Science, Sharjah, United Arab Emirates).

Strauss, S., and R. Jungmann, 2020, "Up to 100-fold speed-up and multiplexing in optimized DNA-PAINT," Nat. Methods **17**, 789–791.

Ströhl, F., and C. F. Kaminski, 2016, "Frontiers in structured illumination microscopy," Optica **3**, 667–677.

Suhling, K., *et al.*, 2015, "Fluorescence lifetime imaging (FLIM): Basic concepts and some recent developments," Med. Photonics **27**, 3–40.

Swoger, J., P. Verveer, K. Greger, J. Huisken, and E. H. Stelzer, 2007, "Multi-view image fusion improves resolution in three-dimensional microscopy," Opt. Express **15**, 8029–8042.

Syed, A. J., and J. C. Anderson, 2021, "Applications of bioluminescence in biotechnology and beyond," Chem. Soc. Rev. **50**, 5668–5705.

Tao, X., O. Azucena, M. Fu, Y. Zuo, D. C. Chen, and J. Kubby, 2011, "Adaptive optics microscopy with direct wavefront sensing using fluorescent protein guide stars," Opt. Lett. **36**, 3389–3391.

Tauer, U., 2002, "Advantages and risks of multiphoton microscopy in physiology," Exp. Physiol. **87**, 709–714.

Tavakoli, M., S. Jazani, I. Sgouralis, W. Heo, K. Ishii, T. Tahara, and S. Pressé, 2020, "Direct photon-by-photon analysis of time-resolved pulsed excitation data using Bayesian nonparametrics," Cell Rep. Phys. Sci. **1**, 100234.

Tavakoli, M., S. Jazani, I. Sgouralis, O. M. Shafraz, S. Sivasankar, B. Donaphon, M. Levitus, and S. Pressé, 2020, "Pitching Single-Focus Confocal Data Analysis One Photon at a Time with Bayesian Nonparametrics," Phys. Rev. X **10**, 011021.

Tbakhi, A., and S. S. Amr, 2007, "Ibn Al-Haytham: Father of modern optics," Ann. Saudi Med. **27**, 464–467.

Thevathasan, J. V., *et al.*, 2019, "Nuclear pores as versatile reference standards for quantitative superresolution microscopy," Nat. Methods **16**, 1045–1053.

Thibodeau, P., 2016, "Ancient optics: Theories and problems of vision," in *A Companion to Science, Technology, and Medicine in Ancient Greece and Rome*, edited by G. L. Irby (John Wiley & Sons, New York), p. 130.

Thiele, J. C., D. A. Helmerich, N. Oleksiievets, R. Tsukanov, E. Butkevich, M. Sauer, O. Nevskyi, and J. Enderlein, 2020, "Confocal fluorescence-lifetime single-molecule localization microscopy," ACS Nano **14**, 14190–14200.

Tian, H., 2000, *Noise Analysis in CMOS Image Sensors* (Stanford University, Stanford).

Tinevez, J.-Y., N. Perry, J. Schindelin, G. M. Hoopes, G. D. Reynolds, E. Laplantine, S. Y. Bednarek, S. L. Shorte, and K. W. Eliceiri, 2017, "`TrackMate`: An open and extensible platform for single-particle tracking," Methods **115**, 80–90.

Toader, B., J. Boulanger, Y. Korolev, M. O. Lenz, J. Manton, C.-B. Schönlieb, and L. Mureşan, 2022, "Image reconstruction in light-sheet microscopy: Spatially varying deconvolution and mixed noise," J. Math. Imaging Vision **64**, 968–992.

Torres, T., and M. Levitus, 2007, "Measuring conformational dynamics: A new FCS-FRET approach," J. Phys. Chem. B **111**, 7392–7400.

Torres-García, E., *et al.*, 2022, "Extending resolution within a single imaging frame," Nat. Commun. **13**, 7452.

Tsai, Y.-C., *et al.*, 2020, "Rapid high resolution 3D imaging of expanded biological specimens with lattice light sheet microscopy," Methods **174**, 11–19.

Tsekouras, K., T. C. Custer, H. Jashnsaz, N. G. Walter, and S. Pressé, 2016, "A novel method to accurately locate and count large numbers of steps by photobleaching," Mol. Biol. Cell **27**, 3601–3615.

Tsien, R. Y., 1998, "The green fluorescent protein," Annu. Rev. Biochem. **67**, 509–544.

Tubbs, R. N., 2003, "Lucky exposures: Diffraction limited astronomical imaging through the atmosphere," arXiv:astro-ph/0311481.

Ulbrich, M. H., and E. Y. Isacoff, 2007, "Subunit counting in membrane-bound proteins," Nat. Methods **4**, 319–321.

Ulku, A. C., C. Bruschini, I. M. Antolović, Y. Kuo, R. Ankri, S. Weiss, X. Michalet, and E. Charbon, 2019, "A 512×512 SPAD image sensor with integrated gating for widefield FLIM,", IEEE J. Sel. Top. Quantum Electron. **25**, 1–12.

Valeur, B., and M. N. Berberan-Santos, 2012, *Molecular Fluorescence: Principles and Applications*, 2nd ed. (Wiley-VCH, Weinheim).

Valm, A. M., S. Cohen, W. R. Legant, J. Melunis, U. Hershberg, E. Wait, A. R. Cohen, M. W. Davidson, E. Betzig, and J. Lippincott-Schwartz, 2017, "Applying systems-level spectral imaging and analysis to reveal the organelle interactome," Nature (London) **546**, 162–167.

Van de Schoot, R., and M. Miocević, 2020, *Small Sample Size Solutions: A Guide for Applied Researchers and Practitioners* (Taylor & Francis, London).

van Dijk, R., D. Kalisvaart, J. Cnossen, and C. S. Smith, 2023, "Bayesian posterior density estimation reveals degeneracy in three-dimensional multiple emitter localization," Sci. Rep. **13**, 22372.

Vangindertael, J., I. Beets, S. Rocha, P. Dedecker, L. Schoofs, K. Vanhoorelbeke, J. Hofkens, and H. Mizuno, 2015, "Super-resolution mapping of glutamate receptors in *C. elegans* by confocal correlated PALM," Sci. Rep. **5**, 13532.

Van Kampen, N. G., 1992, *Stochastic Processes in Physics and Chemistry*, Vol. 1 (Elsevier, New York).

Vaughan, J. C., S. Jia, and X. Zhuang, 2012, "Ultrabright photoactivatable fluorophores created by reductive caging," Nat. Methods **9**, 1181–1184.

Vettenburg, T., H. I. Dalgarno, J. Nylk, C. Coll-Lladó, D. E. Ferrier, T. Čižmár, F. J. Gunn-Moore, and K. Dholakia, 2014, "Light-sheet microscopy using an Airy beam," Nat. Methods **11**, 541–544.

Vogelsang, J., R. Kasper, C. Steinhauer, B. Person, M. Heilemann, M. Sauer, and P. Tinnefeld, 2008, "A reducing and oxidizing system minimizes photobleaching and blinking of fluorescent dyes," Angew. Chem., Int. Ed. **47**, 5465–5469.

Voie, A. H., D. Burns, and F. Spelman, 1993, "Orthogonal-plane fluorescence optical sectioning: Three-dimensional imaging of macroscopic biological specimens," J. Microsc. **170**, 229.

Volpe, G., *et al.*, 2023, "Roadmap on deep learning for microscopy," arXiv:2303.03793v1.

von Diezmann, L., Y. Shechtman, and W. Moerner, 2017, "Three-dimensional localization of single molecules for super-resolution imaging and single-particle tracking," Chem. Rev. **117**, 7244–7275.

Wade, O. K., *et al.*, 2019, "124-Color super-resolution imaging by engineering DNA-PAINT blinking kinetics," Nano Lett. **19**, 2641–2646.

Wang, J., and C. Wang, 2008, "Optics in China", in *Encyclopaedia of the History of Science, Technology, and Medicine in Non-Western Cultures*, edited by H. Selin (Springer Netherlands, Dordrecht), pp. 1790–1792.

Wang, Q., and W. E. Moerner, 2013, "Lifetime and spectrally resolved characterization of the photodynamics of single fluorophores in solution using the anti-Brownian electrokinetic trap," J. Phys. Chem. B **117**, 4641–4648.

Wang, Z., *et al.*, 2021, "Real-time volumetric reconstruction of biological dynamics with light-field microscopy and deep learning," Nat. Methods **18**, 551–556.

Weiss, S., 1999, "Fluorescence spectroscopy of single biomolecules," Science **283**, 1676–1683.

Wells, N. P., G. A. Lessard, P. M. Goodwin, M. E. Phipps, P. J. Cutler, D. S. Lidke, B. S. Wilson, and J. H. Werner, 2010, "Time-resolved three-dimensional molecular tracking in live cells," Nano Lett. **10**, 4732–4737.

Weyl, H., 1919, "Ausbreitung elektromagnetischer wellen über einem ebenen leiter [Propagation of electromagnetic waves over a plane conductor]," Ann. Phys. (Berlin) **365**, 481–500.

Wildanger, D., R. Medda, L. Kastrup, and S. Hell, 2009, "A compact STED microscope providing 3D nanoscale resolution," J. Microsc. **236**, 35–43.

Wildanger, D., B. R. Patton, H. Schill, L. Marseglia, J. Hadden, S. Knauer, A. Schönle, J. G. Rarity, J. L. O'Brien, and S. W. Hell, 2012, "Solid immersion facilitates fluorescence microscopy with nanometer resolution and sub-ångström emitter localization," Adv. Mater. **24**, OP309–OP313.

Williams, R. M., W. R. Zipfel, and W. W. Webb, 2001, "Multiphoton microscopy in biological research," Curr. Opin. Chem. Biol. **5**, 603–608.

Winter, S., T. Campbell, L. Lin, S. Srivastava, and D. B. Dunson, 2023, "Machine learning and the future of Bayesian computation," arXiv:2304.11251.

Winterflood, C. M., T. Ruckstuhl, D. Verdes, and S. Seeger, 2010, "Nanometer Axial Resolution by Three-Dimensional Supercritical Angle Fluorescence Microscopy," Phys. Rev. Lett. **105**, 108103.

Wombacher, R., M. Heidbreder, S. Van De Linde, M. P. Sheetz, M. Heilemann, V. W. Cornish, and M. Sauer, 2010, "Live-cell super-resolution imaging with trimethoprim conjugates," Nat. Methods **7**, 717–719.

Wong, Y., Z. Lin, and R. J. Ober, 2011, "Limit of the accuracy of parameter estimation for moving single molecules imaged by fluorescence microscopy," IEEE Trans. Signal Process. **59**, 895–911.

Woringer, M., X. Darzacq, C. Zimmer, and M. Mir, 2017, "Faster and less phototoxic 3D fluorescence microscopy using a versatile compressed sensing scheme," Opt. Express **25**, 13668–13683.

Wu, L., C. Huang, B. P. Emery, A. C. Sedgwick, S. D. Bull, X.-P. He, H. Tian, J. Yoon, J. L. Sessler, and T. D. James, 2020, "Förster resonance energy transfer (FRET)-based small-molecule sensors and imaging agents," Chem. Soc. Rev. **49**, 5110–5139.

Wu, T., J. Lu, and M. D. Lew, 2022, "Dipole-spread-function engineering for simultaneously measuring the 3D orientations and 3D positions of fluorescent molecules," Optica **9**, 505–511.

Wu, Y., A. Ghitani, R. Christensen, A. Santella, Z. Du, G. Rondeau, Z. Bao, D. Colón-Ramos, and H. Shroff, 2011, "Inverted selective plane illumination microscopy (*i*SPIM) enables coupled cell identity lineaging and neurodevelopmental imaging in Caenorhabditis elegans," Proc. Natl. Acad. Sci. U.S.A. **108**, 17708–17713.

Wu, Y., and H. Shroff, 2018, "Faster, sharper, and deeper: Structured illumination microscopy for biological imaging," Nat. Methods **15**, 1011–1019.

Wunderlich, B., D. Nettels, S. Benke, J. Clark, S. Weidner, H. Hofmann, S. H. Pfeil, and B. Schuler, 2013, "Microfluidic mixer designed for performing single-molecule kinetics with confocal detection on timescales from milliseconds to minutes," Nat. Protoc. **8**, 1459–1474.

Xiao, S., H. Gritton, H.-A. Tseng, D. Zemel, X. Han, and J. Mertz, 2020, "High-contrast multifocus microscopy with a single camera and *z*-splitter prism," Optica **7**, 1477–1486.

Xu, L. W., I. Sgouralis, Z. Kilic, and S. Presse, 2023, "BNP-Track: A framework for multi-particle superresolved tracking," 10.1101/2023.04.03.535440.

Xu, L. W. Q., S. Jazani, Z. Kilic, and S. Presse, 2023, "Single-molecule reaction-diffusion," 10.1101/2023.09.05.556378.

Yang, B., *et al.*, 2022, "DaXi—High-resolution, large imaging volume and multi-view single-objective light-sheet microscopy," Nat. Methods **19**, 461–469.

Yang, Z., M. Prokopas, J. Nylk, C. Coll-Lladó, F. J. Gunn-Moore, D. E. Ferrier, T. Vettenburg, and K. Dholakia, 2014, "A compact Airy beam light sheet microscope with a tilted cylindrical lens," Biomed. Opt. Express **5**, 3434–3442.

Yeh, P., 1988, *Optical Waves in Layered Media* (Wiley, New York), p. 102.

York, A. G., P. Chandris, D. D. Nogare, J. Head, P. Wawrzusin, R. S. Fischer, A. Chitnis, and H. Shroff, 2013, "Instant super-resolution imaging in live cells and embryos via analog image processing," Nat. Methods **10**, 1122–1126.

York, A. G., A. Ghitani, A. Vaziri, M. W. Davidson, and H. Shroff, 2011, "Confined activation and subdiffractive localization enables whole-cell PALM with genetically expressed probes," Nat. Methods **8**, 327–333.

York, A. G., S. H. Parekh, D. D. Nogare, R. S. Fischer, K. Temprine, M. Mione, A. B. Chitnis, C. A. Combs, and H. Shroff, 2012, "Resolution doubling in live, multicellular organisms via multifocal structured illumination microscopy," Nat. Methods **9**, 749–754.

Zhang, B., J. Zerubia, and J.-C. Olivo-Marin, 2007, "Gaussian approximations of fluorescence microscope point-spread function models," Appl. Opt. **46**, 1819–1829.

Zhang, J., R. E. Campbell, A. Y. Ting, and R. Y. Tsien, 2002, "Creating new fluorescent probes for cell biology," Nat. Rev. Mol. Cell Biol. **3**, 906–918.

Zhang, W., and Q. Chen, 2009, "Signal-to-noise ratio performance comparison of electron multiplying CCD and intensified CCD detectors," in *Proceedings of the 2009 International Conference on Image Analysis and Signal Processing, Taizhou, China, 2009* (IEEE, New York), pp. 337–341.

Zhao, B., and J. Mertz, 2023, "Resolution enhancement with deblurring by pixel reassignment," Adv. Photonics **5**, 066004.

Zhao, T., S. C. Lau, Y. Wang, Y. Su, H. Wang, A. Cheng, K. Herrup, N. Y. Ip, S. Du, and M. Loy, 2016, "Multicolor 4D fluorescence microscopy using ultrathin Bessel light sheets," Sci. Rep. **6**, 26159.

Zheng, Q., S. Jockusch, Z. Zhou, and S. C. Blanchard, 2014, "The contribution of reactive oxygen species to the photobleaching of organic fluorophores," Photochem. Photobiol. **90**, 448–454.

Zheng, Q., *et al.*, 2019, "Rational design of fluorogenic and spontaneously blinking labels for super-resolution imaging," ACS Cent. Sci. **5**, 1602–1613.

Zitzmann, S., O. Lüdtke, A. Robitzsch, and M. Hecht, 2021, "On the performance of Bayesian approaches in small samples: A comment on Smid, McNeish, Miocevic, and van de Schoot (2020)," Struct. Equation Model. **28**, 40–50.

Zosel, F., D. Mercadante, D. Nettels, and B. Schuler, 2018, "A proline switch explains kinetic heterogeneity in a coupled folding and binding reaction," Nat. Commun. **9**, 3332.